

# **The Study of $^{116}\text{Sn}$ via Conversion-Electron Spectroscopy and $\gamma$ - $\gamma$ Angular Correlations**

**by**

**David Cross**

M.Sc., Simon Fraser University, 2009

B.Sc., Simon Fraser University, 2006

Thesis Submitted in Partial Fulfillment of the  
Requirements for the Degree of  
Doctor of Philosophy

in the  
Department of Chemistry  
Faculty of Science

**© David Cross 2017**

**SIMON FRASER UNIVERSITY**

**Fall 2017**

All rights reserved.

However, in accordance with the *Copyright Act of Canada*, this work may be reproduced without authorization under the conditions for “Fair Dealing.” Therefore, limited reproduction of this work for the purposes of private study, research, criticism, review and news reporting is likely to be in accordance with the law, particularly if cited appropriately. In addition, permission is granted for the copying and reproduction of this work for non-profit use without restriction.

## Approval

**Name:** David Cross  
**Degree:** Doctor of Philosophy (Chemistry)  
**Title:** *The Study of  $^{116}\text{Sn}$  via Conversion-Electron Spectroscopy and  $\gamma$ - $\gamma$  Angular Correlations*  
**Examining Committee:** **Chair:** Dr. Michael H. Eikerling  
Professor

**Dr. Corina Andreoiu**  
Senior Supervisor  
Associate Professor

---

**Dr. Gary W. Leach**  
Supervisor  
Associate Professor

---

**Dr. Krzysztof Starosta**  
Supervisor  
Associate Professor

---

**Dr. Loren Kaaake**  
Internal Examiner  
Assistant Professor  
Department of Chemistry

---

**Dr. Zsolt Podolyák**  
External Examiner  
Professor  
Department of Physics  
University of Surrey

---

**Date Defended/Approved:** December 6, 2017

## Abstract

The  $\beta^-$  decay of  $^{116m1}\text{In}$  ( $I^\pi = 5^+$ ), studied using the  $8\pi$  array at TRIUMF-ISAC, predominantly populated  $4^+$  states in the semi-magic daughter  $^{116}\text{Sn}$ , with 50 protons and 66 neutrons. The resulting electromagnetic decays to the ground state were studied through conversion-electron spectroscopy and through angular correlations of coincident gamma rays. Conversion-electron spectroscopy allowed measuring K-shell internal conversion coefficients ( $\alpha_K$ ), and angular correlations of coincident gamma rays allowed determinations of  $E2/M1$  mixing ratios ( $\delta$ ). These values are reported and used to infer aspects of the underlying nuclear structure of  $^{116}\text{Sn}$ . In the course of the analysis, several  $\alpha_K$  values were measured, of which three were measured for the first time in decay spectroscopy. Additionally, ten mixing ratios were measured, eight of which were not previously reported.

The 819 keV mixing ratio was re-measured with excellent agreement to literature results, whereas the 931 keV mixing ratio re-measurement indicates that the previously reported measurement requires a sign change. The 138 keV mixing ratio and  $\alpha_K$  were combined to measure an  $E0$  component, a possible signature of shape coexistence.

Measured transition mixing ratios between  $4^+$  states reveal that these highly-mixed states have similar  $M1$  transition strengths among them, but the  $E2$  transition strengths to lower-lying  $2^+$  states suggest underlying wavefunction differences that should be explored and interpreted with current and improved theoretical models of tin nuclei.

**Keywords:** angular correlations; mixing ratios; conversion electrons; gamma rays; nuclear spectroscopy

## **Acknowledgements**

First and foremost, I would like to thank Dr. Corina Andreoiu for her support through my time as a Ph, D student. In particular, in always demanding clarity of writing and expression, you have aided me in communicating my results without needless obfuscation. It has been a pleasure to work with you.

As well, I thank Dr. Gary Leach and Dr. Krzystof Starosta for their helpful suggestions and comments over the course of my work, even if they sometimes came as some tough questions to answer in committee meetings!

To Jennifer Pore, Fatima Garcia, Kenneth Whitmore, Aaron Chester, Jonathan Williams and Thomas Domingo, it has been a pleasure working with you all. Cheers!

The GRIFFIN/TIGRESS group have all been a pleasure to work with as well. Several people within that group deserve special mention for their helpful assistance in the course of my analysis. Dr, Adam Garnsworthy's data analysis meetings helped clarify some issues regarding the PACES analysis to obtain conversion-electron data.

Dr. Peter Bender helped me understand the theory and practice of angular correlations, as well as helping understand the mysteries of the programming language ROOT. In addition, Dr. David Miller also helpfully explained aspects of the angular-correlation method in assisting with some of the early stages of my analysis.

Dr. Paul Garrett of the University of Guelph helpfully clarified several questions I had from time to time, always graciously making time to do so.

I also must add my particular thanks to Dr. Gordon Ball, my former M. Sc. supervisor, who kindly devoted considerable time in discussions with me about the progress and course of my angular correlation analyses, as well as assisting in proofreading numerous drafts of my discussions of my results. Your help is greatly appreciated.

My roommate's cat, Khan, provided moral support by his relaxing presence in his many years with us.

And finally, my mother and father, Norita and James Cross, have been unwavering in their encouragement throughout my time at university, every step of the way from the beginning of my undergraduate studies onward. Thank you both very much.

# Table of Contents

Approval .....	ii
Abstract .....	iii
Acknowledgements .....	iv
Table of Contents .....	vi
List of Tables .....	ix
List of Figures .....	xi
Foreword .....	xx
<b>Chapter 1. Introduction .....</b>	<b>1</b>
1.1. The Atomic Nucleus .....	1
1.2. Nuclear Quantum Properties and Models .....	2
1.2.1. The Shell Model .....	6
1.2.2. Intruder States .....	11
1.2.3. The Collective Model: Rotations and Vibrations .....	13
1.3. Quantum Mechanical Mixing .....	17
1.3.1. Two-State Mixing .....	18
1.3.2. Multi-State Mixing .....	19
<b>Chapter 2. Nuclear Decays and Transitions .....</b>	<b>21</b>
2.1. Radioactive Decay .....	21
2.1.1. Beta Decay and Selection Rules .....	22
2.1.2. Gamma Emission and Selection Rules .....	26
2.1.3. Conversion-Electron Emission .....	28
2.2. Transition Strengths .....	31
2.2.1. $E0$ Transitions and Shape Coexistence .....	32
2.2.2. $E2$ and $M1$ Transitions .....	34
2.3. Theory of Angular Correlations .....	37
2.3.1. Angular Correlations in Radioactive Decay Experiments .....	37
2.3.2. The Angular Correlation Function .....	39
2.3.3. Mixing Ratios .....	41
2.3.4. $E0$ Components .....	44
<b>Chapter 3. Radiation Detectors and the <math>8\pi</math> Array .....</b>	<b>46</b>
3.1. Interactions of Ionizing Radiation and Particles with Matter .....	46
3.1.1. Charged Particles .....	46
3.1.2. Gamma Rays .....	47
3.2. Detecting Ionizing Radiation .....	48
3.2.1. HPGe Detectors .....	50
3.2.2. Lithium-Drifted Silicon Detectors .....	51

<b>Chapter 4. Objective and Motivation .....</b>	<b>55</b>
4.1. Overview of $^{116}\text{Sn}$ .....	55
4.2. Literature Review.....	58
4.3. The Low-Lying $2^+$ States .....	63
4.4. The Low-Lying $4^+$ States .....	67
4.5. The Vibrational Model Applied to $^{116}\text{Sn}$ .....	69
4.6. Other Models Applied to $^{116}\text{Sn}$ .....	71
4.7. Open Questions Regarding $^{116}\text{Sn}$ .....	73
<b>Chapter 5. Experimental Apparatus .....</b>	<b>75</b>
5.1. Generation of Radioactive Beams at TRIUMF-ISAC .....	75
5.2. The $8\pi$ Array at TRIUMF-ISAC .....	79
5.3. Detector Signal Flow Overview.....	84
5.4. Preparation for the Experiment.....	86
5.5. Beam Production and Delivery .....	87
5.6. Data Acquisition Setup .....	87
5.7. Calibrations for the Experiment.....	88
<b>Chapter 6. Analysis and Results.....</b>	<b>89</b>
6.1. Sorting the Data .....	89
6.1.1. Time Cuts .....	90
Removing Invalid Events Recorded by TDCs.....	90
Software BGO Suppression.....	92
HPGe-HPGe Coincidence Time Cuts.....	94
HPGe-PACES Coincidence Time Cuts .....	95
6.1.2. Gain Matching.....	97
6.1.3. The HPGe Array Efficiency Curve .....	98
6.1.4. The PACES Efficiency Curve.....	102
6.2. Conversion-Electron Data and Results .....	105
6.2.1. HPGe Singles and PACES Singles .....	105
6.2.2. PACES Relative Intensities in Singles.....	107
6.2.3. HPGe-PACES Coincidences.....	107
6.2.4. Experimentally Measured Internal Conversion Coefficients .....	112
6.2.5. K/L and L/M Ratios .....	113
6.2.6. Experimental $EO$ Strengths.....	114
6.3. Angular Correlation Results .....	117
6.3.1. $\gamma$ - $\gamma$ Angular Correlations .....	120
Analysis of the Symmetrized Matrices.....	123
Analysis of the Unsymmetrized Matrices.....	124
Plotting and Fitting Angular Correlation Data .....	125
6.3.2. Mixing Ratios in $^{116}\text{Sn}$ .....	132
<b>Chapter 7. Discussion .....</b>	<b>144</b>
7.1. The $2^+$ States .....	145

7.1.1.	The 2112 keV $2_2^+$ and 2225 keV $2_3^+$ Levels .....	145
7.1.2.	The 2650 keV $2_4^+$ Level .....	146
7.2.	The $4^+$ States .....	148
7.2.1.	The 2391, 2529, 2801, 3046 and 3097 keV $4_{1-5}^+$ Levels.....	149
7.3.	Absolute Transition Probabilities .....	160
<b>Chapter 8. Conclusion.....</b>		<b>161</b>
<b>References .....</b>		<b>163</b>
Appendix A.	Level Scheme of $^{116}\text{Sn}$ .....	173
Appendix B.	Gamma Ray Intensities and Branching Ratios.....	174
Appendix C.	$B(E2)$ and $B(M1)$ Values for Selected Transitions .....	176
Appendix D.	Derivation of $B(M1)$ and $B(E2)$ Formulas .....	177
Appendix E.	Nilsson Model Energy Level Diagrams .....	181
Appendix F.	The $m$ -scheme.....	184
Appendix G.	Wigner 3-j and 6-j Symbols .....	186
Appendix H.	GEANT4 Simulated Efficiency Comparison .....	187
Appendix I.	The Arns-Wiedenbeck Plot for the 819 keV $\delta$ .....	189
Appendix J.	Angular Correlation and $\chi^2/\nu$ Plots.....	191

## List of Tables

Table 1.	Selection rules showing permitted changes in spin ( $I$ ), isospin ( $T$ ) and parity ( $\pi$ ), as well as ranges of $\log ft$ values for given beta decays [2,34].	26
Table 2.	The $4_{1-5}^+$ states in $^{116}\text{Sn}$ and their half-lives.	68
Table 3.	Summary of two-broken-pair character of the $4_{1-5}^+$ states from Ref. [83]. States also assigned as part of the two-phonon triplet by Raman <i>et al.</i> are indicated by (2-ph).	68
Table 4.	The efficiency parameters for the $8\pi$ HPGe array.	101
Table 5.	The efficiency parameters for the PACES array.	104
Table 6.	K electron line relative intensities with respect to the 1294 keV transition. The energy shift to the corresponding K line is 29 keV. Dashes indicate no data reported. Asterisks mark transitions used to construct the PACES efficiency curve.	107
Table 7.	K-shell internal conversion coefficients for transitions in $^{116}\text{Sn}$ . Dashes indicate no data reported. Asterisks indicate values obtained from coincidence data. For mixed transitions, the last column gives the extreme limits for the pure transition multipolarities.	112
Table 8.	Experimental and theoretical K/L and L/M ratios for transitions in $^{116}\text{Sn}$ compared to those calculated from BrIccFO; in the last two columns the extreme limits are given for pure transition multipolarities if the transition is mixed. Asterisks mark transitions used in the PACES efficiency curve.	114
Table 9.	$\rho^2(E0)$ strengths in $^{116}\text{Sn}$ for $0^+ \rightarrow 0^+$ transitions.	115
Table 10.	Properties of the 1757 keV $0_2^+$ state in $^{116}\text{Sn}$ .	116
Table 11.	List of correlation angles (second column), obtained from the geometry in Figure 61, and the number of detector pairs in each angle (third column).	118
Table 12.	Summary of intense cascades in $^{116}\text{Sn}$ containing pure $E2$ transitions to test the angular correlation method. The first column labels the spins and parities according to Figure 18. The $A_{22}$ and $A_{44}$ values quoted here are theoretical values (see text).	128
Table 13.	Summary of $\chi^2$ analysis of the fits using the $A_{22}$ and $A_{44}$ coefficients given in Table 12. The second column labels the spins and parities according to Figure 18, with subscripts indicating the $n^{\text{th}}$ occurrence of the state.	129

Table 14.	Results of all angular correlation measurements on mixed-multipolarity transitions in $^{116}\text{Sn}$ , including those discussed in detail in the text. The second column gives the starting level energy of the cascade ( $E_1$ ) in keV, corresponding to $I_1^\pi$ . The third column labels the spin-parities of the states in the cascade for that row. The values of $A_{22}$ and $A_{44}$ are the ones obtained from the chosen values of $\delta$ . .....	134
Table 15.	For each row, the mixing ratio consistent with the associated absolute $B(E2)$ value, $\mu_K$ and $X$ is given, yielding the $E0$ strength in the final column for those values. ....	141
Table 16.	Relative $B(M1)$ values for transitions among the $4^+$ states, based on gamma ray intensities computed by Pore <i>et al.</i> (see Appendix B), and mixing ratios from this work. The largest relative $B(M1)$ exiting each level is normalized to 100. Transitions marked with an asterisk are assumed to be pure $M1$ . The 51 keV transition was not observed in the present work but is included for completeness. ....	150
Table 17.	Relative $B(E2)$ values for transitions to $2^+$ states, based on gamma ray intensities computed by Pore <i>et al.</i> (see Appendix B). The largest relative $B(E2)$ exiting each level is normalized to 100. Gamma rays in parentheses were not found in the level scheme but are included to illustrate the differences in decay patterns. ....	152

## List of Figures

Figure 1.	Oblate (left) and prolate (right) nuclear shapes. ....	3
Figure 2.	The Chart of the Nuclides, with proton number ( $Z$ ) on the $y$ -axis and neutron number ( $N$ ) on the $x$ -axis (stable isotopes – black; neutron-rich – pink; proton-rich – blue; alpha-decaying – yellow). The white $N = Z$ line and stable Sn isotopes (red box) are indicated. The $A \approx 16$ (blue circle) and $A \approx 209$ (purple circle) regions are also indicated. Adapted from Ref. [3]. ....	4
Figure 3.	The nuclear density function, shown semi-qualitatively with density on the $y$ -axis and the radius scaled to the atomic mass on the $x$ -axis. Adapted from [4] with permission. ....	5
Figure 4.	Qualitative nuclear average potential energy functions for protons (black) and neutrons (red). The potential energy is on the $y$ -axis and the distance away from the nuclear center is on the $x$ -axis. Adapted from [5] with permission. ....	5
Figure 5.	Representative shell-model energy level diagram. The magic numbers are circled in blue. ....	8
Figure 6.	Ground-state shell model occupancy of protons and neutrons for $^{116}\text{Sn}$ (left). Proton 2p-2h excitation in $^{116}\text{Sn}$ , assuming that the proton shell-model ordering above the $Z = 50$ gap follows the neutron occupancy (right). ....	10
Figure 7.	Experimental (white points) and theoretical (black points, see text) energies for the $2_1^+$ ( $\sim 1.2$ MeV) and $4_1^+$ states ( $\sim 2 - 2.5$ MeV) from $^{102}\text{Sn}$ to $^{128}\text{Sn}$ . Note the almost constant $2_1^+$ energies which are characteristic of seniority as a good quantum number. Reproduced with permission. [15] ....	11
Figure 8.	The evolution of “normal” shell model states (left) into the $^{32}\text{Ne}$ intruder configuration (right). Adapted from Ref. [17] with permission. ....	12
Figure 9.	Systematics of even- $A$ Sn isotopes with “normal” positive-parity states (green) originating from neutron broken-pair excitations and intruder positive-parity states (red) originating from proton 2p-2h excitations. Note the arrow indicating $^{116}\text{Sn}$ . Reproduced with permission [20]. ....	13
Figure 10.	Qualitative energy level diagram of rotational (left) and vibrational (right) states in nuclei, labelled with relative $B(E2)$ transition strength values (italicized numbers) between selected states. Adapted from Ref. [25]. ....	16

Figure 11.	A qualitative energy level diagram which shows the vibrational states up to the three-phonon level and the relative $E2$ transition strengths expected according to the vibrational model [26]. The arrows show the allowed transitions in this model. Reprinted with permission from Garrett, Green and Wood. Phys. Rev. C 78, 044307 [26]. Copyright 2008 American Physical Society. ....	17
Figure 12.	A general case of two-state mixing showing the unperturbed eigenstates ( $\phi_{1,2}$ ) and perturbed eigenstates ( $\psi_{1,2}$ ) and their corresponding energy separations $\Delta E_u$ and $\Delta E_p$ .....	18
Figure 13.	Generalized case of N-state mixing, showing the shift of energies with respect to the barycenter of the degenerate unmixed states.....	20
Figure 14.	Mass parabola for $A = 116$ as a function of atomic number $Z$ . Note that $Z = 50$ , $^{116}\text{Sn}$ , has the lowest mass and so is stable for this isobar. Data obtained from Ref. [31]. ....	23
Figure 15.	Shape coexistence in $^{186}\text{Pb}$ shown as a function of energy and position within the nuclear potential well. Note the energetic minima at $\sim 1.2$ MeV for the deformed $0^+$ states. Reprinted by permission from Macmillan Publishers Ltd: Nature 405, 430 (2000), copyright 2000.....	34
Figure 16.	A general representation of an angular correlation apparatus. The HPGe detector numbered 1 struck by $\gamma_1$ defines the first vector about which angles can be defined, for example with respect to $\gamma_2$ striking HPGe 2, so that the angle $\theta$ between them can be determined.....	38
Figure 17.	Qualitative 0-1-0 cascade. The blue arrows indicate transitions observed under the condition of examining gamma rays emitted at angles with respect to a chosen detector, while the red arrows indicate transitions that will not be observed. Adapted from [49] with permission.....	38
Figure 18.	Generalized cascade showing the coefficients involved in measuring angular correlations and the nuclear states involved, labelled by their spins. The transition gamma rays are labelled in the order they follow in a cascade.....	43
Figure 19.	Graph showing contributions to the total absorption of gamma radiation, with $Z_{\text{absorber}}$ on the y-axis and the energy on the x-axis (logarithmic scale). Note the dotted lines indicating the dominant gamma ray interactions for germanium and silicon. Reproduced and adapted with permission [61]. ....	48

Figure 20.	Schematic gamma ray spectrum, with energy in keV on the $x$ -axis and intensity in arbitrary units on the $y$ -axis. The solid peaks represent a detector with a delta-function energy resolution, while the dashed peaks represent a detector with a finite energy resolution. Image courtesy Nucleonica.com [63].	51
Figure 21.	Schematic diagram of a Si(Li) detector.	52
Figure 22.	Theoretical photon-response efficiency curves for Si(Li) detectors [65]. Reprinted from Nuclear Instruments and Methods Vol. 122, by Gallagher and Cipolla, page 405, copyright 1974, with permission from Elsevier.	52
Figure 23.	Conversion-electron spectrum (top) and gamma-ray spectrum (bottom) showing the 1063 keV transition in $^{207}\text{Pb}$ , as detected by a PACES Si(Li) detector and an $8\pi$ HPGe detector. Note the shifted K, L, M, etc. lines in the electron spectrum (e.g. the K binding energy is 88 keV [66], placing the 1063 keV K line at 975 keV).	53
Figure 24.	Close-up on one possible ordering of the shell-model orbitals that can be occupied by neutrons in $^{116}\text{Sn}$ .	56
Figure 25.	The peak at 1.84 MeV indicates that the $(^3\text{He},n)$ transfer reaction [87] populates the $0_2^+$ and $0_3^+$ states in $^{116}\text{Sn}$ . The $y$ -axis shows counts per channel and the $x$ -axis is the channel number. FIG. 2 reprinted from Fielding <i>et al.</i> , Nuclear Physics A 281, pages 389-404, copyright 1977, with permission from Elsevier.	57
Figure 26.	Partial level scheme adapted from Appendix A, with $E0$ transitions marked with dashed lines. Transitions not observed by Pore <i>et al.</i> [103] are noted in parentheses. The levels with thick black lines are two-phonon states according to Raman <i>et al.</i> [84]. States marked with red lines are part of the proton 2p-2h band as suggested by studies in the 1970s and 1980s [59,82,88,93]. The ground-state band in the middle is thought to be composed primarily of neutron broken-pair configurations with good seniority. The widths of the arrows are proportional to the relative gamma-ray intensities ( $I_\gamma(1294) = 100$ ).	58
Figure 27.	Comparison of experimental level energies to two different models, showing that the closely-spaced experimental $0_{2,3}^+$ states (red box) are not well-reproduced (blue boxes) from the models employed by Wenes <i>et al.</i> Reprinted FIG. 4 with permission from G. Wenes <i>et al.</i> , Phys. Rev. C, 23, 2291 (1981). Copyright 1981 by the American Physical Society.	61

Figure 28.	B( $E2$ ) values predicted by Wenes <i>et al.</i> for $^{116}\text{Sn}$ compared to then-current experimental data. Reprinted image of TABLE VI with permission from G. Wenes <i>et al.</i> , Phys. Rev. C, 23, 2291 (1981). Copyright 1981 by the American Physical Society. ....	62
Figure 29.	Relative B( $E2$ ) values for transitions in $^{116}\text{Sn}$ computed by Chen <i>et al.</i> , and compared to then-current experimental data. The calculations marked “b” are from the work by Chen <i>et al.</i> , while “c” is from the previous work by Song <i>et al.</i> [108]. Reproduced image of Table 4 from CHEN XiaoLin, LU DaHai, and YANG LiMing, Vol. 34, No. 2, September 15, 2000 pp.267-272 of Communications in Theoretical Physics with permission. ....	63
Figure 30.	Partial Nilsson model proton energy level diagram indicating the $\pi(g_{7/2} [431]1/2^+)$ orbital occupied in a 2p-2h excitation. The single-particle energies are on the y-axis in MeV and the deformation is on the x-axis. Diagram reproduced from Table of Isotopes, 1996 with permission (refer to Appendix E for the full-scale diagram). ....	65
Figure 31.	Partial Nilsson neutron energy level diagram indicating the $\nu(d_{5/2} [413]5/2)$ orbital occupied in the energetically-preferred neutron configuration of the 2225 keV $2_3^+$ state. As in Figure 30, the y-axis shows the single-particle energies and the x-axis, the deformation. Diagram reproduced from Table of Isotopes, 1996 with permission (refer to Appendix E for the full-scale diagram) .....	66
Figure 32.	Close-up on $4_{1-5}^+$ states in $^{116}\text{Sn}$ , adapted from the level scheme in Appendix A. Dashed blue boxes indicate states with fragmented $L = 4$ strength according to the ( $p.p'$ ) experiment of Wienke <i>et al.</i> [83]; the 51 keV transition was not observed in the present work or in the previous analysis by Pore <i>et al.</i> [102,103] due to experimental limitations (see the full discussion in Section 6.3). ....	67
Figure 33.	Representative relative B( $E2$ ) values from systematic studies of $^{110-116}\text{Cd}$ [113]; dashed lines indicate as-yet unobserved transitions for which upper limits are given on the B( $E2$ ) values. © IOP Publishing. Reproduced with permission. All rights reserved. ....	70
Figure 34.	Comparison of vibrational model predictions (left) of B( $E2$ ) values (boxed numbers) and level energies to experimental data (right, from the Nuclear Data Sheets [55]) for $^{116}\text{Sn}$ . The arrow widths are proportional to B( $E2$ ; 1294 keV) = 12.4(4) W.u. ....	70
Figure 35.	B( $E2$ ) trends in isotopes of Sn showing deviations from predictions assuming pure $\nu = 2$ wavefunctions for the first $2^+$ state (shown by the black curve) [97]. Other more complex models involving mixing together different shell-model occupancies are shown by the dashed and green curves. Reproduced and adapted with permission. ....	72

Figure 36.	QRPA predictions (black points) of the $2_1^+$ level energies (top) and $B(E2)$ values (bottom) compared to experimental data (red points). Reproduced from Ref. [117] under the Creative Commons Attribution License (CC BY).....	72
Figure 37.	The ISAC experimental hall (foreground) with the superconducting LINAC and ISAC-II experimental hall (background, with TIGRESS and EMMA). The $8\pi$ apparatus is shown in the stopped-beam area near the TRINAT and $\beta$ -NMR apparatus. Image courtesy of the TRIUMF Design Office [119]. .....	76
Figure 38.	Cross-sectional view of a TRIUMF-ISAC target holder. Note how the laser beam, if a laser ion source is used, shines directly into the surface ionization tube to enhance ionization of a desired isotope. (Courtesy Jens Lassen, TRIUMF. Used with permission) .....	77
Figure 39.	ISAC target stations and mass separator system, Fig. 1 reproduced from <i>Hyperfine Interactions</i> (2014) 225, pages 25 – 49, with permission from Springer [121].....	78
Figure 40.	The east half of the $8\pi$ array is shown here, surrounding the black Delrin target chamber. ....	80
Figure 41.	A view of the east half of the $8\pi$ array, which shows the HPGe detector Heavimet collimators without the Delrin absorbers. ....	82
Figure 42.	Cross-section of an $8\pi$ HPGe detector, showing the surrounding BGO shields as well as the Heavimet collimator and a Delrin absorber. Adapted from [61] with permission. ....	82
Figure 43.	The PACES array mounted in the upstream half of the Delrin target chamber.....	83
Figure 44.	The Zero-Degree plastic Scintillator (recessed) in the downstream half of the Delrin target chamber. The aluminized Mylar tape (black) is also visible. ....	83
Figure 45.	The $8\pi$ array with the open Moving Tape Collector box.....	84
Figure 46.	Flow diagram of the signal processing originating from a detector (either HPGe or SI(Li)) and terminating at the front-end. ....	85
Figure 47.	The raw HPGe array TDC times with blue lines showing where the TDC gate range was set. Note the logarithmic scale on the y-axis. There are 2 ns per channel on the x-axis.....	91
Figure 48.	The raw PACES array TDC times with blue lines showing where the TDC gate range was set. Note the logarithmic scale on the y-axis. There are 2 ns per channel on the x-axis. ....	92

Figure 49.	A representative TDC difference spectrum between HPGe 0 and its BGO shields, showing the region of zero counts caused by the hardware BGO suppression. There are 4 ns per channel on the $x$ -axis. ....	93
Figure 50.	HPGe-HPGe TDC difference spectrum. The dark blue lines represent approximately the gate region and the light purple lines, the background region. There are 4 ns per channel on the $x$ -axis. ....	94
Figure 51.	HPGe-PACES delta-ULM spectrum; note the logarithmic scale on the $y$ -axis. The centroid at 0 ns apart has been shifted to channel #8192. Each bin on the $x$ -axis represents 100 ns per channel, since each ULM tick is 100 ns long. The gate is between channels 8190 and 8193. ....	95
Figure 52.	HPGe-PACES TDC difference spectrum. The dark blue lines represent approximately the gate region and the light purple lines, the background region. There are 4 ns per channel on the $x$ -axis. ....	96
Figure 53.	HPGe array relative efficiency with $\ln \epsilon$ vs Energy (log scale) in keV. The $\chi^2/\nu = 0.80$ for this fit. ....	101
Figure 54.	Si(Li) efficiency curves compiled by Willett using two different HPGe efficiency curves (Groups A and B in the figure) [136]. Reprinted from Nuclear Instruments and Methods Volume 84, by Willett (1970), page 165, with permission from Elsevier. ....	103
Figure 55.	PACES relative efficiency curve from $^{116}\text{Sn}$ and $^{116\text{m}2}\text{In}$ gamma rays and corresponding K electron lines. The $\chi^2/\nu = 3.02$ for this fit. ....	104
Figure 56.	HPGe singles spectrum, with selected intense gamma rays labelled in keV. The 162 keV transition is from the $^{116\text{m}2}\text{In}$ isomer, visible in runs taken when the $^{116}\text{In}$ beam was directed into the $8\pi$ Delrin chamber. ....	106
Figure 57.	PACES singles spectrum with selected K electron lines labelled by their measured energies and corresponding gamma ray energies in parentheses. ....	106
Figure 58.	PACES conversion-electron spectra showing the 304 keV K electron line at 274 keV, visible in a background-subtracted coincidence gate on the 931 keV $\gamma$ ray (top), which is almost completely undetectable in singles (arrow, bottom). ....	108
Figure 59.	Close-up on a background-subtracted gate on the 463 keV gamma ray showing the effect of Compton scattering from the 819 keV gamma ray in introducing an artifact into the resulting projection. ....	109

Figure 60.	A series of gates (insets) and their projections revealing that the 56 keV (85 K) electron line is only visible when taking a gate around the 734 keV gamma ray. ....	111
Figure 61.	Pictorial representation of the $8\pi$ array as assembled at TRIUMF-ISAC, with numbers indicating which detector is at which position. The beam direction is from the left front to the right rear at an angle to the page. Reproduced with permission [47].....	117
Figure 62.	Close-up on the 400 – 500 keV region showing symmetrized (left) and unsymmetrized (right) $\gamma$ - $\gamma$ coincidence matrices. The indicated regions show that the events in the unsymmetrized matrix at (463 keV, 417 keV) are not identical to those at (417 keV, 463 keV).....	119
Figure 63.	Flow diagram of the angular correlation analysis depicting the creation and usage of symmetrized and unsymmetrized coincidence matrices. ....	120
Figure 64.	The eighteen $8\pi$ individual HPGe detector relative efficiency data points plotted with $\ln \epsilon$ vs Energy (log scale) in keV. The points are from standard sealed $^{133}\text{Ba}$ , $^{56}\text{Co}$ and $^{152}\text{Eu}$ sources. For clarity the error bars have been omitted. ....	121
Figure 65.	Close-up on the 0 – 500 keV region of Figure 64 showing representative relative efficiency curves from HPGe detectors 5 (red), 12 (green), and 15 (blue); the data points have been omitted for clarity. This illustrates the similarity of the curves above $\sim 200$ keV, but that they deviate quite significantly below that energy.....	122
Figure 66.	Angular correlation of the $2^+ - 0^+ - 2^+$ cascade in $^{116}\text{Sn}$ , yielding $N = 0.998 \pm 0.004$ . The data points are the averaged efficiency-corrected peak areas divided by the number of detector pairs in each correlation angle, scaled so the 180 degree point is exactly equal to 1.0. The $\chi^2/\nu$ of this data set is 0.39.....	126
Figure 67.	Plot of an angular correlation from symmetrized matrices, without an efficiency correction, of the $4_1^+ - 2_1^+ - 0_1^+$ cascade in $^{116}\text{Sn}$ , with $A_{22} = +0.1020$ and $A_{44} = +0.0091$ . The minimum $\chi^2/\nu$ of this fit was 5.52 for a $W(\theta) N = 0.9150$ . The uncertainties in each data point include only the statistical errors. ....	130
Figure 68.	Plot of an efficiency-corrected angular correlation of the $4_1^+ - 2_1^+ - 0_1^+$ cascade in $^{116}\text{Sn}$ , with $A_{22} = +0.1020$ and $A_{44} = +0.0091$ . The minimum $\chi^2/\nu$ of this fit was 0.14 for a $W(\theta) N = 0.9086$ , where the statistical errors of each data point have been augmented with the efficiency-correction and normalization systematic uncertainties. ....	131

Figure 69.	Plot of an efficiency-corrected angular correlation of the $0_2^+ - 2_1^+ - 0_1^+$ cascade in $^{116}\text{Sn}$ , with $A_{22} = +0.3571$ and $A_{44} = +1.1429$ . The minimum $\chi^2/\nu$ of this fit was 5.68 for a $W(\theta) N = 0.4439$ , where the statistical errors of each data point have been augmented with the efficiency-correction and normalization systematic uncertainties. ....	132
Figure 70.	Plot of the efficiency-corrected angular correlation of the $2_2^+ - 2_1^+ - 0_1^+$ cascade. The minimum $\chi^2/\nu$ of this fit was 1.43, and yielded $\delta = -1.83(8)$ , corresponding to $A_{22} = +0.31$ and $A_{44} = +0.25$ . ....	135
Figure 71.	Plot of $\chi^2/\nu$ as a function of $\arctan(\delta)$ in degrees for the 819-1294 cascade. The blue bar indicates the uncertainty limits at $\chi^2 + 1$ . ....	136
Figure 72.	Plot of the efficiency-corrected angular correlation of the $2_3^+ - 2_1^+ - 0_1^+$ cascade. The minimum $\chi^2/\nu$ of this fit was 1.87, and yielded $\delta = +1.75_{-0.47}^{+0.74}$ , corresponding to $A_{22} = -0.31$ and $A_{44} = +0.25$ . ....	137
Figure 73.	Plot of $\chi^2/\nu$ as a function of $\arctan(\delta)$ in degrees for the 931-1294 cascade. The blue bar indicates the uncertainty limits at $\chi^2 + 1$ . ....	138
Figure 74.	Plot of the efficiency-corrected angular correlation of the $3_1^- - 2_1^+ - 0_1^+$ cascade. The minimum $\chi^2/\nu$ of this fit was 1.60, and yielded $\delta = +0.02(6)$ , corresponding to $A_{22} = -0.058$ and $A_{44} = -0.000023$ . ....	139
Figure 75.	Plot of $\chi^2/\nu$ as a function of $\arctan(\delta)$ in degrees for the 973-1294 cascade. The blue bar indicates the uncertainty limits for the chosen value of $\delta$ . ....	140
Figure 76.	Plot of the efficiency-corrected angular correlation of the $4_2^+ - 4_1^+ - 2_1^+$ cascade. The minimum $\chi^2/\nu$ of this fit was 0.10, and yielded $\delta = -0.13(8)$ , corresponding to $A_{22} = +0.23$ and $A_{44} = +0.0026$ . ....	142
Figure 77.	Plot of $\chi^2/\nu$ as a function of $\arctan(\delta)$ in degrees for the 138-1097 cascade. The blue bar indicates the uncertainty limits at $\chi^2 + 1$ . ....	143
Figure 78.	Selected transitions de-exciting the 2225 keV $2_3^+$ and 2112 keV $2_2^+$ levels are shown, adapted from Figure 26. ....	145
Figure 79.	Selected transitions de-exciting the 2650 keV $2_4^+$ state are shown, adapted from Figure 26. Transitions indicated by parentheses have not been observed (see text for more detail). ....	146
Figure 80.	Partial level scheme showing the $4_{1-5}^+$ states as well as the 3033 keV $6^+$ state, and selected transitions to lower-lying states. Arrow widths are proportional to gamma-ray relative intensities ( $I_\gamma(1294) = 100$ ). ....	149

Figure 81.	The decays of the 2801 keV state, with transitions to the lower-lying $4_{1,2}^+$ states on the left and to the $2_{1,2}^+$ states on the right, with corresponding central values of the relative $MI$ and $E2$ strengths in red text (arrow widths are proportional to these values).....	153
Figure 82.	The decays of the 3033 keV state. The arrow widths are proportional to the relative $E2$ transition probabilities ( $B(E2; 503 \text{ keV}) = 100$ [88]). .....	154

## Foreword

**NI ƱAIRYƱEITƱANAƱAM ƱIZEI ƱASƱIOƱANƱNE, ƱR ƱIZEI ƱNƱƱASƱIOƱANƱNE.**

“Fixing a gaze not upon that which is seen, but upon that which is unseen.”

-- II Corinthians 4:18, Gothic Bible (Codex Ambrosianus)

# **Chapter 1. Introduction**

## **1.1. The Atomic Nucleus**

The atomic nucleus can never be seen with the naked eye. As such, it is the “unseen” whose presence nonetheless fundamentally governs the structure of matter that we can see and perceive. The electric charge of the nucleus affects the electrons surrounding it, giving rise to the chemical properties of atoms which underlie all of chemistry: from the organic molecules that make us up as human beings, to the exotic new materials fabricated in laboratories which transform the lives of all of humanity.

The nucleus itself is not merely a featureless point of positive charge, but a complex object in its own right. The properties of nuclei give rise to the rich structure of the nuclear landscape: from the stable isotopes that are manipulated chemically by nature and by humankind, to the heavy radioactive isotopes uranium and thorium, without which much of the modern world would be very different.

Although a nucleus cannot be seen directly, it can nevertheless be probed in several ways. One of them is through the emission of light (as gamma rays) as well as other forms of radiation as excited energy levels of a nucleus depopulate and eventually reach the ground state. From these radiations, much can be deduced about the properties of the nucleus under consideration.

## 1.2. Nuclear Quantum Properties and Models

Atomic nuclei, composed of protons and neutrons bound by the strong nuclear force, can be identified by their proton number ( $Z$ ), neutron number ( $N$ ), and mass number ( $A = Z + N$ ). For example, the nucleus  $^{116}\text{Sn}$  has 50 protons ( $Z = 50$ ) and 66 neutrons ( $N = 66$ ) to give  $A = 116$ . It is common to refer to protons and neutrons as nucleons when discussing aspects of their existence or behavior within a nucleus which do not uniquely depend on the fact that the proton has a positive charge while the neutron has no charge.

Nuclei also possess angular momentum ( $I$ ) which may be integer or half-integer, and definite parity ( $\pi$ ), which is either + or – and represents the symmetry of the nuclear wavefunction within the nuclear potential well; it is analogous to the molecular orbital symmetry labels gerade (g), which is even parity and ungerade (u), which is odd parity. For example, the ground-state spin and parity of  $^{116}\text{Sn}$  is  $I^\pi = 0^+$ .

Owing to the fact that the proton and neutron are very nearly identical in mass, another way to characterize them, and by extension, nuclei, is with a property termed isospin ( $T$ ), originally conceived by Wigner in analogy to the quantum theory of angular momentum [1]. In this formalism, the proton and neutron have  $T = 1/2$ , analogous to the intrinsic electron angular momentum  $s = 1/2$ . Consequently, just as the electron spin can be projected out on an arbitrary  $z$ -axis to yield  $m_s = +1/2$  or  $-1/2$ , so too can the neutron be assigned  $T_3 = +1/2$  and the proton,  $T_3 = -1/2$ . Therefore, for a nucleus, its isospin projection can be calculated by Equation (1),

$$T_3 = \frac{N - Z}{2} . \tag{1}$$

A nuclear state with a given 3-projection of isospin must have at least that magnitude of isospin (e.g.  $T_3 = -1$  implies at least  $T = 1$ ), much as a state of  $m_l = -1$  implies that  $l = 1$  at least.

Nuclei can also possess a nonspherical distribution of charge, quantified by the quadrupole moment  $Q_0$ . Depending on the value and sign, this means a nucleus can be spherical ( $Q_0 = 0$ ), or as shown in Figure 1, oblate ( $Q_0 < 0$ ) or prolate ( $Q_0 > 0$ ). A related measure of the nonsphericity of a nucleus is the quadrupole deformation parameter  $\beta_2$  (note that the subscripted 2 is sometimes omitted in the literature), and can be computed from the difference between the nuclear semimajor and semiminor axes  $\Delta R$  in Equation (2), where  $R_0 A^{1/3}$  is the average radius of a spherical nucleus with the same mass [2] ( $R_0$  is typically taken as 1.2 fm),

$$\beta_2 = \frac{4}{3} \sqrt{\frac{\pi}{5}} \frac{\Delta R}{R_0 A^{1/3}}. \quad (2)$$

The quadrupole moment  $Q_0$  and the deformation  $\beta_2$  are proportional to each other.

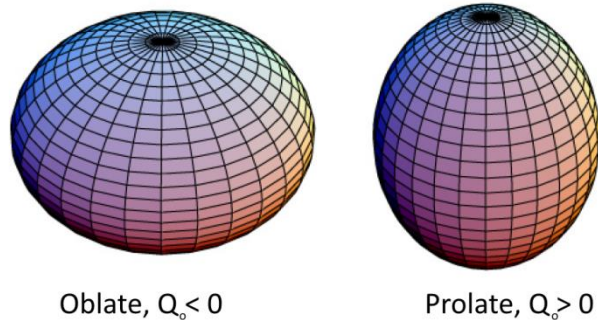


**Figure 1.** Oblate (left) and prolate (right) nuclear shapes.

In order to systematize nuclear properties, the Periodic Table (which itself systematizes atomic properties) can be expanded with proton number  $Z$  along the vertical axis and neutron number  $N$  along the horizontal axis, as seen in the Chart of the Nuclides in Figure 2. This chart shows that nuclei heavier than  $A \approx 16$  tend to favor a  $N/Z$  ratio larger than one, and that there is an energetically favored minimum with respect to radioactive decay, the valley of beta stability, along which the stable isotopes reside. Many of the nuclei on the nuclear chart below  $A = 209$  will tend to decay through  $\beta$  decay (see Section 2.1 for a discussion of nuclear decay modes).

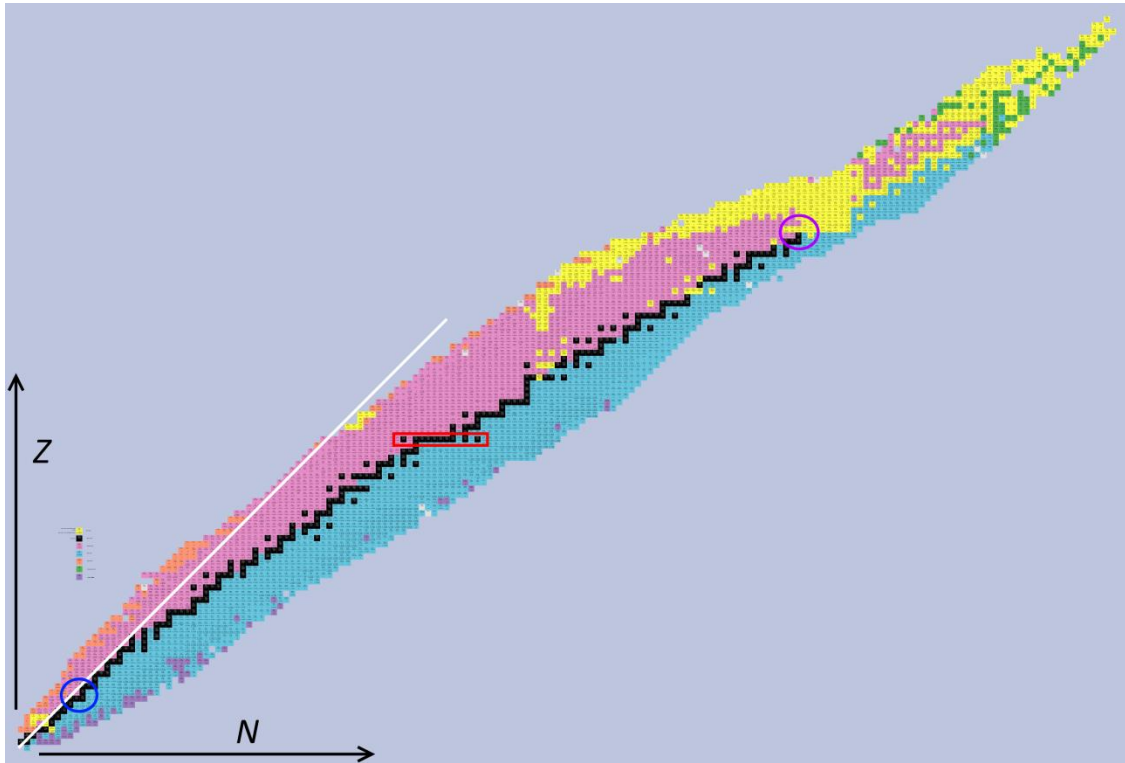


**Figure 2.** The Chart of the Nuclides, with proton number ( $Z$ ) on the  $y$ -axis and neutron number ( $N$ ) on the  $x$ -axis (stable isotopes – black; neutron-rich – pink; proton-rich – blue; alpha-decaying – yellow). The white  $N = Z$  line and stable Sn isotopes (red box) are indicated. The  $A \approx 16$  (blue circle) and  $A \approx 209$  (purple circle) regions are also indicated. Adapted from Ref. [3].

Nuclear models tend to be phenomenologically motivated from experimental results. One example was the need to develop a description of the forces within a nucleus: that is, what form does the nuclear potential energy function have? From charged-particle scattering experiments, it was found that the nuclear density was approximately constant through the bulk of the nuclear volume and decreased to zero near the edge, as seen in Figure 3. This behavior of the nuclear density can be assumed to arise from the properties of the strong interaction between nucleons, which are [2]:

- The interaction is of equal strength between two protons, two neutrons, or a proton and a neutron,
- The interaction is limited to the nearest neighbors of a given nucleon within the nucleus.

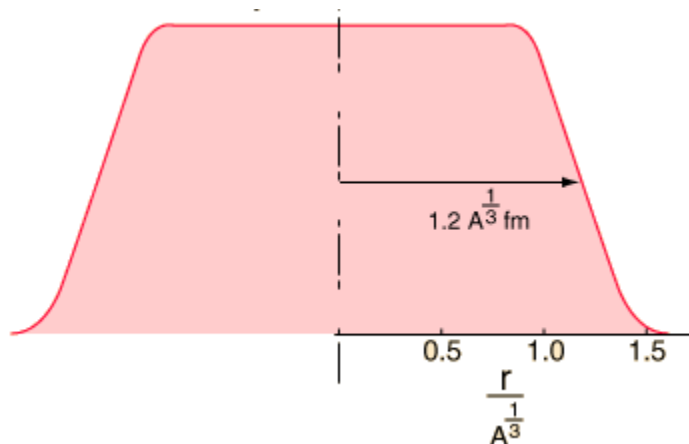


**Figure 3.** The nuclear density function, shown semi-qualitatively with density on the  $y$ -axis and the radius scaled to the atomic mass on the  $x$ -axis. Adapted from [4] with permission.

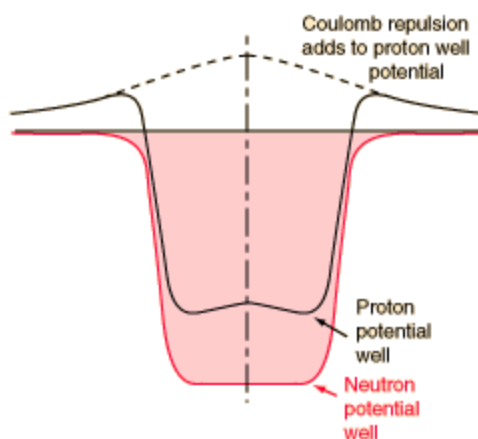


**Figure 4.** Qualitative nuclear average potential energy functions for protons (black) and neutrons (red). The potential energy is on the  $y$ -axis and the distance away from the nuclear center is on the  $x$ -axis. Adapted from [5] with permission.

The above-described features, taken together, indicate that like a droplet of water, the nuclear strong interaction saturates in the nuclear volume and decreases in strength only at the edges. Thus, Woods and Saxon [6] suggested that the potential energy function of a nucleus,  $U(r)$ , mimicked the density function in its shape, described in Equation (3), with a potential well depth  $U_0$  of approximately 50 MeV (the exact value depends on the nucleus), the spherical nuclear radius  $R = R_0 A^{1/3}$ , and a nuclear skin

thickness  $a$ , which accounts for the fact that a nucleus does not have a definite edge as seen in Figure 3 ( $a$  is typically on the order of 0.5 fm).

$$U(r) = \frac{-U_o}{1 + e^{\left(\frac{r-R}{a}\right)}} \quad (3)$$

Equation (3) gives rise to the shape of the neutron nuclear potential as seen in Figure 4, and with the addition of a Coulomb potential term, also gives rise to the proton nuclear potential seen in the same figure. The nuclear potential is self-generated within the nucleus because it arises from the forces between nucleons themselves, rather than being imposed by an external body, as is the case with electrons in atoms where the positively charged nucleus provides the attractive force experienced by the electrons.

### 1.2.1. The Shell Model

Nuclei, composed of fermions, have a shell structure analogous to the well-known shell structure of atoms. It was found experimentally that there were certain particularly stable proton and neutron “magic number” nuclear occupancies of  $Z, N = 2, 8, 20, 28, 50, 82$  and  $126$ , which represent fully-closed-shell configurations akin to the noble gases in chemistry, in which their valence s and p orbitals are fully populated with electrons. Also, in analogy to the high ionization energies and low electron affinities of the noble gases, nuclei with magic-number occupancies for  $Z$  or  $N$  have local maxima in their proton or neutron separation energies as well as local minima in their proton or neutron capture cross-sections. These observations led to the development of the shell model by Goeppert-Mayer [7] and Haxel, Jensen and Suess [8] in 1949. This model has as its basis the assumption that any given nucleon experiences an average potential energy that is spherically symmetric, which is exerted by all the other nucleons in the nucleus. One such potential is the previously-mentioned Woods-Saxon potential, which is an intermediate between a finite square well and a harmonic oscillator.

However, in order to theoretically reproduce the magic-number configurations within the nuclear shell model, it was necessary to add a very strong spin-orbit coupling to the nuclear Hamiltonian (Equation (4)),

$$U_{so}\langle \ell \bullet s \rangle = U_{so}(j(j+1) - \ell(\ell+1) - s(s+1)) . \quad (4)$$

Adding spin-orbit coupling to the shell model lifts the degeneracy of a shell-model state with orbital angular momentum  $\ell$  and intrinsic nucleon spin  $s = 1/2$  which combine to give an overall angular momentum  $j$ . Energetically, the rising part of the Woods-Saxon potential is shifted downwards when  $j = \ell + s$  and upwards when  $j = \ell - s$ .

In addition to the  $j$  and  $\ell$  quantum numbers that label  $2j+1$  degenerate shell-model states along with the intrinsic nucleon spin  $s$ , there is a numbering value  $n$  that is incremented with increasing energy for every time an orbital angular momentum (labelled by s, p, d, f, etc.) appears. This is not an analog to the principal quantum number in atomic structure; the value  $n$  does not fix a limit on  $\ell$ . The origin of ground state spins and parities in nuclei can be motivated by the shell model's aufbau-like rules about placing protons and neutrons independently within shell-model states, in which spin pairing is favored over spin multiplicity, and  $\pi = (-1)^\ell$ . Because of the spin-pairing preference, all nuclei with an even  $Z$  and  $N$  (even-even nuclei) have a ground-state  $I^\pi = 0^+$  as all the proton and neutron angular momenta are coupled together. For odd-even or even-odd nuclei, the shell model indicates that only the unpaired proton or neutron will govern the spin and parity for the entire nucleus, while for odd-odd nuclei the vector coupling of the unpaired proton and neutron angular momenta requires supplemental rules to choose which spin and parity is energetically favored.

Nuclei with a magic number of protons or neutrons, or both, will be spherical or have only a small deformation, i.e.  $\beta_2 \approx 0$  and  $Q_0 \approx 0$ . Another deformation parameter,  $\gamma$ , is the deviation from axial symmetry, typically also very small for magic-number nuclei. The nucleus  $^{116}\text{Sn}$ , which is the focus of this thesis, has a magic number of protons, with  $Z = 50$ . As such, it has a nearly spherical ground state, and thus  $\beta_2 \approx 0$ ,  $Q_0 \approx 0$  and  $\gamma \approx 0$ .

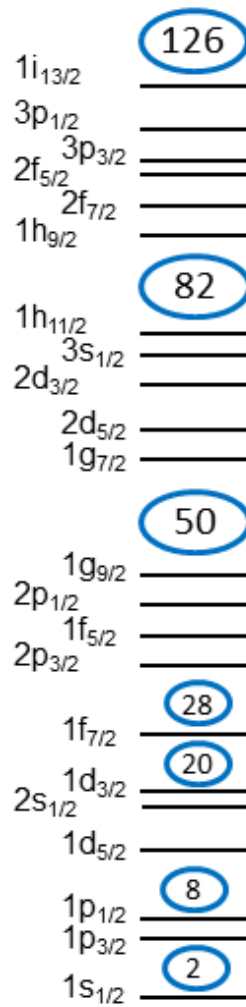


**Figure 5.** Representative shell-model energy level diagram. The magic numbers are circled in blue.

A representative shell-model orbital ordering, indicating the magic numbers, can be seen in Figure 5. The ordering is not absolute and there can be minor shifts in the energies of closely-spaced orbitals between major shell gaps as their occupancies change from one nucleus to the next. An example of these minor shifts can be seen in the systematics of the ground-state spins and parities of the stable or near-stable odd-*A* isotopes of tin: from <sup>113</sup>Sn through to <sup>119</sup>Sn, their ground-state spin-parities are all  $I^\pi = 1/2^+$  [9], suggesting that the valence 3s<sub>1/2</sub> orbital smoothly moves upward in energy with increasing neutron occupancy [10,11], so that the lone unpaired neutron would occupy that orbital for those isotopes.

Even within the rather large simplification of assuming only a spherically symmetric potential energy function, the shell model can be invoked to explain how excited-state spins and parities manifest from single-particle excitations within stable (or near-stable) nuclei which are close in proton or neutron number (or both) to the magic numbers. Moving further away from the magic numbers on the chart of the nuclides, it has been found that nuclei become deformed even in their ground states [2,12], which can be explained on the basis of a deformed nuclear potential lifting the degeneracy of  $m_j$  substates for given shell-model  $j$ -values, favoring a lower energetic minimum for the highest occupied nuclear orbital. For this reason, as well as requiring consideration of the interactions of all possible valence nucleons (in analogy to atoms whose outer electrons are of the most importance, “valence” here refers to nucleons occupying orbitals above the magic-number “core”), the shell model becomes computationally intractable in attempting to characterize the excited states of even-even deformed nuclei, and ground-state spins and parities for deformed odd-even, even-odd and odd-odd isotopes are not always easily predicted from a shell-model ordering like that of Figure 5.

The Nilsson model [13] accounts for the effect of lifting of the  $2j+1$  degeneracy of shell-model states by projecting out shell-model quantum numbers into a new set of quantum numbers (refer to Appendix E for more detail). Within the limits of computational tractability, this model can be used to relate orbital occupancies and the deformation of the state in question.

The shell model in the  $Z = 50$  region does not provide a complete description of excited states due to computational limitations, which comes from the fact that the stable isotopes of tin occupy a region near  $N = 66$ , which is between the  $N = 50$  and  $N = 82$  major shell gaps. This gives rise to the possibility, briefly discussed above, of low-lying excitations of the valence neutrons into the empty neutron orbitals between those major shell gaps, and so the neutron broken-pair excitations alone could potentially be computed 600 million different ways for  $^{116}\text{Sn}$ . The problem becomes multiplied enormously if a two-particle-two-hole (2p-2h) proton excitation occurs, bringing proton

pairs across the  $Z = 50$  major shell gap (One possible shell-model ordering is shown in Figure 6).

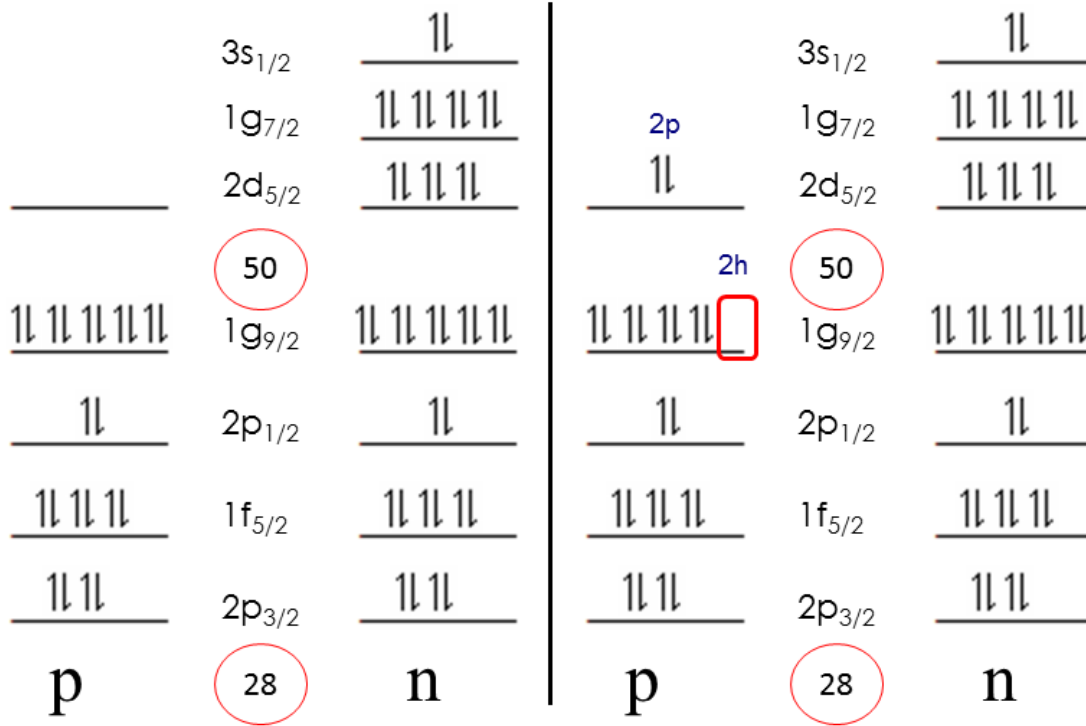


**Figure 6.** Ground-state shell model occupancy of protons and neutrons for  $^{116}\text{Sn}$  (left). Proton 2p-2h excitation in  $^{116}\text{Sn}$ , assuming that the proton shell-model ordering above the  $Z = 50$  gap follows the neutron occupancy (right).

To make the shell model computationally more tractable, a way to reduce the number of particles involved (“truncate the model space”) is to treat the nucleons as paired particles rather than individually. This is the basis of the seniority quantum number, denoted  $\nu$  [14]. As such,  $\nu = 0$  means no pairs are “broken” – that is, there is no particle coupling to generate excited states. For even-even nuclei such as the even- $A$  isotopes of tin, the ground state wavefunction will be predominantly  $\nu = 0$ .

The use of seniority as a good quantum number for some of the excited states of the even- $A$  isotopes of tin is evidenced in the ability to predict the  $2_1^+$  and  $4_1^+$  level energies reasonably accurately (Figure 7, showing experimental level energies compared to theoretical energies derived from Large-Scale Shell Model (LSSM) calculations based

on seniority model spaces). To generate these states, one neutron pair is broken, generating  $\nu = 2$  states, which, upon coupling their magnetic substates (a similar process can be undertaken when promoting one of the paired particles into a higher-lying orbital) yields even-spin angular momenta from  $0 \leq I \leq j_1 + j_2$  where  $j_1$  and  $j_2$  are the angular momenta of the broken pair of nucleons, subject to the Pauli Exclusion Principle. The method can be extended to  $\nu = 4$ , or a larger number of broken pairs as desired.

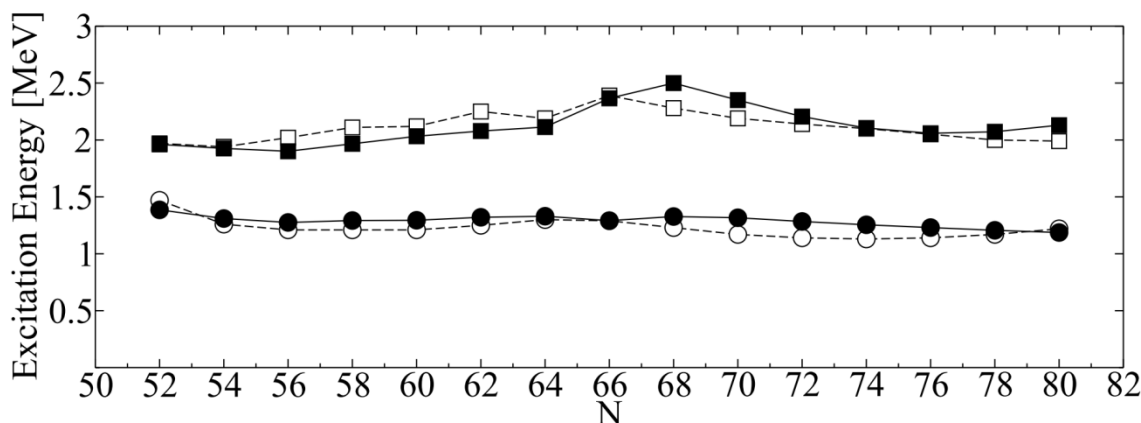


**Figure 7.** Experimental (white points) and theoretical (black points, see text) energies for the  $2_1^+$  ( $\sim 1.2$  MeV) and  $4_1^+$  states ( $\sim 2 - 2.5$  MeV) from  $^{102}\text{Sn}$  to  $^{128}\text{Sn}$ . Note the almost constant  $2_1^+$  energies which are characteristic of seniority as a good quantum number. Reproduced with permission. [15]

### 1.2.2. Intruder States

Interactions within nuclei can cause situations where a set (or manifold) of ground and excited states dominated by a (generally energetically-preferred) particular configuration are “intruded” upon by a state or states of a different configuration because the interactions lower the energy of the intruder alternate-configuration states. One example of intruder-state presence comes from drastic shifts in shell-model ordering, as opposed to the more typical slight changes caused by smoothly varying proton or neutron occupancies along the valley of beta stability (compare Figure 5 and Figure 6). For example, intruder states have been found in the vicinity of the nuclide  $^{32}\text{Na}$  in an “island of inversion” [16]. This is explained by a drastic shift downward in energy of a shell-

model orbital, usually across a major shell gap (Figure 8), “intruding” into an energy regime inhabited by orbitals that are normally expected to be present.

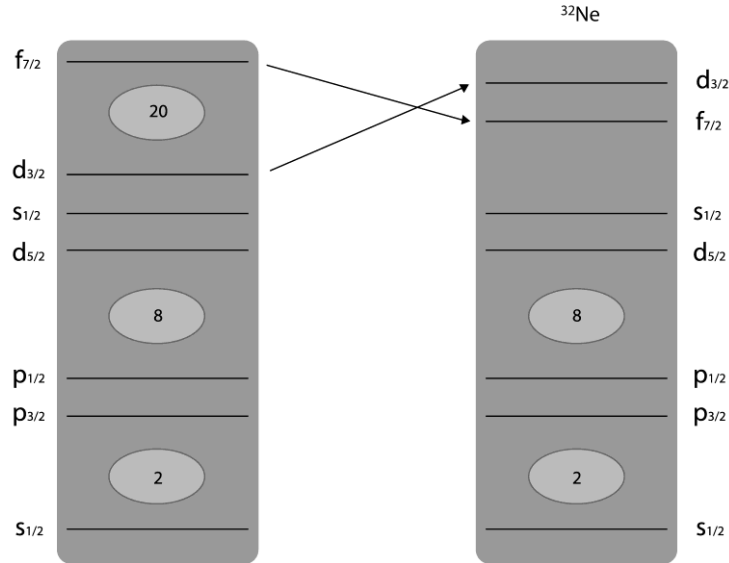


**Figure 8.** The evolution of “normal” shell model states (left) into the  $^{32}\text{Ne}$  intruder configuration (right). Adapted from Ref. [17] with permission.

Another way that an interaction can manifest in the form of low-lying intruder states is in the 2p-2h excitation in  $^{116}\text{Sn}$  mentioned in Section 1.2.1. The normal-configuration states in  $^{116}\text{Sn}$  are the yrast (lowest-energy for a given angular momentum)  $0_1^+$ ,  $2_1^+$  and  $4_1^+$  states, dominated by energetically-preferred neutron broken-pair configurations considered to be states of good seniority. The intruder 2p-2h  $0_2^+$ ,  $2_2^+$ , and  $4_2^+$  states arise from the two-proton excitation out of the closed proton “core”. Ordinarily the energy required to bring two protons across the  $Z = 50$  shell gap should be on the order of about 6 – 8 MeV [18]. However, the pairing interaction and coupling with the valence neutrons reduces this energy to about 2 MeV; in fact the pairing interaction can be shown, to first order, to vary in strength proportionally to the number of available neutron particles or holes, and so is at a maximum at  $N = 66$  [19]. This means that the 2p-2h states “intrude” into the energy range occupied by the normal-configuration states, analogous to the previous shell-model inversion example. The level energy systematics of

known “normal” (i.e. from neutron-only excitations) states and intruder states (from 2p-2h excitations) for isotopes of tin illustrate this effect as shown in Figure 9.

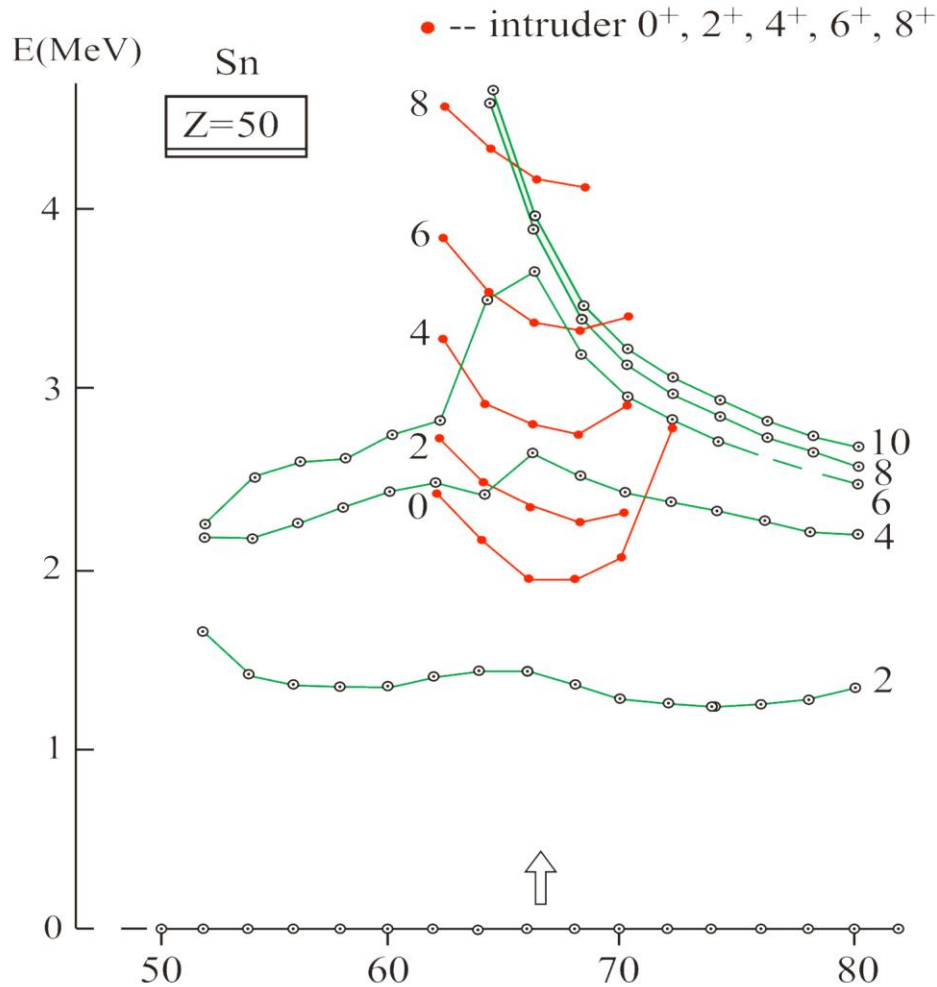


**Figure 9.** Systematics of even- $A$  Sn isotopes with “normal” positive-parity states (green) originating from neutron broken-pair excitations and intruder positive-parity states (red) originating from proton 2p-2h excitations. Note the arrow indicating  $^{116}\text{Sn}$ . Reproduced with permission [20].

### 1.2.3. The Collective Model: Rotations and Vibrations

Given the computational difficulties in applying the shell model when the occupancy of protons and neutrons is not near a magic number, or when attempting to reproduce excitations within magic-number nuclei that do not originate from single-

particle or quasiparticle excitations, the collective model, developed by Bohr and Mottelson [21], is used as an alternative. Here, the nucleus is described not in terms of its individual protons and neutrons, but rather by considering it as a whole in terms of linear combinations of spherical harmonics to describe its ground and excited states.

The collective model has proven to be very successful in explaining the features of deformed nuclei with rotational excited states; for example, the nucleus  $^{174}\text{Hf}$  [22]. This model can be invoked to explain not only the level energies of rotational excited states, but also the transition strengths (which are proportional to the squares of matrix elements) between those states. Equation (5) predicts the level energies of rotational states in nuclei, in which  $I$  is the nuclear spin,  $K$  is the projection of the nuclear angular momentum onto the body-fixed rotational symmetry axis and  $J$  is the moment of inertia.

$$E = \frac{\hbar^2}{2J} (I(I+1) - K^2) \quad (5)$$

Equation (5) thus predicts, based on the symmetry requirements for wavefunctions in a  $K = 0$  ground-state rotational band, a ratio of 3.33 between the level energies of the  $I^\pi = 4^+$  and the  $2^+$  states. In the case of  $^{174}\text{Hf}$ , with rotational level energies of 297 and 91 keV respectively, the ratio is 3.27. It is not exactly 3.33 due to the fact that a nucleus is not quite a rigid rotor [2].

Vibrational states within nuclei could be explained on the basis of a harmonic-oscillator type model, similar to that for the low-energy vibrational excitations within molecules, in which the ratios of excited-state energies to ground-state energies could be predicted on the basis of quadrupole phonon<sup>1</sup> excitations and the selection rule of only allowing a change of one phonon unit per transition. In this simple model, the level energy of the two-phonon excited state (a degenerate triplet with  $I^\pi = 0_2^+, 2_2^+$  and  $4_1^+$ ) will be twice that of the one-phonon excited state ( $I^\pi = 2_1^+$ ), and similarly for the higher-

---

<sup>1</sup> A phonon is a bosonic quantum with a spin  $\lambda = 2$ . Please consult Appendix F for a detailed description of the coupling of two phonons to generate the nuclear spins of the one and two-phonon states.

phonon states. Mathematically, this is expressed in Equation (6), and can be understood on the basis of the quantum mechanics of the five-dimensional harmonic oscillator<sup>2</sup> as outlined in Bohr and Mottelson [21].

$$\frac{E(4_1^+, 2_2^+, 0_2^+)}{E(2_1^+)} = 2 \quad (6)$$

The isotopes of cadmium were long considered good examples of vibrational nuclei. For example, the nuclide  $^{112}\text{Cd}$  [23] has a one-phonon excited state ( $I^\pi = 2_1^+$ ) at 618 keV, and two-phonon excited states at 1224, 1312 and 1416 keV ( $I^\pi = 0_2^+$ ,  $2_2^+$  and  $4_1^+$ , respectively). Just as molecular vibrational energy levels deviate from a ratio predicted in a similar manner to Equation (6) due to anharmonicities, the deviations from the exact ratio of 2 have been attributed to nuclear anharmonicities [21]. In fact for  $^{112}\text{Cd}$  the ratios are 2.0, 2.1 and 2.3, respectively, for the two-phonon excited states.

In addition to predicting the ratios of energy levels, the collective model as proposed by Bohr and Mottelson and further developed by Iachello and Arima [24] is also capable of predicting the transition strengths ( $B(E2)$  values, discussed in more detail in Section 2.2.2) between the states attributed to rotational or vibrational behavior. For rotational states in nuclei, the transition strength between rotational levels is proportional to the Clebsch-Gordan coefficients which connect the initial ( $I_i$ ) and final ( $I_f$ ) states and their projections ( $K$ ) onto the body-fixed symmetry axis [21], as shown in Equation (7), assuming a downward transition. It is also sensitive to the deformation expressed by the quadrupole moment  $Q_0$ . The value  $e$  is the fundamental unit of charge.

$$B(E2 \downarrow; I_i \rightarrow I_f) = \frac{5}{16\pi} e^2 Q_0^2 \left| \langle I_i 2K0 | I_i 2I_f K \rangle \right|^2 . \quad (7)$$

---

<sup>2</sup> There are some similarities to the three-dimensional harmonic oscillator in that the energies always increase by a multiple of  $\hbar\omega$ .

For vibrational nuclei, the transition strength of the two-phonon to one-phonon level should be twice that of the transition strength of the one-phonon level to the ground state. The formalism to describe these transition strengths is somewhat complex and not as easily reduced to Clebsch-Gordan projections as can be done for rotational states, but the resulting ratio of strengths is proportional to the number of phonons involved in the transition.

Figure 10 shows the relative energy differences of rotational and vibrational states in nuclei, as well as theoretical  $B(E2)$  values scaled to  $B(E2; 2_1^+ \rightarrow 0_1^+) = 1.00$  up to the two-phonon level. Figure 11 is a more detailed description of the model of vibrational states in nuclei which shows the transition strengths up to the three-phonon level, and the  $B(E2)$  values are scaled similarly.

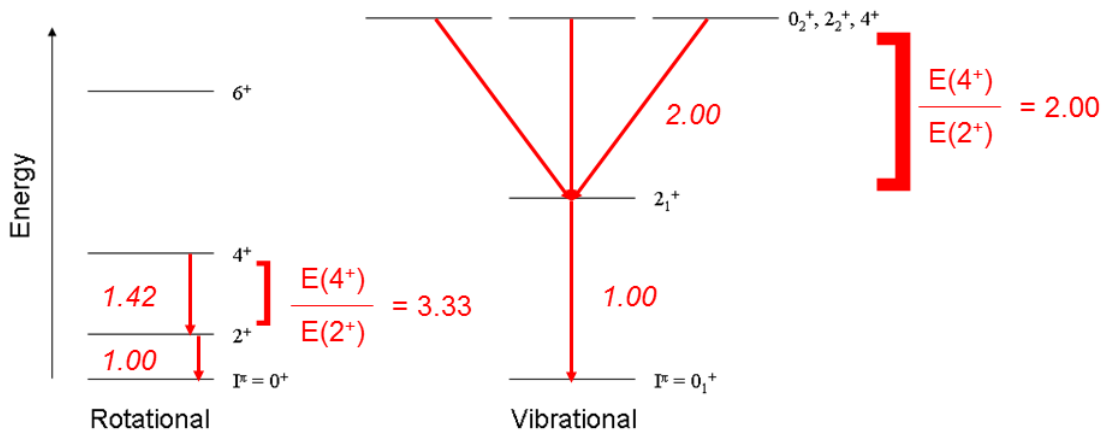


**Figure 10.** Qualitative energy level diagram of rotational (left) and vibrational (right) states in nuclei, labelled with relative  $B(E2)$  transition strength values (italicized numbers) between selected states. Adapted from Ref. [25].

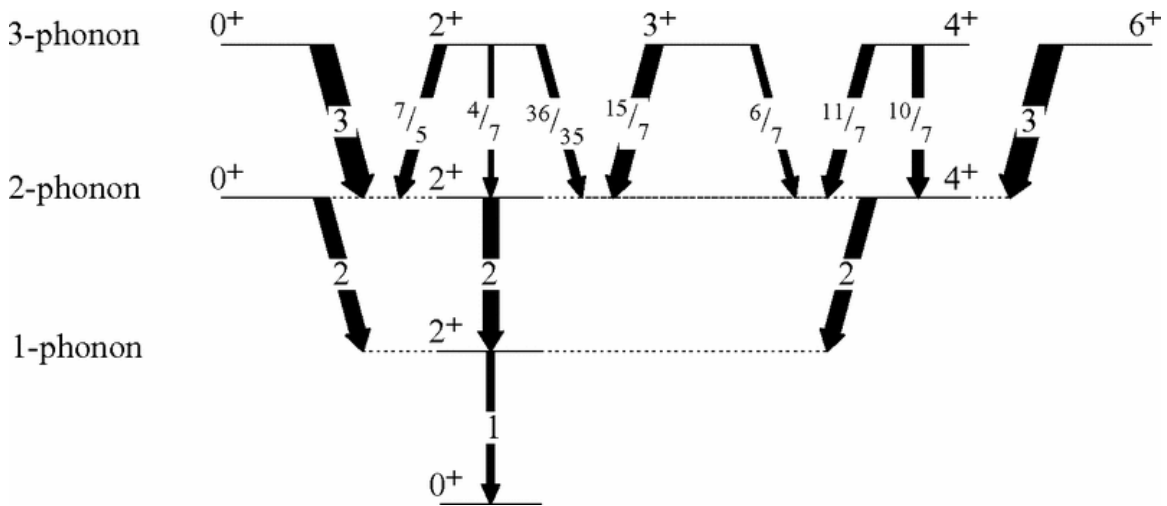


**Figure 11.** A qualitative energy level diagram which shows the vibrational states up to the three-phonon level and the relative  $E2$  transition strengths expected according to the vibrational model [26]. The arrows show the allowed transitions in this model. Reprinted with permission from Garrett, Green and Wood. Phys. Rev. C 78, 044307 [26]. Copyright 2008 American Physical Society.

It should be noted that in general, the shell and collective models as applied to nuclei with pure wavefunctions rarely hold true in practice. For example, deviations of vibrational-state energies from predicted values are attributed to nuclear anharmonicities. This implies that the wavefunctions of phonon states could contain admixtures of other components that lift the degeneracy of two-phonon or three-phonon states. Similarly, rotational states may couple to non-rotational excitations, which would introduce admixtures to the rotational wavefunctions. There are also single-particle (for odd-even or even-odd nuclei) or quasiparticle (commonly seen in even-even nuclei) excitations which themselves may be composed of admixtures of different shell-model orbitals.

### 1.3. Quantum Mechanical Mixing

Quantum mechanical eigenstates do not always have a single wavefunction component. In the nuclear case, oftentimes the wavefunction for a given ground or excited state is best expressed as a linear combination of some chosen set of basis functions with a Hamiltonian that includes any interactions between them. The following

two sections describe two special cases: two-state mixing and degenerate multi-state mixing. These special cases often yield useful physical insights into otherwise complex quantum-mechanical systems.

### 1.3.1. Two-State Mixing

A rather simple model of quantum mechanical systems, which can be applied to a number of situations, is the idea of two-state mixing [27] for either degenerate or nondegenerate states. In this model, the originating states experience an interaction between them; the exact nature of the interaction varies from system to system and may be phenomenological rather than motivated by any underlying properties of the system. Ultimately, the interaction modifies the energies of the mixed states; as shown in Figure 12, the separation between the states increases.

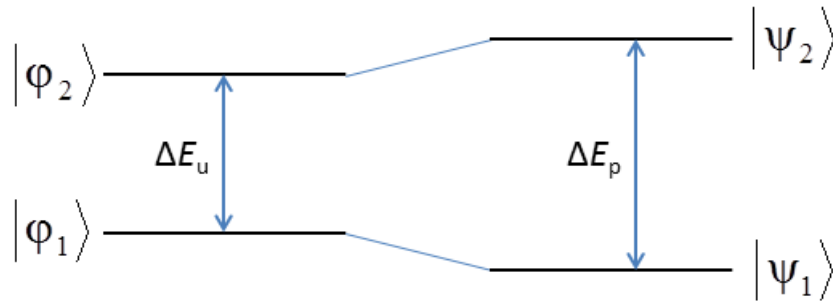


**Figure 12.** A general case of two-state mixing showing the unperturbed eigenstates ( $\phi_{1,2}$ ) and perturbed eigenstates ( $\psi_{1,2}$ ) and their corresponding energy separations  $\Delta E_u$  and  $\Delta E_p$ .

Mathematically, the unperturbed system of eigenstates  $|\phi_1\rangle$  and  $|\phi_2\rangle$  is affected by an interaction operator  $\hat{V}$  with a corresponding energy eigenvalue  $V$ , resulting in the perturbed eigenstates  $|\psi_1\rangle$  and  $|\psi_2\rangle$ . The resulting effect of the interaction on the state energies in terms of the energy separations  $\Delta E_u$  (for unperturbed) and  $\Delta E_p$  (for perturbed) is shown in Equation (8),

$$\Delta E_p = \Delta E_u \sqrt{1 + \frac{4V^2}{(\Delta E_u)^2}} \quad (8)$$

The corresponding wavefunctions can then be written in terms of two parameters  $\alpha$  and  $\beta$ , in which enforcement of normalization requires  $\alpha^2 + \beta^2 = 1$ . Upon expressing  $\beta$  in terms of the unperturbed-state separation  $\Delta E_u$  and the interaction energy  $V$ ,

$$\beta = \frac{1}{\sqrt{1 + \left( \frac{\Delta E_u}{2V} + \sqrt{1 + \frac{(\Delta E_u)^2}{4V^2}} \right)^2}}, \quad (9)$$

the perturbed eigenstates are then expressed as in Equation (10).

$$\begin{aligned} |\psi_1\rangle &= \alpha|\phi_1\rangle + \beta|\phi_2\rangle \\ |\psi_2\rangle &= -\beta|\phi_1\rangle + \alpha|\phi_2\rangle \end{aligned} \quad (10)$$

This model can be invoked to explain nuclear phenomena such as shape coexistence, discussed further in Section 2.2.1, in which the parameters  $\alpha$  and  $\beta$  can be related to the difference in nuclear radii of the states involved [28]. Another example of the use of two-state mixing is to show that when two states differing by one phonon unit mix together [29], the resulting interaction parameters can be related to an experimentally measured quantity called the  $E2/M1$  mixing ratio, discussed further in Section 2.3.3.

### 1.3.2. Multi-State Mixing

As there are different possibilities for how three, four, etc. states can mix together, this work will present the final result of the case where the states are initially degenerate, and they are all affected by the interaction operator  $\hat{V}$  (see Ref. [27] for details). The resulting effect on the energies is to raise all the states but one by the eigenvalue  $V$ , and lower one by a factor proportional to the number of states participating ( $N$ ), as shown in Figure 13.

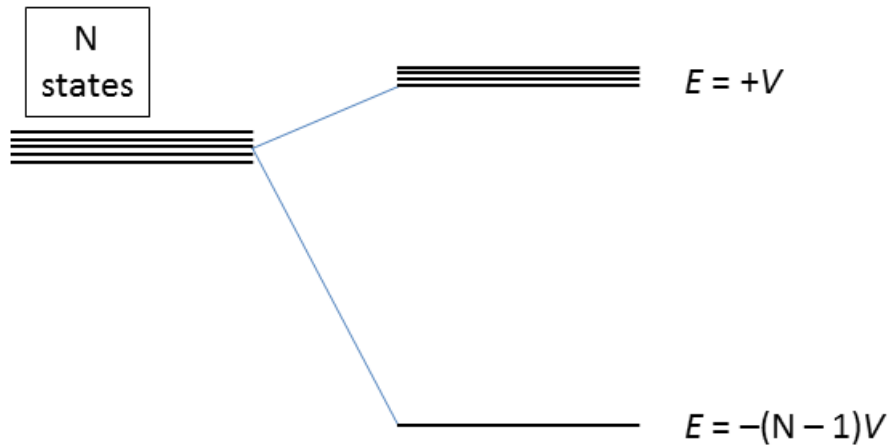


**Figure 13.** Generalized case of  $N$ -state mixing, showing the shift of energies with respect to the barycenter of the degenerate unmixed states.

Qualitatively, this effect can be seen in the way residual nucleon pairing interactions considerably lower the  $0^+$  ground state in even-even nuclei with respect to the  $2^+$  and higher-spin excited states [27]. The resulting wavefunction is a coherent linear combination of the unperturbed eigenstates in this model. It will be shown later in this work that one possible use of this model applies to certain states in  $^{116}\text{Sn}$ .

## Chapter 2. Nuclear Decays and Transitions

### 2.1. Radioactive Decay

Not all nuclei are stable. As such, unstable nuclei are radioactive and will decay by energetically favorable modes until their final products are stable. The unstable nuclide is usually called the parent and its decay product, the daughter. Radioactive decay rates ( $\lambda$ ) ordinarily cannot be altered<sup>3</sup>. Thus, a unique property of every radioactive isotope is the half-life,  $t_{1/2}$ , which is the time it takes for half of the parent nuclei in a given sample to decay to their daughter products [2], and is related to the decay rate,

$$\lambda = \frac{\ln 2}{t_{1/2}} . \quad (11)$$

On thermodynamic grounds, the spontaneity of a decay mode is governed by the  $Q$ -value using the sign convention defined by Krane [2]. In this convention a positive value indicates the decay mode will be favorable. The  $Q$ -value, in units of electron-volts (eV), is computed via Equation (12), stating atomic masses in  $\text{eV}/c^2$  and ignoring electron binding energy differences as being negligible between closely-spaced nuclides on the nuclear chart.

$$Q = (\sum m_{\text{before}} - \sum m_{\text{after}})c^2 \quad (12)$$

In Equation (12), in the specific case of radioactive decays, “before” refers to the parent (akin to the reactant), and “after” refers to the daughter and other emitted particles (akin

---

<sup>3</sup> For an example of a rare exception, see Ref. [30].

to the product(s)). For example, in alpha ( $\alpha$ ) decay, as the daughter is formed an  $\alpha$  particle ( ${}^4_2\text{He}$  nucleus) is emitted. In this case, the  $Q$ -value must include the masses of the parent, daughter and the alpha particle. Other decay modes will be discussed in more detail in the subsequent sections: beta ( $\beta$ ) decay, gamma ( $\gamma$ ) emission and conversion-electron emission.

### 2.1.1. Beta Decay and Selection Rules

Radioactive nuclei that undergo beta decay do so because they are less bound than their daughters. This decay mode, a manifestation of the weak interaction involving changes of bound protons into neutrons or vice versa, is the predominant decay mode for the majority of unstable nuclei. For nuclides with a given mass number  $A$  there are parabolic minima of their exact atomic masses, and consequently maxima in the binding energies [2]. Thus, nuclei with the lowest exact atomic mass within a given isobar are the stable isotopes, which explains the origin of the valley of beta stability in Figure 2. For the example of  $A = 116$ , it can be seen  ${}^{116}\text{Sn}$  has the lowest exact atomic mass [31] with  ${}^{116}\text{In}$  being slightly higher. Therefore  ${}^{116}\text{Sn}$  is stable while  ${}^{116}\text{In}$  is radioactive (Figure 14).

Beta minus ( $\beta^-$ ) decay is the emission of a high-energy electron and an antineutrino (the antineutrino emission conserves lepton number, angular momentum and linear momentum). One parent neutron is converted to a proton in the daughter; the atomic number  $Z$  increases by one, and this is energetically favorable for neutron-rich nuclei. For historical reasons the high-energy electron ejected in this process is termed the beta minus particle; the general form of the decay is written as in Equation (13), where  $X$  represents the parent and  $Y$ , the daughter.



The corresponding  $Q$ -value (the decay energy) is given by Equation (14), taking care to use atomic masses according to Equation (12) so that the mass of the ejected electron is correctly accounted for.

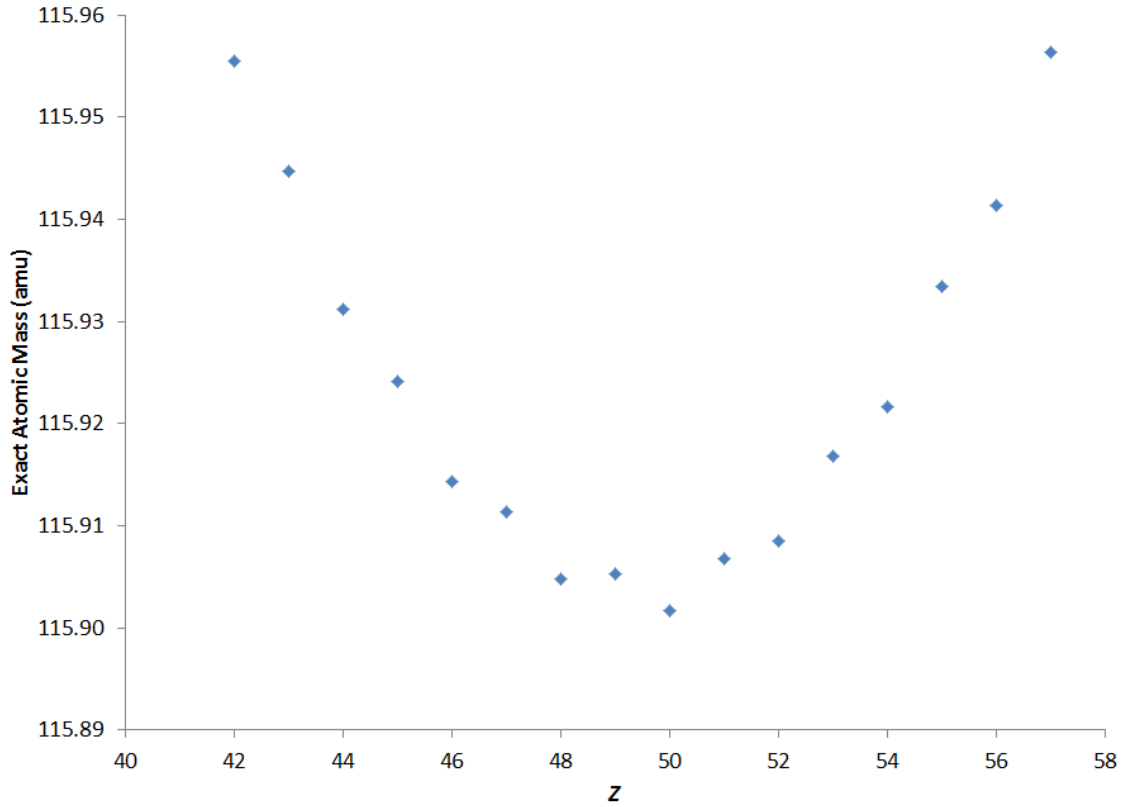


**Figure 14.** Mass parabola for  $A = 116$  as a function of atomic number  $Z$ . Note that  $Z = 50$ ,  $^{116}\text{Sn}$ , has the lowest mass and so is stable for this isobar. Data obtained from Ref. [31].

$$Q_{\beta^-} = [m_X - (m_Y + m_\nu)]c^2 \quad (14)$$

The (anti)neutrino is so light that the effect on the  $Q$ -value calculation is negligible if its mass is set to zero. Therefore, Equation (15) and all subsequent beta-decay  $Q$ -value formulas in this section result from this approximation.

$$Q_{\beta^-} = [m_X - m_Y]c^2 \quad (15)$$

Beta plus ( $\beta^+$ ) decay is the emission of a high-energy positron and neutrino, in which one parent proton is converted to a neutron in the daughter;  $Z$  therefore decreases by one, and this mode is favorable for proton-rich nuclei. The general form of this decay is expressed by Equation (16).



The corresponding  $Q$ -value is given by Equation (17), which accounts for the energy released when the positron encounters an electron in the vicinity of the decaying nucleus, and annihilates to release two 511 keV gamma rays. This energy cannot be neglected and causes a threshold effect for beta plus decay.

$$Q_{\beta^+} = [m_X - (m_Y + 2m_e)]c^2 \quad (17)$$

A competing mode to beta plus decay with no threshold effect is electron capture, abbreviated EC. Here, an electron, usually from an s atomic orbital, is captured by the nucleus according to Equation (18).



The  $Q$ -value is given by Equation (19), and it can be seen that when beta plus decay is energetically forbidden, electron capture is the sole decay mode.

$$Q_{EC} = [m_X - m_Y]c^2 \quad (19)$$

All the above  $Q$ -values assume that the ground state of the parent has decayed to the ground state of the daughter. However, under circumstances relating to beta-decay selection rules it is possible that excited states in the daughter will be preferentially populated. Thus, the energy of decay would be decreased by the energy of excitation ( $E_{exc}$ ) within the daughter (Equation (20)),

$$Q_{decay} = Q_{gs \rightarrow gs} - E_{exc} \cdot \quad (20)$$

Other factors affecting beta decay besides the decay energy (phase space) are the selection rules related to the change of spin, parity and isospin during the process. The

Fermi transitions are those in which the spins of the outgoing particles (the lepton<sup>4</sup> and the (anti)neutrino) are antiparallel, leading to  $S = 0$  as an overall spin; consequently the nuclear spin may not change:  $\Delta I = 0$ . Gamow-Teller transitions occur when the spins of the outgoing particles are parallel ( $S = 1$ ) resulting in  $\Delta I = 0$  or 1. These transitions, when there is no change of parity between the parent and daughter, are called allowed [2].

A special category of beta decays exists, called superallowed transitions. These are Fermi transitions in which the parent and daughter are analog  $I^\pi = 0^+$  states. Because the states are isobaric analog states, this means that while  $T_3$  may change, the isospin  $T$  may not. As a result, the overlapping nuclear wavefunctions are nearly identical and while beyond the scope of this work, such properties of superallowed decays are of importance to tests of new physics beyond the Standard Model [32,33].

When there is no possibility of a  $\Delta I = 0$  or 1 in beta decay, higher degrees of change of angular momentum are possible, but their decay rates are much slower as the outgoing particles must carry away not just intrinsic spin angular momentum, but orbital angular momentum  $L$  as well. These are called forbidden transitions, i.e. first forbidden ( $L = 1$ ), second forbidden ( $L = 2$ ), and so forth. The selection rules for beta decays can become quite complex owing to the fact that the parity change associated with the change of nuclear spin also affects the decay rate and degree of forbiddenness. Table 1 classifies beta decays either by their change of angular momentum and parity, or by their  $\log ft$  values.

The  $\log ft$  value is the logarithm of Equation (21), and relates the forbiddenness of a beta decay to its nuclear matrix element,  $M_{fi}$ , containing the initial and final states. As well, it contains  $m_e$ , the mass of the electron and the weak interaction coupling constant  $g$ , as well as Planck's constant and the speed of light. Thus, the decay rate is related to the

---

<sup>4</sup> *Leptons* are particles that do not feel the strong interaction (e.g. electrons or positrons). *Hadrons* are particles that do feel the strong interaction (protons and neutrons due to their underlying quark structure).

overlap of the parent and daughter nuclear states, and becomes larger (the corresponding  $\log ft$  value decreases) as the states become more similar.

$$ft_{1/2} = \frac{(\ln 2) 2\pi^3 \hbar^7}{m_e^5 c^4 g^2} \left( \frac{1}{|M_{fi}|^2} \right) \quad (21)$$

**Table 1.** Selection rules showing permitted changes in spin ( $I$ ), isospin ( $T$ ) and parity ( $\pi$ ), as well as ranges of  $\log ft$  values for given beta decays [2,34].

Decay Type	$\Delta I$	$\Delta T$	$\Delta\pi$	$\log ft_{1/2}$
Superallowed	$0^+ \rightarrow 0^+$ only	0	no	3.1 – 3.6
Allowed	0, 1	0, 1	no	2.9 – 10
First forbidden	0, 1, 2	0, 1	yes	5 – 19
Second forbidden	1, 2, 3	0, 1	no	10 – 18
Third forbidden	2, 3, 4	0, 1	yes	17 – 22
Fourth forbidden	3, 4, 5	0, 1	no	22 – 24

### 2.1.2. Gamma Emission and Selection Rules

Both radioactive and stable nuclei can have excited states which are rearrangements of their protons and neutrons with respect to their ground state. These states will de-excite (relax) back to the ground state by an electromagnetic transition involving the emission of a real or virtual photon, which carries an intrinsic angular momentum of  $1\hbar$ . In the case of the virtual photon, the nuclear multipole field interacts with the surrounding electrons or the vacuum, which can result in modes other than gamma-ray emission. This section will focus on gamma rays (real photons), with the succeeding section devoted to internal conversion.

If the nuclear recoil is neglected<sup>5</sup>, then the  $Q$ -value of gamma emission (more commonly referred to as the transition energy) is written as in Equation (22), where  $E_{\text{upper}}$

---

<sup>5</sup> Usually a good approximation as the recoil correction  $(E_\gamma)^2 / (2Mc^2)$ , where  $M = 0.9315A \text{ GeV}/c^2$ , is typically on the order of eV or less, while an  $A = 116$  nuclear mass is on the order of 100 GeV.

is the energy of the higher-lying state and  $E_{\text{lower}}$  is the energy of the lower-lying state, resulting in a detected gamma-ray energy  $E_\gamma$ .

$$Q = \Delta E = E_\gamma = E_{\text{upper}} - E_{\text{lower}} \quad (22)$$

The quantum-mechanical treatment of electromagnetic transitions in nuclei utilizes operators on wavefunctions corresponding to transition multiplicities (algebraic changes of angular momentum  $L$ ). For example, the electric dipole ( $E1$ ) operator, involving a  $1\hbar$  change of angular momentum, can be defined  $\hat{\mu}_E = e\hat{r}$  where  $e$  is the charge on the nucleon undergoing the transition and  $\hat{r}$  has an eigenvalue of the distance away from the nuclear center. A magnetic dipole transition is called  $M1$  and the associated operator is, depending on the particle involved, either  $\hat{\mu}_B = \mu_N(\vec{L} + g_p\hat{S})$ , or  $\hat{\mu}_B = (\mu_N g_n\hat{S})$  where  $\mu_N$  is the nuclear magneton,  $g_p$  is the proton  $g$ -factor and  $g_n$  the neutron  $g$ -factor,  $\vec{L}$  is the nucleon orbital angular momentum, and  $\hat{S}$  being the intrinsic spin operator with an eigenvalue of the nucleon spin. Transitions involving the electric quadrupole operator ( $\hat{Q}_E = e^2(3z^2 - \hat{r}^2)$  for a case where the nuclear symmetry axis is lined up with the  $z$ -axis) will change the nuclear angular momentum by  $2\hbar$ , and are  $E2$  in nature. Other higher-order operators exist for higher multiplicities, as well. For any electromagnetic transition, the lowest and highest allowed multiplicities are governed by the vector coupling of the initial ( $I_i$ ) and final ( $I_f$ ) spins of the states involved, given by the triangle inequality of Equation (23),

$$|I_f - I_i| \leq L \leq I_f + I_i . \quad (23)$$

The resulting change in parity for a given  $L$  is governed by the symmetries of the wavefunctions on which the operators act, and so given initial ( $\psi_i$  labelled by  $|i\rangle$ ) and final eigenstates ( $\psi_f$  labelled by  $|f\rangle$ ), the following rules hold for the lowest-order transitions ( $E0$  transitions, forbidden to the emission of a photon, are a special case involving transitions between states of the same angular momentum and will be discussed in Sections 2.1.3 and 2.2.1):

$$\begin{aligned}
\langle f | \hat{\mu}_E | i \rangle & \quad E1 \text{ transition – nonzero for } \Delta\pi = \text{yes} \\
\langle f | \hat{\mu}_B | i \rangle & \quad M1 \text{ transition – nonzero for } \Delta\pi = \text{no} \\
\langle f | \hat{Q}_E | i \rangle & \quad E2 \text{ transition – nonzero for } \Delta\pi = \text{no}
\end{aligned}$$

In general the higher-order transitions ( $M2$ ,  $E3$ , ...) are more rarely observed in gamma-ray spectroscopy because their decay rates are much slower ( $\sim 10^{-10}$  compared to the  $E1$  decay rate), as discussed later in Section 2.2. The  $E2$  transitions, being quadrupole in nature, are common in even-even nuclei as they are associated with transitions among vibrational or rotational states (see Sections 1.2.3 and 2.2.2).

### 2.1.3. Conversion-Electron Emission

Competing with gamma-ray emission is the process of internal conversion. This is the process whereby the nuclear multipole field transfers the transition energy to an orbital electron. The electron carries away that energy as kinetic energy, decreased by the binding energy of the electron ( $E_B$ ) as shown in Equation (24),

$$E_e = Q - E_B = \Delta E - E_B = (E_{upper} - E_{lower}) - E_B. \quad (24)$$

The ratio of probabilities of conversion-electron emission to gamma-ray emission is the internal conversion coefficient  $\alpha$ , defined in Equation (25) as the ratio of decay rates:

$$\alpha = \frac{\lambda_e}{\lambda_\gamma}. \quad (25)$$

Since the internal conversion coefficient is a ratio of decay rates involving physically distinct particles that can each be individually detected, the experimental internal conversion coefficient is the ratio of the number of electrons detected ( $N_e$ ) to the number of gamma rays detected ( $N_\gamma$ ), taking into account detector efficiencies  $\varepsilon_e$  and  $\varepsilon_\gamma$ , and is expressed in Equation (26),

$$\alpha = \frac{N_e / \epsilon_e}{N_\gamma / \epsilon_\gamma} . \quad (26)$$

Since the binding energy is different for the K (1s), L (2s [L<sub>I</sub>], 2p [L<sub>II</sub>,L<sub>III</sub>]), etc. shells, the individual subshell coefficients can also be experimentally measured. For example, measuring the ratio for K-shell electrons alone yields Equation (27),

$$\alpha_K = \frac{N_K / \epsilon_K}{N_\gamma / \epsilon_\gamma} . \quad (27)$$

Accordingly, the total internal conversion coefficient can be determined by Equation (28),

$$\alpha_{tot} = \alpha_K + \alpha_L + \alpha_M + \dots . \quad (28)$$

The decay rates in Equation (25) may be expressed as matrix elements involving products of the electronic ( $\phi$ ) and nuclear ( $\psi$ ) wavefunctions; then, if the transition operator operates identically on the nuclear eigenstates involved regardless of whether the de-excitation proceeds by a gamma ray or by transfer to a conversion electron, Equation (25) can be substituted with the matrix elements for a given multipolarity operator  $\hat{O}(\sigma L)$ , with  $\sigma = E$ (lectric) or  $M$ (agnetic), and  $L$  being the multipolarity between initial and final nuclear eigenstates with a similar nomenclature to Section 2.1.2. The initial state involves a bound electron wavefunction  $|\phi_{bound}\rangle$  and the final state involves a free unbound electron wavefunction  $|\phi_{free}\rangle$ . The transition operator does not affect the electronic wavefunctions since it involves a purely nuclear rearrangement, resulting in Equation (29), in which the decay rates are related to the squares of the transition matrix elements, as discussed in more detail in Section 2.2:

$$\alpha = \frac{\lambda_e}{\lambda_\gamma} \propto \frac{\left| \langle f | \hat{O}(\sigma L) | i \rangle \right|^2}{\left| \langle f | \hat{O}(\sigma L) | i \rangle \right|^2} \left| \langle \phi_{free} | \phi_{bound} \rangle \right|^2 = \left| \langle \phi_{free} | \phi_{bound} \rangle \right|^2 . \quad (29)$$

It is clear from the quantum mechanical treatment in Equation (29) that the overlap of the free and bound electron wavefunctions in the vicinity of the nucleus at the moment the transition occurs implies that K-shell electrons will have the greatest probability of interacting with the nuclear multipole field. A derivation performed by Krane [2] shows how the internal conversion coefficient reveals multipolarity information about a transition, and its dependence on the nucleus under consideration, as seen in Equations (30) and (31), for a given atomic number  $Z$ , transition energy  $E$  and multipolarity  $L$ .

$$\alpha(EL) = \frac{Z^3}{n^3} \left( \frac{L}{L+1} \right) \left( \frac{e^2}{4\pi\epsilon_0\hbar c} \right)^4 \left( \frac{2m_e c^2}{E} \right)^{L+5/2} \quad (30)$$

$$\alpha(ML) = \frac{Z^3}{n^3} \left( \frac{e^2}{4\pi\epsilon_0\hbar c} \right)^4 \left( \frac{2m_e c^2}{E} \right)^{L+3/2} \quad (31)$$

The internal conversion coefficient is therefore large for low principal quantum numbers  $n$ , heavy nuclei (large  $Z$ ), high transition multiplicities (large  $L$ ), and low transition energies ( $E$ ), and because of the multipolarity and electric or magnetic sensitivity, the coefficient will change depending on the nature of a transition. Thus, for a given nucleus and transition energy, experimental conversion coefficients can give information about the spin and parity of one of the two states involved in a transition if the other is already known.

Because the ejected conversion electrons may have high kinetic energies, a full treatment requires relativistic quantum mechanics to obtain theoretical values of  $\alpha$  that accord well with experiment (given that comparing experimental  $\alpha$  values to theoretical values verifies transition multiplicities). Computer programs are used for this purpose,

and the most recent one developed is BrIcc by Band and Raman [35], which is subdivided into BrIccFO (for “Frozen Orbitals”), or BrIccNH (for “No Hole”). The BrIccFO calculation is recommended as it generally predicts values of  $\alpha$  in closer agreement with precision measurements of internal conversion coefficients [36].

One final aspect of conversion-electron emission is that while it is a competing mechanism for  $E1$ ,  $M1$ , and higher-multipole transitions within nuclei, for  $E0$  (electric monopole) transitions it is the only decay mechanism if pair production is not energetically possible. Thus, spectroscopically the signature of an  $E0$  transition (especially a  $0^+ \rightarrow 0^+$  transition) is when it goes unobserved in the gamma-ray spectrum, but is present with visible peaks in the corresponding conversion-electron spectrum (see Section 3.2.2 for a comparison of spectra).

## 2.2. Transition Strengths

The transition strength, or transition probability, for radiations emitted from an excited state of a nucleus is proportional to how fast or slow that state decays. Decay rates of nuclear states are proportional to squares of matrix elements, which are also related to transition strengths that can be used to determine the properties of the states involved, as discussed semi-quantitatively in Section 1.2.2 on rotations and vibrations. As discussed in Krane [2], a quantization of the classical problem of determining the power emitted in the radiations of a moving charge or current yields a general formula for the decay rate of an excited nuclear state. This is shown in Equation (32), for a given transition energy  $E$  in which the initial and final states, using the same nomenclature of Section 2.1, are operated on by a generalized electromagnetic transition operator  $\hat{O}(\sigma L)$ .

$$\lambda = \frac{2(L+1)}{\varepsilon_0 \hbar L [(2L+1)!!]^2} \left( \frac{E}{\hbar c} \right)^{2L+1} \left| \langle f | \hat{O}(\sigma L) | i \rangle \right|^2 \quad (32)$$

The slower decay rates of higher-order transitions such as  $E2$ ,  $M3$ , etc. can be explained partly by the inverse proportionality of the decay rate to the double factorial in the denominator, although there is also a sensitivity to the exponent of the transition energy and the form of the matrix element as well.

Fermi's Golden Rule [2], generally applicable to many types of transitions (e.g. beta decay as well as the de-excitations of atomic or molecular excited states), is a more general form of the expression for nuclear-state decay rates discussed above, and so with similar nomenclature for the matrix element as in Equation (32), and given a density of final states  $\rho(E_f)$ ,

$$\lambda = \frac{2\pi}{\hbar} \left| \langle f | \hat{O}(\sigma L) | i \rangle \right|^2 \rho(E_f). \quad (33)$$

Thus, electromagnetic transitions between nuclear states are governed by the overlap of the initial and final eigenstates, such that the larger the overlap the more intense a transition will be. Radiation emitted from nuclei in transitions from one state to the next probes the underlying wavefunctions of the two states involved, because the quantum mechanical operators are related to the associated electromagnetic transitions involved.

### 2.2.1. $E0$ Transitions and Shape Coexistence

$E0$  transitions are described quantum mechanically by  $E0$  operators [28], which can be expressed in different ways depending on the model used. One simple form is given by Equation (34), sensitive essentially to the shape of a nucleus rather than to the nonspherical distribution of charge as is the case for the  $E2$  quadrupole operator. In this particular form the charge of each nucleon is multiplied by the square of its distance, and all nucleons are then summed together.

$$\hat{T}(E0) = \sum_k e_k r_k^2 \quad (34)$$

The transition strength is called  $\rho^2(E0)$  and can be related to the  $E0$  decay rate  $\lambda(E0)$  as seen in Equation (35) [28], where  $R$  is the average nuclear radius ( $R = 1.2A^{1/3}$ ), and the values of  $\Omega$  are the “electronic factors”. These factors are derived from the theory of  $E0$  transitions, and represent probabilities of emission among the K, L, M, etc. shells as well as by pair production and two-photon production.

$$\lambda_{E0} = \left( \sum_i \Omega_i \right) \rho_{fi}^2(E0) = \left( \sum_i \Omega_i \right) \left| \frac{\langle f | \hat{T}(E0) | i \rangle}{eR^2} \right|^2 \quad (35)$$

The two-state mixing model discussed in Section 1.3.1 can be used to relate the  $E0$  matrix element to either probe the change in shape of the nucleus between the states involved, or the mixing of the states which would otherwise have a forbidden transition. If simplifying assumptions cannot be made about the orthogonality of the initial and final states or about the strength of the mixing, then it is possible for a combination of the above two factors to play a role in the  $E0$  strength.

The presence of  $E0$  transitions between states of the same spin and parity is of interest to researchers with regard to shape coexistence, a phenomenon in which two nuclear states of the same spin and parity, but of different *shape*, are close to each other in energy. The seminal example of shape coexistence is the study of the singly-magic  $^{186}\text{Pb}$  [37] which revealed three states of  $I^\pi = 0^+$ , one being the energetically preferred spherical ground state, and two more at about 1.2 MeV within ~300 keV of one another: an oblate and prolate pair of excited  $0^+$  states (Figure 15). The case of  $^{116}\text{Sn}$  is remarkably similar: there exist two excited  $0^+$  states within ~300 keV of each other at about 2 MeV. While the focus of shape coexistence studies has been on  $I^\pi = 0^+$  states, in principle there is the possibility of coexisting states with nonzero spins if  $E0$  components can be measured in transitions between such states.

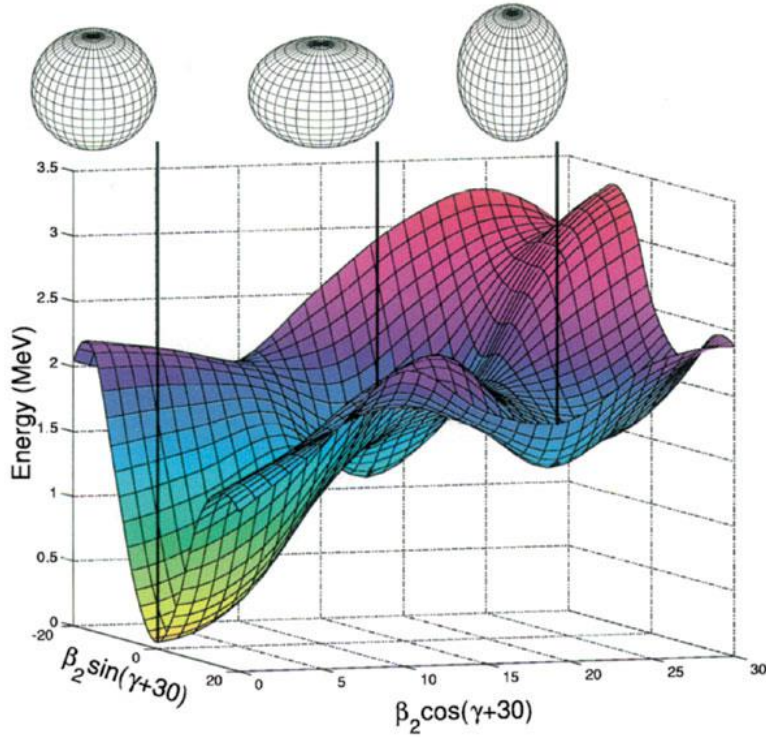


**Figure 15.** Shape coexistence in  $^{186}\text{Pb}$  shown as a function of energy and position within the nuclear potential well. Note the energetic minima at  $\sim 1.2$  MeV for the deformed  $0^+$  states. Reprinted by permission from Macmillan Publishers Ltd: Nature 405, 430 (2000), copyright 2000.

### 2.2.2. $E2$ and $M1$ Transitions

A non- $E0$  transition strength is usually measured with the quantity  $B(\sigma L)$  with similar nomenclature to the underlying transition operator  $\hat{O}(\sigma L)$ . In particular, as  $E2$  transitions are very common within nuclei,  $B(E2)$  values are very important experimental probes of nuclear structure.  $B(E2)$  values can be determined from experimentally measured decay rates in Equation (36), adapted from Ref. [38]. The quantities include  $E_\gamma$  in MeV,  $A$  as the nuclear mass number, the branching ratio B.R., decay rates ( $\lambda$ ) in  $\text{s}^{-1}$ , and transition probabilities ( $B(E2)$ ) in  $e^2\text{-fm}^4$  where  $e$  is the fundamental unit of charge,

or in Weisskopf units (W.u.)<sup>6</sup>. This formula assumes that the transition is pure  $E2$  (“unmixed”). The treatment will start with the direction preferred in decay spectroscopy, from higher energy to lower energy, i.e. downward.

$$\begin{aligned} B(E2)_{unmixed} \downarrow &= (1.374 \times 10^{-8}) (\text{B.R.}) \frac{\lambda(E2)}{E_\gamma^5 A^{4/3}} [\text{W.u.}] \\ B(E2)_{unmixed} \downarrow &= (8.156 \times 10^{-10}) (\text{B.R.}) \frac{\lambda(E2)}{E_\gamma^5} [e^2 \text{fm}^4] \end{aligned} \quad (36)$$

Decay rates are related to lifetimes or half-lives as shown in Equation (37),

$$\lambda(E2) = \frac{1}{\tau_{E2}} = \frac{\ln 2}{(t_{1/2})_{E2}} . \quad (37)$$

The branching ratio (B.R.) is defined in Equation (38), in which the gamma intensity for the  $k$ -th transition exiting a state is divided by the total gamma and conversion-electron intensity exiting a state [39],

$$\text{B.R.} = \frac{I_{\gamma,k}}{\sum_i I(\gamma + ce)_i} = \frac{I_{\gamma,k}}{\sum_i I_{\gamma,i} (1 + \alpha_i)} . \quad (38)$$

When there is only one transition exiting a state, the branching ratio B.R. need only account for internal conversion (Equation (39)),

$$\text{B.R.} = \frac{I_\gamma}{I_\gamma (1 + \alpha)} = \frac{1}{1 + \alpha} . \quad (39)$$

---

<sup>6</sup> Converting to Weisskopf units involves dividing by the estimate of the transition strength assuming only one nucleon is involved, called the *single particle estimate*, and such estimates can be done for other types of transitions besides just  $E2$ . For  $E2$  transitions in particular,  $B(E2) \gg 1$  W.u. are considered to be collective.

When a transition is not pure  $E2$ , the  $B(E2)$  value must include the mixing ratio  $\delta$ , as shown in Equation (40)<sup>7</sup>,

$$B(E2) \downarrow = B(E2)_{unmixed} \downarrow \left( \frac{\delta^2}{1 + \delta^2} \right). \quad (40)$$

Statistical spin factors affect  $B(E2)$  measurements; Equation (41) corrects for the case where a transition is measured going “upwards”, i.e. from lower energy ( $I_{lower}$ ) to higher energy ( $I_{upper}$ ). The arrows indicate the direction of a transition with respect to the states involved.

$$B(E2) \uparrow = \frac{2I_{upper} + 1}{2I_{lower} + 1} B(E2) \downarrow. \quad (41)$$

Similar to the discussion above for  $E2$  strengths,  $M1$  transition strengths can also be computed from Equation (42), including branching ratios and statistical spin factors analogously to the  $E2$  case. The units for  $B(M1)$  are either the square of the nuclear magneton ( $\mu_N^2$ ) or Weisskopf units (W.u.). The formula assumes that the transition is pure  $M1$  (“unmixed”).

$$\begin{aligned} B(M1)_{unmixed} \downarrow &= (3.181 \times 10^{-14}) (\text{B.R.}) \frac{\lambda(M1)}{E_\gamma^3} [\text{W.u.}] \\ B(M1)_{unmixed} \downarrow &= (5.697 \times 10^{-14}) (\text{B.R.}) \frac{\lambda(M1)}{E_\gamma^3} [\mu_N^2] \end{aligned} \quad (42)$$

The  $B(M1)$  value of a mixed transition is given by Equation (43)<sup>8</sup>,

$$B(M1) \downarrow = B(M1)_{unmixed} \downarrow \left( \frac{1}{1 + \delta^2} \right). \quad (43)$$

---

<sup>7</sup> When the mixing ratio  $\delta \rightarrow \infty$ , the transition is pure  $E2$ .

<sup>8</sup> Here, when the mixing ratio  $\delta \rightarrow 0$ , the transition is pure  $M1$ .

Similar derivations can be done for other transition multiplicities; the appendixes in the Table of Isotopes contain a detailed treatment for all possible multiplicities [39], and a detailed derivation of Equations (36) and (42) is in Appendix D of this thesis.

## **2.3. Theory of Angular Correlations**

The theory of angular correlations of radiation was discussed by D. R. Hamilton in 1940 [40], and further applied to the coincidence spectroscopy of nuclei by Biedenharn & Rose in 1953 [41], followed by Rose & Brink in 1967 [42] and Krane & Steffen in 1970 [43] (based on a more general treatment by Becker & Steffen in 1969 [44]). Experimentally, the coincidence-spectroscopy technique of angular correlations has been used as far back as the 1950s for both  $\gamma$ - $\gamma$  and  $\gamma$ - $e^-$  coincidences [45,46]. The  $8\pi$  array has been previously used to conduct  $\gamma$ - $\gamma$  angular correlation measurements; the formalisms developed by Schmelzenbach [47] and Loats [48] in their experiments and analyses have been used and/or adapted in this thesis.

### **2.3.1. Angular Correlations in Radioactive Decay Experiments**

Decay-spectroscopy experiments typically involve gamma rays emitted from room-temperature nuclei with no surrounding strong orienting magnetic fields. They are also usually stationary (i.e. at rest with respect to the surrounding detectors). Consequently, the excited daughter nuclei have randomly-oriented angular momentum vectors and the emission radiation has no preferred direction. Therefore, to obtain the underlying anisotropy of the emitted gamma rays, coincidences of gamma rays in a cascade can be examined by two detectors at defined angles with respect to each other. The gamma ray emission directions become vectors pointed from the nuclei at the source position to the two chosen detectors. The combination of two vectors (equivalent to the coincidence of two gamma rays) defines a plane and an angle within that plane, as shown in Figure 16.

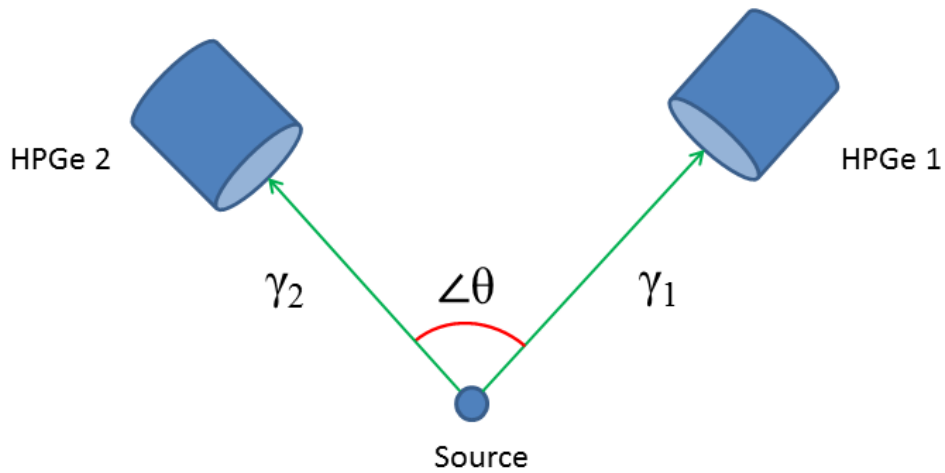


**Figure 16.** A general representation of an angular correlation apparatus. The HPGe detector numbered 1 struck by  $\gamma_1$  defines the first vector about which angles can be defined, for example with respect to  $\gamma_2$  striking HPGe 2, so that the angle  $\theta$  between them can be determined.

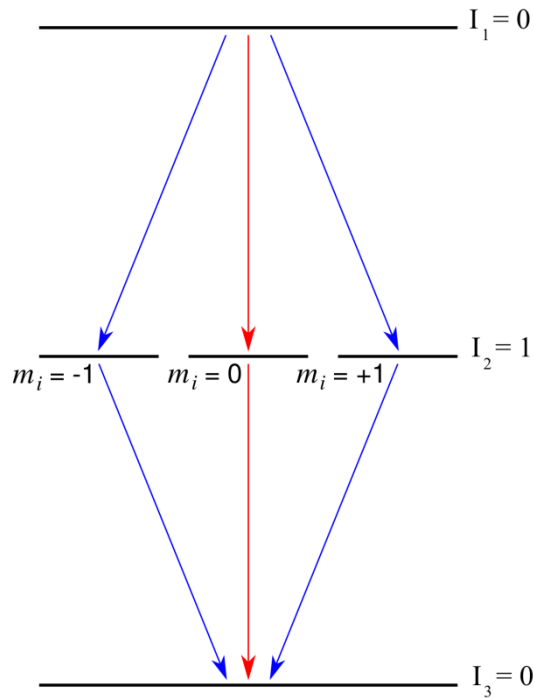


**Figure 17.** Qualitative 0-1-0 cascade. The blue arrows indicate transitions observed under the condition of examining gamma rays emitted at angles with respect to a chosen detector, while the red arrows indicate transitions that will not be observed. Adapted from [49] with permission.

This method of computing angles from vectors is how one translates the physical geometry of an array of detectors (with rings of detectors in fixed physical space) into groups of angles, termed correlation angles (sometimes termed “pseudo-rings” although they are not physically circular rings in three-dimensional space). This also has the effect of imposing preferred directions (akin to the case of imposing the  $z$ -axis as the preferred projection axis for quantized angular momenta) on nuclear transitions observed through the emission of radiation.

Imposing preferred directions on an isotropic distribution of emitted radiation is equivalent to, in the simplest case of a 0-1-0 ( $I_1$ - $I_2$ - $I_3$ ) cascade of nuclear spins, non-observation of the  $\Delta m_1 = 0$  transitions that would otherwise, along with the  $\Delta m_1 = \pm 1$  transitions, result in an equal population of the intermediate  $I_2 = 1$  state. Figure 17 shows this effect in the form of a level scheme and corresponding transitions, when a preferred axis is imposed by examining gamma-ray coincidences by the method exemplified in Figure 16.

### 2.3.2. The Angular Correlation Function

Mathematically, imposing preferred directions on the emission of radiation in the cascade of Figure 17 is equivalent to writing out an isotropic angular correlation function  $W(\theta)$ , as below in Equation (44a), and removing the sine term (44b):

$$W(\theta) \propto \frac{1}{2}(1 + \cos^2 \theta) + \sin^2 \theta + \frac{1}{2}(1 + \cos^2 \theta) = \text{constant} \quad (44a)$$

$$W(\theta) \propto \frac{1}{2}[(1 + \cos^2 \theta) + (1 + \cos^2 \theta)] = 1 + \cos^2 \theta \quad (44b)$$

A more general mathematical formalism for angular correlations for any cascade (adapted from Refs. [47,48]) expresses the angular correlation function  $W(\theta)$  (Equation (45)) in terms of Legendre polynomials  $P_k(\cos \theta)$  whose coefficients  $a_k$  depend on the nuclear spins involved in the cascades being analyzed. The removal of sine terms

corresponds to the removal of the associated  $\Delta m_I$  transitions in an angular correlation measurement.

$$W(\theta) = \sum_{k=0}^{\infty} a_k P_k(\cos \theta) \quad (45)$$

In practice,  $W(\theta)$  is restricted to even values of  $k$ , and furthermore generally only taken over  $k = 0, 2$  and  $4$ ; the truncation at  $4$  is due to the prevalence of dipole and quadrupole modes within nuclei [41--43]. The  $a_k$  coefficients can be expanded out in terms of Racah [42] or  $F$  coefficients [43,50], such that  $a_k = B_k U_k A_k$ , where  $B_k$  is associated with the first transition in a cascade,  $U_k$  with intermediate transition(s), and  $A_k$  with the final transition of a cascade, as seen in Equation (46),

$$W(\theta) = \sum_{k=0,2,4} B_k U_k A_k P_k(\cos \theta) . \quad (46)$$

There are further corrections to be made to Equation (46) when experimentally measuring angular correlation coefficients, which require accounting for lifetimes of nuclear states considerably longer than picoseconds. This lifetime effect causes a deorientation of the state and so succeeding transitions appear more isotropic. The lifetime correction factor is  $G_k$ , and is equal to one when state lifetimes are very short.

Radiation detectors have a finite size and so when radiation strikes them, there is a solid angle over which the angular distribution of that radiation is “smeared out”. This, as with state lifetime effects, causes an angular correlation to appear more isotropic unless it is accounted for. This additional finite-size correction to Equation (46) is the  $Q_k$  attenuation factor for each detector registering a gamma ray and modifies  $B_k$ ,  $U_k$ , and  $A_k$  as a result. Thus, Equation (46) can now be restated as follows in Equation (47):

$$W(\theta) = \sum_{k=0,2,4} Q_k^B B_k Q_k^U U_k Q_k^A A_k G_k P_k(\cos \theta), \quad (47)$$

where  $G_k$  has not been distributed over the coefficients as it is unlikely for multiple states in a cascade to all have nonnegligible lifetimes.

It is generally the case that for nuclei with in which few (if any) of the excited states have lifetimes much longer than picoseconds, the lifetime-correction factor  $G_k = 1$  in Equation (47). The factor  $U_k$  is associated with possible intermediate transitions when the nuclear level scheme has not been conclusively established; it can be set equal to 1 when the level scheme is well-understood so that one transition is known to be directly in coincidence with a succeeding transition. With these conditions, Equation (47) can be rewritten to introduce a normalization factor ( $N$ ) to account for the fact that the relative change of  $W(\theta)$  with respect to angle is what matters, rather than the value of  $W(\theta)$  specifically for a given angle. Upon combining the  $Q_k$  factors together ( $Q_{kk} = Q_k^B Q_k^A$ ) and the  $B_k$  and  $A_k$  factors together ( $A_{kk} = B_k A_k$ ), then expanding the sum and introducing the normalization results in Equation (48):

$$W(\theta) = N[1 + A_{22}Q_{22}P_2(\cos\theta) + A_{44}Q_{44}P_4(\cos\theta)] . \quad (48)$$

### 2.3.3. Mixing Ratios

There can be cases when the initial and final nuclear spins of a transition connecting two states will be the same. As noted in Section 2.1.2, the resulting vector coupling of the spins (Equation (23)) can result in several possible choices of transition multipolarities. For example, in the case of a  $2^+ - 2^+ - 0^+$  cascade, the  $2^+ \rightarrow 0^+$  transition is restricted solely to pure  $E2$ , but the  $2^+ \rightarrow 2^+$  transition may be  $E0$ ,  $M1$  or  $E2$  or some mixture thereof. Given  $\sigma = E$  or  $M$  under the requirement of parity conservation for two competing transition multipolarities  $L$  and  $L'$  differing by one unit of angular momentum, one multipolarity being electric ( $E$ ) requires the other to be magnetic ( $M$ ). The resulting quantitative admixture of the two multipolarities is the *mixing ratio* ( $\delta$ ) of the transitions involved, and is defined by Equation (49), where the eigenstates involved are labelled by their angular momenta.

$$\delta \propto \frac{\langle I_{final} | \hat{O}(\sigma L') | I_{initial} \rangle}{\langle I_{final} | \hat{O}(\sigma L) | I_{initial} \rangle} \quad (49)$$

The proportionality can be made exact using the Bohr-Mottelson reduced matrix elements [43], which include the necessary statistical weights, and in the specific case of  $E2/M1$  mixing ( $L = 1$ , and  $L' = 2$ ) which is the focus of this thesis, Equation (50) expresses the mixing ratio as developed in the framework of Krane & Steffen. Similar arguments were developed by Rose & Brink in their framework.

$$\delta = \frac{\langle I_{final} | \hat{M}(E2) | I_{initial} \rangle}{\langle I_{final} | \hat{M}(M1) | I_{initial} \rangle} \quad (50)$$

The percentage of  $M1$  or  $E2$  character can be computed from the value of  $\delta$  in Equations (51a) and (51b).

$$\%(E2) = \frac{\delta^2}{1 + \delta^2} \times 100 \quad (51a)$$

$$\%(M1) = \frac{1}{1 + \delta^2} \times 100 \quad (51b)$$

The sign of the mixing ratio is useful since certain nuclear models can incorporate the magnitude and sign to extract other nuclear properties, such as the quadrupole moment [48]. However, the sign of the mixing ratio depends, in turn, on the signs of the  $E2$  and  $M1$  matrix elements, which ultimately come from the forms of the operators and the wavefunctions involved, which means that the choice of convention for the sign of  $\delta$  is important (as the quadrupole moment has a sign with physical meaning). Therefore, a consistent use of convention throughout an analysis for the sign of  $\delta$  will allow it to be correctly related to the quadrupole moment or other nuclear properties.

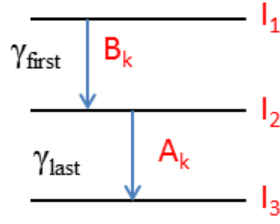


**Figure 18.** Generalized cascade showing the coefficients involved in measuring angular correlations and the nuclear states involved, labelled by their spins. The transition gamma rays are labelled in the order they follow in a cascade.

The connection to the theory of angular correlation coefficients  $A_{22}$  and  $A_{44}$  is that either the  $A_k$  or  $B_k$  coefficients (Figure 18), or both, can be modified by the value of  $\delta$  for the given transition. This means that the shape of an angular correlation is related to the value of  $\delta$ , as well. The  $A_k$  and  $B_k$  coefficients are expressed in terms of  $F$  coefficients that arise from transitions between any two nuclear states labelled with their spins  $I_a$  and  $I_b$  and any two transition multiplicities<sup>9</sup> labelled  $L_1$  and  $L_2$ . The coefficients are computed from Equation (52) [51].

$$F_k(L_1 L_2 I_a I_b) = \left[ (-1)^{I_a + I_b + 1} \sqrt{(2k+1)(2L_1+1)(2L_2+1)(2I_b+1)} \right] \times \begin{matrix} \left( \begin{matrix} L_1 & L_2 & k \\ 1 & -1 & 0 \end{matrix} \right) \left\{ \begin{matrix} L_1 & L_2 & k \\ I_b & I_b & I_a \end{matrix} \right\} \end{matrix} \quad (52)$$

The collection of values between the ordinary brackets ( ) are part of the Wigner 3-j symbol, while the collection of values between the curly brackets { } are part of the Wigner 6-j symbol [52]. As they are both made up of Clebsch-Gordan coefficients (see Appendix G for details) they can be calculated using computer programs developed for the purpose (for example, see Ref. [53]).

Becker & Steffen expressed the formulas for  $A_k$  and  $B_k$  in a general form, which Krane & Steffen then adapted specifically for the case of  $E2/M1$  mixing, in terms of the

<sup>9</sup> The  $F$  coefficient is calculated differently for each term in the  $A_k$  or  $B_k$  coefficient, so  $L_1$  and  $L_2$  are different for each one.

above-mentioned  $F$  coefficients [50,54]. Equations (53) and (54) thus result, where  $F_k$  ( $k = 2$  or  $4$ , corresponding to  $A_{22}$  or  $A_{44}$ ) are the corresponding  $F$  coefficients for given nuclear spins and transitions as labelled in Figure 18 with multipolarities  $L' = L + 1$ .

$$B_k = \frac{1}{1 + \delta_{first}^2} \left[ F_k(L L I_1 I_2) + (-1)^{L-L'} (2\delta_{first} F_k(L L' I_1 I_2)) + \delta_{first}^2 F_k(L' L' I_1 I_2) \right] \quad (53)$$

$$A_k = \frac{1}{1 + \delta_{last}^2} \left[ F_k(L L I_3 I_2) + (2\delta_{last} F_k(L L' I_3 I_2)) + \delta_{last}^2 F_k(L' L' I_3 I_2) \right] \quad (54)$$

The sign of  $\delta$ , when measured this way, is governed by the underlying theory of the changes of angular momentum occurring in a nucleus. The two main conventions used are Rose & Brink [42] and Krane & Steffen [43,44] (the second is used by the Nuclear Data Sheets [55]). The technical report by M. J. Martin in 1987 [56] enumerated all the then-known conventions and showed that as a general rule,  $\delta$ (Rose & Brink) always has an opposite sign to  $\delta$ (Krane & Steffen). For ease of comparison to the Nuclear Data Sheets, the Krane & Steffen convention will be used in this thesis.

#### 2.3.4. $E0$ Components

In addition to the aforementioned  $E2/M1$  mixing in a transition between states in  $^{116}\text{Sn}$  of the same spin and parity, there is the potential for an  $E0$  component to the transition. In order to obtain the  $E0$  component relative to the  $E2$  component for a given transition, it is necessary to know the mixing ratio  $\delta$ , the theoretical  $M1$  and  $E2$  K conversion coefficients ( $\alpha_K(M1)$  and  $\alpha_K(E2)$ , usually obtained from the BrIccFO calculation [35]), and the experimentally measured K conversion coefficient of the mixed transition,  $\alpha_K(\text{exp})$ , and substitute them into Equation (55), adapted from Refs. [57,58],

$$\alpha_K(\text{exp}) = \frac{(\mu_K + \alpha_K(E2))\delta^2 + \alpha_K(M1)}{1 + \delta^2}. \quad (55)$$

The value  $\mu_K$  is the K electron line intensity due to the  $E0$  part divided by the gamma ray intensity in the  $E2$  part, which is akin to a conversion coefficient. A related quantity,  $q^2 = \mu_K / \alpha_K(E2)$ , is the ratio of  $E0$  to  $E2$  transition strengths using the theoretical  $E2$   $\alpha_K$ . Either  $\mu_K$  or  $q^2$  can be used to obtain the  $\rho^2(E0)$  of a transition provided the absolute  $B(E2)$  is known. To do this, first the dimensionless ratio of  $E0$  to  $E2$  strengths (the  $X$ -value) is calculated via Equation (56) [58], which includes  $\mu_K$ , the nuclear mass  $A$ , the transition energy  $E_\gamma$  in MeV, and the K-shell electronic factor  $\Omega_K$ .

$$X = \frac{B(E0)}{B(E2)} = \frac{2.54 \times 10^9 A^{4/3} E_\gamma^5 (\mu_K)}{\Omega_K} \quad (56)$$

The resulting  $\rho^2(E0)$  from this  $X$ -value, as adapted from Kibédi *et al.*, is given by Equation (57),

$$\rho^2(E0) = \frac{X[B(E2)]}{e^2 (R_0 A^{1/3})^4}, \quad (57)$$

where the  $B(E2)$  value is in  $e^2\text{-fm}^4$  and  $R_0 A^{1/3}$  is the spherical nuclear radius for the mass number  $A$ , in units of fm.

A slightly different  $X$ -value is related to the  $E0$  to  $E2$  strengths for the case of a state which decays by two or more transitions, one of which is pure  $E2$  and the other(s), pure  $E0$ . The other form of the  $X$ -value is discussed in more detail in Section 6.2.6, as well as by Bäcklin *et al.* [59].

## **Chapter 3. Radiation Detectors and the $8\pi$ Array**

### **3.1. Interactions of Ionizing Radiation and Particles with Matter**

Radiations emitted by decaying nuclei involve high-energy particles that are not detectable by the human eye, but which nonetheless interact with matter in detectable ways. Since the energy of such radiations is greater than the energy of a chemical bond ( $\sim 1-10$  eV) they can break these bonds and ionize atoms or molecules. Thus,  $\alpha$  particles,  $\beta$  particles as well as  $\gamma$  rays are all considered ionizing radiation, which interact with matter in different ways.

#### **3.1.1. Charged Particles**

Positively charged particles (protons,  $\alpha$  particles, nuclei), as well as electrons and positrons, both interact with matter by colliding with electrons in the surrounding medium. Through these collisions, they can ionize the atoms of the absorber before coming to rest. The heavier charged particles do not experience much scattering in the absorber medium so they lose their kinetic energy in a predictable manner as a function of their initial kinetic energy [60]. Electrons and positrons have less predictable energy loss relationships, since they scatter appreciably through the absorber medium. In addition they may lose energy through radiative emission (Bremsstrahlung) because of large scattering angles. When a positron comes to rest, it will annihilate the first electron it contacts, resulting in the emission of two back to back 511 keV gamma rays.

### 3.1.2. Gamma Rays

Gamma rays are energetic photons which ionize matter through different mechanisms than charged particles. Their absorption is similar to the Beer's Law description of the absorption of visible light in a liquid, according to Equation (58), where  $\mu$  is the linear absorption coefficient characteristic of the absorber medium (analogous to the molar extinction coefficient) and  $I$  and  $I_0$  represent the intensity at a given distance  $x$  and the initial gamma ray intensity, respectively, [2]

$$I = I_0 e^{-\mu x} . \quad (58)$$

There are three major modes of interaction of gamma rays with matter:

1. Photoelectric absorption: gamma rays are completely absorbed, the energy being transferred to electrons in the medium through the photoelectric effect. The probability of interaction per atom ( $\tau$ ) is expressed in Equation (59) [60], in which the exponent  $n$  is an empirically determined number between 4 and 5.

$$\tau \propto \frac{Z^n}{E_\gamma^{3.5}} \quad (59)$$

This probability cannot be reduced to an angle-dependent scattering probability (differential cross-section) because of the numerous processes that go into the total absorption probability.

2. Compton scattering: gamma rays transfer a portion of their energy to the medium through inelastic scattering off atomic electrons, reducing the outgoing gamma ray energy after the collision. The energy loss is dependent on the scattering angle  $\theta$ , and so can be expressed in the form of a differential cross-section ( $d\sigma/d\Omega$ ), via the Klein-Nishina formula [60]:

$$\frac{d\sigma}{d\Omega} = Zr_0^2 \left( \frac{1}{1 + \alpha(1 - \cos \theta)} \right)^2 \left( \frac{1 + \cos^2 \theta}{2} \right) \left( 1 + \frac{\alpha^2(1 - \cos \theta)^2}{(1 + \cos^2 \theta)[1 + \alpha(1 - \cos \theta)]} \right) \quad (60)$$

In Equation (60),  $r_0$  is the classical electron radius, and  $\alpha$  is the ratio of the gamma ray energy to the electron rest energy.

3. Pair production: when gamma rays have an energy above 1.022 MeV, their interactions with the nuclear electromagnetic fields in the absorber medium can cause the formation of positron-electron pairs. The 1.022 MeV threshold is required because of the combined masses of the electron and positron produced during this process. Any remaining energy is transferred to the newly formed electron and positron. The probability for pair production per atom ( $\kappa$ ), as with the photoelectric effect, can only be approximately determined [60],

$$\kappa \propto Z^2 . \tag{61}$$

Equation (61) shows that the dominant effect is the atomic number of the absorber.

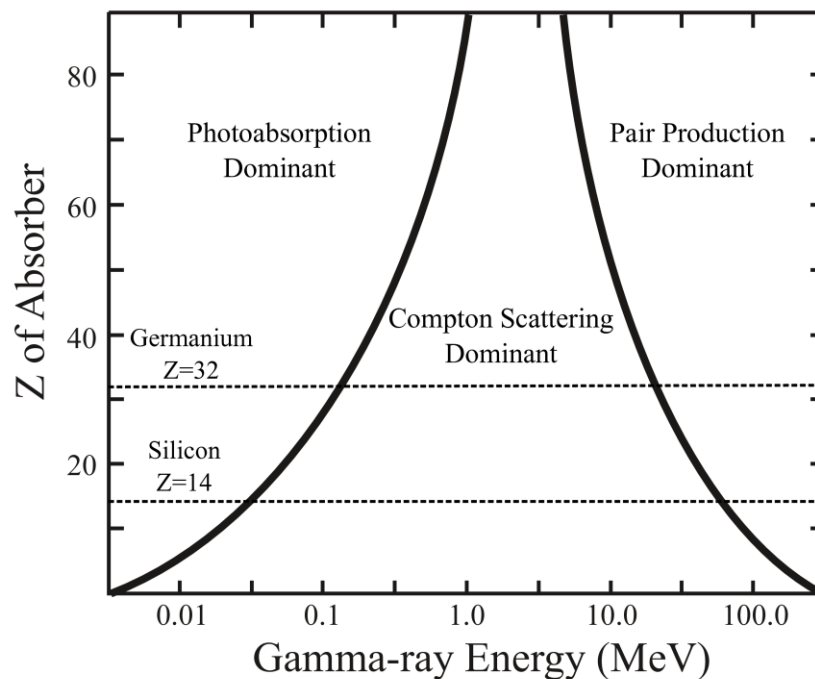


**Figure 19.** Graph showing contributions to the total absorption of gamma radiation, with  $Z_{\text{absorber}}$  on the y-axis and the energy on the x-axis (logarithmic scale). Note the dotted lines indicating the dominant gamma ray interactions for germanium and silicon. Reproduced and adapted with permission [61].

### 3.2. Detecting Ionizing Radiation

There are different types of detectors for detecting various forms of ionizing radiation. The two detector types of interest in this work are HPGe (High Purity Germanium) detectors, and Si(Li) (Lithium-drifted Silicon) detectors. Both are

semiconductor type detectors. The general principle of a semiconductor detector is that a pure crystal is connected to a reverse-bias voltage such that it becomes depleted of charge carriers within the bulk volume. Upon interacting with the crystal, gamma rays or conversion electrons will create electron-hole pairs, causing a transient electrical pulse whose peak amplitude is proportional to the energy deposited. A pre-amplifier in the detector allows the signal to be observed on an oscilloscope or processed further with analog and/or digital equipment to record an energy spectrum.

HPGe detectors of the coaxial type used in the present experiment are optimal for gamma ray detection owing to their good energy resolution [60] (approximately 2-3 keV FWHM) and the establishment of techniques for fabricating large-volume crystals to increase the interaction probability (which depends on the  $Z$  and  $\mu$  of a given absorber) of gamma ray detection; a larger crystal means there is less of a chance that a gamma ray will escape its volume without depositing its energy.

Si(Li) detectors of the 5 mm thick disk type used in the present experiment are optimal for conversion-electron detection owing to their good energy resolution (approximately 2.5-4 keV FWHM) and their lower backscattering probability compared to HPGe, since the probability is proportional to the square of the atomic number of the absorber [62].

$Q$ -values in  $\beta^-$  decay near the valley of beta stability are at most a few MeV; additionally, transition energies in the daughter nuclei will generally be less than 2 MeV. It can be seen from Figure 19 that for gamma-ray detection, silicon ( $Z = 14$ ) and germanium ( $Z = 32$ ) will predominantly experience the photoelectric and Compton effects in this energy regime. It can also be shown for a maximum energy of  $\sim 2$ -3 MeV [60] that electron radiative losses are at most about 4% of the collisional losses, so the predominant mode of interaction for conversion electrons or  $\beta$  particles will be collisions with the atomic electrons in a Si(Li) detector and/or any surrounding absorber material.

### 3.2.1. HPGe Detectors

A gamma-ray spectrum is composed of three major components, which can be related to the way gamma rays interact with matter (Section 3.1.2) [2,60].

1. The energy of the gamma ray can be recorded at the Full Energy Peak (FEP), also termed the photopeak, originating from the full deposition of that energy into the crystal.
2. At energies below the photopeak, Compton interactions, governed by the dependence on the scattering angle, result in a continuum if a gamma ray scatters once or several times before leaving the detector and not depositing its full energy. The scattering-angle dependence (energies in MeV) is given by Equation (62), which determines the shifted energy  $E'$  relative to the incident energy  $E$ . When  $\theta = 180^\circ$ , this gives the maximum shift. Also, the energy of the Compton edge in a gamma ray spectrum is at  $E - E'(\theta = 180^\circ)$ .

$$E' = \frac{E}{1 + \frac{E}{0.511}(1 - \cos \theta)} \quad (62)$$

3. The annihilation of the positron after a pair production event results in the production of two back-to-back 511 keV gamma rays which may escape the detector. If one (single escape) or both (double escape) of the 511 keV gamma rays leaves the detector without interacting with it, then the energy of the FEP will be shifted by 511 keV for a single escape event, or 1022 keV for a double escape event. Additionally, the 511 keV gamma ray itself may be detected as a separate event in the HPGe detector.

A schematic representation of a spectrum resulting from a gamma ray at  $E_\gamma$  is depicted in Figure 20, which shows the above three modes occurring in a detector along with one more mode, which is the escape of an X-ray photon emitted during the photoelectric effect, i.e. an electron vacancy in an atom of HPGe is filled by an electron from a higher orbital, and in that electron transition an X-ray is released. In practice, this peak is often obscured by other components of the background and in a large volume crystal the probability of X-ray escape is small, since low-energy gamma rays are more likely to be absorbed within the crystal.

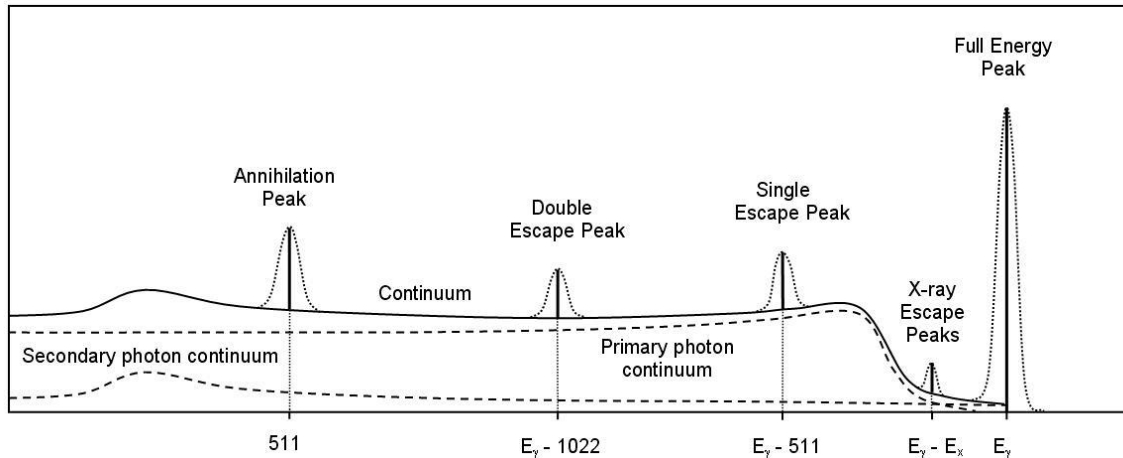


**Figure 20.** Schematic gamma ray spectrum, with energy in keV on the  $x$ -axis and intensity in arbitrary units on the  $y$ -axis. The solid peaks represent a detector with a delta-function energy resolution, while the dashed peaks represent a detector with a finite energy resolution. Image courtesy Nucleonica.com [63].

A schematic diagram showing the parts of a coaxial-type HPGe detector can be seen in the section on the  $8\pi$  detector array (Figure 42), and the principle of operation is similar to that of a Si(Li) detector (Figure 21) in which germanium is used in place of silicon. The dimensions of a coaxial HPGe detector can vary depending on the application but typical specifications obtained from Ortec [64] range from 70 – 100 mm in diameter and 130 – 200 mm in length.

### 3.2.2. Lithium-Drifted Silicon Detectors

A schematic view of the components of a Si(Li) detector is shown in Figure 21; the 5 mm thickness is typical for these detectors, while the diameter of the disk may vary depending on the application [60]. As discussed briefly in Section 3.2, the predominant mode of detection of electrons is in the collisional-loss deposition of the incident electron's kinetic energy within the Si(Li) crystal itself. Background radiations detected by Si(Li) detectors include the continuum of beta particles, backscattered electrons which deposit Bremsstrahlung, and incomplete electron-energy deposition due to multiple scattering events followed by escape from the detector.

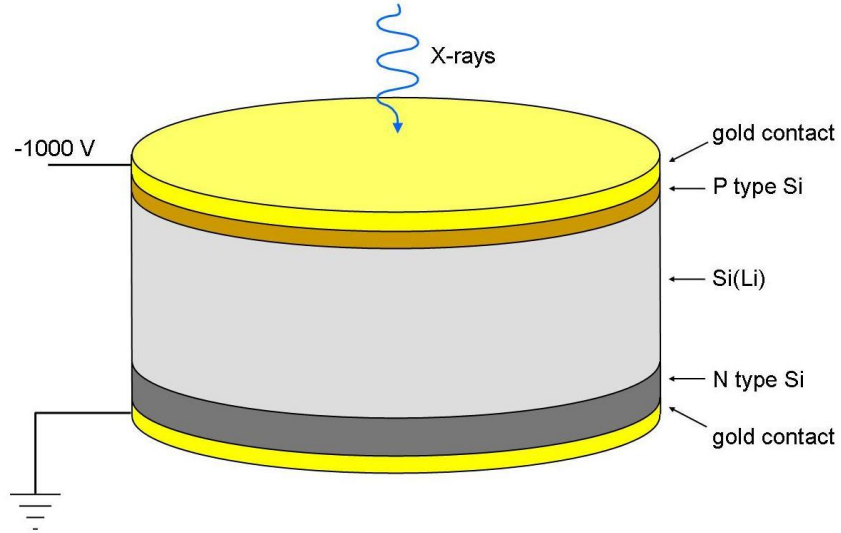


**Figure 21.** Schematic diagram of a Si(Li) detector.

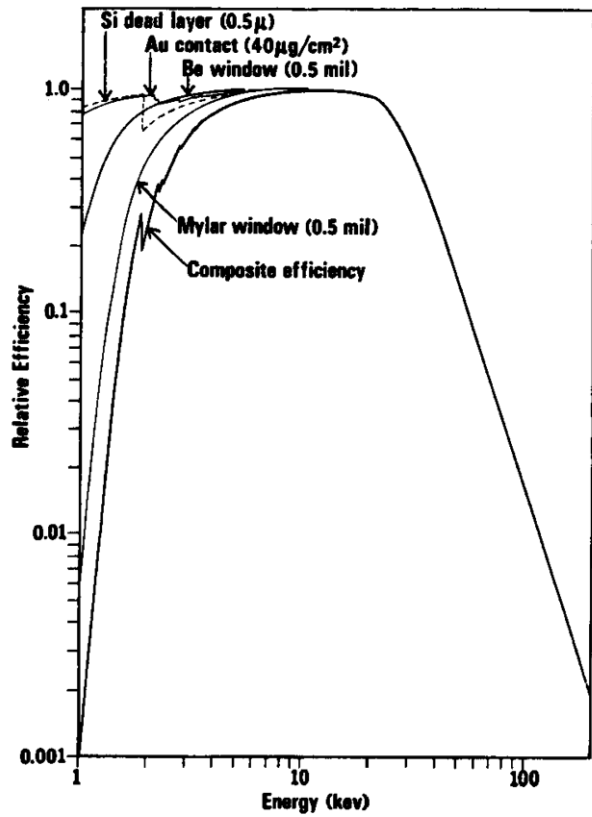


**Figure 22.** Theoretical photon-response efficiency curves for Si(Li) detectors [65]. Reprinted from Nuclear Instruments and Methods Vol. 122, by Gallagher and Cipolla, page 405, copyright 1974, with permission from Elsevier.

Si(Li) detectors do have a non-zero efficiency for the detection of gamma and X-rays, though the probability of interaction decreases very sharply above 100 keV [60] (refer to Figure 22). As such the same possible photopeak and escape-peak features seen in HPGe detector spectra may appear in a Si(Li) detector spectrum, but they will be largely undetectable since Si(Li) detectors have much higher efficiencies for detecting conversion electrons, beta particles and Compton-scattered gamma rays (refer to Figure 19). The Compton continuum therefore convolutes with the electron continuum, discussed above.

As discussed in Section 2.1.3, for photopeak-like events in which the full energy of a conversion electron is detected within the Si(Li) crystal, the measured energies, visible as peaks in a spectrum, will be shifted with respect to the corresponding gamma ray transition by the binding energy characteristic of the nucleus ejecting the conversion electron. A conversion-electron spectrum compared to a gamma-ray spectrum for the same transition in  $^{207}\text{Pb}$  is depicted in Figure 23.

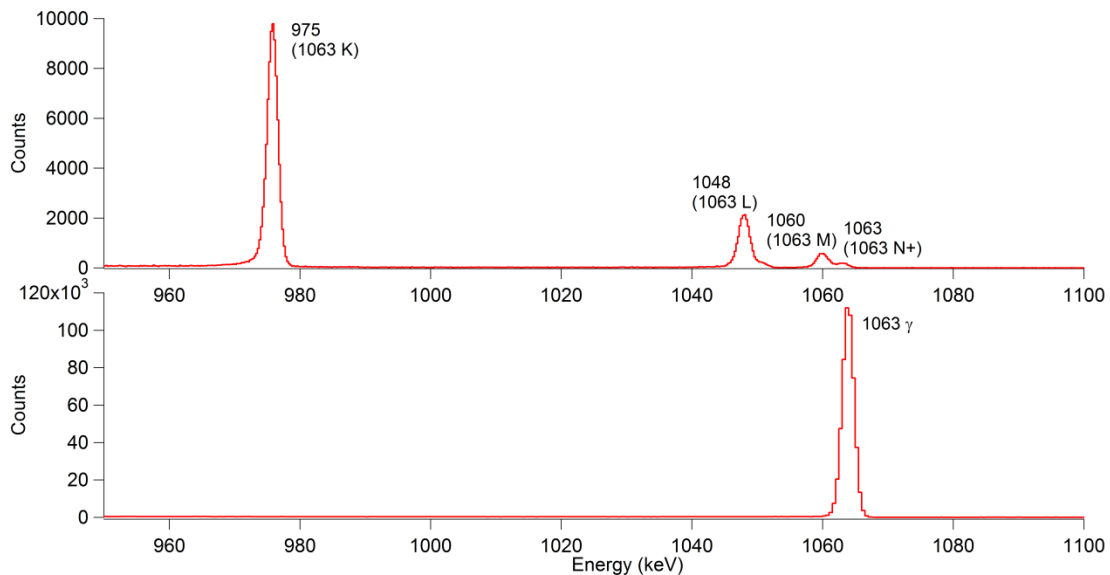


**Figure 23.** Conversion-electron spectrum (top) and gamma-ray spectrum (bottom) showing the 1063 keV transition in  $^{207}\text{Pb}$ , as detected by a PACES Si(Li) detector and an  $8\pi$  HPGe detector. Note the shifted K, L, M, etc. lines in the electron spectrum (e.g. the K binding energy is 88 keV [66], placing the 1063 keV K line at 975 keV).

The presence of K, L, M and possibly resolvable N+ lines in a conversion-electron spectrum makes the spectroscopy more complicated since large energy shifts can potentially place K lines in between the K and L lines of another lower-energy transition. For example, a hypothetical 1000 keV transition in the spectrum in Figure 23 would result in a K electron line at 912 keV, and an L electron line at 985 keV. An even greater challenge is the possibility of the overlap of different electron lines, which would distort measured internal conversion coefficients unless accounted for.

## Chapter 4. Objective and Motivation

### 4.1. Overview of $^{116}\text{Sn}$

The  $^{116}\text{Sn}$  nucleus, with  $Z = 50$  has a magic number of protons, and with its neutron occupancy at  $N = 66$ , is situated at the midpoint between the two major neutron shell closures  $N = 50$  and  $N = 82$ . Its ground state is nearly spherical with a quadrupole moment  $|Q_0| < 0.1$  b [12], due to its magic number of protons.

Several decades of intensive experimental studies of  $^{116}\text{Sn}$  have been performed by various techniques:

- Radioactive decays of  $^{116}\text{In}$  and  $^{116}\text{Sb}$  [57,67--77],
- Proton or neutron capture and/or scattering on appropriate precursor isotopes [78--84]
- Transfer reactions [85--90],
- Coulomb excitation [59,91--97], and
- Fusion evaporation [98,99].

These techniques have shown there is an interplay of single-particle and collective effects in this semi-magic spherical nucleus manifesting as a number of several low-lying states below 3.4 MeV. Single-particle effects manifest as states generated from primarily neutron couplings, while collective effects manifest from other phenomena, such as intruder excitations or what are thought to be vibrational excitations.

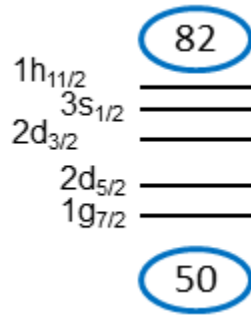


**Figure 24.** Close-up on one possible ordering of the shell-model orbitals that can be occupied by neutrons in  $^{116}\text{Sn}$ .

Given the major proton shell closure, the ground state of  $^{116}\text{Sn}$  can reasonably be expected to be described by admixtures of neutron configurations above  $N = 50$  and below  $N = 82$ . It was experimentally shown by Schippers *et al.* [89] that this is indeed true, with the ground state containing predominantly  $2d_{5/2}$  and  $1g_{7/2}$  character.

It was further shown that the level energies of the yrast  $2_1^+$  and  $4_1^+$  states can be reasonably well-reproduced (as discussed by Flynn and Kunz [100]) assuming neutron-only excitations among the  $1g_{7/2}$ ,  $2d_{5/2}$ ,  $2d_{3/2}$ ,  $3s_{1/2}$ , and  $1h_{11/2}$  shell-model orbitals (Figure 24), whose ordering can fluctuate depending on the choice of potential energy function in the Hamiltonian and the chosen model space. This is further reinforced by the existence of seniority of neutrons as a good quantum number for  $Z = 50$ , as discussed in Section 1.2.1.

Similarly, other low-lying states in  $^{116}\text{Sn}$  can be attributed to neutron-only excitations. However, transfer reactions as well as fusion-evaporation reactions [87--89,99] showed that, as briefly noted in Section 1.2.1, there is a proton 2p-2h intruder excitation which couples to the valence neutrons, generating a collective quasi-rotational band with a deformation of  $\beta_2 \approx 0.20$  [59]. The  $0^+$  member of this band is termed the band-head. This means that proton degrees of freedom are accessible for low-lying states, and the structure of  $^{116}\text{Sn}$  is actually more complex from a theoretical point of view.

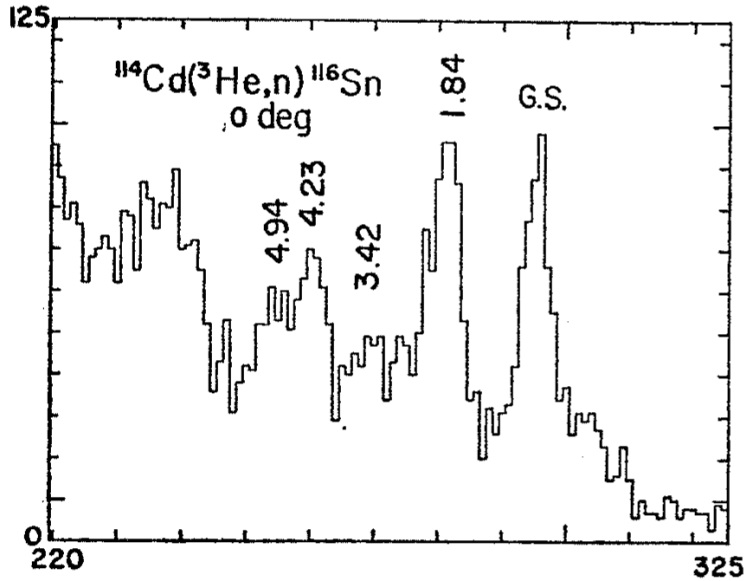


**Figure 25.** The peak at 1.84 MeV indicates that the ( ${}^3\text{He},n$ ) transfer reaction [87] populates the  $0_2^+$  and  $0_3^+$  states in  ${}^{116}\text{Sn}$ . The y-axis shows counts per channel and the x-axis is the channel number. FIG. 2 reprinted from Fielding *et al.*, Nuclear Physics A 281, pages 389-404, copyright 1977, with permission from Elsevier.

The 1757 keV  $0_2^+$  state was considered to be the 2p-2h band-head [82] based on the ( ${}^3\text{He},n$ ) transfer reaction performed by Fielding *et al.* [87], although this state is strongly mixed with the 2027 keV  $0_3^+$  state; the 271 keV transition between them has a relatively large  $\rho^2(E0) \times 10^3 = 87(19)$  [101]. The FWHM of the G.S. peak in Figure 25 is  $\sim 5$  channels, or  $\sim 0.5$  MeV. The 1.84 MeV peak, however, has a FWHM of  $\sim 7$  channels, or  $\sim 0.8$  MeV. The broadening of the 1.84 MeV peak suggests that both the 1757 and 2027 keV states were being populated, supporting the strong mixing of these states, since the ( ${}^3\text{He},n$ ) transfer is sensitive to proton-pairing correlations in the outgoing states. The barycenter of the 1.84 MeV peak indicates that these states were populated in about a 70% (1757 keV):30% (2027 keV) ratio. This strong mixing was later revisited by Pore *et al.* [102,103], and it was found that the 2p-2h quasi-rotational band distributes its rotational character between the  $0_2^+$  and  $0_3^+$  states such that the  $0_3^+$  state is more plausible as the quasi-rotational band-head.

## 4.2. Literature Review

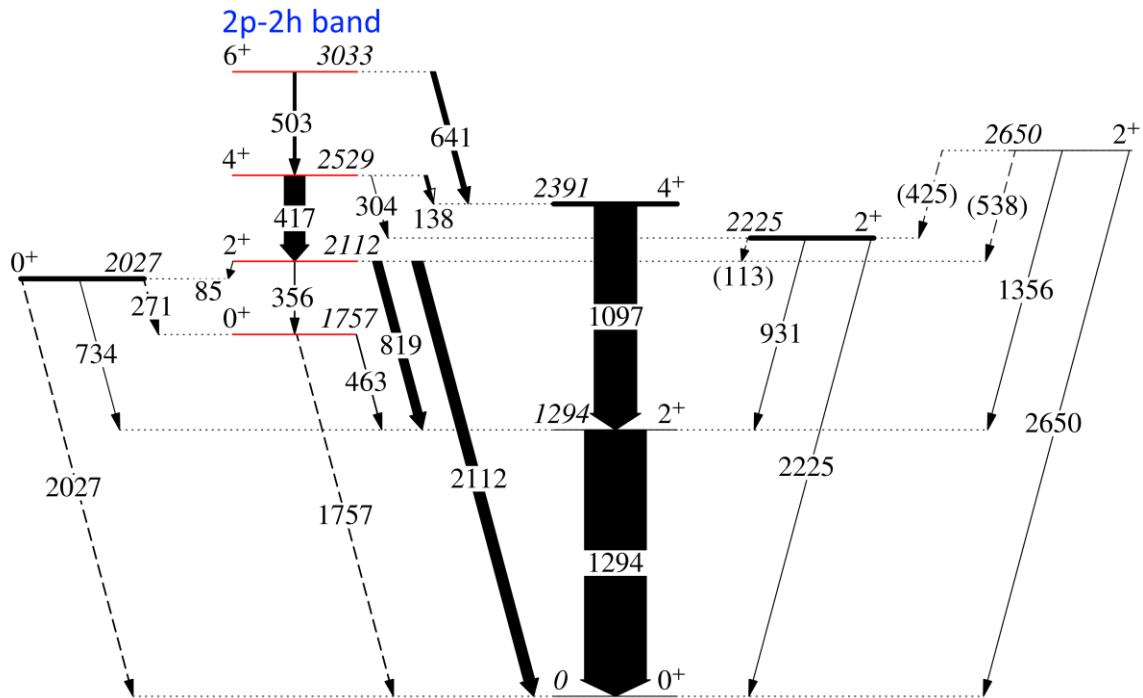


**Figure 26.** Partial level scheme adapted from Appendix A, with  $E0$  transitions marked with dashed lines. Transitions not observed by Pore *et al.* [103] are noted in parentheses. The levels with thick black lines are two-phonon states according to Raman *et al.* [84]. States marked with red lines are part of the proton 2p-2h band as suggested by studies in the 1970s and 1980s [59,82,88,93]. The ground-state band in the middle is thought to be composed primarily of neutron broken-pair configurations with good seniority. The widths of the arrows are proportional to the relative gamma-ray intensities ( $I_\gamma(1294) = 100$ ).

The most recent comprehensive evaluation of the low-lying level scheme of  $^{116}\text{Sn}$  is the work of Raman *et al.* [84], in which  $(n,\gamma)$  and  $(n,n'\gamma)$  data were compared to the models of Wenes *et al.* [104] and Bonsignori *et al.* [105], in order to characterize states in  $^{116}\text{Sn}$  in terms of broken-pair components, phonon states or proton 2p-2h states (see Figure 26 for some examples of these states in  $^{116}\text{Sn}$ ). In addition, the level scheme of  $^{116}\text{Sn}$  up to 4.3 MeV was compared to past experiments in order to verify level energies and gamma-ray placements. However, detailed spectroscopic data such as  $B(E2)$  and

$B(M1)$  strengths, or mixing ratios, was not discussed by Raman *et al.*, as this data was not obtained in the inelastic neutron-scattering experiment.

Previous experimental work which has furnished spectroscopic data useful for models of  $^{116}\text{Sn}$  involved various forms of Coulomb excitation, as well as inelastic proton and neutron scattering [59,84,93--95]. The resulting interpretation of the  $B(E2)$  and  $\rho^2(E0)$  values by Kantele *et al.* [93], Bäcklin *et al.* [59], and Jonsson *et al.* [82] ultimately focused on the issue of mixing of excited  $0_{2,3}^+$  states in isotopes of tin (including  $^{116}\text{Sn}$ ), and this mixing is of ongoing interest as noted in Section 4.1.

Similarly, the  $2^+$  and  $4^+$  states were probed in experiments such as the  $(d,p)$  work of Schneid *et al.* [85] (followed by that of Schippers *et al.* [89], who also performed  $(d,t)$  reactions), the  $(p,p')$  work by Wienke *et al.* [83] and more recently, the  $(p,t)$  work of Guazzoni *et al.* [90]. Each of these experiments probed different aspects of the states in  $^{116}\text{Sn}$  in the following ways:

- $(d,p)$  and  $(d,t)$  probed the underlying shell-model compositions of the wavefunctions (or parts of the wavefunctions) of the outgoing states when adding a neutron to  $^{115}\text{Sn}$ , or removing a neutron from  $^{117}\text{Sn}$ ,
- $(p,p')$  probed the shell-model and vibrational configurations when exciting  $^{116}\text{Sn}$  from the ground  $0^+$  state into excited states (that is, the change in angular momentum could be correlated with what excited-state orbitals were likely to be involved),
- $(p,t)$  probed the similarities of the outgoing states to the  $0^+$  ground state of  $^{118}\text{Sn}$ ; the resulting angular momentum transfers and cross-sections can probe the neutron content of the outgoing  $^{116}\text{Sn}$  wavefunctions, although qualitatively only very intense peaks are likely to be definitively associated with considerable neutron character.

The calculation by Guazzoni *et al.* joins other theoretical work [100,104--111] undertaken in parallel with extensive experimental work on  $^{116}\text{Sn}$ . The main factor

underlying the approaches taken is the computational intractability of the shell model in reproducing  $B(E2)$  values or mixing ratios. In the 1970s, the semi-empirical treatment by Flynn and Kunz [100] examined aspects of the structure of  $^{116}\text{Sn}$  in a rather simple way, treating them as pairing vibrations in a harmonic-vibrator model. Their predictions were compared to experimental data available at the time, and so mainly relied on transfer reaction data from Ref. [87]. In doing so it was observed that for the  $Z = 50$  isotopes, among them  $^{116}\text{Sn}$ , the  $I^\pi = 0_2^+$  1757 keV state was considerably lower in energy than that predicted by the simple vibrational model, and this effect was attributed to a “large Coulomb particle-hole interaction” [100] by Flynn and Kunz.

Other approaches, which reduce or avoid the need for a full shell-model treatment, involve model-space truncation using seniority to examine level energies, as done by Raman *et al.* [84], and collective-model wavefunctions were used by Wenes *et al.* to make  $B(E2)$  value calculations computationally tractable, resulting in the data shown in Figure 28. Other kinds of simplifications include the work by Bonsignori, in mixing broken-pair excitations with vibrational states to generate seniority states in  $^{116}\text{Sn}$  [105]. Alternatively, Song and Yang, and later Chen *et al.* [108,109], attempted to predict  $B(E2)$  values among excited states using the Interacting Boson Model, which is analogous to seniority in treating protons and neutrons as paired particles. These values are shown in Figure 29. In all cases (Wenes, Bonsignori, Song and Chen), it can be seen that their models sometimes predict very different  $B(E2)$  values for transitions in  $^{116}\text{Sn}$  compared to experimental data.

It was, however, possible for the theoretical approaches taken, in particular by Wenes *et al.*, to reproduce the presence of the proton 2p-2h intruder band, suggesting at the time that rotational-vibrational coupling was a reasonable way to describe the admixtures in the even-spin even-parity states in  $^{116}\text{Sn}$  up to about 4 MeV. Arguing against the complete success of this approach, besides the deviations in  $B(E2)$  value predictions already noted, is that the level energies of the highly-mixed  $0_{2,3}^+$  states were not well-reproduced by Wenes *et al.* (Figure 27). Within these limitations, however, the

computations formed part of the comprehensive analysis of the level scheme of  $^{116}\text{Sn}$  by Raman *et al.* in a synthesis with experimental data.

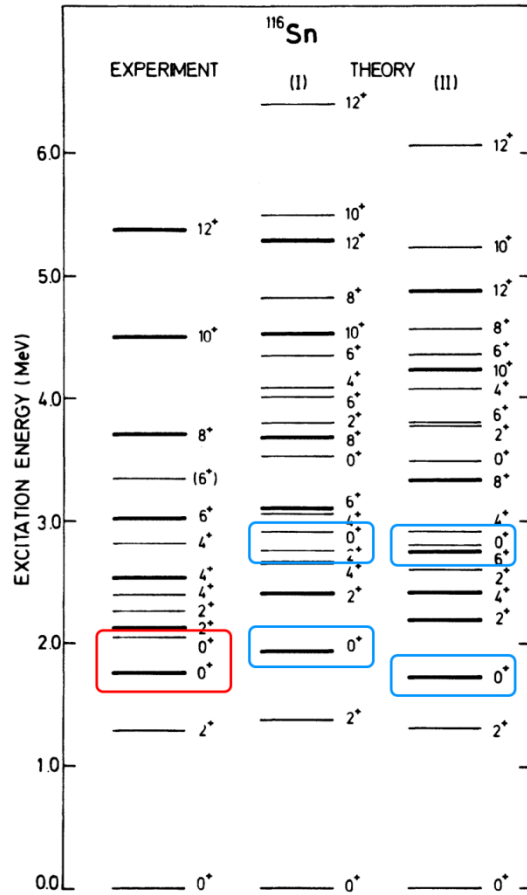


**Figure 27.** Comparison of experimental level energies to two different models, showing that the closely-spaced experimental  $0_{2,3}^+$  states (red box) are not well-reproduced (blue boxes) from the models employed by Wenes *et al.* Reprinted FIG. 4 with permission from G. Wenes *et al.*, Phys. Rev. C, 23, 2291 (1981). Copyright 1981 by the American Physical Society.

TABLE IV. Comparison of calculated [(I) and (II) correspond with a coupling strength  $\xi_2 = 7.5$  and  $8.0$ , respectively] and very recent experimental  $B(E2)$  values in  $^{116}\text{Sn}$  (Ref. 32).

$J_i^\pi \rightarrow J_f^\pi$	$B(E2)$ (W.u.)		Experiment <sup>a</sup>
	Theory		
	(I)	(II)	
$2_1^+ \rightarrow 0_1^+$	15.1	15.7	13
$2_2^+ \rightarrow 0_1^+$	0.03	0.12	0.06
$\rightarrow 0_2^+$	7.1	18	26
$\rightarrow 0_3^+$	8.9	12.2	32
$\rightarrow 2_1^+$	26.8	23	4
$2_3^+ \rightarrow 0_1^+$	0.014	0.0007	0.05
$\rightarrow 0_2^+$	23.7	15.7	0.7
$\rightarrow 0_3^+$	13.1	4.1	<2
$\rightarrow 2_1^+$	7.0	18.1	5
$\rightarrow 2_2^+$	14.7	7.9	<3
$0_2^+ \rightarrow 2_1^+$	46.5	65.8	17
$0_3^+ \rightarrow 2_1^+$	0.67	0.99	0.5
$4_1^+ \rightarrow 2_1^+$	6.6	16.1	23
$\rightarrow 2_2^+$	12.5	11.3	60
$\rightarrow 2_3^+$	13	0.3	<2
$4_2^+ \rightarrow 2_1^+$	27.4	24.5	<0.003
$\rightarrow 2_2^+$	7.0	27	>17
$\rightarrow 2_3^+$	17.3	15.8	>0.3
$\rightarrow 4_1^+$	15.4	11.3	

<sup>a</sup> Reference 32.

**Figure 28.**  $B(E2)$  values predicted by Wenes *et al.* for  $^{116}\text{Sn}$  compared to then-current experimental data. Reprinted image of TABLE VI with permission from G. Wenes *et al.*, Phys. Rev. C, 23, 2291 (1981). Copyright 1981 by the American Physical Society.

**Table 4.** Comparison of calculated and experimental values of  $B(E2; J_i \rightarrow J_f)/B(E2; 2_1^+ \rightarrow 0_1^+)$  for  $^{116}\text{Sn}$ .

$J_i \rightarrow J_f$	Exp. <sup>a</sup>	Cal. <sup>b</sup>	Cal. <sup>c</sup>	$J_i \rightarrow J_f$	Exp. <sup>a</sup>	Cal. <sup>b</sup>	Cal. <sup>c</sup>
$4_2 \rightarrow 2_3$	$> 0.017$	0.014	0.012	$2_3 \rightarrow 0_2$	0.025	0.084	0.074
$4_2 \rightarrow 2_2$	$> 0.92$	8.85	11.4	$2_3 \rightarrow 0_1$	$1.25 \times 10^{-3}$	0.0086	0.0613
$4_2 \rightarrow 2_1$	$> 1.7 \times 10^{-5}$	0.97	1.93	$2_2 \rightarrow 2_1$	0.33	0.135	0.213
$4_1 \rightarrow 2_3$	$< 0.17$	0.23	0.197	$2_2 \rightarrow 0_3$	2.83	2.31	1.24
$4_1 \rightarrow 2_2$	3.92	6.42	11.1	$2_2 \rightarrow 0_2$	1.83	2.15	4.39
$4_1 \rightarrow 2_1$	1.58	2.06	3.15	$2_2 \rightarrow 0_1$	0.005	0.23	0.104
$2_3 \rightarrow 2_2$	$< 0.083$	0.098	0.345	$0_3 \rightarrow 2_1$	0.042	0.74	1.56
$2_3 \rightarrow 2_1$	0.12	0.0029	$3.85 \times 10^{-4}$	$0_2 \rightarrow 2_1$	1.5	2.10	0.401
$2_3 \rightarrow 0_3$	$< 0.05$	0.71	6.794				

<sup>a</sup>Taken from Ref. [2] and the references therein. <sup>b</sup>From the present work. <sup>c</sup>Taken from Ref. [9].

**Figure 29.** Relative  $B(E2)$  values for transitions in  $^{116}\text{Sn}$  computed by Chen *et al.*, and compared to then-current experimental data. The calculations marked “b” are from the work by Chen *et al.*, while “c” is from the previous work by Song *et al.* [108]. Reproduced image of Table 4 from CHEN XiaoLin, LU DaHai, and YANG LiMing, Vol. 34, No. 2, September 15, 2000 pp.267-272 of Communications in Theoretical Physics with permission.

### 4.3. The Low-Lying $2^+$ States

In discussing the low-lying excited states in  $^{116}\text{Sn}$ , Raman *et al.* relied heavily on a  $(p,p')$  experiment performed by Wienke *et al.* [83]. In accordance with the nearly-spherical ground state, along with the  $(p,p')$  results as well as by analogy to the cadmium and tellurium even-even isotopes, the 1294 keV  $2_1^+$  state ( $t_{1/2} = 0.374(10)$  ps [55]) was assigned one-phonon character, and has a seniority of  $\nu = 2$ . Wienke *et al.* reported that this state has a deformation<sup>10</sup> of  $((\beta_2)^2)^{1/2} = 0.134$ , suggesting that an excitation from the  $0^+$  ground state involves a collective component (which can justify the one-phonon assignment).

In the 1970s, the 2112 keV  $2_2^+$  state ( $t_{1/2} = 1.89(10)$  ps [55]) was originally thought to be vibrational [29]. Wienke *et al.* assigned the 2112 keV state 15% two-phonon character from a determination of the vibrational contribution to the deduced

<sup>10</sup> The original value reported by Wienke *et al.* is the square root of the expectation value of  $(\beta_2)^2$ , which was reported in that work as  $\beta_2$ .

cross-section from the angular momentum transfer, utilizing a two-state mixing model calculation. Other experiments conducted in the late 1970s and early 1980s revealed that the 2112 keV state is actually part of the intruder quasi-rotational band [88,98,99]. This is confirmed from the lack of population of this state in the  $(d,p)$  experiment of Schneid *et al.* [85], as well as various transfer reactions performed by Schippers *et al.* [89] showing negligible spectroscopic strength entering this state; this confirms that the dominant wavefunction constituent is the proton 2p-2h pairing correlation.

The 2225 keV  $2_3^+$  state ( $t_{1/2} = 2.4(12)$  ps [55]) has proven less tractable. By implication from the  $(p,p')$  results, this state should have 85% two-phonon character; Raman *et al.* thus assigned this state as the  $2^+$  member of the two-phonon triplet. However, as shown in Figure 34, even the most collective 931 keV transition exiting this state only has an absolute  $B(E2) = 5(3)$  W.u. [55] (as compared to the vibrational model prediction<sup>11</sup> of 24.8 W.u.) implying that the 2225 keV state is less collective than the 1294 keV state. Additionally, as noted by Wienke *et al.*, the two-phonon assignment for this state does not agree with the experimental outgoing proton angular distribution, partly because the 2266 keV  $3_1^-$  state is also strongly populated in  $(p,p')$  and cannot be resolved from the 2225 keV  $2_3^+$  state.

The likely interpretation of the 2225 keV  $2_3^+$  state is that its dominant wavefunction constituent is based on broken-pair couplings between neutrons in  $3s_{1/2}$  and  $2d_{3/2}$  or  $2d_{5/2}$  orbitals [98,104]. This is supported by the spin-weighted spectroscopic factor of  $S' = 0.98$  in  $(d,p)$  [85], as well as spectroscopic strengths and theoretical calculations of wavefunction admixtures reported by Schippers *et al.* [89]. Further, there is the allowed  $\log ft$  value of 4.78 [55] in the  $\beta^+$ /EC decay of  $^{116}\text{Sb}$  from the  $3^+$  ground state, whose configuration is one odd proton  $\pi(d_{5/2})$  coupled with one odd neutron  $\nu(s_{1/2})$ . Another point of interest regarding the excited  $2_{2,3}^+$  states in  $^{116}\text{Sn}$  is that a 113 keV

---

<sup>11</sup> Refer to Section 1.2.3 for an overview of the vibrational model predictions of level energies and  $B(E2)$  values.



$[402]5/2^+$  orbital likely does not dominate the ground state wavefunction on the basis of  $B(M1)/B(E2)$  transition strength ratios within the corresponding positive-parity bands in  $^{115}\text{Sn}$  [99]. The lowest-energy neutron orbital is  $\nu(d_{5/2} [413]5/2^+)$ , so it is reasonable to argue that this orbital dominates the 2225 keV  $2_3^+$  state wavefunction, consistent with the two-neutron coupling description outlined earlier in this section.

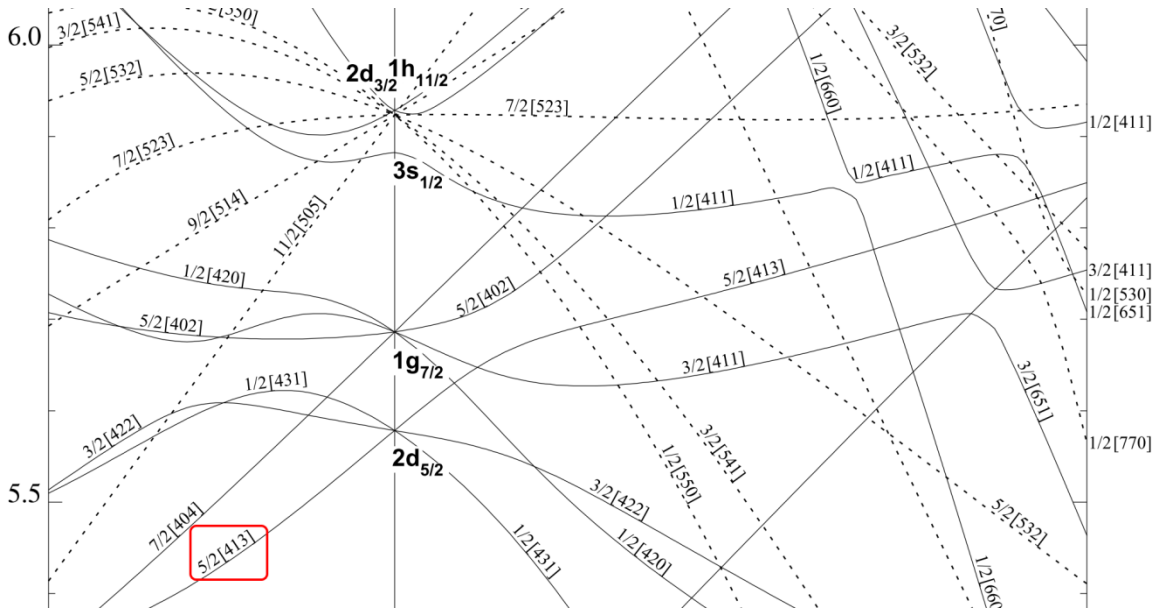


**Figure 31.** Partial Nilsson neutron energy level diagram indicating the  $\nu(d_{5/2} [413]5/2)$  orbital occupied in the energetically-preferred neutron configuration of the 2225 keV  $2_3^+$  state. As in Figure 30, the y-axis shows the single-particle energies and the x-axis, the deformation. Diagram reproduced from Table of Isotopes, 1996 with permission (refer to Appendix E for the full-scale diagram)

To summarize, in  $^{116}\text{Sn}$  the 2112 keV  $2_2^+$  state likely has a wavefunction containing mainly  $\pi(g_{7/2} [431]1/2^+)^2$  proton character in a down-sloping Nilsson orbital favoring a prolate deformation. On the other hand, the 2225 keV  $2_3^+$  state would have predominantly  $\nu(d_{5/2} [413]5/2^+)^2$  neutron character in a down-sloping Nilsson orbital favoring a slightly oblate deformation at most, if not a nearly spherical shape, consistent with  $\beta_2 \approx 0$ .

There is comparatively little information about the 2650 keV  $2_4^+$  state; its half-life was measured to be  $t_{1/2} = 0.55^{+1.2}_{-0.24}$  ps [112], but such a large uncertainty on this

measurement means that the corresponding absolute  $B(E2)$  values for transitions exiting the state also have large uncertainties. Also, if this state mixes with the lower-lying  $2_{2,3}^+$  states, it may mix only weakly with them, and thus may not contain phonon character missing from those states. The  $(p,p')$  work of Wienke *et al.* shows that unlike the 2112 keV  $2_2^+$  or 2225 keV  $2_3^+$  states, the  $L = 2$  angular momentum transfer angular distribution is more consistent with DWBA calculations, suggesting that this state couples  $3s_{1/2}$  and  $2d_{5/2}$  neutrons.

#### 4.4. The Low-Lying $4^+$ States

The low-lying  $4_{1-5}^+$  states in  $^{116}\text{Sn}$  occupy an energy range from  $\sim 2.4 - 3.0$  MeV (Figure 32). There are numerous known transitions among the various  $4^+$  states, several of which were analyzed in this work.

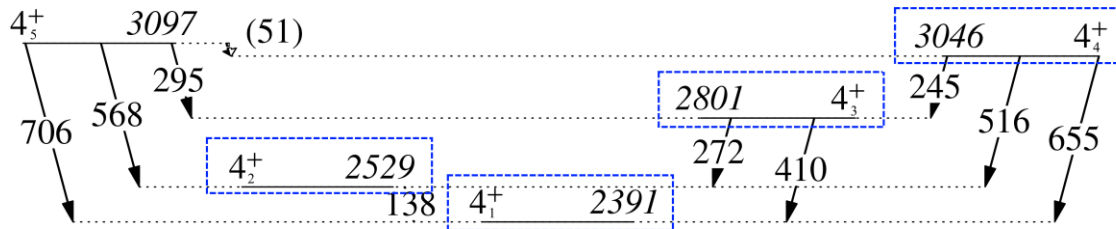


**Figure 32.** Close-up on  $4_{1-5}^+$  states in  $^{116}\text{Sn}$ , adapted from the level scheme in Appendix A. Dashed blue boxes indicate states with fragmented  $L = 4$  strength according to the  $(p,p')$  experiment of Wienke *et al.* [83]; the 51 keV transition was not observed in the present work or in the previous analysis by Pore *et al.* [102,103] due to experimental limitations (see the full discussion in Section 6.3).

The half-lives of the  $4^+$  states, obtained from the Nuclear Data Sheets as well as a private communication, are summarized in Table 2. As with the  $2^+$  states, the assignments of the  $4_{1-4}^+$  states by Raman *et al.* are largely based on the work by Wienke *et al.*; interference from a close-lying  $2^+$  3093 keV state meant that the  $4_5^+$  state (populated in the  $^{116}\text{In}$  decay experiment) could not be observed in the  $(p,p')$  experiment. What was found was that the  $L = 4$  excitation from the ground state was likely a one-step process,

and that the strength of this excitation was fragmented over the  $4_{1-4}^+$  states (refer to Figure 32). These results imply that those states possess similar neutron broken-pair configurations of the form  $(1g_{7/2})^{-1}(3s_{1/2})$ , and so they are also highly mixed. Raman *et al.* therefore expressed the wavefunctions of the low-lying  $4_1^+$  and  $4_{3,5}^+$  states as linear combinations of one (1bp) and two broken-pair (2bp) constituents as shown in Table 3, and were able to reasonably reproduce the level energies with very similar 2bp percentages.

**Table 2.** The  $4_{1-5}^+$  states in  $^{116}\text{Sn}$  and their half-lives.

Level Energy (keV)	$t_{1/2}$ (Refs. [55,112])
2391	0.28(14) ps
2529	0.29 – 100 ps *
2801	$0.253^{+0.229}_{-0.087}$ ps †
3046	$0.77^{+1.3}_{-0.42}$ ps †
3097	N/A

\* The lower limit is from J. Weil, private communication [112] and the upper limit, from the NDS [55].

† Obtained from J. Weil, private communication [112].

**Table 3.** Summary of two-broken-pair character of the  $4_{1-5}^+$  states from Ref. [84]. States also assigned as part of the two-phonon triplet by Raman *et al.* are indicated by (2-ph).

Level Energy (keV)	$4^+$ State Number	% 2bp
2391	1	23 (2-ph)
2529	2	— (2p-2h)
2801	3	28 (2-ph)
3046	4	19
3097	5	21

The 2391 keV  $4_1^+$  state is considered to be the  $4^+$  member of the two-phonon triplet in the simple vibrational model on energy level grounds (further discussion follows in the next section). The analysis by Raman *et al.*, based on the  $(p,p')$  results, excluded the 2529 keV  $4_2^+$  state due to its 2p-2h character and then assigned the 2801 keV  $4_3^+$  and 2391 keV  $4_1^+$  states together as a shared “two-phonon”  $4^+$  state. This leaves open the question of how the the constituents of the  $4_4^+$  and  $4_5^+$  states might be better described.

The 138 keV transition connecting the 2529 keV  $4_2^+$  and 2391 keV  $4_1^+$  states can be considered in light of intruder-yrast mixing, normally characterized by highly collective  $B(E2)$  values (i.e.  $\sim 10 - 100$  W.u. or sometimes even larger). Since other transitions between the 2p-2h band states and the yrast states have high  $B(E2)$  values (e.g. the 279 keV  $4_1^+$  (yrast)  $\rightarrow 2_2^+$  (intruder) [59] transition), the fact that the 138 keV transition was assigned an  $M1$  multipolarity suggests that a form of two-state mixing could explain why it is quite intense but not collective. To this end, measuring an  $E2$  and/or  $E0$  component may better elucidate the nature of the mixing.

#### 4.5. The Vibrational Model Applied to $^{116}\text{Sn}$

It has emerged within the last decade that the major deficiency with the vibrational model as applied to nuclei is that it does not correctly predict the transition strengths between states assumed to be of vibrational character. Systematic studies of the isotopes of cadmium [26,113--115] have revealed that consistently, the experimentally measured transition strengths do not agree with the model (compare to Figure 11). Disagreements can be seen most severely in Figure 33 for the situation of the  $6_1^+ \rightarrow 4_1^+$  transition with a value much greater than predicted, and for the  $0_2^+ \rightarrow 2_1^+$  transition which is much less than predicted.

One possible factor affecting these  $E2$  strengths is that the states are assumed to be purely vibrational in character. If the vibrational states and intruder states are mixed (as has been discussed by Heyde *et al.* [116]), then the vibrational selection rules become modified and the  $E2$  strengths are redistributed into multiple allowed transitions. However, the intruder-phonon mixing adjustments to the phonon model depend on certain assumptions about the nature of the mixing (especially among the phonon and intruder  $2^+$  states) and this has since been brought into question for the Cd isotopes [26]. Therefore, other sources of mixing among the excited states in  $^{116}\text{Sn}$  should be considered as explanations for the experimentally observed  $B(E2)$  values in transitions between states that are thought to be vibrational.

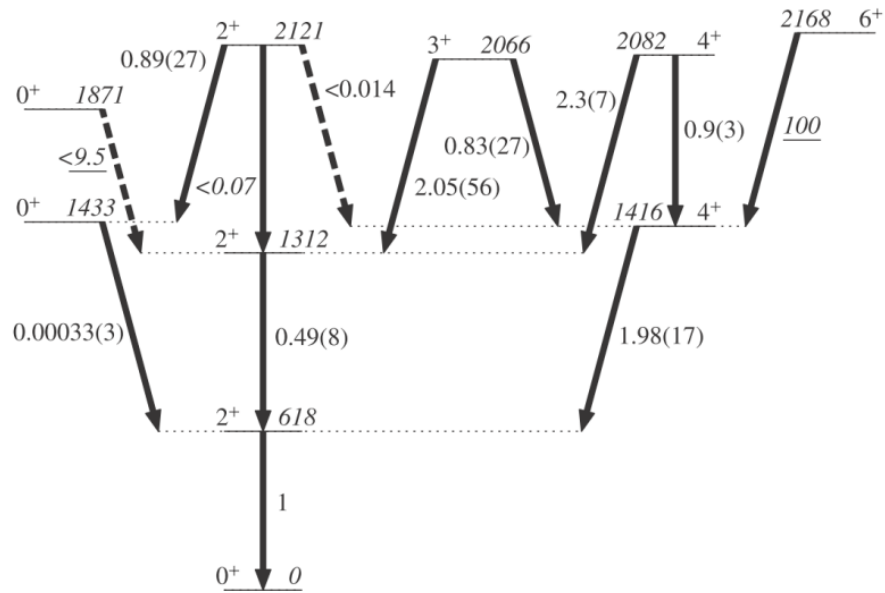


**Figure 33.** Representative relative  $B(E2)$  values from systematic studies of  $^{110-116}\text{Cd}$  [113]; dashed lines indicate as-yet unobserved transitions for which upper limits are given on the  $B(E2)$  values. © IOP Publishing. Reproduced with permission. All rights reserved.

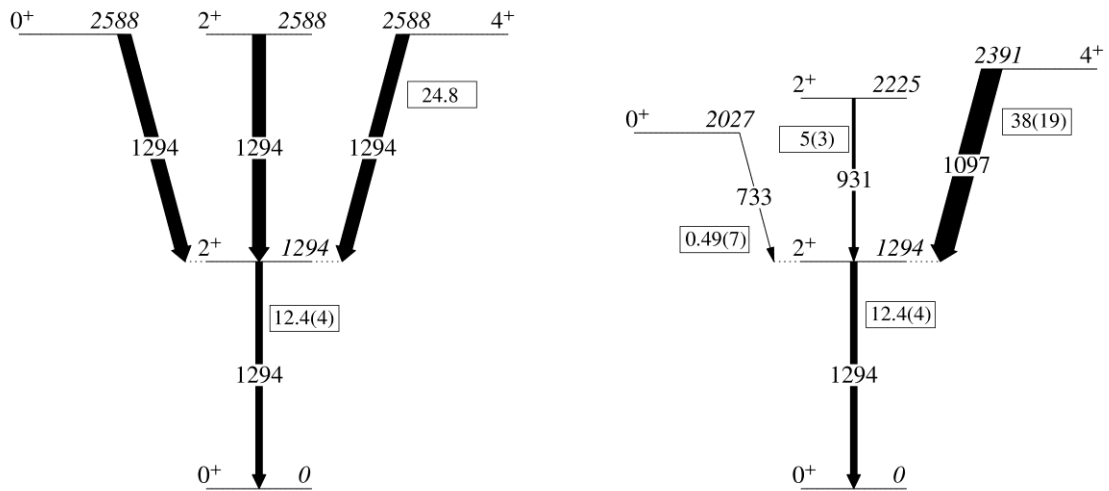


**Figure 34.** Comparison of vibrational model predictions (left) of  $B(E2)$  values (boxed numbers) and level energies to experimental data (right, from the Nuclear Data Sheets [55]) for  $^{116}\text{Sn}$ . The arrow widths are proportional to  $B(E2)$ ;  $1294 \text{ keV} = 12.4(4) \text{ W.u.}$ .

The breakdown of the phonon model when applied to isotopes of cadmium motivated a reinterpretation of their excited states as being characteristic of quasi-rotational nuclei, or “ $\gamma$ -soft rotors” [113]. As seen in Figure 34,  $^{116}\text{Sn}$  has similar discrepancies at the two-phonon level akin to cadmium (Figure 33), in which only the 1097 keV  $4_1^+ \rightarrow 2_1^+$  transition, with  $B(E2) = 38(19)$  W.u.<sup>13</sup> [55] reasonably agrees with the model prediction of 24.8 W.u., while the 734 keV  $0_3^+ \rightarrow 2_1^+$  transition has  $B(E2) = 0.49(7)$  W.u., which is far too small to reconcile with the classification of the 2027 keV  $0_3^+$  state as the  $0^+$  member of the two-phonon triplet. In fact, in the 1980s, classification of tin nuclei as  $\gamma$ -soft rotors was tentatively advanced [59], but difficulties arose in reconciling the  $\gamma$ -soft model with phonon selection rules as applied in particular to  $E0$  transitions in  $^{116}\text{Sn}$ . However, since the cadmium isotopes do not exhibit well-defined vibrational degrees of freedom (as suggested by Garrett *et al.* [26,113,114]), it is likely that the same is true for the tin isotopes.

#### 4.6. Other Models Applied to $^{116}\text{Sn}$

The vibrational model is not the only model used to characterize states in  $^{116}\text{Sn}$ . As discussed in Section 1.2, the shell model in the form of seniority (or LSSM) can be used to characterize some of its excited states. Another model is the Quasiparticle Random Phase Approximation (QRPA), which characterizes nuclear states using mixtures of phonon and broken-pair wavefunctions [117]. While both the LSSM and QRPA models prove effective at predicting level energies in isotopes of tin, the LSSM is less able to predict  $B(E2; 0_1^+ \rightarrow 2_1^+)$  values compared to the QRPA (compare Figure 35 and Figure 36), and neither have been used to predict  $B(E2)$  values for higher-lying transitions. Additionally, the proton 2p-2h band is outside both the QRPA and LSSM model spaces [97], so for these two reasons, neither model completely describes the excited states in  $^{116}\text{Sn}$ .

---

<sup>13</sup> Pore *et al.* recently recomputed this value to be 22.5(43) W.u., which also agrees with the vibrational model.

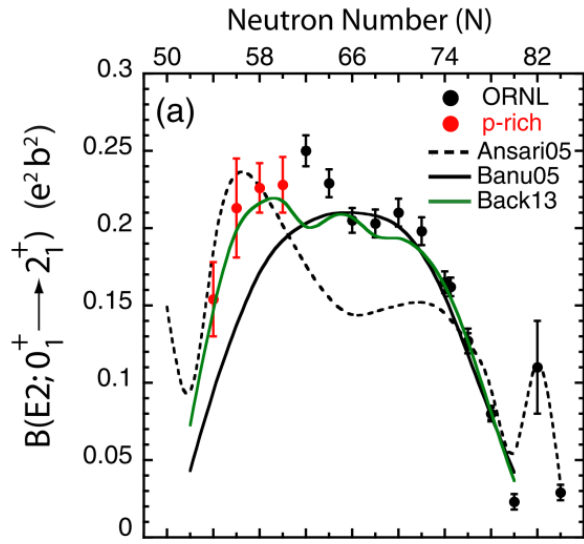


**Figure 35.**  $B(E2)$  trends in isotopes of Sn showing deviations from predictions assuming pure  $\nu = 2$  wavefunctions for the first  $2^+$  state (shown by the black curve) [97]. Other more complex models involving mixing together different shell-model occupancies are shown by the dashed and green curves. Reproduced and adapted with permission.

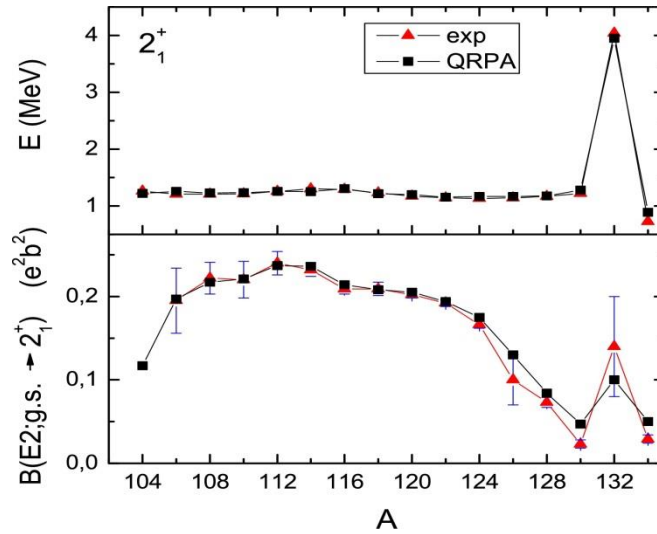


**Figure 36.** QRPA predictions (black points) of the  $2_1^+$  level energies (top) and  $B(E2)$  values (bottom) compared to experimental data (red points). Reproduced from Ref. [117] under the Creative Commons Attribution License (CC BY).

## 4.7. Open Questions Regarding $^{116}\text{Sn}$

Given the deficiencies in various models discussed in the previous sections, it is clear that in order to better characterize excited states in  $^{116}\text{Sn}$ , more spectroscopic data is needed. One area where such data is lacking is that the half-lives (or lifetimes) of some of the even-parity states have very high uncertainties (see Section 4.4). This limits the usefulness of absolute  $B(E2)$  values as inputs to models, or as data for comparison to model outputs. Another area where data is lacking is that the mixing ratios for transitions among the  $4^+$  states are not known. The prevailing interpretation of the low-lying  $4^+$  states as phonon, 2p-2h or neutron broken-pair states rests on the  $(p,p')$  work [83,84]. The lack of mixing ratio data, in particular, motivated the analysis presented in this thesis; more complete data means that models of  $^{116}\text{Sn}$  and neighboring isotopes can be improved.

As a consequence of the deficiencies in the existing models of  $^{116}\text{Sn}$  as well as the need to obtain a more complete body of experimental data, open questions regarding the  $2^+$  states in  $^{116}\text{Sn}$  are:

1. If the 2112 keV  $2_2^+$  and 2225 keV  $2_3^+$  states are not mixed unlike the situation with the  $0_{2,3}^+$  and  $4^+$  states, what might explain this lack of mixing?
2. Consequently, is the phonon  $E2$  strength actually spread out across the  $2_2^+$ ,  $2_3^+$  and  $2_4^+$  states, or does another explanation exist which better rationalizes the experimental  $B(E2)$  values and vibrational model predictions?

Further, some open questions regarding the  $4^+$  states in  $^{116}\text{Sn}$  are thus:

1. Given the very intense apparently pure  $MI$  138 keV transition, how do the 2529 keV  $4_2^+$  and 2391 keV  $4_1^+$  states mix amid the clear evidence of intruder-yrast mixing between the 2p-2h and ground state bands?
2. What is the nature of the 3046 keV  $4_4^+$  and 3097 keV  $4_5^+$  states?
3. Is there an alternative explanation to shared phonon character for the existence of multiple  $4^+$  states within an energy range of 800 keV, especially given that the  $0^+$  and  $2^+$  states indicate possible deficiencies in applying the phonon model?

Conversion-electron spectroscopy and angular correlations, as discussed in Sections 2.1.3 and 2.3, are probes of the multipolarities of transitions in a nucleus,

yielding information about the underlying matrix elements, and probing the nuclear states involved. Therefore, the results presented in this thesis will answer or clarify the above stated open questions, or objectives.

## Chapter 5. Experimental Apparatus

This chapter outlines the TRIUMF-ISAC experimental facility, where radioactive beams are generated and delivered to experimental stations. A detailed description of the  $8\pi$  array, which was in use in the low-energy area when the  $^{116}\text{In}$  decay spectroscopy experiment was performed, is included in this chapter.

### 5.1. Generation of Radioactive Beams at TRIUMF-ISAC

The Isotope Separation and Acceleration (ISAC) facility is shown in Figure 37. Several research groups conduct their activities with radiation detectors and other equipment in this experimental hall. Several of the experimental stations depend on the production of radioactive ion beams, produced via spallation reactions (the break-up of the heavy nuclei into smaller ones under impact from small, energetic projectiles), or by fission (the break-up of heavy nuclei into two or three lighter constituents of approximately equal mass), or by fragmentation (the break-up of a nucleus into multiple smaller constituents) by bombarding 500 MeV protons on selected production targets.

The singly-charged ions which leave the production target are then separated via the Isotope Separation On-Line (ISOL) technique. This method utilizes a magnetic dipole to separate ions based on the charge-to-mass ratio, and can produce either stable or radioactive beams. Alternatively, stable beams can be generated by the Off-Line Ion Source (OLIS), which can ionize appropriate elements (for example, noble gases or certain metals) via a plasma or Electron Cyclotron Resonance (ECR) ion source [118].

## ISAC-I and ISAC-II Facility

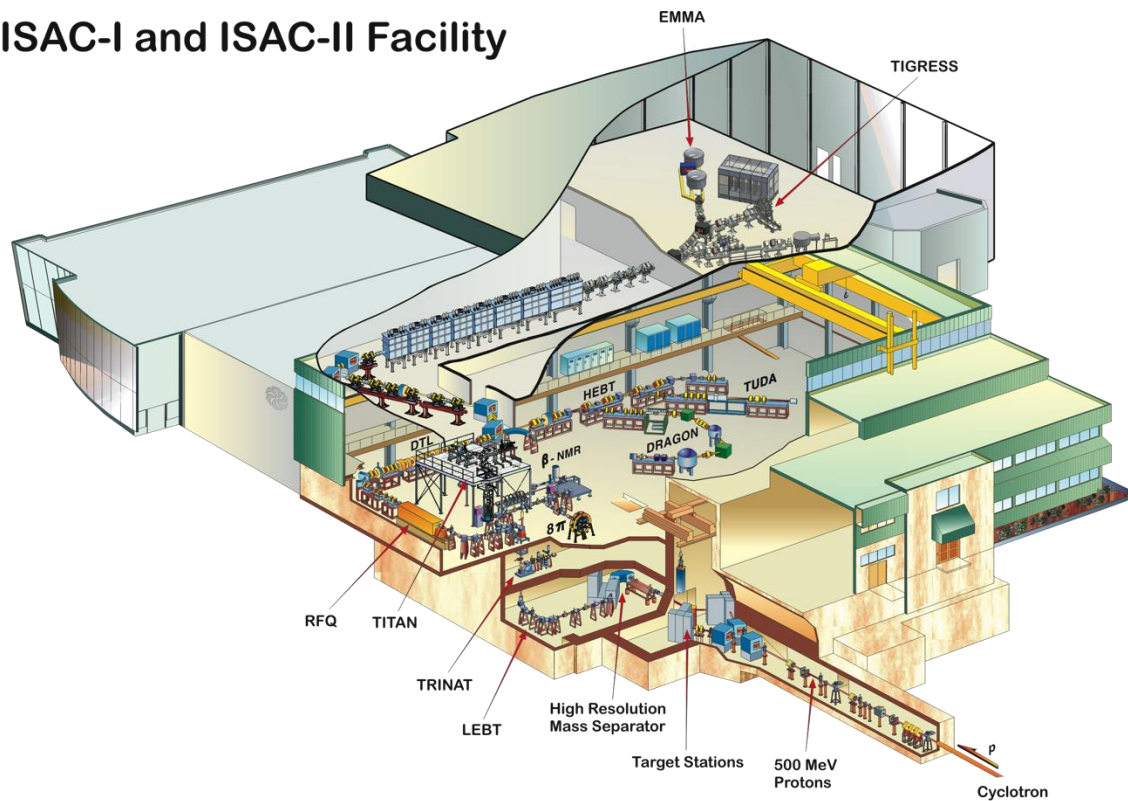


**Figure 37.** The ISAC experimental hall (foreground) with the superconducting LINAC and ISAC-II experimental hall (background, with TIGRESS and EMMA). The  $8\pi$  apparatus is shown in the stopped-beam area near the TRINAT and  $\beta$ -NMR apparatus. Image courtesy of the TRIUMF Design Office [119].

The ISOL technique is used in several facilities worldwide [120]. One of the challenges of the ISOL technique is isobaric contamination (that is, beams of multiple isotopes all having the same  $A$ -value) as it is not possible to completely separate them via the magnetic dipole separator. The isobaric contamination can be particularly troublesome due to the ease with which alkali metals are ionized compared to other elements.

Production of a radioactive beam at TRIUMF is done at one of the two target stations, designated ITW and ITE (for the west and east stations, respectively). A typical

target is high-power Tantalum, which has 525 0.001-inch disks placed very close to one another inside the target holder (which makes the entire target approximately the diameter of a dime and 1 cm thick). Ion production is accomplished by bombarding a beam of 500 MeV protons onto the production target. The resulting products from the reactions inside the target then migrate out of the foil towards the ionizer tube. Figure 38 shows a detailed view of the target holder assembly.

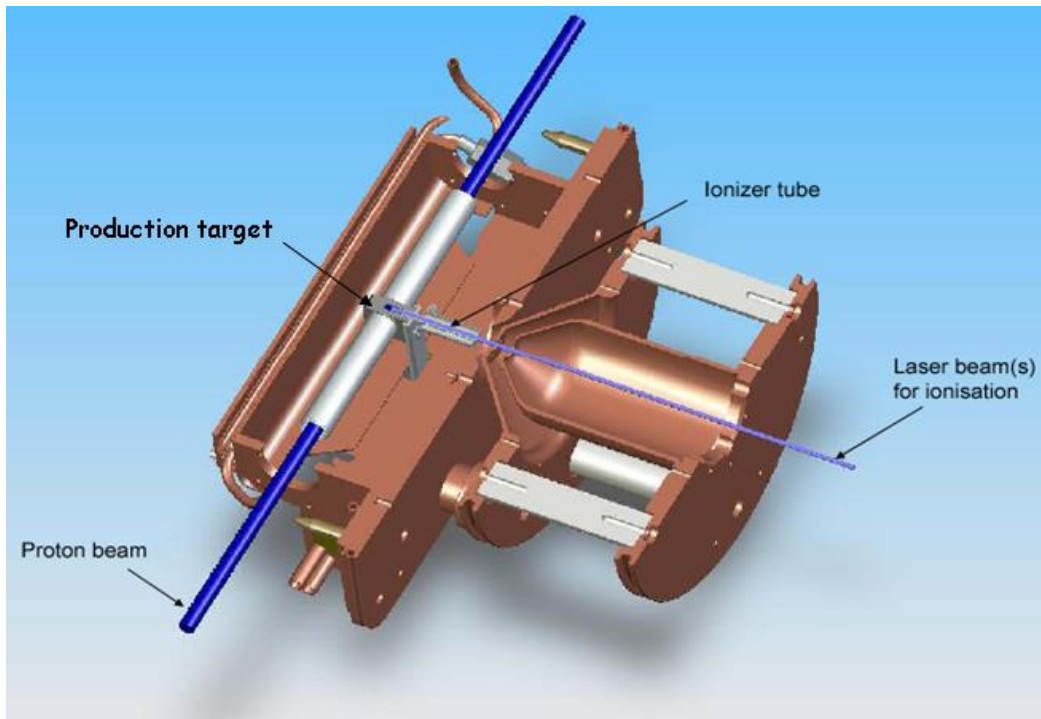


**Figure 38.** Cross-sectional view of a TRIUMF-ISAC target holder. Note how the laser beam, if a laser ion source is used, shines directly into the surface ionization tube to enhance ionization of a desired isotope. (Courtesy Jens Lassen, TRIUMF. Used with permission)

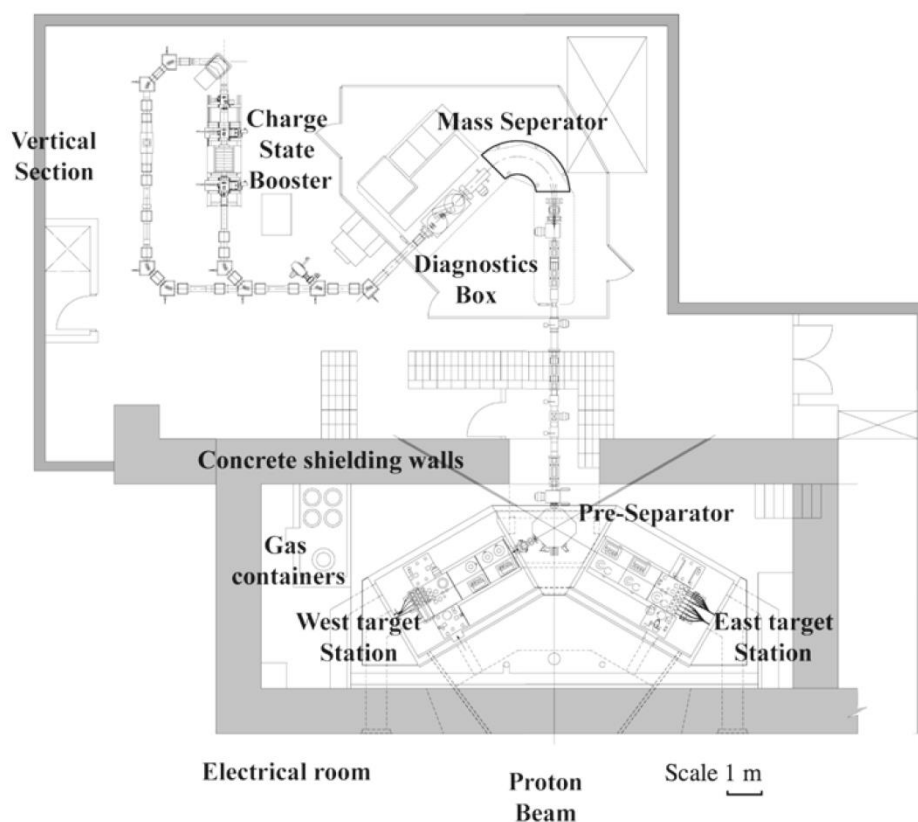


**Figure 39.** ISAC target stations and mass separator system, Fig. 1 reproduced from *Hyperfine Interactions* (2014) 225, pages 25 – 49, with permission from Springer [121].

TRIUMF-ISAC usually uses a surface ionization technique when the desired isotope is relatively easily ionized (i.e. most metals). The ionizer tube (Figure 38) has a sleeve of rhenium inside it, which has an ionization energy of 706 kJ/mol (or work function of 7.84 eV). The reaction products leaving the target, on contacting the heated rhenium sleeve ( $T = 2200\text{ }^{\circ}\text{C}$ ), give up electrons to it during collisions, becoming positively ionized in the process. An applied voltage of  $\leq 60\text{ kV}$  accelerates the ions out of the tube into exit modules which focus and direct the beam into the pre-separator. A series of quadrupole magnets guides this beam to the mass-separator dipole, as seen in Figure 39. A laser ion source, called TRILIS [121], provides element-specific ionization in order to enhance ion production rates above what surface ionization can provide. There is also an electron beam ionizer, called FEBIAD [121], which can be used to ionize noble gases or halogens; surface ionization is difficult or impossible for those elements.

The radius of curvature for a non-relativistic ion of mass  $m$  and charge  $q$  travelling through a magnetic dipole mass separator with a field strength  $B$ , given the kinetic energy  $E_k$  of the incoming beam (which is related to the voltage since  $E_k = qV$ ) is shown in Equation (62),

$$R = \frac{p}{qB} = \frac{\sqrt{2mE_k}}{qB} = \frac{1}{B} \sqrt{\frac{2mV}{q}}. \quad (63)$$

The radius of curvature is therefore proportional to the reciprocal of the charge to mass ratio. The non-relativistic formula is valid for the conditions in the TRIUMF-ISAC radioactive-beam ion source, and is the basis for the ISOL method. It also explains the origin of isobaric contamination, since two ions of the same  $A$ -value with the same charge will have nearly the same exact atomic masses and may likely be non-resolvable with a mass-separator dipole designed according to Equation (63); the one in use at TRIUMF-ISAC has a resolution of one part in 2000 [121].

After the mass separation, the beam is delivered to the main floor of the experimental hall where, in the case of the  $8\pi$  array, the beam, of a few tens of keV kinetic energy, is stopped on the aluminized Mylar tape inside the  $8\pi$  target chamber. The radioactive ions, at rest, emit beta particles, gamma rays and conversion electrons into the detectors surrounding them.

## 5.2. The $8\pi$ Array at TRIUMF-ISAC

The  $8\pi$  detector array [122], when it was in operation at TRIUMF-ISAC, consisted of twenty HPGe detectors (Figure 40) in a truncated icosahedral arrangement [123,124] for gamma-ray detection. Depending on the experiment, the array can be augmented with other detectors that are optimized to detect other types of radiation, or whose timing characteristics are superior to HPGe detectors. The array has since been moved to Simon Fraser University to be reconfigured for the spectroscopy of fission

fragments, while at TRIUMF-ISAC the  $8\pi$  array has been replaced by GRIFFIN, the Gamma-Ray Infrastructure For Fundamental Investigations of Nuclei [124]. Both the  $8\pi$  and GRIFFIN arrays have been used to measure half-lives of nuclear excited states, half-lives of decaying parent nuclei, gamma-ray branching ratios, and internal conversion coefficients, all of which are important both to superallowed decay measurements as well as expanding or improving the knowledge of nuclear structure.

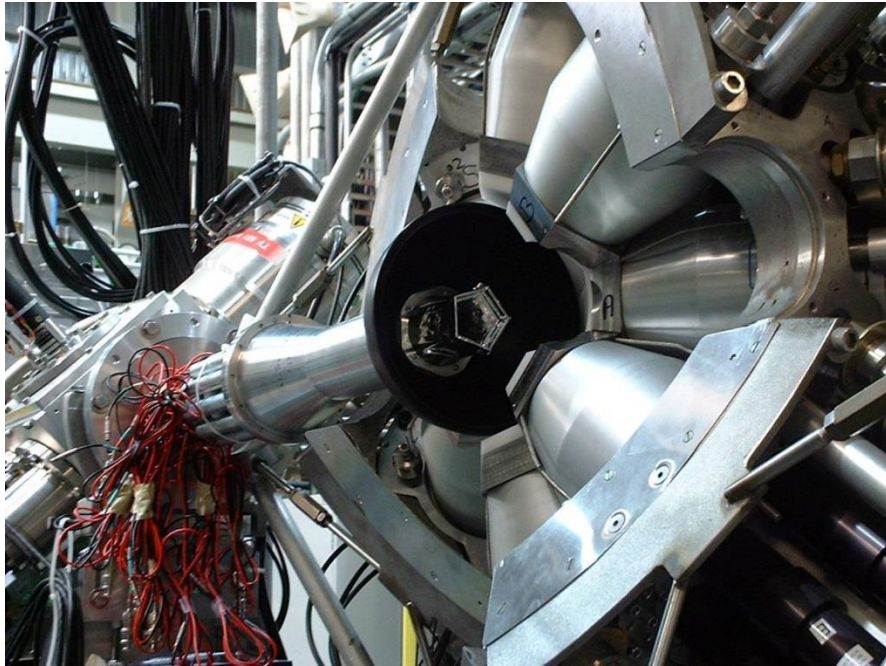


**Figure 40.** The east half of the  $8\pi$  array is shown here, surrounding the black Delrin target chamber.

The HPGe detectors in the  $8\pi$  array contain cylindrically coaxial germanium crystals approximately 70 mm long and 76 mm in diameter. They are surrounded by active bismuth germanate<sup>14</sup> (BGO) Compton-suppression shields as well as internal BGOs mounted behind the germanium crystal, and these scintillation detectors are attached to photomultiplier tubes (PMTs). Heavimet collimators (which are 2.54 cm thick and have a 2.5 cm aperture, primarily consisting of tungsten) are mounted in front of the HPGe detectors (Figure 41) to absorb gamma rays which would otherwise falsely trigger

---

<sup>14</sup> The formula is  $\text{Bi}_4\text{Ge}_3\text{O}_{12}$

the BGO detectors, causing spurious Compton suppression. In addition, they can passively suppress backscattering events where a gamma ray would deposit part of its energy in one HPGe detector, then enter the detector opposite and deposit the remainder of its energy, which would cause spurious coincidence events to be detected. Additionally, Delrin plastic absorbers can be mounted onto the Hevimet collimators to absorb undesired low-energy gamma rays and/or Bremsstrahlung from scattered beta particles inside the target chamber. A schematic showing a cross-section of an  $8\pi$  HPGe detector is shown in Figure 42.

In addition to the HPGe detector array, there were also mounted the DANTE<sup>15</sup> array of BaF<sub>2</sub> and LaBr<sub>3</sub>(Ce) detectors in the pentagonal gaps of the  $8\pi$  frame [25,125,126] (optimized for fast coincidence timing). Inside the Delrin target chamber were mounted the upstream PACES<sup>16</sup> array of liquid nitrogen cooled Si(Li) detectors, which are 5 mm thick and have a 250 mm<sup>2</sup> surface area [127], and a downstream Zero-Degree Scintillator, consisting of a 1 mm thick BC422Q<sup>17</sup> scintillator attached to a photomultiplier tube. The conical tip of a DANTE BaF<sub>2</sub> detector as well as a cylindrical LaBr<sub>3</sub>(Ce) detector can be seen in Figure 41, and the PACES array and Zero-Degree Scintillator are shown in Figure 43 and Figure 44, respectively.

---

<sup>15</sup> Di-Pentagonal Array for Nuclear Timing Experiments

<sup>16</sup> Pentagonal Array for Conversion Electron Spectroscopy

<sup>17</sup> Commonly termed “plastic”, the actual chemical composition primarily consists of polyvinyltoluene.

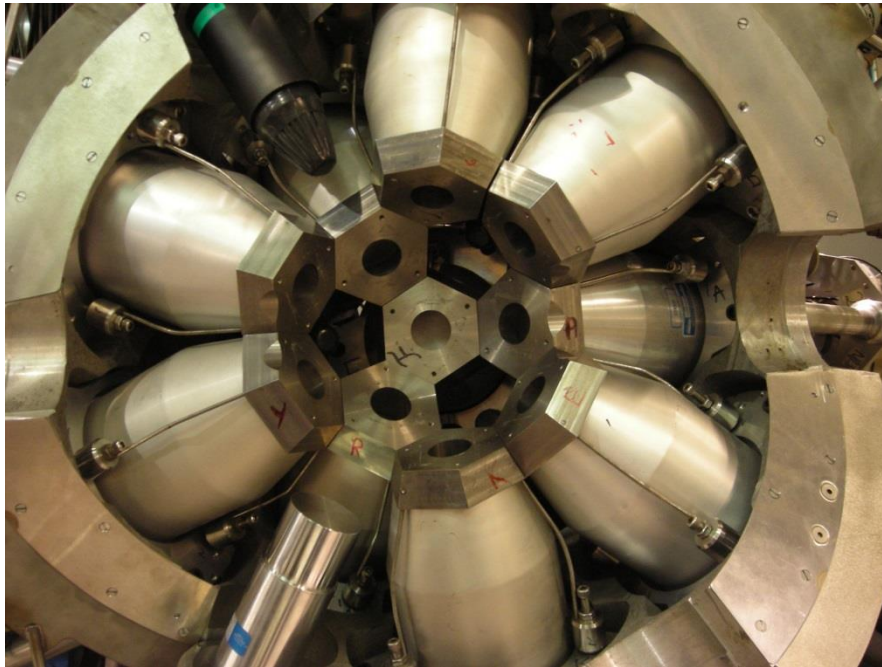


**Figure 41.** A view of the east half of the  $8\pi$  array, which shows the HPGe detector Hevimet collimators without the Delrin absorbers.

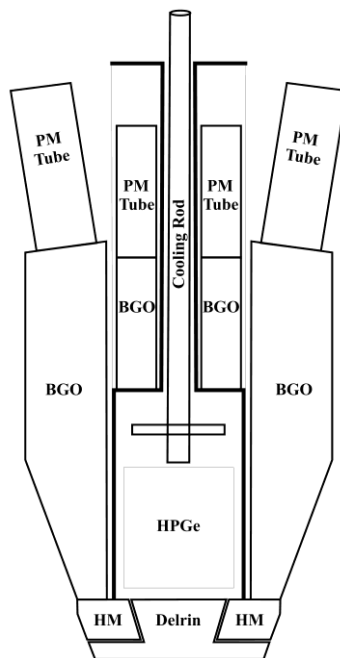


**Figure 42.** Cross-section of an  $8\pi$  HPGe detector, showing the surrounding BGO shields as well as the Hevimet collimator and a Delrin absorber. Adapted from [61] with permission.

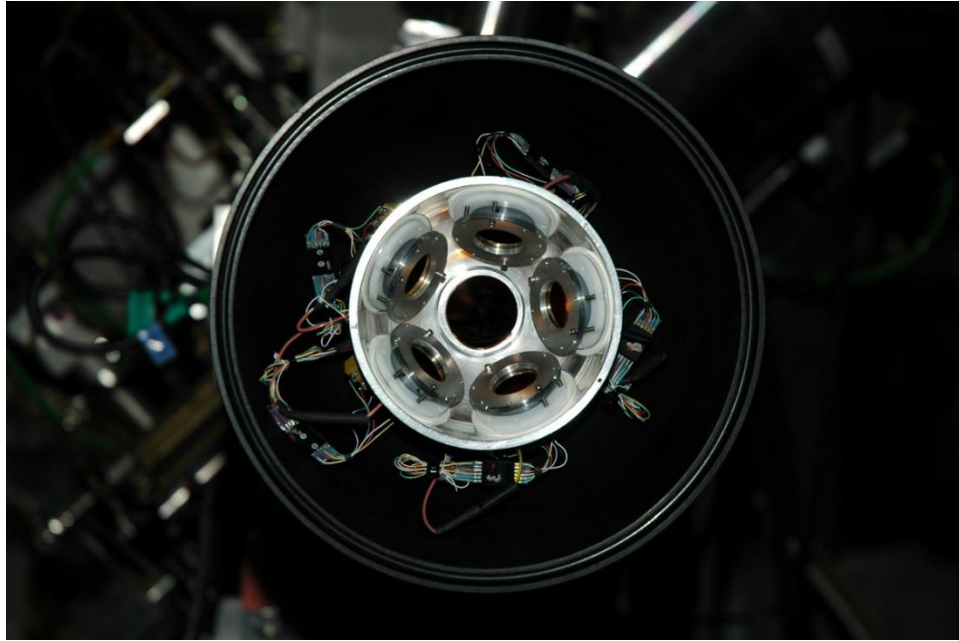


**Figure 43.** The PACES array mounted in the upstream half of the Delrin target chamber.

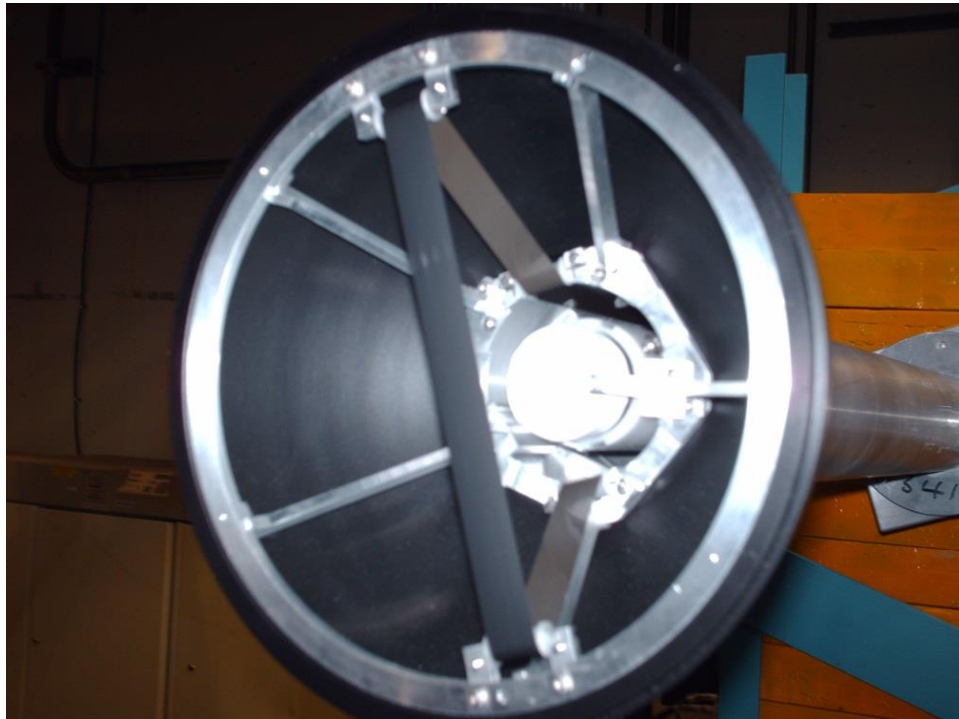


**Figure 44.** The Zero-Degree plastic Scintillator (recessed) in the downstream half of the Delrin target chamber. The aluminized Mylar tape (black) is also visible.

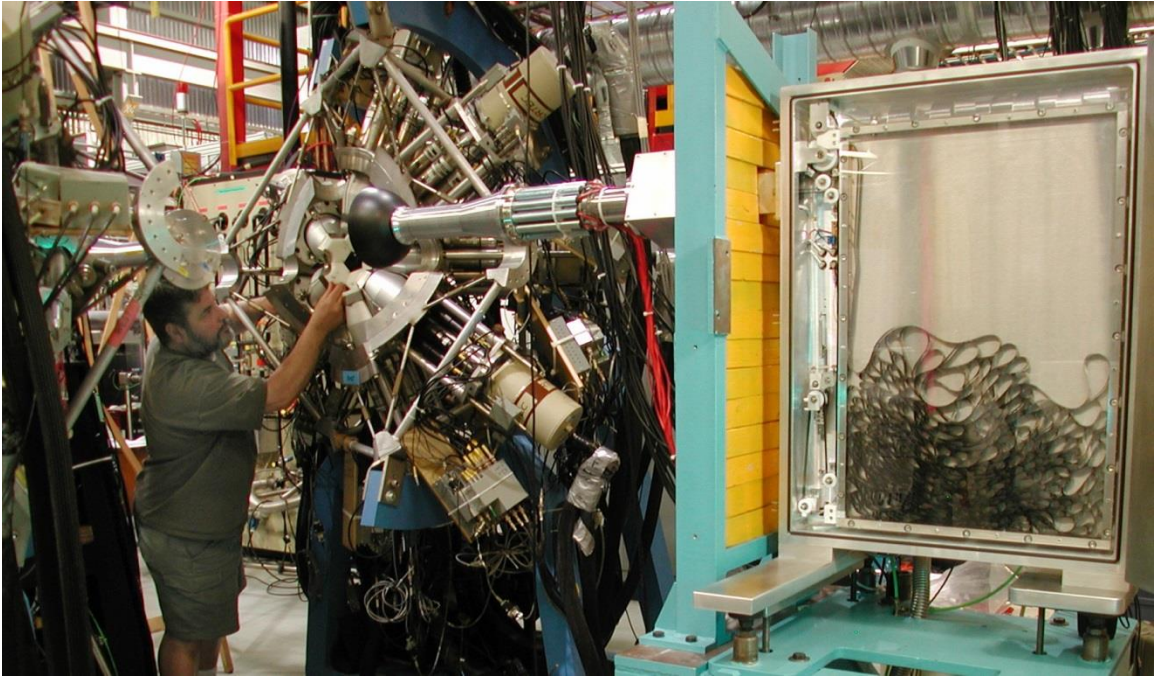


**Figure 45.** The  $8\pi$  array with the open Moving Tape Collector box.

Also visible in Figure 44 is the aluminized Mylar tape, part of the Moving Tape Collector (MTC) which is mounted behind a lead shield to prevent accidental detection of gamma rays from long-lived nuclides that have been implanted onto the tape. The tape spool itself is approximately 120 m long and is 13 mm wide and 50  $\mu\text{m}$  thick. The MTC can move 46 cm of tape behind the lead wall within 340 ms [122] (a speed of  $\sim 100$  cm/s), ensuring minimal loss of time between one beam cycle and the next. The tape box can be seen in Figure 45, along with the lead shield in front of it. In normal operation, the metal door of the tape box covers it and the tape spool is not visible.

### 5.3. Detector Signal Flow Overview

The detectors in the  $8\pi$  array which are of interest to the present analysis of the  $\gamma$  singles and electron singles, along with  $\gamma\text{-}\gamma$  and  $\gamma\text{-}e^-$  coincidences, are the twenty Compton-suppressed HPGe detectors and PACES array of five Si(Li) detectors. The flow of data from either HPGe or Si(Li) detectors to the VME (Versa Module Europa) front-end is diagrammed in Figure 33, and discussed in detail in the text below, including the

subsequent connections to the DAQ (Data Acquisition) system for offline storage of detector events for later analysis.

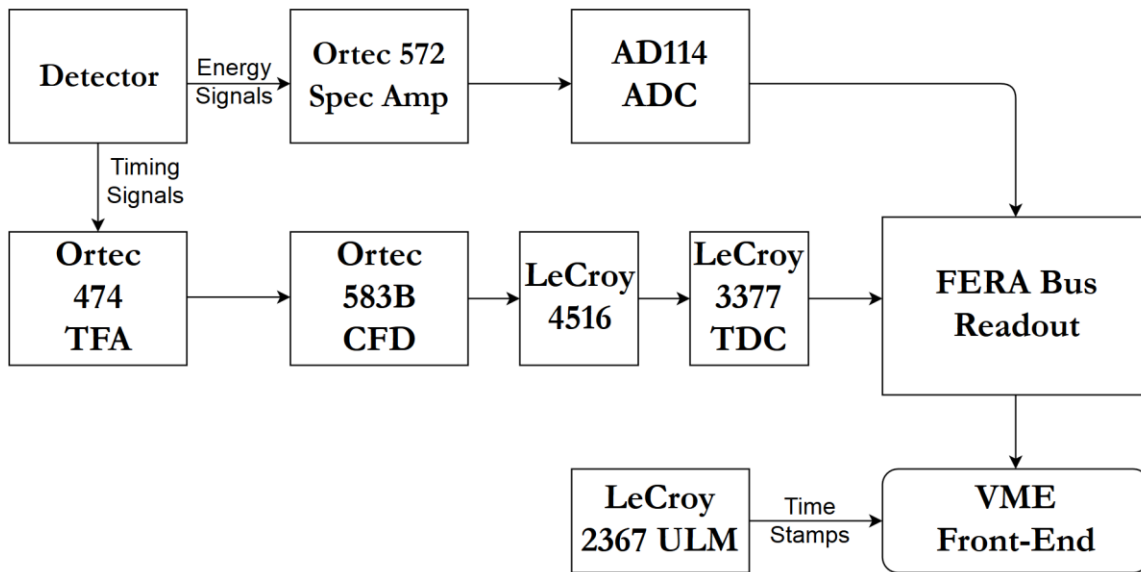


**Figure 46.** Flow diagram of the signal processing originating from a detector (either HPGe or Si(Li)) and terminating at the front-end.

Both the HPGe and PACES Si(Li) detector arrays were, at the time of operation, connected to analog Ortec 572 spectroscopy amplifiers, one for each HPGe or Si(Li) detector; the outputs were shaped pulses which were then fed to AD114 ADCs (Analog to Digital Converters) which had 16384 channels. The Ortec 572 amplifiers also had a hardware pileup reject signal which could be examined in conjunction with energy pulses on an oscilloscope; if the rejection rate was too high, indicating noise-generated trigger signals, the amplifier could be adjusted to change the pileup threshold. The outputs of the ADCs were fed to Fast Encoding and Readout ADC (FERA bus).

As the detectors had dual outputs, duplicate signals from each detector were also fed into Ortec 474 TFAs (Timing Filter Amplifiers), whose outputs were fed into Ortec 583B CFDs (Constant Fraction Discriminators). The logic outputs of the CFDs were then fed into LeCroy 4516 logic modules, and ultimately to multihit LeCroy 3377 TDCs (Time to Digital Converters) before being fed to the FERA bus readout.

For the HPGe detector array, their associated BGO veto signals (not shown in Figure 46 for simplicity) from the photomultiplier tubes were fed into TDCs as well to provide time stamps for offline software vetoing in addition to the hardware veto present in the trigger logic. When examining a TDC difference spectrum between a HPGe detector and its corresponding BGO suppressor (Section 6.1.1), there will be a region of few or no events which indicates the hardware suppression is functioning. Even so, for high-rate experiments as in the case of the decay of  $^{116}\text{In}$ , additional offline vetoing in software is necessary.

In addition to the above energy and timing logic, a 10 MHz LeCroy 2367 ULM (Universal Logic Module) provided master triggers and time stamps (each tick is 100 ns long) for each event and each data stream (of which there are four, one for each detector array type; type 0 is HPGe and type 3 is PACES). The ULM times are necessary to determine coincidences between different detector types, while the TDC times alone are sufficient to determine coincidences between detectors of the same type.

The LeCroy FERA bus modules are connected to a VME front-end which is the endpoint of all signal processing, and which thereupon translates the digital signals and time stamps into MIDAS format [128] for offline analysis.

## 5.4. Preparation for the Experiment

The HPGe detectors were preliminarily gain matched to approximately 0.5 keV per channel, the CFD lower-level thresholds checked and adjusted to avoid triggering on electrical noise in the circuits, and the amplifier pileup thresholds checked and adjusted to avoid noise as well; standard sources (typically  $^{60}\text{Co}$ , but  $^{152}\text{Eu}$  and  $^{207}\text{Bi}$  were also available and used) were used for this preliminary-stage adjustment. Final adjustment of pileup thresholds for the higher decay rates of the  $A = 116$  beam constituents was done in the early stages of the experiment. The upper-level threshold was set to 4 MeV, which covered the entire  $Q$ -value phase-space available of  $\sim 3.4$  MeV in the  $^{116\text{m1}}\text{In}$  decay.

A similar check and adjustment was done for the PACES Si(Li) detectors once they had cooled down to operating temperature and so the decay of the  $^{116}\text{In}$  beam could be used for optimization; using the open  $^{207}\text{Bi}$  source prior to the experiment, they were preliminarily gain matched to approximately 0.25 keV per channel and lower-level thresholds set to just over the noise level. Based on the physics of a 5-mm Si(Li) detector under ideal conditions, the conversion-electron detection efficiency declines very quickly above 2 MeV, so the upper-level threshold setting of 2 MeV took this into account.

## 5.5. Beam Production and Delivery

The TRIUMF main cyclotron [129] bombarded a High-Power Tantalum target with a 70  $\mu\text{A}$  beam of 500 MeV protons. The spallation reactions, along with fission and fragmentation reactions, produced various surface-ionized reaction products which were separated using the ISOL technique. The resulting  $A = 116$  beam contained  $^{116\text{m}2}\text{In}$  ( $t_{1/2} = 2.18$  s,  $I^\pi = 8^-$ ) at  $3.2 \times 10^5$  ions/second,  $^{116\text{m}1}\text{In}$  ( $t_{1/2} = 54.29$  min,  $I^\pi = 5^+$ ) at  $4.0 \times 10^6$  ions/second and  $^{116\text{g}}\text{In}$  ( $t_{1/2} = 14.10$  s,  $I^\pi = 1^+$ ) at  $3.2 \times 10^4$  ions/second. This beam was delivered to the  $8\pi$  array over a period of approximately three days, with manually controlled beam-on and beam-off cycles of  $\sim 45$ -55 minutes each. The cycle time lengths avoided saturating the PACES array, which would cause unacceptably large dead times in the resulting data streams. Additionally, the cycle times took advantage of the  $\sim 100\times$  greater ion production rate of the  $^{116\text{m}1}\text{In}$   $5^+$  isomer, which has a longer half-life.

## 5.6. Data Acquisition Setup

Control over the experiment was accomplished via the Maximum Integrated Data Acquisition System (MIDAS) [128], which operates via a web-based interface to the front-end, which itself controls subprograms that read out data from ADCs, as discussed in Section 5.3, which are connected to the various detectors mounted in the  $8\pi$  array. The MIDAS system has a specified data format which it uses to write out on-line histogrammed data (.root) as well as the raw data for later playback and analysis (.mid);

additionally it writes out the contents of the run-time parameters within the On-Line Database (ODB) as an .odb file. The ODB contains data such as the run number, trigger type, beam cycle times, tape cycle times, etc.

Due to the high ion production rates in this experiment, a complex trigger was used to acquire data at rates which would not overwhelm the data storage system and produce unacceptably large data files. The overall trigger consisted of the following subtriggers:

- Scaled down HPGe  $\gamma$  singles with a factor of 255,
- Unscaled HPGe  $\gamma$ - $\gamma$  coincidences,
- Unscaled  $\beta$ -HPGe-DANTE coincidences,
- HPGe-DANTE-DANTE coincidences,
- Scaled down PACES singles with a factor of 1 (equivalent to no scale-down),
- Unscaled PACES-PACES coincidences,
- Unscaled HPGe-PACES coincidences.

Over the course of the experiment, approximately one terabyte of data was recorded and written to disk.

## 5.7. Calibrations for the Experiment

Standard sealed sources of  $^{133}\text{Ba}$ ,  $^{152}\text{Eu}$ ,  $^{60}\text{Co}$  and  $^{56}\text{Co}$  were used to calibrate the HPGe array to determine the relative efficiency over the energy range of 50 – 3500 keV. An open  $^{207}\text{Bi}$  source could, in principle, serve as an efficiency calibration for PACES. However, a PACES Si(Li) efficiency curve is optimally obtained by using in-beam measurements [130]. Thus, to develop a usable PACES efficiency curve, strong transitions in  $^{116}\text{Sn}$  or  $^{116\text{m}2}\text{In}$  with known multipolarities were used. Further details of the construction of the HPGe and PACES efficiency curves are given in Chapter 6.

## Chapter 6. Analysis and Results

The offline analysis of the data set from this experiment has been broken up into two stages. The first stage, using the  $8\pi$  array as a whole, focused only on  $\gamma$  singles and  $\gamma$ - $\gamma$  coincidences without reference to angular correlations. This was intended to determine relative intensities, locate new weak transitions and set new limits on branching ratios for transitions within  $^{116}\text{Sn}$ , and has been reported on in the work of Pore *et al.* [102,103].

The second stage, which is the present work in this thesis, extends the analysis to the conversion-electron portion of the data set, both in singles and in coincidence with gamma rays, as well as angular correlation measurements to extract mixing ratios and  $E0$  components of transitions within  $^{116}\text{Sn}$ . The deduced level scheme from the work by Pore *et al.* has been adapted to include reported  $E0$  transitions from the literature [55], while focusing mainly on transitions analyzed in the present work; it is shown in Appendix A.

### 6.1. Sorting the Data

The raw data, in .mid form, must be translated into spectra and matrices usable and manipulable by experimenters. A computer program called a sort code accomplishes this task of processing the data, and for the purposes of the analysis the bulk of the processing was done using a program called *gsort*, furnished by the Nuclear Physics Group at the University of Guelph [131], and which is user-modifiable for different tasks such as adapting the program to perform angular correlations.

The program *gsort* unpacks events from .mid files, and filters (“sorts”) them into various user-defined spectra and matrices for subsequent analysis. During the sorting, the

code applies various time cuts to the data set (Section 6.1.1) as needed along with on-the-fly gain matching, which can compensate for gain drift within a run (Section 6.1.2).

### 6.1.1. Time Cuts

It was necessary over the course of the analysis to define time cuts (time gates) for several reasons:

1. To remove spurious invalid events,
2. To perform software BGO suppression,
3. To establish HPGe-HPGe coincidence windows, and
4. To establish HPGe-PACES coincidence windows

The first time cut involved setting a range of valid TDC events to be accepted by the sort code. This removes spurious events accepted by the master trigger but which do not correspond to a detected gamma ray or conversion electron. The second time cut augments the hardware BGO suppression (which removes an event from the HPGe data stream if it occurs in coincidence with a BGO signal), because the hardware suppression alone does not sufficiently remove Compton-scattering events at the high rates of the  $^{116}\text{In}$  decay experiment. The third and fourth time cuts are for the purposes of defining what a real coincidence is versus a random coincidence. By removing coincidences that appear too far apart in time from one another, the sort code can generate  $\gamma$ - $\gamma$  and  $\gamma$ - $e^-$  coincidence matrices for which events within that matrix give rise to useful analysis of the level scheme. The method of applying these time cuts will be discussed in the following sections.

#### ***Removing Invalid Events Recorded by TDCs***

The raw TDC spectrum for both the HPGe and PACES arrays have a complex shape of multiple peaks and backgrounds, which correspond to various triggers within the overall master trigger (discussed in Section 5.6). However, there will be regions in these spectra where hits occur in the TDC, but are not useful as they do not correspond to any of the triggers generated by the ULM master trigger, and so would produce spurious

coincidences in the coincidence-mode triggers if they were included. Figure 47 and Figure 48 show the HPGe and PACES TDC time spectra and the cuts taken to remove the events that are likely due to noise or other random events not associated with a valid trigger.

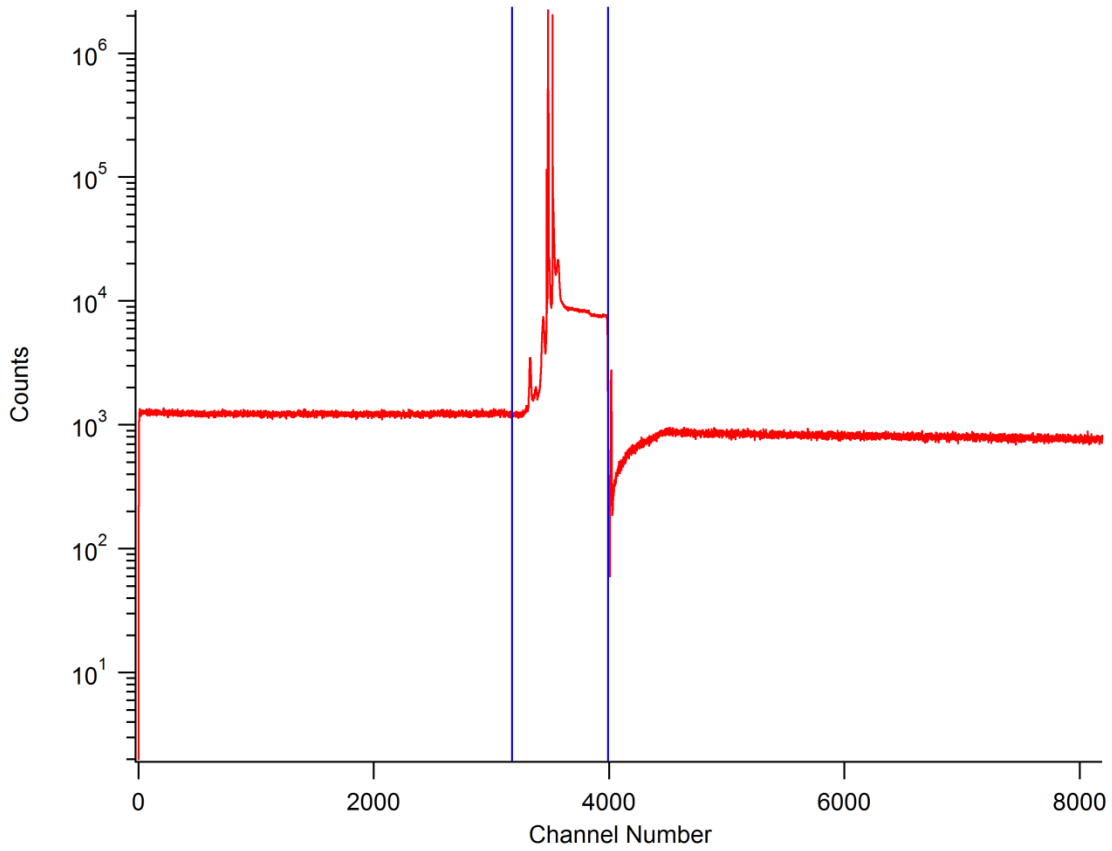


**Figure 47.** The raw HPGe array TDC times with blue lines showing where the TDC gate range was set. Note the logarithmic scale on the y-axis. There are 2 ns per channel on the  $x$ -axis.

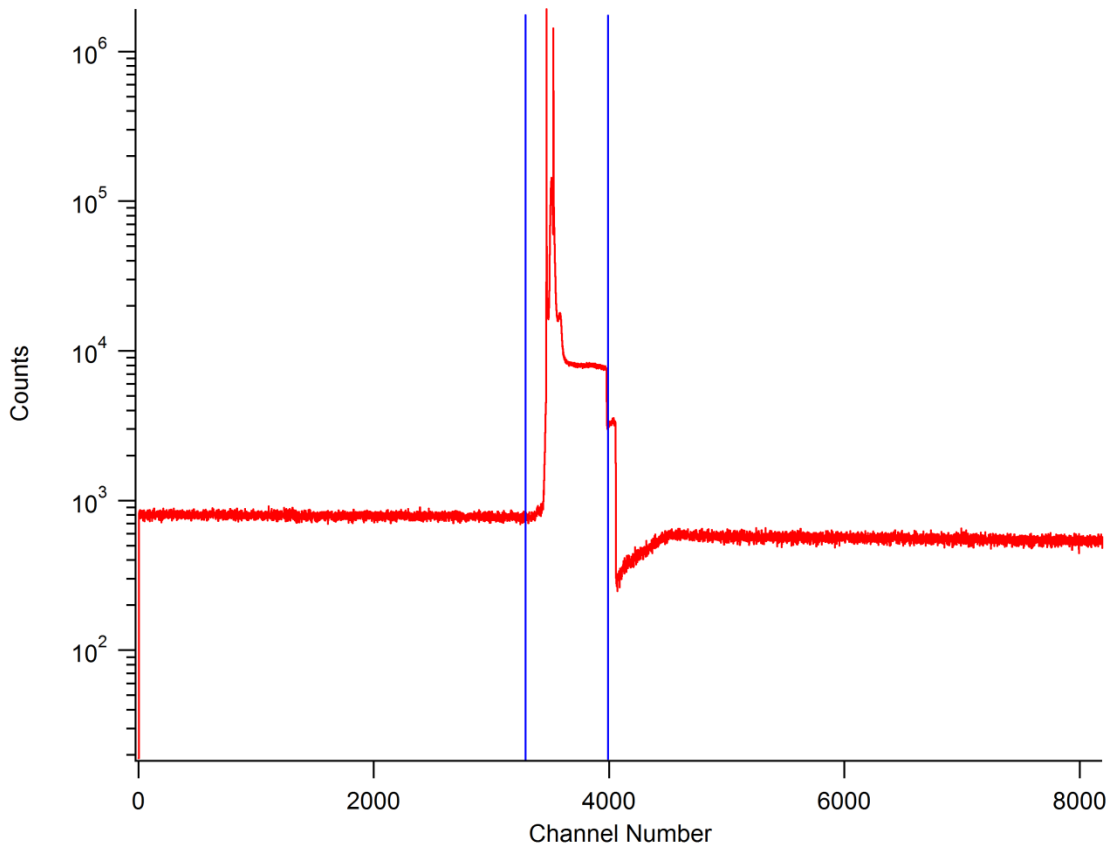


**Figure 48.** The raw PACES array TDC times with blue lines showing where the TDC gate range was set. Note the logarithmic scale on the  $y$ -axis. There are 2 ns per channel on the  $x$ -axis.

### *Software BGO Suppression*

The method of software suppression is to generate a TDC difference, or delta-TDC spectrum, which takes the difference in TDC timestamps recorded from an HPGe detector and TDC timestamps recorded from its surrounding BGO crystals. The “veto” (rejection) of a HPGe event occurs if a BGO timestamp occurs within a user-defined window defined from the hardware-suppressed delta-TDC spectrum.

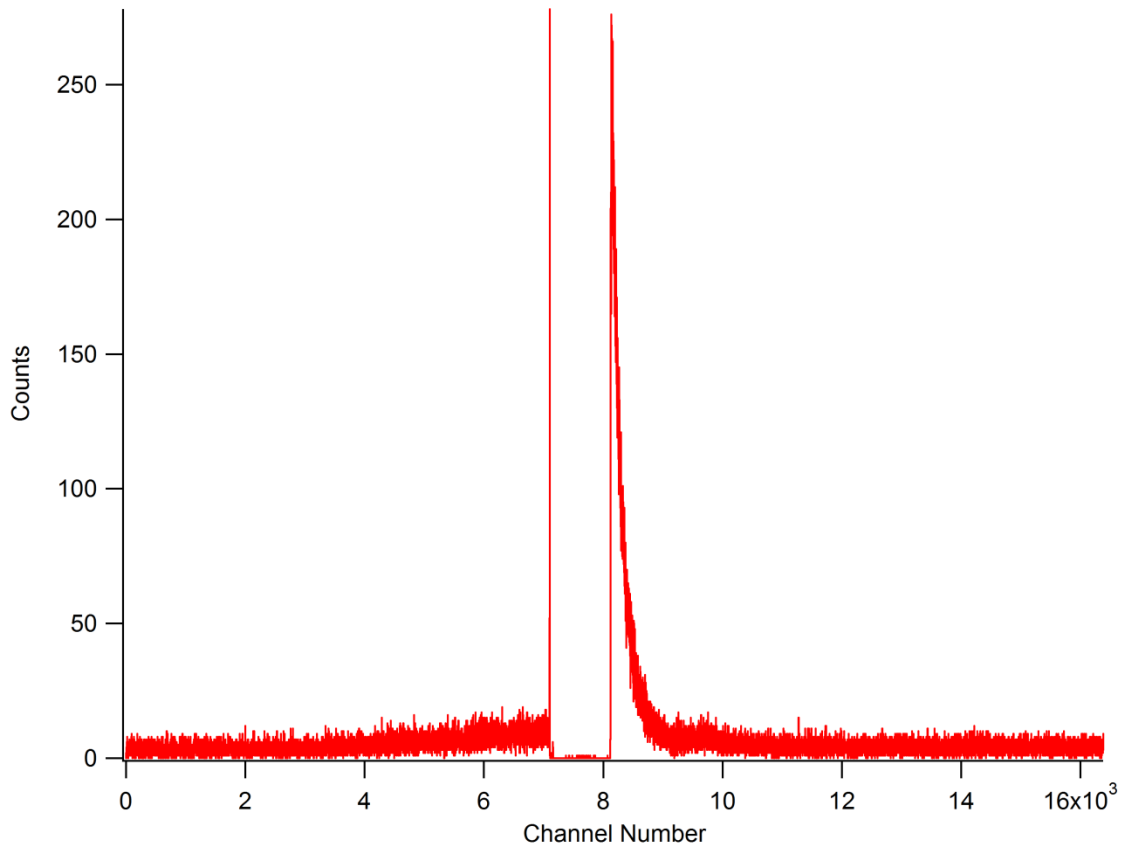


**Figure 49.** A representative TDC difference spectrum between HPGe 0 and its BGO shields, showing the region of zero counts caused by the hardware BGO suppression. There are 4 ns per channel on the  $x$ -axis.

Figure 49 displays the hardware-suppressed delta-TDC spectrum obtained between an  $8\pi$  detector and its BGO shields. The effect of the hardware suppression can be seen where there are few or no counts between channels  $\sim 7200$  and  $\sim 8200$ . However, the hardware suppression does not sufficiently veto scattering events at high rates; this can be seen in the decay curve still present after channel 8200. The software veto window can be set as wide as desired; for this experiment it was set between channels 4000 and 10700, corresponding to the slight rise of events prior to the hardware window, and ending just after the return of events to baseline after the hardware window.

### *HPGe-HPGe Coincidence Time Cuts*

To determine valid coincidence events, a delta-TDC spectrum (Figure 50) can be generated from all coincidence events in a run (or group of runs) which is essentially the sum of all the time differences between all possible pairs of detectors in the HPGe array in the  $8\pi$ .

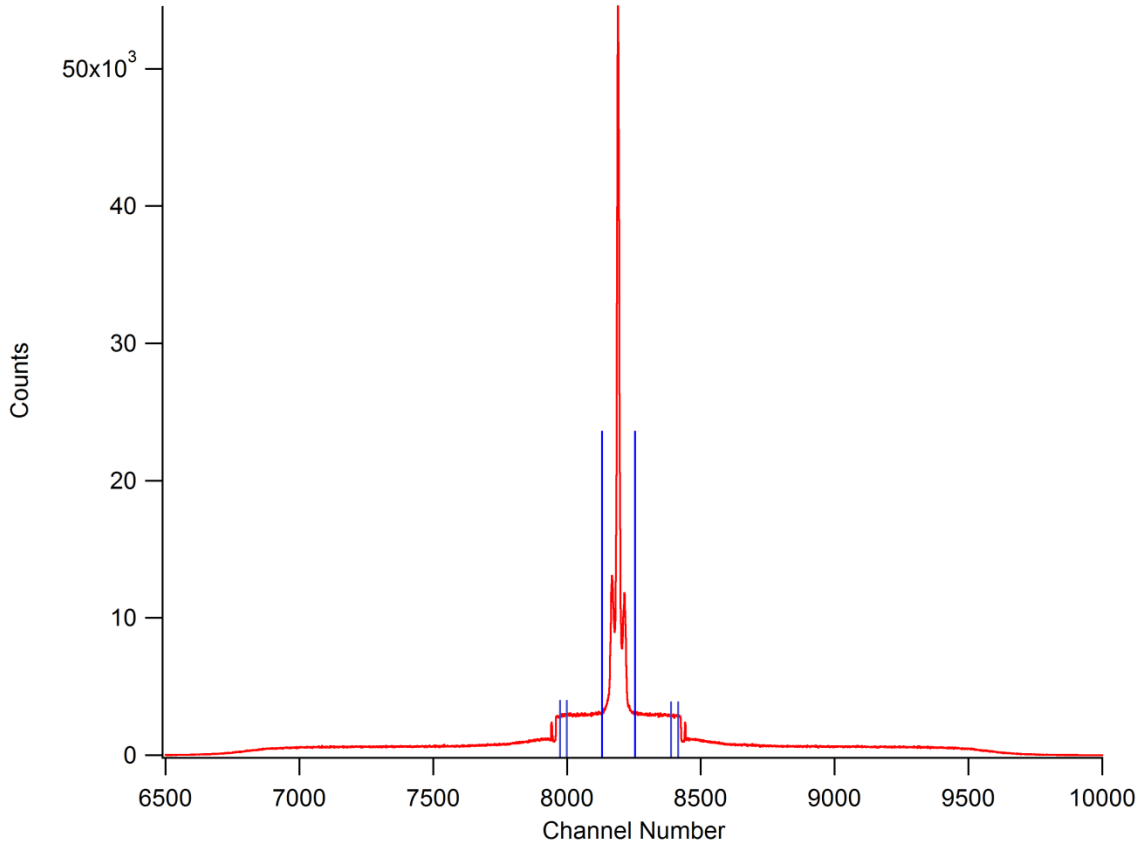


**Figure 50.** HPGe-HPGe TDC difference spectrum. The dark blue lines represent approximately the gate region and the light purple lines, the background region. There are 4 ns per channel on the  $x$ -axis.

The triple peak in the center of Figure 50 represents the true coincidences (that is, they are events corresponding to two gamma rays emitted from the same  $^{116}\text{Sn}$  nucleus, and observed in two different HPGe detectors), and the “table” structure to the left and right of it represent background events. The presence of multiple “tables” is due to delayed coincidences from transitions through the 2366 keV state in  $^{116}\text{Sn}$ , whose half-

life is 348 ns [55]. The time gate and background gates were optimized for prompt or near-prompt coincidences, since no angular correlation or conversion-electron measurements were made on cascades which passed through that state.

### *HPGe-PACES Coincidence Time Cuts*

An extra step must be taken to obtain valid coincidence events between different data streams. In the case of HPGe-HPGe coincidences, a “doubles” event automatically has the same ULM time for both detectors involved, and the TDC, being multihit, will thus record the times for both detectors for that event.

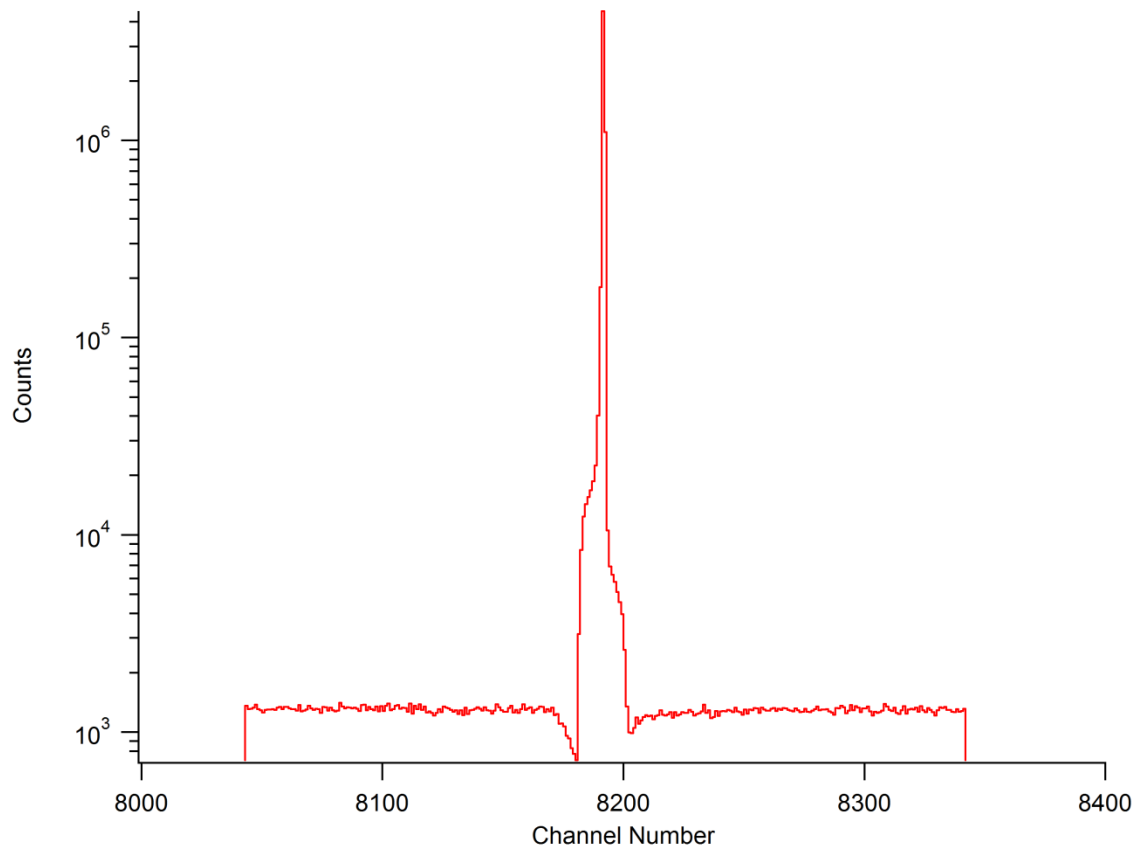


**Figure 51.** HPGe-PACES delta-ULM spectrum; note the logarithmic scale on the y-axis. The centroid at 0 ns apart has been shifted to channel #8192. Each bin on the  $x$ -axis represents 100 ns per channel, since each ULM tick is 100 ns long. The gate is between channels 8190 and 8193.

In the case of different data streams, as with HPGe and PACES, they do not necessarily have to have the same ULM timestamps, so before a delta-TDC spectrum across the two streams can be used to obtain the valid coincidences, a delta-ULM cut has to be made first. The thousand-fold increase in valid coincidences over background makes it unnecessary to set a background gate for ULM time differences. Once the gate region of the delta-ULM time spectrum (Figure 51 and caption) is established over the region where the majority of the coincident events occur, the next step is to establish gates and backgrounds for the delta-TDC spectrum.

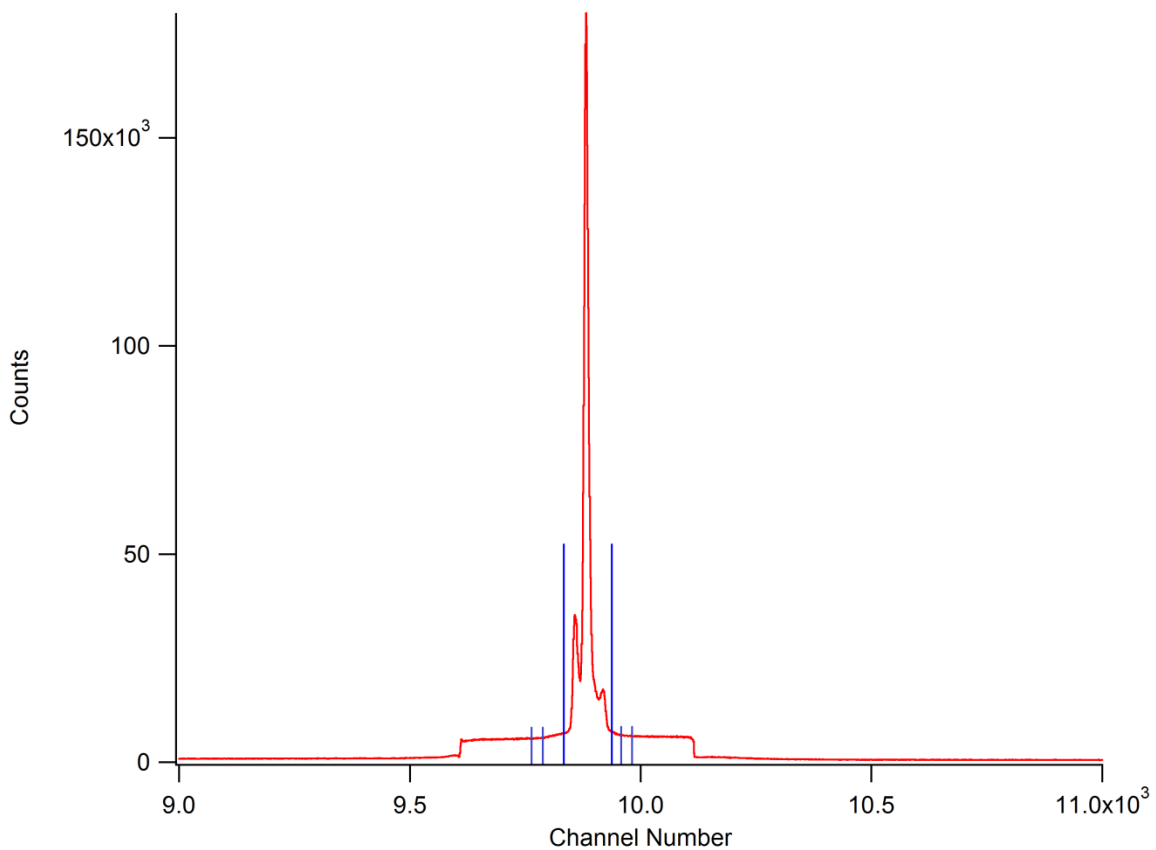


**Figure 52.** HPGe-PACES TDC difference spectrum. The dark blue lines represent approximately the gate region and the light purple lines, the background region. There are 4 ns per channel on the  $x$ -axis.

The HPGe-PACES delta-TDC spectrum, analogous to the HPGe-HPGe delta-TDC, is shown in Figure 52, with corresponding gates and backgrounds. The similar peak and table structure to that of Figure 50 shows that gamma-ray/conversion-electron

coincidence timing is similar to the gamma-gamma timing. The differences in relative peak heights on the left and right of the central peak in the two figures are attributable to the stronger influence of the Compton background on the HPGe-PACES timing, since PACES cannot be BGO-suppressed. As long as the gate window is sufficiently wide, with suitably wide background windows, then this effect is not important for the present work.

### 6.1.2. Gain Matching

Gain matching, for both the HPGe detectors and PACES detectors, involved a linear correction of raw channel numbers to energies. This was done according to Equation (64) in which the slope or gain,  $g_n$ , has units of keV/channel and the intercept (offset)  $o_n$  has units of keV, and the correction is for a particular detector  $n$  (where  $n$  ranges from 0 to 19 for the HPGe array or from 0 to 4 for the PACES array). Proper gain matching results in the ability to sum the individual detector spectra into one spectrum to take advantage of higher statistics, without broadening peaks due to slight differences in centroid positioning.

$$E_n = g_n x + o_n \tag{64}$$

For the HPGe detectors, two channel windows were defined within the sort code over which its peak searching algorithm would find the largest peak. From each pair of peaks in the detectors, it generated slopes and intercepts to be used in keeping the peaks gain matched, based on windows around the 416.86 keV and 2112.312 keV gamma-ray lines<sup>18</sup> in <sup>116</sup>Sn [55]. Over the course of this analysis, it was found that that two detectors had to be removed; one, HPGe #4, had a setting on its amplifier changed partway through

---

<sup>18</sup> In general, gamma-ray energies quoted in this thesis are rounded to the nearest keV. The energies are given to the second or third decimal place in this section from the Nuclear Data Sheets for the purposes of discussion of gain matching for the HPGe and PACES arrays.

the experiment, and the other, HPGe #17, had substantial gain drift that could not be compensated for in the gsort gain matcher.

All five PACES detectors were found to be stable against gain drift throughout the experiment. Therefore, gain correction coefficients were determined by a manual two point fit for each detector from the 138.327 keV K electron line at 109.127 keV and the 1293.558 keV K electron line at 1264.358 keV, and inserted into the sort code at runtime.

The gainmatch routine in gsort produced spectra with reasonably accurate gamma-ray energies when compared to those reported by Pore *et al.* [103]. In the main body of this thesis, gamma-ray energies are rounded to the nearest keV (e.g. as seen in Figure 56).

Since the binding energies of atomic electrons are well-known, electron line energies are quoted based on the binding-energy shift from the measured gamma-ray energy. In the case of  $^{116}\text{Sn}$ , that shift is 29.2 keV for the K line, an average of 4.2 keV for the L line (the individual  $L_I$ , etc. lines are not resolvable), and an average of 0.7 keV for the M line (again, the individual components are not resolvable) [66]. The gainmatch routine produced spectra with conversion-electron energies which corresponded to the reported gamma-ray energies in Appendix B, after accounting for the binding energy. As with gamma rays, conversion-electron energies are rounded off to the nearest keV (e.g. as seen in Figure 57).

### **6.1.3. The HPGe Array Efficiency Curve**

The gamma rays from the standard  $^{133}\text{Ba}$ ,  $^{152}\text{Eu}$ ,  $^{60}\text{Co}$  and  $^{56}\text{Co}$  sources were used to construct a relative efficiency curve for the purpose of correcting gamma-ray energies for the energy dependent response of the HPGe array. This curve must have as small an uncertainty as practically achievable in order to minimize the propagation of uncertainty into the PACES efficiency curve.

It is necessary, for an accurate efficiency curve, to account for the fact that the energy-dependent response is affected by coincidence summing. Summing of gamma rays changes the relative efficiency such that at higher energy, where the summed gamma rays are detected, the efficiency appears higher than it should be. Conversely, at lower energy, the removal of peak intensity reduces the apparent efficiency. Summing depends on the geometry of the detector array due to the solid-angle coverage (the size of the detector and the source-detector distance are both factors here) and on the nucleus involved<sup>19</sup>. The summing corrections were incorporated into the source efficiency curve using the values for each decay cascade outlined in Gehrke [132] for HPGe detectors of similar characteristics to those used in the  $8\pi$  array, where the percentages reported in that work add to or subtract from the deduced efficiency at a given energy for a given source and have been corrected for the geometry of the  $8\pi$  array.

The peaks chosen for the efficiency curve had energies well-established in the literature and whose intensities per 100 decays of the parent were known to about 1% uncertainty. Peaks known to overlap with others (e.g. the 1085 and 1089 keV peaks in the decay of  $^{152}\text{Eu}$ ) were omitted where other non-overlapping peaks in the same energy range could be fitted. The peak intensities in the summed singles spectrum were fitted for the chosen energies, then corrected for the absolute intensity per 100 decays of the parent and the coincidence-summing. Finally, because of the fact that relative efficiency curves are self-consistent only for a given nucleus, the different curves had to be re-scaled (or normalized) to an arbitrarily chosen benchmark, which were the  $^{60}\text{Co}$  source peaks, as the summing corrections are minimal and the energies and intensities are well-established to an uncertainty of much less than 0.1%. The process of normalization followed this sequence: first, the  $^{152}\text{Eu}$  data points were fitted near the 1 MeV energy range using a suitable low-order polynomial, then calculating the efficiency at 1173 and 1332 keV

---

<sup>19</sup> For example, a nucleus that emits only one gamma ray has no summing correction, e.g.  $^{137\text{m}}\text{Ba}$  from the decay of  $^{137}\text{Cs}$ . By contrast a complex cascade, e.g.  $^{56}\text{Fe}$  from  $^{56}\text{Co}$ , will have summing-in and summing-out effects which together produce a net positive or net negative correction to the efficiency for each gamma ray emitted.

permitted normalizing all the  $^{152}\text{Eu}$  data points to the  $^{60}\text{Co}$  data points. Then, the  $^{56}\text{Co}$  data points were normalized to the overlapping energy ranges between that source and the  $^{60}\text{Co}/^{152}\text{Eu}$  sources. Finally, the  $^{133}\text{Ba}$  source was normalized to the low-energy  $^{152}\text{Eu}$  data points.

The form of the efficiency function that is usually used to characterize HPGe detectors has the general form of a polynomial in  $\ln(\varepsilon)$  as a function of  $\ln(E_\gamma)$ , where the energy  $E_\gamma$  is in keV, as shown in Equation (65) (obtained from a treatment of applicable efficiency functions for the range from 50 – 3500 keV in Ref. [133]),

$$\ln(\varepsilon) = \sum_{i=0}^n [a_i \ln(E_\gamma)^i] . \quad (65)$$

To determine the order of the polynomial that best fitted the data set, the order of the polynomial ( $n$ ) was varied from 3 to 9 and the one that produced the lowest value of  $\chi^2/\nu$  without unduly adding extra terms was chosen. Since the  $\chi^2/\nu$  decreased very little when going from  $n = 8$  to 9, there seemed to be little benefit to adding another power to the formula, and previous work with the  $8\pi$  array has generally restricted efficiency functions of this type to order 8 or less (for example, see Ref. [134]). Thus, the resulting efficiency function was a polynomial in 8<sup>th</sup> order for  $\ln(\varepsilon)$  as a function of  $\ln(E_\gamma)$ . The resulting data points and efficiency plot are shown in Figure 53, and the resulting fit parameters are shown in Table 4. The global relative uncertainty consistent with a 68% confidence interval is  $\sim 1\%$  for this efficiency curve, and is reasonable given the  $\chi^2/\nu$  of 0.80 for the fit. The absolute efficiency of the  $8\pi$  array is not required for the present analysis, but was determined to be  $\sim 0.8\%$  at 1 MeV [135] in a superallowed beta decay experiment, where it is necessary to know the number of decays for precision analysis.

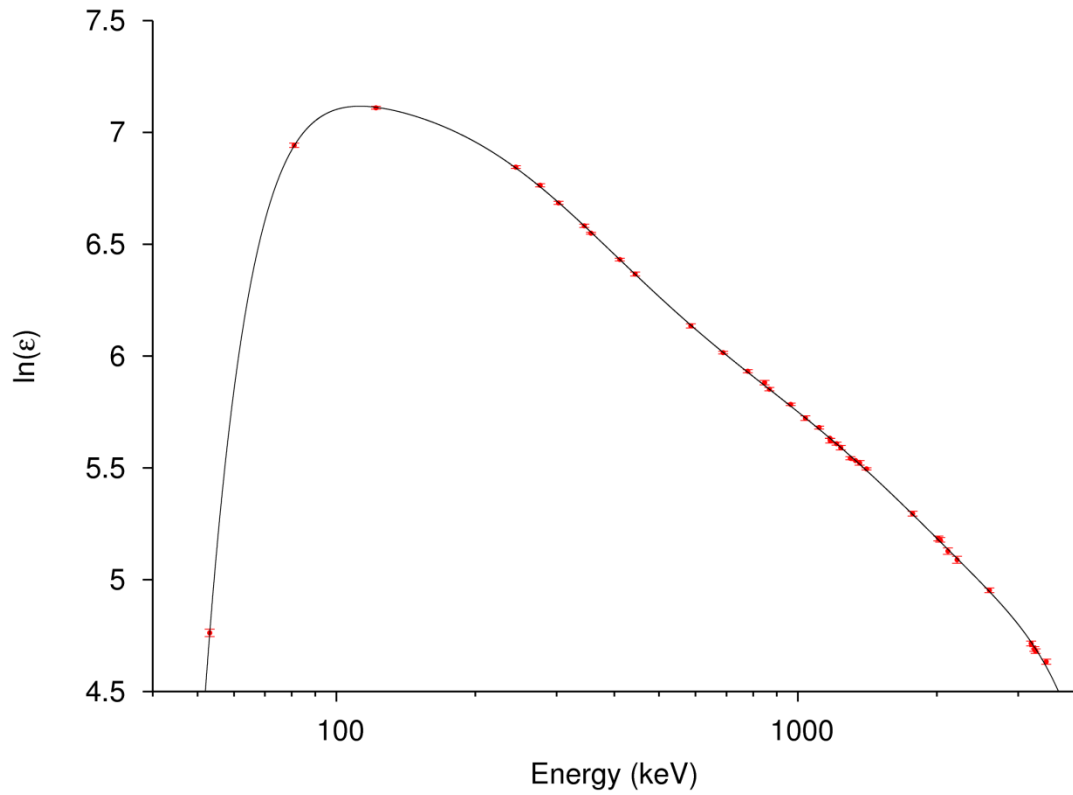


**Figure 53.** HPGe array relative efficiency with  $\ln \epsilon$  vs Energy (log scale) in keV. The  $\chi^2/\nu = 0.80$  for this fit.

**Table 4.** The efficiency parameters for the  $8\pi$  HPGe array.

Parameter	Value	Uncertainty
$a_0$	-23208.8	1190
$a_1$	30749.5	1638
$a_2$	-17711.8	978.7
$a_3$	5793.59	331.3
$a_4$	-1176.9	69.56
$a_5$	152.022	9.273
$a_6$	-12.194	0.7668
$a_7$	0.555361	0.03597
$a_8$	-0.0109966	0.000733

#### 6.1.4. The PACES Efficiency Curve

Unlike the case of the  $8\pi$  HPGe array, in which standard calibration sources counted in singles can be used to determine the relative efficiency, the PACES Si(Li) array relative efficiency must be determined from a source counted under the same conditions as the experiment. Therefore, to characterize the efficiency of PACES over the 0 – 2 MeV energy range, the 162 keV  $E3$  transition in  $^{116\text{m}2}\text{In}$  and selected strong transitions in  $^{116}\text{Sn}$  were used from the corresponding gamma and electron singles spectra, involving transitions with known multiplicities (either pure  $E2$  or  $E2/M1$  with well-known mixing ratios as tabulated in Ref. [55]). The method developed by Willett [136] was used to obtain relative efficiency values for the PACES Si(Li) array, as shown in Equation (66), where  $A_K$  is the uncorrected electron line peak area,  $\alpha_K$  from BrIccFO [36] is the theoretical K-shell conversion coefficient, and  $\varepsilon_\gamma/A_\gamma$  is the reciprocal of the efficiency-corrected gamma-ray peak area,

$$\varepsilon_{Si} = \left( \frac{A_K}{\alpha_K} \right) \frac{\varepsilon_\gamma}{A_\gamma}. \quad (66)$$

In order to characterize the efficiency at low energy, the 100 keV peak in the gamma singles spectrum was used, which has a 71 keV K electron line visible in the PACES singles spectrum. However, these gamma and electron peaks are actually composed of two overlapping  $5_1^- \rightarrow 3_1^-$  pure  $E2$  and  $4_5^+ \rightarrow 3_1^+$  mixed  $E2/M1$  transitions. The second transition requires an assumption of its dominant multipolarity in computing the implied  $\alpha_K$  for use with Equation (66). Because of the reported neutron  $g_{7/2}$  character of the  $3_1^+$  state [55] and the  $4_5^+$  state [89] and the relative weakness of the second mixed transition, it is likely that the  $E2$  component is small; thus, it is assumed to be  $M1$ . Therefore the implied  $\alpha_K$  for the 71 keV electron line was computed to be 0.86(6), based on the gamma-ray intensities determined by Pore *et al.* [103].

Previous work characterizing Si(Li) detector efficiency curves for conversion electrons was performed by Willett [136] using Si(Li) detectors of similar characteristics

to those in PACES, albeit at 3 mm thickness instead of 5 mm (Figure 54). The data showed that there is a rising efficiency as electrons begin to penetrate past the dead layer, a plateau as they deposit their energy fully within the active layer, and then a slow decline as electrons of high enough energy pass through the Si(Li) crystal.

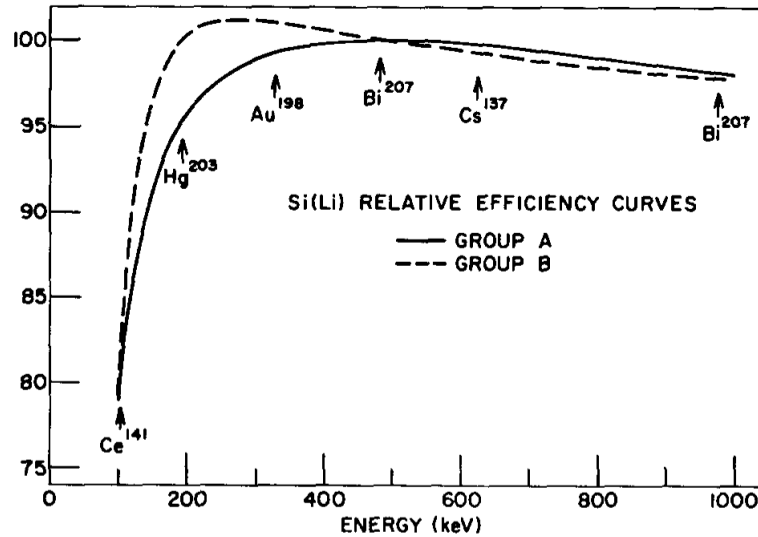


**Figure 54.** Si(Li) efficiency curves compiled by Willett using two different HPGe efficiency curves (Groups A and B in the figure) [136]. Reprinted from Nuclear Instruments and Methods Volume 84, by Willett (1970), page 165, with permission from Elsevier.

The resulting efficiency parameterization chosen by Willett, and adopted in this work, is given in Equation (67), where  $E$  is the electron line energy in keV, and  $A'$ ,  $B'$ ,  $C'$  and  $D$  are parameters obtained from a nonlinear least-squares fit to experimental data,

$$\ln(\varepsilon_{Si}) = A' \ln(E) + B' [\ln(E)]^2 - \frac{C'}{E^3} + D \quad (67)$$

In the course of fitting the  $^{116}\text{Sn}/^{116\text{m}2}\text{In}$  data to Equation (67) it was found that as the inverse cubic term only affects the relative efficiency curve at low energy,  $C'$  can take on a wide range of values and yet for given values of  $A'$ ,  $B'$  and  $D$ , the  $\chi^2$  value and appearance of the efficiency curve will not change very much. Physically, the analogous HPGe parameter accounts for low-energy absorption of gamma rays by absorber material (e.g. a beryllium window) placed in front of a detector [136]. Therefore for conversion

electrons,  $C'$  accounts for low-energy electrons not being recorded by the detector due to absorption within, or backscattering from, the dead layer.

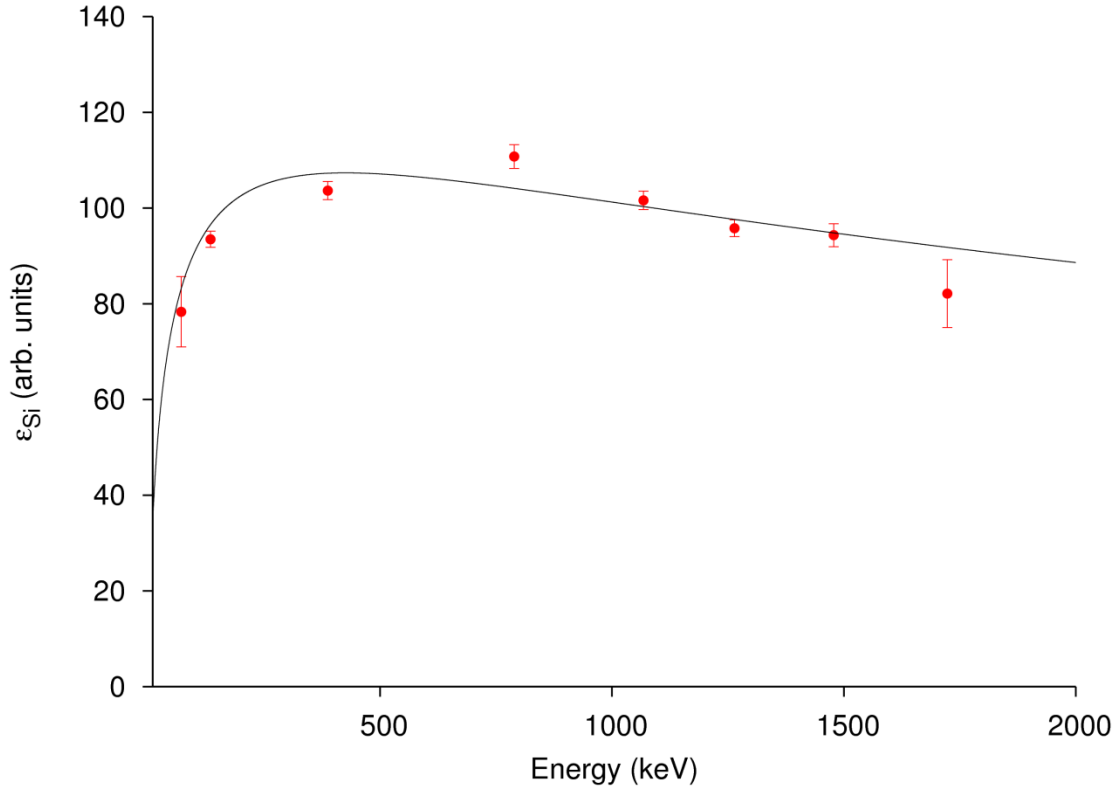


**Figure 55.** PACES relative efficiency curve from  $^{116}\text{Sn}$  and  $^{116\text{m}2}\text{In}$  gamma rays and corresponding K electron lines. The  $\chi^2/\nu = 3.02$  for this fit.

**Table 5.** The efficiency parameters for the PACES array.

Parameter	Value	Uncertainty
$A'$	0.9688	0.0018
$B'$	-0.0800	0.0003
$C'$	-1	0
$D$	1.744	0.012

Since the resulting efficiency curve was very insensitive to small changes in  $C'$  and much more sensitive to small changes in the  $A'$ ,  $B'$  and  $D$  parameters,  $C'$  was fixed at  $-1$ , and the other three parameters were then free to vary for the final function adopted in this work. Figure 55 shows the data points and fit for the PACES efficiency curve, and Table 5 shows the fit parameters. The global relative uncertainty, obtained from the 90%

confidence interval, is ~6% for this efficiency curve. This is consistent with the adopted uncertainty of 5% by Jigmeddorj *et al.* [137] in an analysis of the  $^{110}\text{Cd}$  nucleus.

Following on from this, a brief discussion of a comparison between two computer simulations of the PACES efficiency and the experimental data in this section is in Appendix H. As with the HPGe array, the absolute efficiency of the PACES array was not necessary for the present analysis but in a superallowed beta decay experiment it was determined to be ~3.4% at 600 keV [135].

## 6.2. Conversion-Electron Data and Results

### 6.2.1. HPGe Singles and PACES Singles

Over the course of the experiment,  $\sim 10^9$  HPGe singles events were recorded, and  $\sim 10^8$  PACES singles events were recorded, as shown respectively in Figure 56 and Figure 57. The gamma and electron singles peak areas were used to measure K internal conversion coefficients, after correcting peak areas for efficiency. The formula to determine an experimental K internal conversion coefficient, given a gamma-ray peak area  $A_\gamma$  and its corresponding HPGe efficiency  $\varepsilon_\gamma$ , a K electron line peak area  $A_K$  and its corresponding Si(Li) efficiency  $\varepsilon_{\text{Si}}$ , is given in Equation (68),

$$\alpha_K = \frac{A_K / \varepsilon_{\text{Si}}}{A_\gamma / \varepsilon_\gamma} = \left( \frac{A_K}{A_\gamma} \right) \left( \frac{\varepsilon_\gamma}{\varepsilon_{\text{Si}}} \right) . \quad (68)$$

The K-shell internal conversion coefficients obtained from the gamma-ray and conversion electron singles data set are reported together with the ones obtained from coincidences in Section 6.2.4.

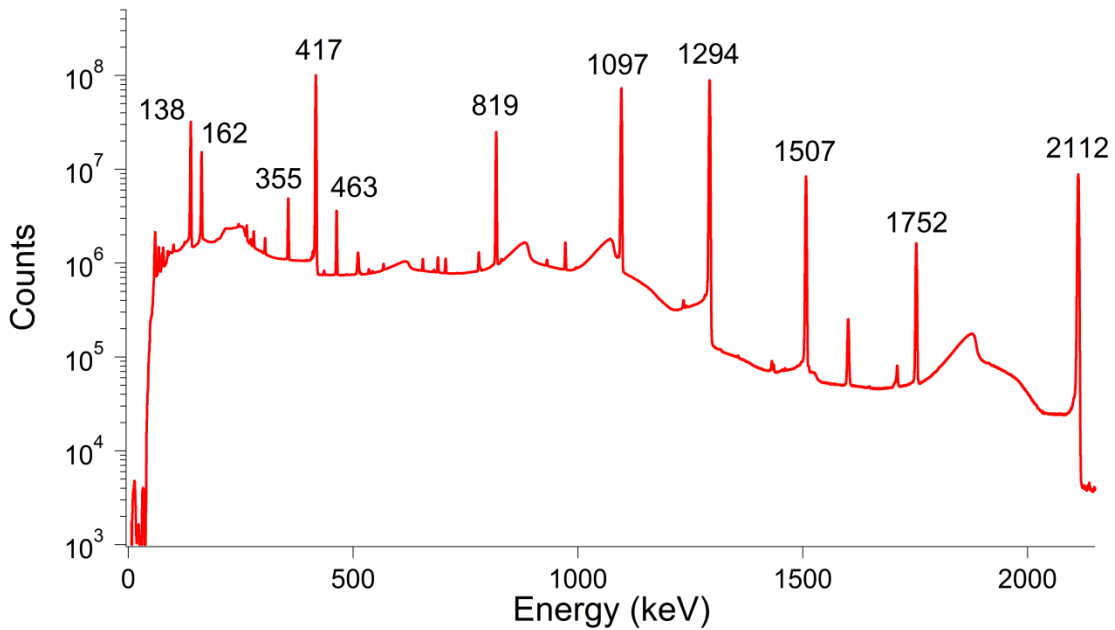


**Figure 56.** HPGe singles spectrum, with selected intense gamma rays labelled in keV. The 162 keV transition is from the  $^{116m2}\text{In}$  isomer, visible in runs taken when the  $^{116}\text{In}$  beam was directed into the  $8\pi$  Delrin chamber.

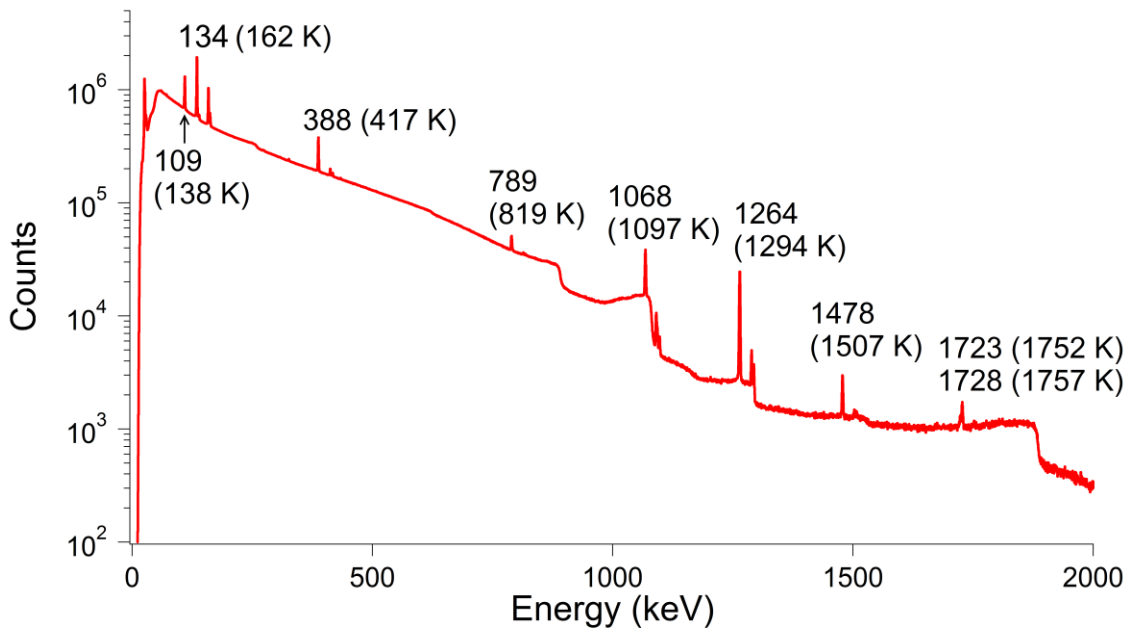


**Figure 57.** PACES singles spectrum with selected K electron lines labelled by their measured energies and corresponding gamma ray energies in parentheses.

### 6.2.2. PACES Relative Intensities in Singles

The intensities of the K electron lines in singles were measured and compared to two previous data sets which involved the decay of  $^{116}\text{In}$ . Table 6 summarizes the results from the present experiment and compares them to the previous literature. The uncertainties for the values quoted by Yamaguchi *et al.* [57] are not given but are assumed to be  $\sim 10\%$  from the values of their internal conversion coefficients. There is reasonable agreement with the previous results for those transitions not used in the PACES efficiency curve.

**Table 6.** K electron line relative intensities with respect to the 1294 keV transition. The energy shift to the corresponding K line is 29 keV. Dashes indicate no data reported. Asterisks mark transitions used to construct the PACES efficiency curve.

Transition Energy (keV)	$I_K$ (this work)	$I_K$ (Ref. [71])	$I_K$ (Ref. [57])
138	1880(160)	1580(85)	1688.8
355	27(3)	28(4)	—
417*	580(50)	565(35)	520.2
463	11.7(15)	—	—
819*	51(5)	55(3)	49.6
1097*	99(9)	97(2)	104.2
1294*	100	100(0)	100
1507*	8.3(7)	8.4(2)	8.3
1752*	1.3(2)	1.7(2)	1.4
1757	4.0(4)	4.7(3)	3.7

### 6.2.3. HPGe-PACES Coincidences

In addition to the singles spectra produced in the offline analysis, a HPGe-PACES ( $\gamma$ - $e^-$ ) coincidence matrix was also created. There were a total of  $\sim 2 \times 10^8$   $\gamma$ - $e^-$  coincidence events in the final time-random background subtracted matrix used for analysis. While such a matrix can be used to check the level scheme when  $E0$  transitions are present, in this work the primary use of the coincidence matrix was to extract some internal conversion coefficients from the HPGe-PACES coincidence data when the large

background in PACES obscured some of the weaker electron lines in singles. The sizable background in PACES is composed of the continuum of beta particle emissions, Compton-scattered gamma rays and backscattered electrons depositing some of their energy into the Si(Li) detectors. This cannot be completely mitigated by means of time-random subtractions on the matrices, and results in a number of “ $\gamma$ - $e^-$ ” coincidence events which are actually coincidences between gamma rays and Compton-scattered gamma rays, not between gamma rays and conversion electrons.

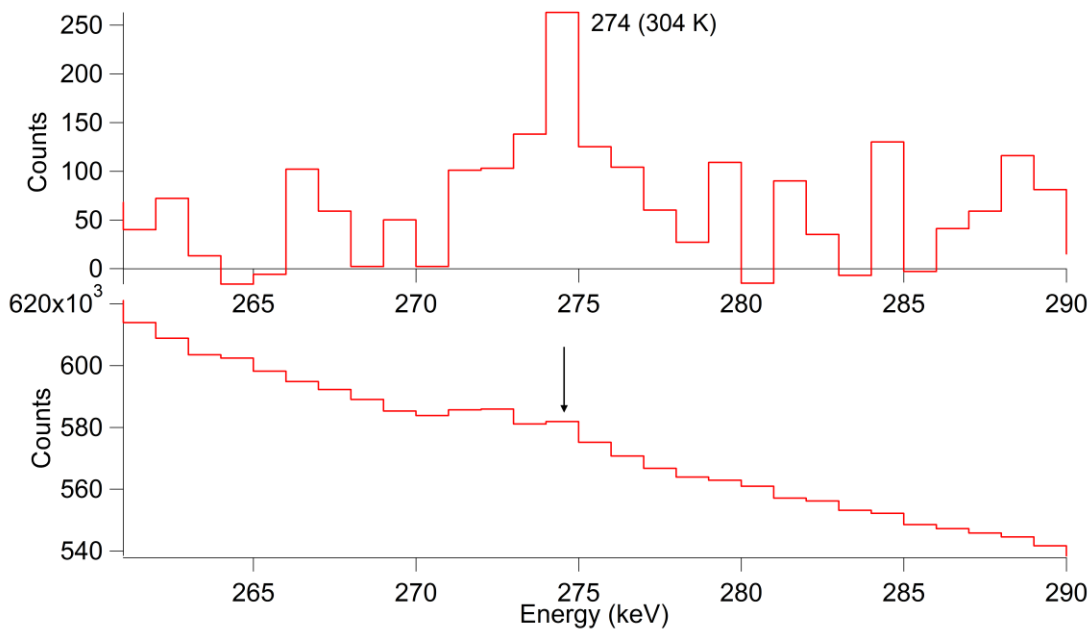


**Figure 58.** PACES conversion-electron spectra showing the 304 keV K electron line at 274 keV, visible in a background-subtracted coincidence gate on the 931 keV  $\gamma$  ray (top), which is almost completely undetectable in singles (arrow, bottom).

Gating (taking a slice over a narrow energy range along an  $x$ - or  $y$ -axis in a  $\gamma$ - $\gamma$  or  $\gamma$ - $e^-$  matrix) on weaker gamma-ray lines reduces the probability of picking up a number of false coincidences with the PACES background; as a result, K electron lines can be enhanced over the background in  $\gamma$ - $e^-$  coincidences, compared to  $e^-$  singles (Figure 58). However, after taking a gate on a gamma-ray line, artifacts in the resulting projected PACES spectrum (the coincident events for a given gamma-ray gate) can be introduced due to Compton scattering in which the energy of the false peak plus the energy of the

gated gamma ray equals that of a higher-energy gamma ray. These artifacts may pose a problem if the width of the gate is small enough, in which case these artifact peaks can appear to be real and could lead to erroneously assigning a coincident  $E0$  transition where none exists.

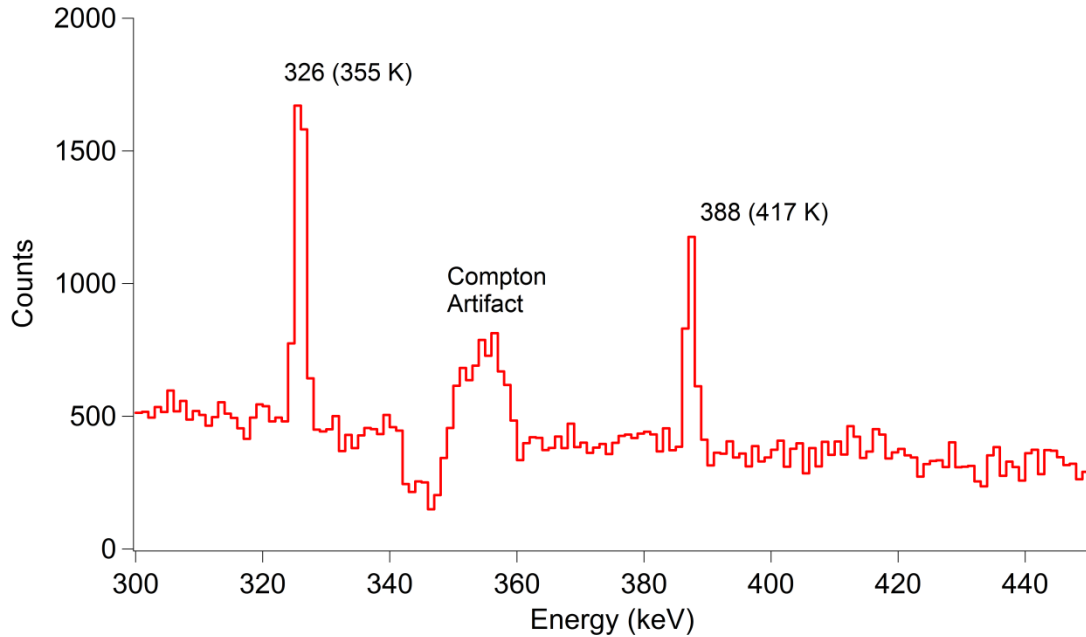


**Figure 59.** Close-up on a background-subtracted gate on the 463 keV gamma ray showing the effect of Compton scattering from the 819 keV gamma ray in introducing an artifact into the resulting projection.

In the analysis of  $^{116}\text{Sn}$  by Pore *et al.* [102,103], one of the main motivations was to examine the mixing of the 2027 keV  $0_3^+$  and 1757 keV  $0_2^+$  states. To do this required knowing the branching ratio of the 85 keV  $2_2^+ \rightarrow 0_3^+$  transition, which could only be found in a coincidence gate on the 734 keV gamma ray. The above-mentioned Compton artifact problem exists when performing  $\gamma$ - $\gamma$  coincidence gating as well, and potentially there could have been a Compton artifact at  $\sim 85$  keV, since the combination of  $\sim 85$  and 734 keV is  $\sim 819$  keV, which corresponds to the 819 keV intense peak. In Figure 2 of the work by Pore *et al.* [103], three gates were shown: one surrounding the 734 keV energy range, one surrounding 728 keV, and a final one surrounding 740 keV. It was shown through the appearance of the 85 keV peak only in the gate at 734 keV that the possible Compton artifact was negligible. Confirmation of the 85 keV transition through  $\gamma$ - $e^-$

coincidence gating in the same sense as the  $\gamma$ - $\gamma$  work should reveal a 56 keV electron line only in the gate at 734 keV, and this is confirmed in Figure 60.

Another use of  $\gamma$ - $e^-$  coincidence measurements is to obtain peak areas and, in combination with a  $\gamma$ - $\gamma$  matrix assembled from the same data set, measure K-shell internal conversion coefficients. However, obtaining  $\alpha_K$  values in coincidence measurements requires accounting for the fact that the total number of events is not the same in the  $\gamma$ - $\gamma$  and  $\gamma$ - $e^-$  matrices, and so the ratio of the efficiency-corrected peak areas of the electron and gamma lines is altered by what is essentially a ratio of coincidence normalizations, as discussed by Garrett *et al.* [138]. To obtain this ratio of coincidence normalizations, the relative efficiency of the PACES array was determined from a gate on the 1294 keV gamma ray, and the deduced coincidence efficiencies of the 417, 819, 1097 and 1507 keV transitions were compared to the singles efficiencies. The resulting matrix normalization factor obtained for the present analysis was 8.4(6).

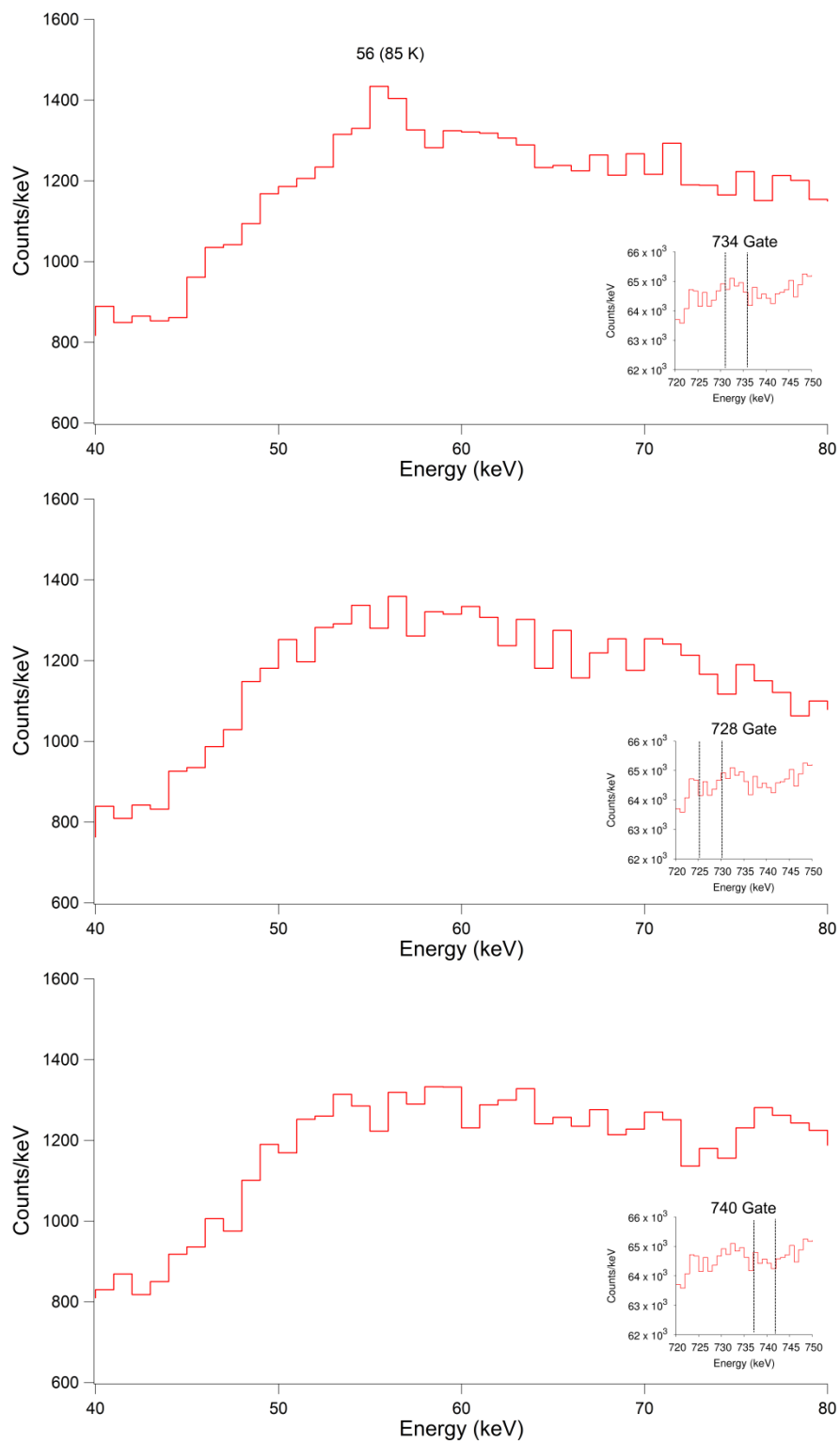


**Figure 60.** A series of gates (insets) and their projections revealing that the 56 keV (85 K) electron line is only visible when taking a gate around the 734 keV gamma ray.

## 6.2.4. Experimentally Measured Internal Conversion Coefficients

Table 7 summarizes the combined singles and coincidence  $\alpha_K$  values obtained from the present analysis and compares them to several previous works as well as the Nuclear Data Sheets, and also to values from theoretical BrIccFO calculations.

**Table 7.** K-shell internal conversion coefficients for transitions in  $^{116}\text{Sn}$ . Dashes indicate no data reported. Asterisks indicate values obtained from coincidence data. For mixed transitions, the last column gives the extreme limits for the pure transition multiplicities.

Transition Energy (keV)	$\alpha_K$ (Ref. [71])	$\alpha_K$ (Ref. [57]) <sup>#</sup>	NDS $\alpha_K$ (Ref. [55])	This Work $\alpha_K$	BrIccFO $\alpha_K$ and multiplicity
85	—	—	— <sup>†</sup>	2.8(4)*	1.94 <i>E2</i>
100 <sup>‡</sup>	—	—	1.4	1.40(16)* <sup>§</sup>	1.16 <i>E2</i>
138	0.218(22)	0.2397(237)	0.26(3)	0.215(13)	0.196 <i>M1</i> / 0.394 <i>E2</i>
162 ( $^{116m2}\text{In}$ IT) <sup>‡</sup>	—	—	1.15(9)	1.05(6)	1.10 <i>E3</i>
304	—	—	—	0.026(7)*	0.02885 <i>E2</i>
355	0.0175(30)	—	0.018(4)	0.0146(11)	0.0174 <i>E2</i>
417 <sup>‡</sup>	0.0089(8)	0.00997(99)	0.0096(10)	0.010(2)	0.0107 <i>E2</i>
463	—	—	—	0.0065(8)	0.00788 <i>E2</i>
819 <sup>‡</sup>	0.0020(2)	0.00212(21)	0.0026(3)	0.00197(12)	0.00214 <i>M1</i> / 0.00177 <i>E2</i>
931	—	—	0.00137(4)	0.0020(8)*	0.001599 <i>M1</i> / 0.00131 <i>E2</i>
1097 <sup>‡</sup>	0.00099(8)	0.000986(98)	0.00094(5)	0.00093(6)	0.00091 <i>E2</i>
1294 <sup>‡</sup>	0.00065(0)	0.00064(0)	0.00065(0)	0.00064(4)	0.000648 <i>E2</i>
1507 <sup>‡</sup>	0.00034(3)	0.000454(68)	0.00046(3)	0.00048(3)	0.000478 <i>E2</i>
1752 <sup>‡</sup>	0.00053(7)	0.000314(47)	0.00038(8)	0.00032(6)	0.000358 <i>E2</i>

# the values and uncertainties from this column are taken exactly from the paper without application of rounding rules.

† the only value reported is  $\alpha_{\text{tot}}$  from a BrIccFO calculation.

‡ the transition involved was used to construct the PACES efficiency curve.

§ this value was obtained for the  $5_1^- \rightarrow 3_1^-$  transition from a  $\gamma$ - $e^-$  coincidence measurement.

Several transitions were used to construct the PACES efficiency curve; consequently, their  $\alpha_K$  values are not truly independent and so in those cases the

measurement of  $\alpha_K$  reflects the goodness of fit to the efficiency curve. In general, the values of  $\alpha_K$  for the transitions listed in the table agree with previously reported data within the overlapping uncertainties, and there are some new measurements for values not previously obtained in decay spectroscopy, most notably for the 85, 304 and 463 keV transitions.

### 6.2.5. K/L and L/M Ratios

The PACES spectrum in singles shows that for some of the more intense transitions in  $^{116}\text{Sn}$ , the L and M electron lines are visible above the background. Therefore, efficiency-corrected ratios of intensities of the K, L and M electron lines could be measured, and these are often quoted in the literature as K/L and L/M ratios, respectively. These are equivalent to the ratios of their internal conversion coefficients, as seen in Equation (69a) and (69b); note that the gamma-ray intensities cancel out. Consequently, this means that a Si(Li) detector alone can obtain transition multipolarity information, and so provides an independent cross check of an assignment via angular correlations.

$$\frac{\alpha_K}{\alpha_L} = \frac{I_K / I_\gamma}{I_L / I_\gamma} = \frac{I_K}{I_L} \quad (69a)$$

$$\frac{\alpha_L}{\alpha_M} = \frac{I_L / I_\gamma}{I_M / I_\gamma} = \frac{I_L}{I_M} \quad (69b)$$

These ratios are reported in Table 8, and while many of them are from transitions used in the PACES efficiency curve, the results do check that the multiplicities assigned to the transitions were justified. The discrepancies of the measured K/L ratios can be attributed to the minor deviations from the fitted efficiency curve. For the L/M ratios, however, the discrepancy is much greater, with experimental L/M ratios being about four

times smaller than the theoretical values for the given multipolarity and this cannot be attributed to the efficiency curve alone. These discrepancies are due to a small (but nonzero) gamma ray efficiency in Si(Li) detectors, as well as the lack of ability to resolve the M lines from the higher energy N, O, etc. lines; the substantial deviation of L/M ratios has been previously observed for  $^{110}\text{Cd}$  L/M ratios measured using the PACES Si(Li) array [139].

**Table 8.** Experimental and theoretical K/L and L/M ratios for transitions in  $^{116}\text{Sn}$  compared to those calculated from BrIccFO; in the last two columns the extreme limits are given for pure transition multiplicities if the transition is mixed. Asterisks mark transitions used in the PACES efficiency curve.

Transition Energy (keV)	This work K/L	BrIccFO K/L	This work L/M	BrIccFO L/M
138	7.8(3)	7.90 <i>MI</i> / 4.41 <i>E2</i>	1.60(13)	4.23 <i>MI</i> / 4.17 <i>E2</i>
162 ( $^{116\text{m2}}\text{In}$ )*	2.4(2)	2.21	3.88(23)	4.13
417*	7.2(4)	7.11	1.53(11)	4.23
819*	8.0(7)	8.33 <i>MI</i> / 7.97 <i>E2</i>	1.75(32)	4.25 <i>MI</i> / 4.24 <i>E2</i>
1097*	7.9(6)	8.21	1.24(15)	4.25
1294*	8.6(4)	8.31	1.27(8)	5.13
1507*	8.5(14)	8.39	1.37(37)	5.13

### 6.2.6. Experimental $E0$ Strengths

The  $E0$  transition strength ( $\rho^2(E0)$ ) can be measured provided the half-life of the originating state is known and the branching ratios, if any, are known for the non- $E0$  transitions exiting the same state. In the case of  $^{116}\text{Sn}$ , the 1757 and 2027 keV states both have measured half-lives. The Nuclear Data Sheets quote the half-lives as 44(6) ps and 160(20) ps, respectively [55]; thus, with these half-lives ( $t_{1/2}$ ) and the corresponding transition branching ratios expressed as sums of intensity ratios of non- $E0$  transitions (as  $I_i = I(\gamma + ce)$ ) to the  $E0$  intensity (as  $I(E0) = I(ce)$  only), Equation (70) can be used to obtain the decay rate  $\lambda(E0)$ ,

$$\lambda(E0) = \frac{\ln 2 / t_{1/2}}{1 + \sum_i \frac{I_i}{I(E0)}} . \quad (70)$$

From the decay rate, one can then obtain the  $E0$  transition strength by dividing the decay rate by the sum over electronic factors  $\Omega_i$ , which are essentially decay probabilities by different modes (e.g. K, L, etc. electron emission), in Equation (71). The electronic factors are computed from the theory of atomic electron emission, using the BrIccFO program [36].

$$\rho^2(E0) = \frac{\lambda(E0)}{\sum_i \Omega_i} \quad (71)$$

For convenience  $E0$  strengths are often multiplied by  $10^3$  because the values tend to be small, and they are reported as such in Table 9. Owing to the very weak population of the 2027 keV state in the  $\beta^-$  decay of  $^{116}\text{In}$  (the decay branch of the  $1^+$  state in  $^{116}\text{In}$  to the 2027 keV state has not been measured and is estimated to be  $<0.005\%$ ; 99% of the decays proceed to the  $0^+$  ground state of  $^{116}\text{Sn}$ ), only upper limits were able to be set on the 271 and 2027 keV transitions de-exciting that state.

**Table 9.**  $\rho^2(E0)$  strengths in  $^{116}\text{Sn}$  for  $0^+ \rightarrow 0^+$  transitions.

Transition Energy (keV)	$\rho^2(E0) \times 10^3$ (this work)	$\rho^2(E0) \times 10^3$ (Ref. [101])	$t_{1/2}$ (Ref. [55])
270	$<261$	87(19)	160(20) ps
1757	2.78(32)	4.3(8)	44(6) ps
2027	$<1.57$	0.87(18)	160(20) ps

A related quantity to the  $E0$  strength, as discussed in Section 2.3.4 when examining *multiple* pure  $E0$  and  $E2$  transitions exiting the same state, is the  $X$ -value [59], which is proportional to the ratio of the  $\rho^2(E0)$  branch to the  $B(E2)$  branch for the  $E0$  and  $E2$  transitions under consideration. The  $X$ -value can be predicted from models of nuclei, or measured experimentally. For example, the vibrational model of nuclei predicts that  $X$

should be proportional to the square of the nuclear deformation ( $\beta^2$ ), as explained briefly in the work of Bäcklin *et al.* [59].

The ratio of K line intensities,  $R$ , between transitions exiting the same  $0^+$  state to two lower-lying  $0^+$  and  $2^+$  states respectively, follows in Equation (72),

$$R = \frac{I_K(0^+_{upper} \rightarrow 0^+_{lower})}{I_K(0^+_{upper} \rightarrow 2^+_{lower})}, \quad (72)$$

which is then used to compute the  $X$ -value in Equation (73) [59], which uses the nuclear mass number  $A$ , the theoretical  $E2$  conversion coefficient for the  $0^+ \rightarrow 2^+$  transition, the theoretical K electronic factor  $\Omega_K$ , and the  $E2$  gamma-ray energy in MeV.

$$X(\text{exp}) = 2.55 \times 10^9 A^{4/3} R \left[ \frac{\alpha_K(E2)}{\Omega_K} \right] E_\gamma^5 \quad (73)$$

The  $X$ -value for the 1757 keV transition in  $^{116}\text{Sn}$  is reported in Table 10 and compared to the value from Ref. [59], and also restated with theoretical  $\Omega_K$  values from the newer BrIccFO calculation, which affect the  $X(\text{exp})$  value, but not enough to be considered statistically significant since the  $X$ -values agree within the mutually overlapping uncertainties.

**Table 10.** Properties of the 1757 keV  $0_2^+$  state in  $^{116}\text{Sn}$ .

	$R$	$X(\text{exp})$
This Work	0.34(5)	0.0074(12)
Ref. [59]	0.38(8)	0.0086(18)
Ref. [59] w/ BrIccFO $\alpha_K(E2)$	0.38(8)	0.0083(18)

Finally, as mentioned the  $X$ -value can be predicted theoretically; the vibrational model of nuclei predicts that for  $^{116}\text{Sn}$ , the  $X$ -value is proportional to  $\beta^2$  ( $X_{\text{vib}} = \beta^2 = 0.013$  [59]), resulting in a deduced deformation of  $|\beta_2| = 0.12$ . From the experimental  $X$ -value of 0.0074(12) measured in the present work, the deduced deformation is  $|\beta_2| = 0.076(6)$ , in

applying the proportional relationship of the vibrational model. This experimentally obtained deformation is somewhat smaller than that predicted by the model, possibly suggesting less vibrational character to the 1757 keV state than previously thought. Alternatively, this suggests that as noted in Section 4.5, the vibrational model may be deficient in explaining the properties of the 1757 keV  $0_2^+$  state.

### 6.3. Angular Correlation Results

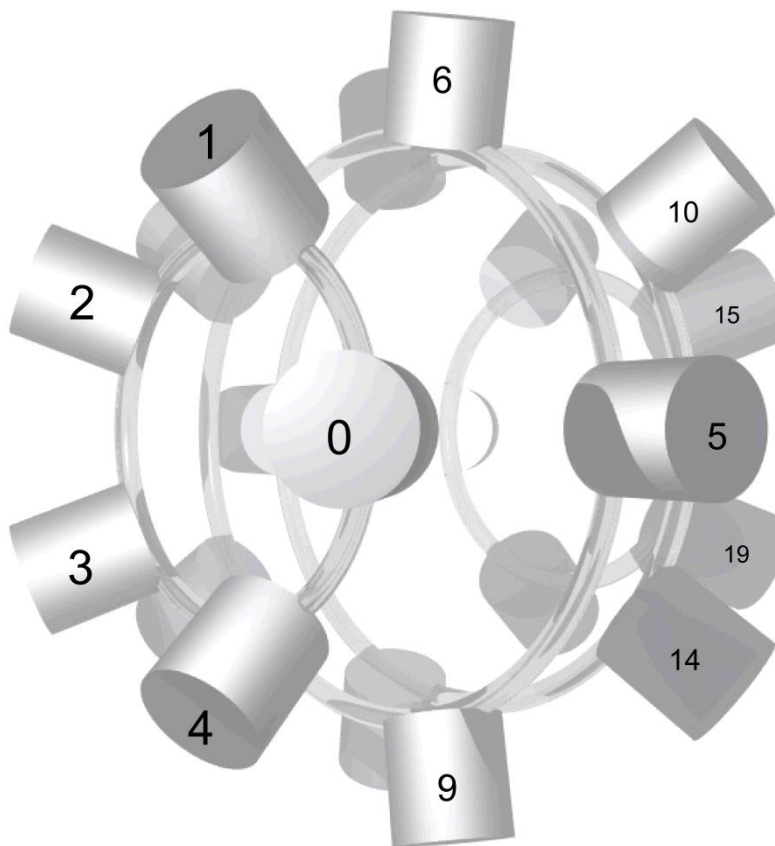


**Figure 61.** Pictorial representation of the  $8\pi$  array as assembled at TRIUMF-ISAC, with numbers indicating which detector is at which position. The beam direction is from the left front to the right rear at an angle to the page. Reproduced with permission [47].

As discussed in Section 2.3.1, the translation of the physical geometry of a detector array into corresponding groups of common correlation angles is required in

order to perform angular correlation measurements. For the  $8\pi$  array (Figure 61), this translation of detector positions into correlation angles between pairs of detectors has been previously worked out [47,48], and so the physical rings of the  $8\pi$  array at 37, 79, 101 and 143 degrees (with the  $\theta_{\text{beam}}$  angle increasing from left to right across the page) can be translated into a logical geometry (the correlation angles) of 41.8, 70.5, 109.5, 138.2, and 180 degrees. For example, the combination of detectors 0 and 4 results in an angle of 41.8 degrees between the vectors pointed at them from the beam-spot position (refer to Figure 16). From this point on, unless otherwise specified, any reference to an angle  $\theta$  is to the correlation angle, and therefore the angle in the  $W(\theta)$  angular-correlation function. Table 11 contains the resulting correlation angles that exist in the  $8\pi$  array and notes how many pairs of detectors are common to each angle for the present experiment; if all 20 detectors were used, the number of pairs would be 30, 60, 60, 30 and 10 respectively in the last column.

**Table 11.** List of correlation angles (second column), obtained from the geometry in Figure 61, and the number of detector pairs in each angle (third column).

Correlation Angle Number	Angle (degrees)	Number of Detector Pairs
1	41.8	24
2	70.5	48
3	109.5	48
4	138.2	25
5	180.0	8

The gsort code used for generating the singles and coincidence data could also be used, with appropriate modifications, to process the  $\gamma$ - $\gamma$  coincidence data into matrices for each pair of coincidences. Normally when analyzing  $\gamma$ - $\gamma$  coincidence data, the matrix or matrices can be symmetrized, meaning that coincidence events between pairs of detectors are binned in a matrix twice. Thus, for a detector (a,b) combination with measured gamma ray energies  $E_\gamma(a)$  and  $E_\gamma(b)$ , the matrix so created has the events binned at  $(x, y) = (E_\gamma(a), E_\gamma(b))$  and at  $(y, x) = (E_\gamma(a), E_\gamma(b))$ .

When efficiency corrections are required, the matrices cannot be symmetrized (coincidence events are thus binned only at  $(x, y) = (E_\gamma(a), E_\gamma(b))$ ), and the reason for this is discussed more fully further in this section. Figure 62 shows the differences between the two types of matrices, which shows that the number of events at an  $(x, y)$  coordinate are not the same as at a  $(y, x)$  coordinate for the unsymmetrized matrix. While there are potentially 380 matrices that must be created to fully analyze angular correlations using the  $8\pi$  array, only 190 are needed since the combinations, e.g. of detector 0 and detector 1 and detector 1 and detector 0 are redundant. This is because in a coincidence event it is only necessary that they both produce events within the same time window; the order of arrival in the raw data stream is unimportant.

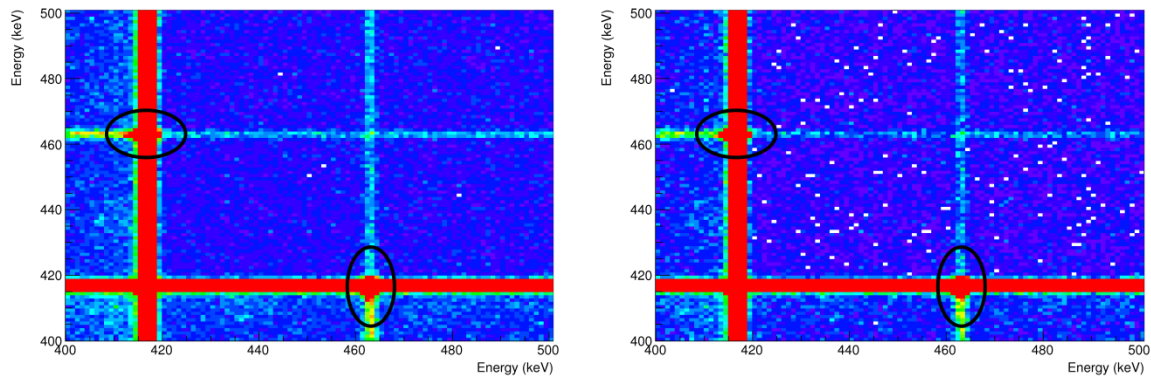


**Figure 62.** Close-up on the 400 – 500 keV region showing symmetrized (left) and unsymmetrized (right)  $\gamma$ - $\gamma$  coincidence matrices. The indicated regions show that the events in the unsymmetrized matrix at (463 keV, 417 keV) are not identical to those at (417 keV, 463 keV).

As has been previously established [47,48], the  $8\pi$  HPGe array has a high degree of symmetry. Consequently, the 190 matrices that would otherwise have to be individually analyzed can be combined into five matrices, one for each correlation angle. In the case of the  $^{116}\text{Sn}$  experiment, the exclusion of detectors 4 and 17 results in  $(17 \times 18) \div 2 = 153$   $\gamma$ - $\gamma$  matrices which were combined into the five correlation-angle matrices.

### 6.3.1. $\gamma$ - $\gamma$ Angular Correlations

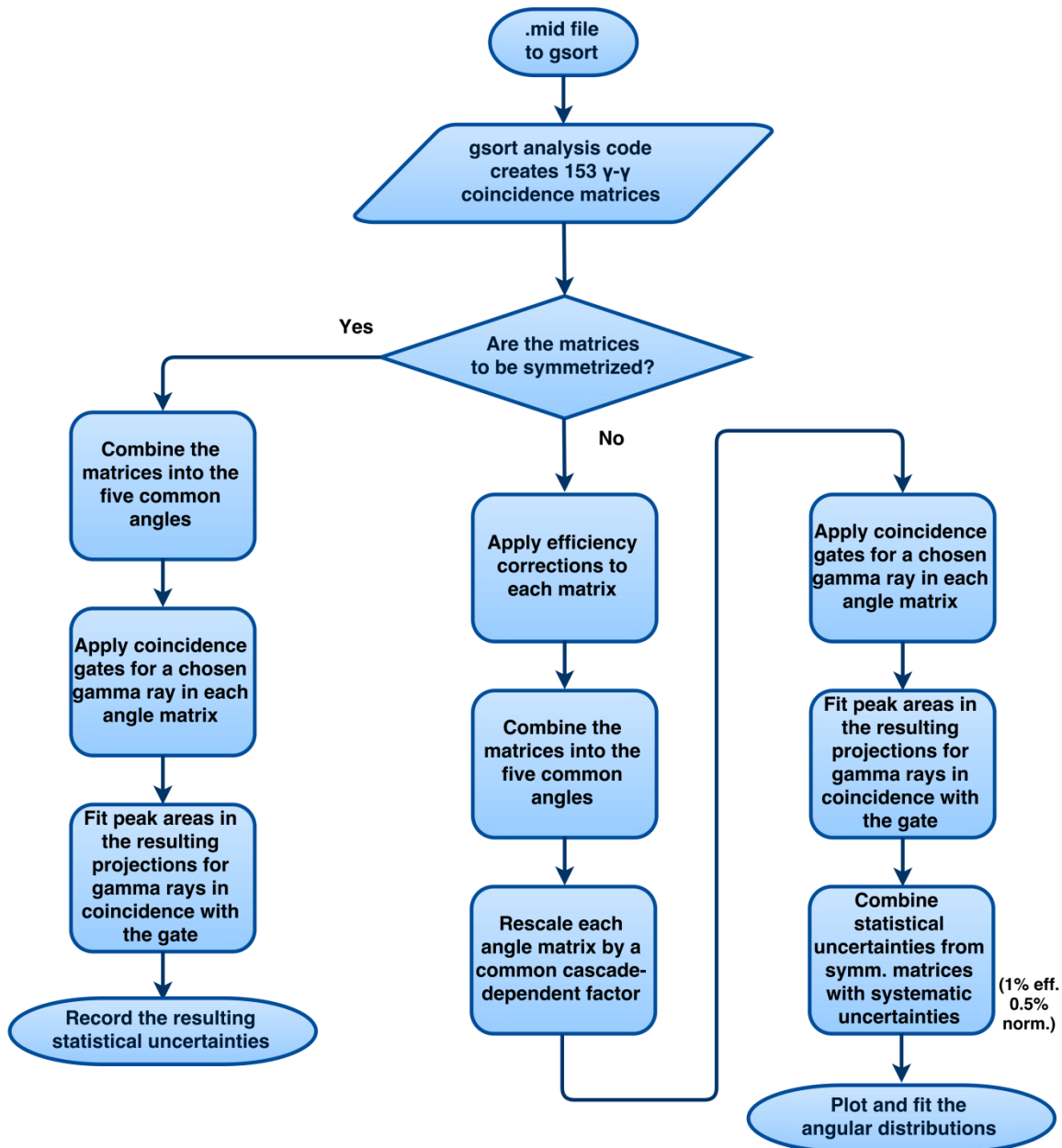


**Figure 63.** Flow diagram of the angular correlation analysis depicting the creation and usage of symmetrized and unsymmetrized coincidence matrices.

As discussed in further detail in this section, Figure 63 depicts the parallel analysis of the angular-correlation data in order to:

1. Quantify the statistical uncertainties in the coincidence gates applied in obtaining angular correlations, and
2. Correct the peak areas obtained in coincidence gates for the relative efficiency of the gamma-ray detectors in each correlation angle in order to obtain  $W(\theta)$  data points.

The discussion that follows will first explain the need for an efficiency correction, and then follow the flow chart in Figure 63, starting with the analysis of the unsymmetrized matrices and then moving to the analysis of the symmetrized efficiency-corrected matrices.

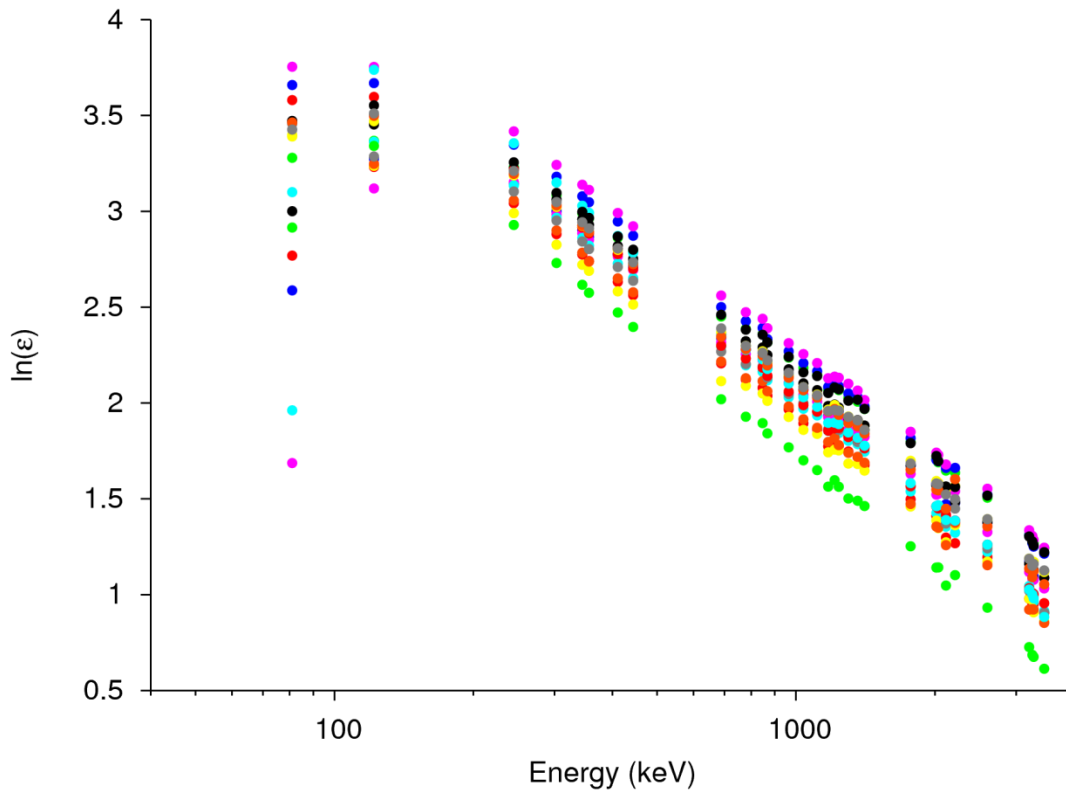


**Figure 64.** The eighteen  $8\pi$  individual HPGe detector relative efficiency data points plotted with  $\ln \epsilon$  vs Energy (log scale) in keV. The points are from standard sealed  $^{133}\text{Ba}$ ,  $^{56}\text{Co}$  and  $^{152}\text{Eu}$  sources. For clarity the error bars have been omitted.

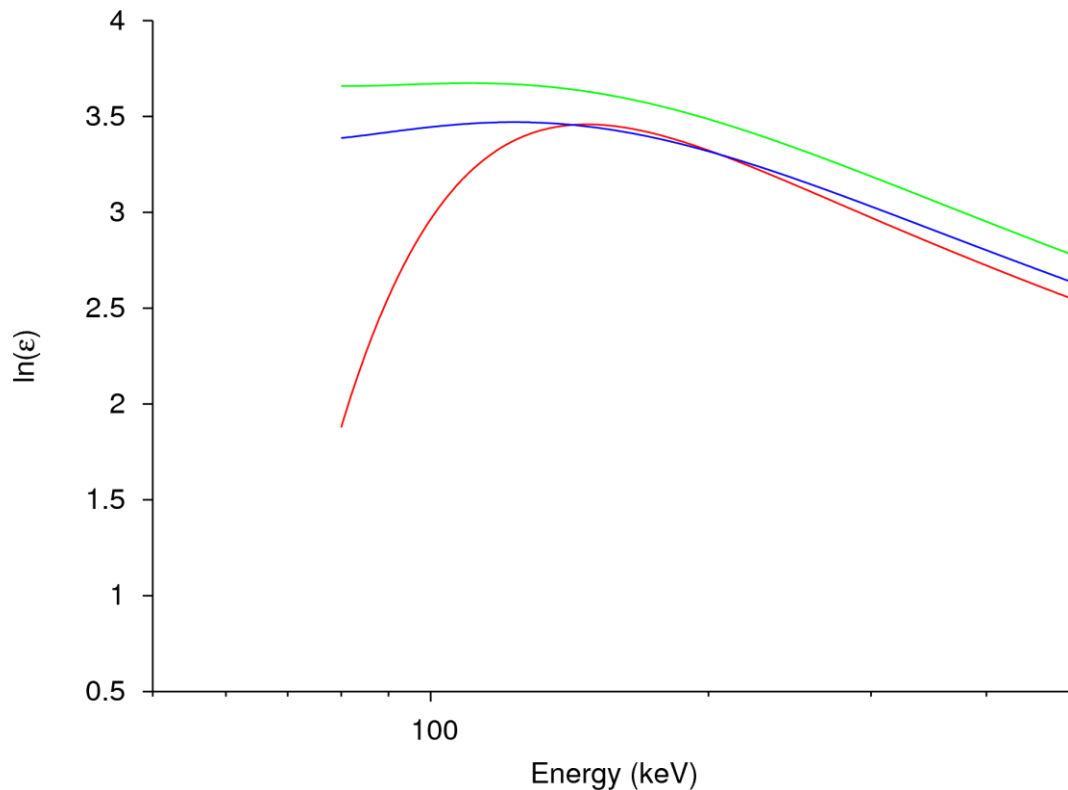


**Figure 65.** Close-up on the 0 – 500 keV region of Figure 64 showing representative relative efficiency curves from HPGe detectors 5 (red), 12 (green), and 15 (blue); the data points have been omitted for clarity. This illustrates the similarity of the curves above  $\sim 200$  keV, but that they deviate quite significantly below that energy.

To analyze the angular-correlation data obtained from the  $8\pi$  array, the sort code created  $153\,4096$  channel  $\times$   $4096$  channel matrices, as discussed in the overview in Section 6.3. These matrices must be efficiency-corrected when analyzing angular correlations, since each individual HPGe detector in the  $8\pi$  array will have its own characteristic energy-dependent response. The different relative efficiencies as a function of gamma ray energy are shown in Figure 64 for all 18 detectors. Figure 65 is a close-up over the range from 0 – 500 keV showing the fitted curves for three representative detectors, where the relative efficiency changes markedly with energy for different detectors.

The relative efficiencies were obtained in a similar manner to the method discussed in 6.1.3 for the whole array, using the peak areas from standard sealed  $^{133}\text{Ba}$ ,  $^{152}\text{Eu}$  and  $^{56}\text{Co}$  sources. The  $^{56}\text{Co}$  and  $^{133}\text{Ba}$  data points were normalized to the  $^{152}\text{Eu}$  data prior to fitting each detector's efficiency curves with a 7<sup>th</sup> degree polynomial; the  $\chi^2/\nu$  did not improve when an 8<sup>th</sup> degree polynomial was used. Because of the considerable variation in the individual detector efficiency curves at low energy (a gamma ray doublet at ~80 keV was the lowest usable  $^{133}\text{Ba}$  source peak for the individual detectors), 80 keV was the cutoff threshold below which no events were binned for the angle matrices.

From the relative efficiency curves (fits of the data points in Figure 64), the residual, which is the discrepancy between the fit and the actual data points, for all eighteen detectors in the analysis, was examined and in general the deviations were on the order of 0.7%. Therefore a systematic global relative 1% detector-pair coincidence efficiency-correction uncertainty was added in quadrature to the statistical uncertainty for a given angular correlation data point. The statistical uncertainty inherent in the data obtained from the efficiency-corrected unsymmetrized matrices was determined by carrying out a similar analysis on symmetrized matrices without an efficiency correction. The subsequent analyses ran in parallel, as depicted in Figure 63. The left side (symmetrized matrices) will be discussed first, followed by the middle and right (unsymmetrized matrices).

### *Analysis of the Symmetrized Matrices*

These correlation-angle matrices were not corrected for efficiency, and were created for the purpose of determining the statistical uncertainties in peaks fitted in projections from gates. The 153 individual detector-pair matrices were added together into the five common correlation angles (Table 11 and Refs. [47,48]), and then gates on gamma rays were taken to fit peaks in the resulting projected spectra.

For example, in the case of the 1097-1294 cascade (from the  $4_1^+$  2391 keV level, through the  $2_1^+$  1294 keV level, and ending at the  $0_1^+$  ground state), the 1294 keV gamma ray peak was gated, and an equivalent number of channels of nearby background were

also gated. The resulting 1097 keV peak areas, obtained by fitting them with gf3 [140], would then be subtracted. The associated statistical uncertainties of the gate and background projection peaks would be added in quadrature.

Similarly, the 1097 keV gamma ray and background were gated, and the resulting projected 1294 keV gamma ray peak areas were fitted and subtracted. The two methods of gating (on the upper or the lower transition) should yield identical peak areas within their mutual uncertainties. If not, then the average uncertainty was increased by the square root of the  $\chi^2/\nu$  [141] for that  $W(\theta)$  data point.

### *Analysis of the Unsymmetrized Matrices*

In the second part of the analysis, the 153 matrices were not symmetrized. This was necessary in order to preserve the knowledge of which detector's events were binned on the  $x$ - and  $y$ -axes of the matrix. For example, given the (0,1) detector combination measuring gamma ray energies  $E_\gamma(0)$  and  $E_\gamma(1)$ , the element at  $(x, y) = (E_\gamma(0), E_\gamma(1))$  only would be incremented. Consequently, an efficiency correction can then be applied to that  $(x, y)$  coordinate by dividing by the product  $\varepsilon_x(0)\varepsilon_y(1)$ , where the numbers in parentheses indicate which detector's efficiency curve is involved, and the subscripts indicate for what energy bin on the given axis. A custom ROOT [142] code was used to perform the efficiency correction on the detector-pair matrices.

The 153 unsymmetrized matrices, corrected for detector coincidence efficiency, were then combined into the five correlation-angle matrices and in doing so, the efficiency product in each bin  $\varepsilon_x(m)\varepsilon_y(n)$  ( $m, n =$  different detector numbers) was divided by a common cascade-dependent scaling factor, so that depending on the cascade a new set of five correlation-angle matrices might be created specifically to analyze that cascade. The cascade-dependent scaling factor ensured that peak areas in projections from gates were approximately equal to those obtained from equivalent projections of gates on the uncorrected symmetrized matrices. Without this factor, the peak areas would be artificially reduced.

In using the unsymmetrized efficiency-corrected matrices, both the  $x$  and  $y$  axes of the angle matrices were gated, and the resulting projection peak areas were then summed. The uncertainties assigned to the resulting peak areas were the quadrature sum of the underlying statistical uncertainties from the symmetrized matrices, a global 1.0% systematic relative uncertainty from the efficiency correction, and a 0.5% systematic relative uncertainty associated with normalizing the angular correlation data. The normalization is discussed in more detail later in this section.

### ***Plotting and Fitting Angular Correlation Data***

For every cascade analyzed, the resulting peak areas from applying gates to the efficiency-corrected unsymmetrized correlation-angle matrices for each angle form the basis of an angular correlation  $W(\theta)$ . Each data point  $W(\theta)_i$  for the  $i^{\text{th}}$  data point ( $i = 1 - 5$ , corresponding to a given angle from Table 11) is described by Equation (74), where the normalized efficiency-corrected peak intensities ( $I_i/I_{\text{norm},i}$ ) are rescaled so the 180 degree (correlation angle number 5) value is at exactly 1.000000, by dividing by  $I'_{180^\circ} = I_{180^\circ}/I_{\text{norm},5}$ .

$$W(\theta)_i = \left( \frac{I_i}{I_{\text{norm},i}} \right) \frac{1}{I'_{180^\circ}} \quad (74)$$

While the adjustment of the 180 degree data point is not strictly necessary, it does mean all the angular correlations analyzed in the present work cover similar numerical ranges. Due to this adjustment, the overall  $W(\theta)$  normalization  $N$  of Equation (48), reproduced here for convenience, is within  $0 < N \leq \sim 1.5$ .

$$W(\theta) = N[1 + A_{22}Q_{22}P_2(\cos\theta) + A_{44}Q_{44}P_4(\cos\theta)] \quad (48)$$

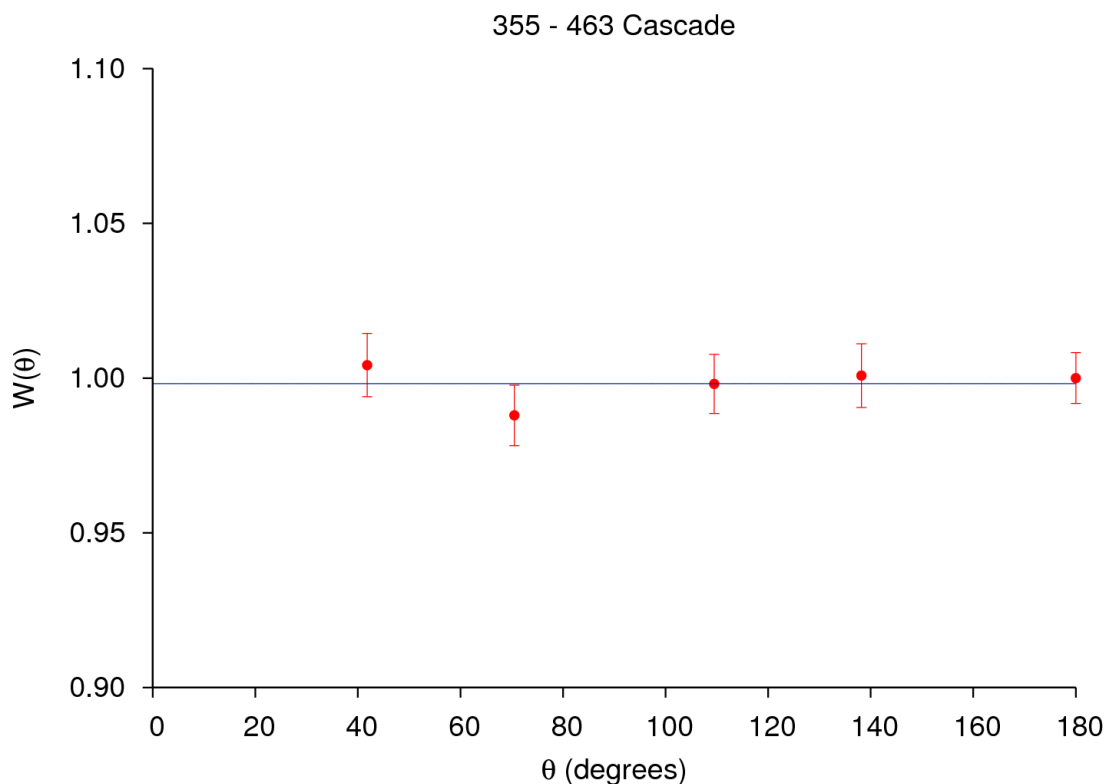


**Figure 66.** Angular correlation of the  $2^+ - 0^+ - 2^+$  cascade in  $^{116}\text{Sn}$ , yielding  $N = 0.998 \pm 0.004$ . The data points are the averaged efficiency-corrected peak areas divided by the number of detector pairs in each correlation angle, scaled so the 180 degree point is exactly equal to 1.0. The  $\chi^2/\nu$  of this data set is 0.39.

The data points of the angular correlations obtained from the  $8\pi$  array must be adjusted to account for counting effects, as different detector numbers are accumulated repeatedly in some angle matrices. These adjusting (normalization) factors are the  $I_{\text{norm},i}$  values in Equation (74) for each angle.  $I_{\text{norm},i}$  can be obtained in one of two ways: either from a known isotropic angular correlation, or from the number of detector pairs in each angle. If an isotropic angular correlation, adjusted by the number of detector pairs, is statistically equivalent to  $A_{22} = 0$ ,  $A_{44} = 0$ , then the number of pairs alone is sufficient to normalize the angular correlation data in the present work. Figure 66 shows that the 355-463  $2_2^+ - 0_2^+ - 2_1^+$  cascade in  $^{116}\text{Sn}$  is statistically isotropic after an efficiency correction.

In re-scaling data points by the number of detector pairs to correct for counting effects, a conservative estimate of the systematic uncertainty in the normalization from the underlying data in Figure 66, obtained via a  $\chi^2$  analysis of the deviations of the points, is 0.5%. This was combined with the efficiency uncertainty and the statistical peak-fitting uncertainty in quadrature for each data point for all other angular correlations.

When fitting angular correlations from the  $8\pi$  array, it is necessary to use a Monte Carlo simulation to obtain the  $Q_{kk}$  attenuation factors. Paul Schmelzenbach conducted such a simulation for the configuration of the  $8\pi$  array at TRIUMF-ISAC and obtained  $Q_{22} = 0.96$  and  $Q_{44} = 0.89$  [47]. The Q-factor energy dependence was found to be negligible for the  $8\pi$  array source-detector distance in the TRIUMF-ISAC configuration.

In fitting known pure  $E2$   $4^+-2^+-0^+$  cascades as well as  $0^+-2^+-0^+$  cascades (Table 12), the  $Q_{22}$  and  $Q_{44}$  values can be used along with the theoretical  $A_{22}$  and  $A_{44}$  values (computed from  $F$  coefficients in Equations (53) and (54) where  $\delta \rightarrow \infty$ ) to determine how well the predicted angular correlations match experimental data. A  $\chi^2$  minimization of  $W(\theta)$  to find the best value of  $N$  in Equation (48) quantifies the goodness of the prediction versus experiment. As outlined by Taras and Haas [143] the  $\chi^2$  for an experimentally measured angular correlation  $W(\theta)_i$  at each angle  $i$  with an associated uncertainty in each data point  $\Delta W(\theta)_i$ , being compared with a calculated angular correlation  $W(\theta)_{fit,i}$ , is computed by Equation (75),

$$\chi^2 = \sum_i \frac{(W(\theta)_i - W(\theta)_{fit,i})^2}{(\Delta W(\theta)_i)^2}, \quad (75)$$

and to obtain  $\chi^2/\nu$  from Equation (75), the number of degrees of freedom  $\nu$  is the number of data points (angles) minus the number of parameters in  $W(\theta)$ . The  $\chi^2$ , or  $\chi^2/\nu$ , can then be minimized to find the best-fit  $W(\theta)$  by varying the parameters in the formula. With no mixing ratio  $\delta$  the free parameter to be varied is  $N$ , upon substituting the theoretical  $A_{22}$ ,  $Q_{22}$ ,  $A_{44}$  and  $Q_{44}$  values into Equation (48) for each angular correlation to be plotted and fitted, summarized in Table 12. Finding the best-fit  $W(\theta)$  is thus equivalent to finding the

best value of N, the  $W(\theta)$  normalization constant that scales the theoretical curve to the data points.

**Table 12.** Summary of intense cascades in  $^{116}\text{Sn}$  containing pure  $E2$  transitions to test the angular correlation method. The first column labels the spins and parities according to Figure 18. The  $A_{22}$  and  $A_{44}$  values quoted here are theoretical values (see text).

Cascade $I_1^\pi - I_2^\pi - I_3^\pi$	Cascade Gamma Rays ( $E_\gamma$ in keV)	$A_{22}$	$A_{44}$
$4^+ - 2^+ - 0^+$	1097-1294, 1507-1294, 1752-1294, 417-355, 417-2112	+0.1020	+0.0091
$0^+ - 2^+ - 0^+$	463-1294	+0.3571	+1.1429

The need for an efficiency correction is shown by the relatively high  $\chi^2/\nu$  of 5.52 for the uncorrected  $4_1^+ - 2_1^+ - 0_1^+$  angular correlation of the 1097-1294 cascade (reflecting that the data points do not match well with the theoretical curve). Although the data point uncertainties are smaller since they are purely statistical and this can artificially increase the  $\chi^2/\nu$  somewhat, it is still clear that such a high  $\chi^2/\nu$  value indicates the presence of a systematic effect, which is the relative efficiency for each detector.

By comparison, the efficiency correction considerably reduces the  $\chi^2/\nu$  for these theoretical fits (e.g. for the 1097-1294 cascade, the fit to the efficiency-corrected data points yields  $\chi^2/\nu = 0.14$ ), as can be seen by comparing Figure 67 and Figure 68. Even accounting for the fact that the uncertainties in Figure 68 are larger because of the systematic contributions it can clearly be seen visually that the fit of the theoretical  $W(\theta)$  curve is better when applying efficiency corrections to unsymmetrized matrices. The values of N for the theoretical fits have been given to four significant figures, consistent with the number of decimal places used for the theoretical  $A_{22}$  and  $A_{44}$  coefficients.

Table 13 summarizes the results obtained from fitting and plotting the pure  $E2$  cascades listed in Table 12. Except for the 463-1294 cascade, the  $\chi^2/\nu$  values are less than 0.84, which corresponds to the  $\chi^2$  distribution probability of  $P = 0.5$  for four degrees of freedom. For these strongly populated pure  $E2$  cascades the uncertainties are dominated by the conservative systematic uncertainties that were added in quadrature with the

statistical uncertainties for all cascades. In the example of the 1097-1294 cascade, the  $\chi^2/\nu$  value increases from 0.14 ( $P = 0.03$ ) to 3.89 ( $P = 0.996$ ) if only the statistical uncertainties are included when fitting the angular correlation, indicating that the systematic errors are overestimated for these strong cascades.

The relatively large  $\chi^2/\nu$  of 5.68 for the 463-1294 cascade (Figure 69) is primarily due to the deviation away from the curve at the 180 degree point. The deviation at  $\theta = 180^\circ$  is likely due to slight discrepancies in source-detector distances, or an effective beam spot size that makes the source not quite pointlike, and which is most sensitive at  $180^\circ$  owing to a lessening of an averaging effect that comes from combining pairs of detectors in different ways (Table 11). This is because at  $180^\circ$ , adding together only eight pairs likely does not completely cancel out slight shifts in the  $Q_{kk}$  factors which come from limitations in the Monte Carlo simulation.

**Table 13.** Summary of  $\chi^2$  analysis of the fits using the  $A_{22}$  and  $A_{44}$  coefficients given in Table 12. The second column labels the spins and parities according to Figure 18, with subscripts indicating the  $n^{\text{th}}$  occurrence of the state.

Cascade Gamma Rays ( $E_\gamma$ in keV)	$I_1^\pi - I_2^\pi - I_3^\pi$	$\chi^2/\nu$
463-1294	$0_2^+ - 2_1^+ - 0_1^+$	5.68
1097-1294	$4_1^+ - 2_1^+ - 0_1^+$	0.14
1507-1294	$4_3^+ - 2_1^+ - 0_1^+$	0.16
1752-1294	$4_4^+ - 2_1^+ - 0_1^+$	0.38
417-355	$4_2^+ - 2_2^+ - 0_2^+$	0.51
417-2112	$4_2^+ - 2_2^+ - 0_1^+$	0.08

However, given the good agreement between theoretical predictions and experimental data for well-understood  $\gamma$ - $\gamma$  cascades, in general the simulations by Schmelzenbach produce  $Q_{kk}$  factors which are appropriate to use in the present work, and thus they can be used in the following section in which  $A_{22}$  and  $A_{44}$  values are obtained experimentally by varying the mixing ratio as well as  $N$  to find the  $\chi^2$  minimum.

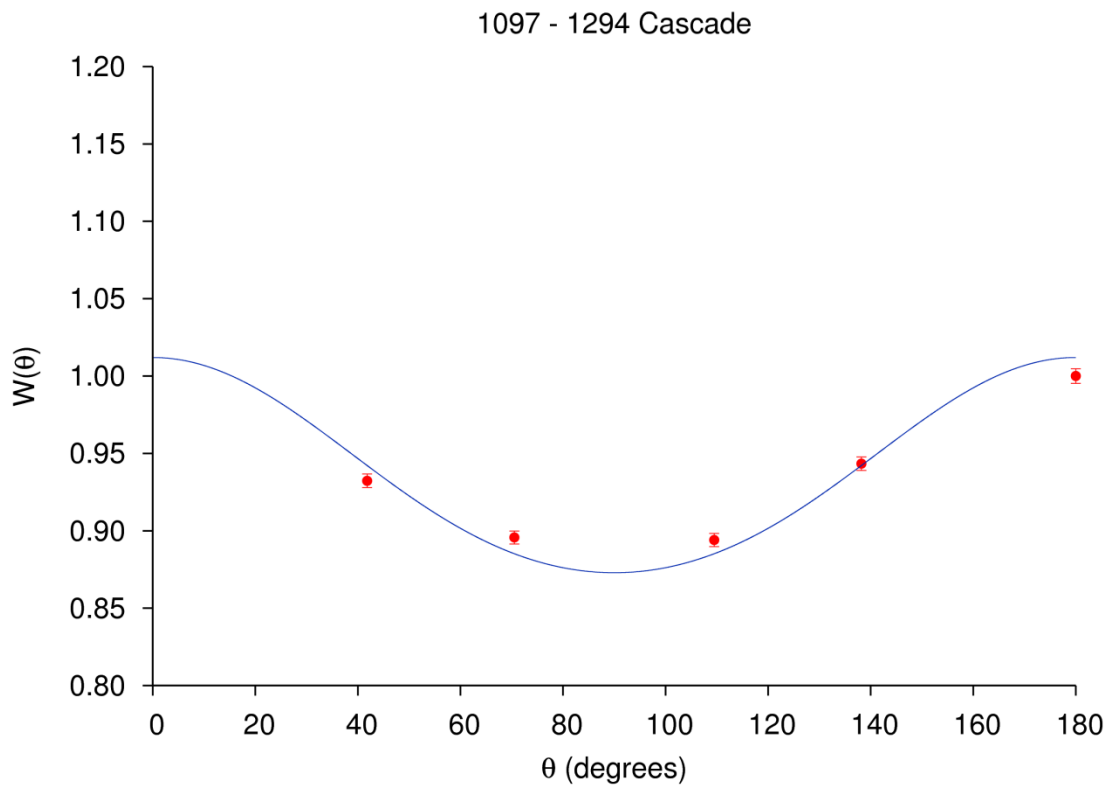


**Figure 67.** Plot of an angular correlation from symmetrized matrices, without an efficiency correction, of the  $4_1^+ - 2_1^+ - 0_1^+$  cascade in  $^{116}\text{Sn}$ , with  $A_{22} = +0.1020$  and  $A_{44} = +0.0091$ . The minimum  $\chi^2/\nu$  of this fit was 5.52 for a  $W(\theta) N = 0.9150$ . The uncertainties in each data point include only the statistical errors.

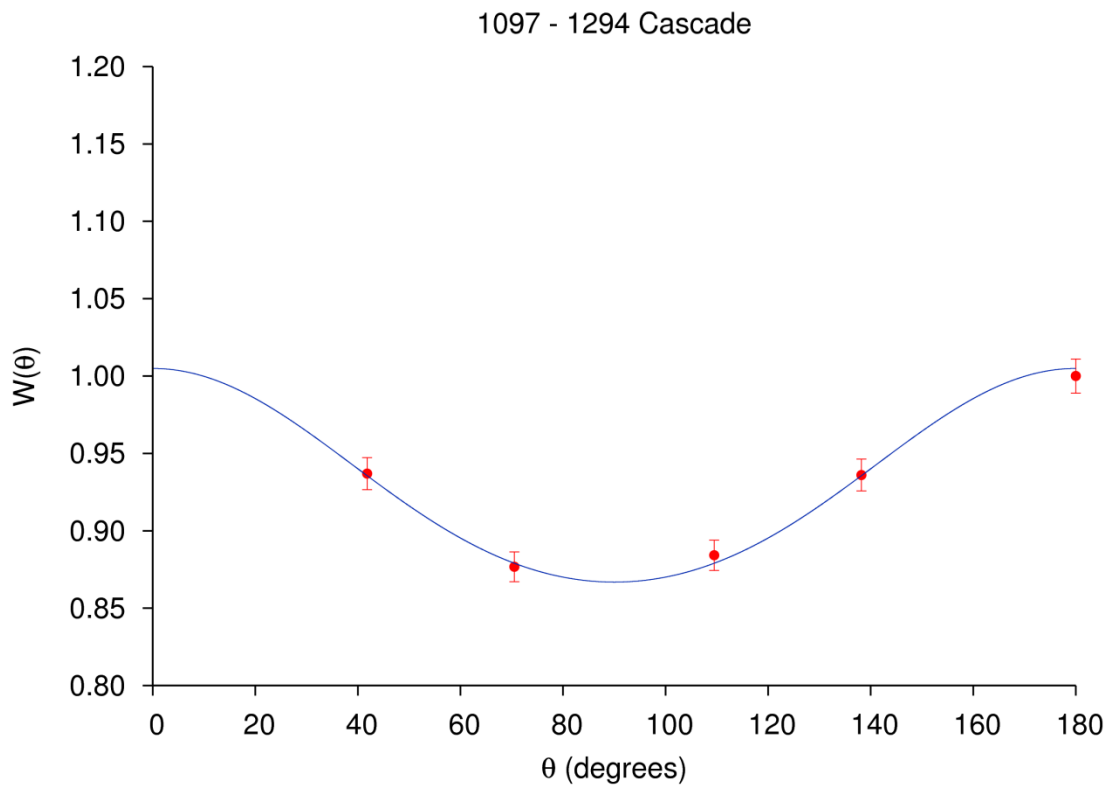


**Figure 68.** Plot of an efficiency-corrected angular correlation of the  $4_1^+ - 2_1^+ - 0_1^+$  cascade in  $^{116}\text{Sn}$ , with  $A_{22} = +0.1020$  and  $A_{44} = +0.0091$ . The minimum  $\chi^2/\nu$  of this fit was 0.14 for a  $W(\theta) N = 0.9086$ , where the statistical errors of each data point have been augmented with the efficiency-correction and normalization systematic uncertainties.

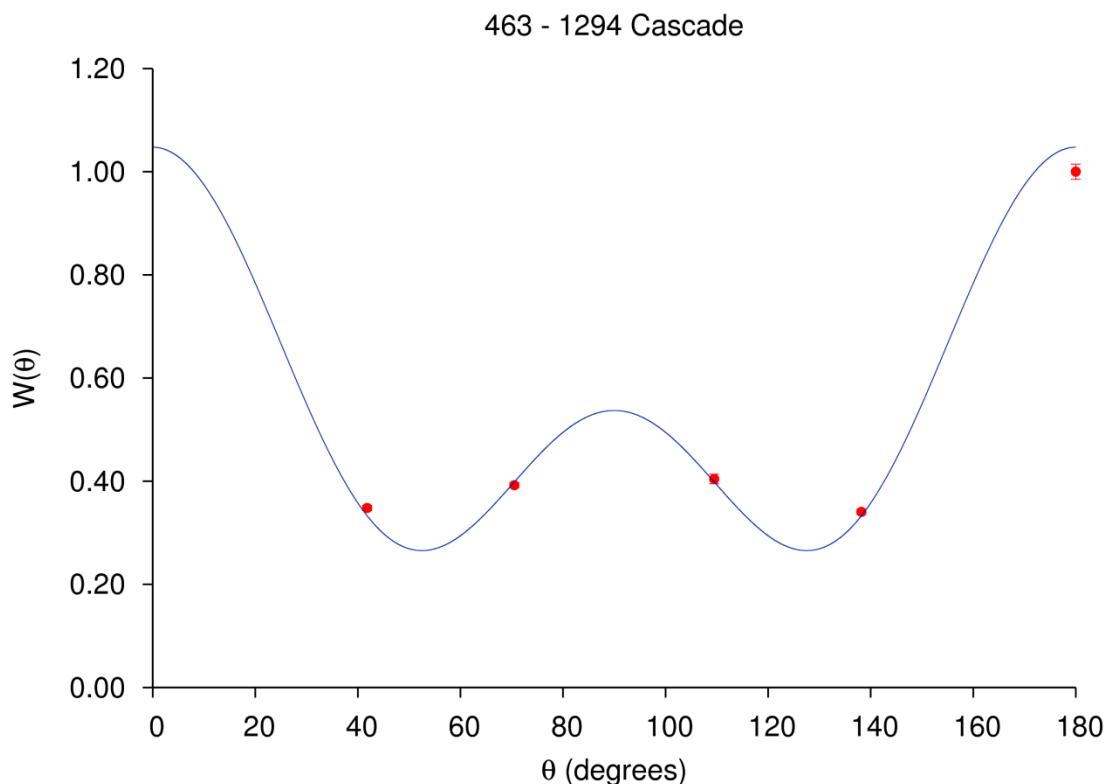


**Figure 69.** Plot of an efficiency-corrected angular correlation of the  $0_2^+ - 2_1^+ - 0_1^+$  cascade in  $^{116}\text{Sn}$ , with  $A_{22} = +0.3571$  and  $A_{44} = +1.1429$ . The minimum  $\chi^2/\nu$  of this fit was 5.68 for a  $W(\theta) N = 0.4439$ , where the statistical errors of each data point have been augmented with the efficiency-correction and normalization systematic uncertainties.

### 6.3.2. Mixing Ratios in $^{116}\text{Sn}$

The method of finding mixing ratios in the present work is simplified because the lower transition in the cascades involved for  $^{116}\text{Sn}$  (417, 1097, 1294 or 1507 keV, depending on the cascade) is unmixed  $E2$ , and the upper one is usually mixed  $E2/M1$ . Therefore, the  $A_{kk}$  coefficients are a quadratic function of  $\delta$  for the upper transition, since the  $A_k$  coefficient is only one  $F$  coefficient and an appropriate range of  $\delta$  values can be sampled in the  $B_k$  coefficient (refer to Equations (53) and (54) in Section 2.3.3). In such cases there will be two minima, at most, in a  $\chi^2/\nu$ -arctan  $\delta$  plot.

As in the previous section, the uncertainties for each data point in the  $W(\theta)$  plots in this section include the combined statistical and efficiency plus normalization systematic uncertainties. For mixed-pure cascades, the computer code that analyzes the angular correlation data now samples through values of  $N$  and  $\delta$  to find the lowest global minimum  $\chi^2/\nu$  value. As a result the  $A_{22}$  and  $A_{44}$  values quoted for the mixed-pure cascades are experimentally determined and correlated with one another through the value of  $\delta$  obtained in the  $\chi^2/\nu$  minimization. Since the uncertainties in  $A_{22}$  and  $A_{44}$  are not independent of the uncertainty in  $\delta$ , these values are quoted to two significant figures only, which is generally the same as the number of decimal places in  $\delta$  set by the uncertainty limits. Confirming this, if  $A_{22}$ ,  $A_{44}$  and  $N$  were to be simultaneously fitted to angular-correlation data instead using LEGFT [144], representative relative uncertainties in the three values are typically on the order of at least 5%, meaning two figures are significant in most cases.

There are several methods for obtaining the value of  $\delta$  and its uncertainty which have been established over the years. The semi-graphical method of Arns and Wiedenbeck [145,146], pioneered in the 1950s and 1960s, has fallen out of use. Another purely graphical method involves plotting  $A_{22}$  and  $A_{44}$  as a function of  $\delta$  and visually ascertaining the value and its uncertainty, as outlined by Schmelzenbach [47]. A plot of  $\chi^2/\nu$  with respect to  $\arctan(\delta)$  was used at Chalk River in experiments on isotopes of Scandium in the 1960s and 1970s [147], and is comparatively much simpler while allowing quantitative uncertainty measurements.

The graphical methods can in some cases give a good visual understanding of the uncertainties, but sometimes the uncertainty is asymmetric. Therefore, for simplicity and for the purposes of correctly ascertaining the uncertainty (or uncertainties, if asymmetric) in  $\delta$ , the method used in this thesis is to minimize  $\chi^2/\nu$  with respect to  $\arctan(\delta)$ ; the uncertainty limits are then given by the usual rule of finding the values of  $\delta$  that correspond to  $\chi^2 + 1$  [148].

Several mixed-multipolarity transitions in  $^{116}\text{Sn}$  were examined, and the results of all mixing ratio measurements conducted in this work are summarized in Table 14, with their angular-correlation and  $\chi^2/\nu$  plots in Appendix J if they are not discussed in detail further in this section. All mixing ratios quoted in this work have + or – signs according to the Krane & Steffen convention [43,44]. In general, these cascades are more weakly populated than the pure  $E2$  cascades and the uncertainties are dominated by the statistical uncertainties. The  $\chi^2/\nu$  values obtained for fits to these angular correlations are distributed about 0.78, which corresponds to the  $\chi^2$  distribution probability of  $P = 0.50$  for three degrees of freedom. The average probability obtained for these ten angular correlations is  $P = 0.48$ , and details may be found in Appendix J as well.

**Table 14.** Results of all angular correlation measurements on mixed-multipolarity transitions in  $^{116}\text{Sn}$ , including those discussed in detail in the text. The second column gives the starting level energy of the cascade ( $E_1$ ) in keV, corresponding to  $I_1^\pi$ . The third column labels the spin-parities of the states in the cascade for that row. The values of  $A_{22}$  and  $A_{44}$  are the ones obtained from the chosen values of  $\delta$ .

Cascade $\gamma$ rays ( $E_\gamma$ in keV)	$E_1$ (keV)	$I_1^\pi$ - $I_2^\pi$ - $I_3^\pi$	$A_{22}$	$A_{44}$	$\delta$	$\chi^2/\nu$
272-417	2801	$4_3^+$ - $4_2^+$ - $2_2^+$	+0.19	+0.072	$-0.93_{-0.42}^{+1.00}$	1.58
568-417	3097	$4_5^+$ - $4_2^+$ - $2_2^+$	+0.21	+0.064	$-0.86_{-0.40}^{+0.98}$	0.40
138-1097	2529	$4_2^+$ - $4_1^+$ - $2_1^+$	+0.23	+0.0026	$-0.13(8)$	0.10
410-1097	2801	$4_3^+$ - $4_1^+$ - $2_1^+$	+0.24	+0.0047	$-0.18_{-0.45}^{+0.21}$	0.52
655-1097	3046	$4_4^+$ - $4_1^+$ - $2_1^+$	+0.10	+0.0096	$+0.26_{-0.20}^{+0.20}$	0.55
706-1097	3097	$4_5^+$ - $4_1^+$ - $2_1^+$	+0.23	+0.0026	$-0.13_{-0.18}^{+0.12}$	0.71
819-1294	2112	$2_2^+$ - $2_1^+$ - $0_1^+$	+0.31	+0.25	$-1.83(8)$	1.43
931-1294	2225	$2_3^+$ - $2_1^+$ - $0_1^+$	-0.31	+0.25	$+1.75_{-0.47}^{+0.74}$	1.87
973-1294	2266	$3_1^-$ - $2_1^+$ - $0_1^+$	-0.058	-0.000023	$+0.02(6)$	1.60
245-1507	3046	$4_4^+$ - $4_3^+$ - $2_1^+$	+0.20	+0.067	$-0.89_{-0.45}^{+0.51}$	0.34

The first cascade measured was the 819-1294 cascade, originating from the 2112 keV  $2_2^+$  level, passing through the 1294 keV  $2_1^+$  level and ending at the  $0_1^+$  ground state. The 1294 keV transition is a pure  $E2$  transition. The 819 keV  $2_2^+ \rightarrow 2_1^+$  transition, however, has been established to be a mixed  $E2/M1$  transition, with a value of  $\delta = -1.8(2)$

[55]. As such, this provided a good benchmark to demonstrate the validity of the method employed in this work to obtain  $\delta$  values (extracting  $\delta$  and the corresponding  $A_{22}$  and  $A_{44}$  coefficients), and comparing the results to fitting  $W(\theta)$  data points to Legendre polynomials using LEGFT [144], which extracts  $A_{22}$  and  $A_{44}$  from which the corresponding value of  $\delta$  is obtained.

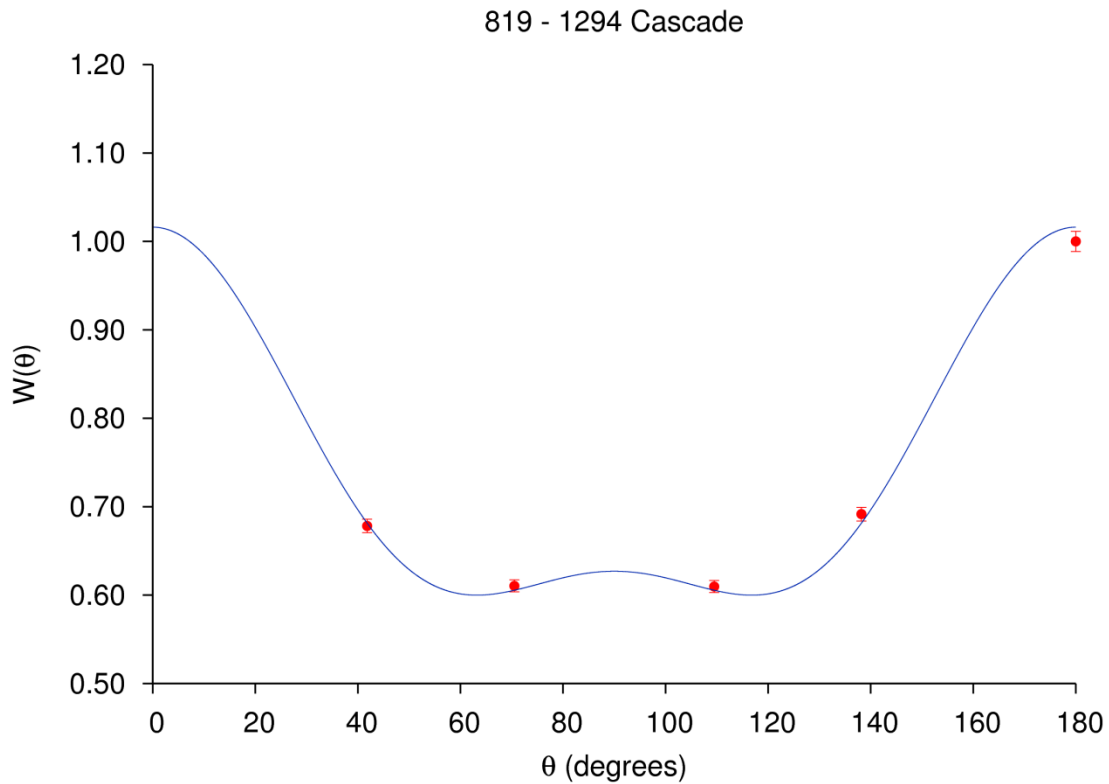


**Figure 70.** Plot of the efficiency-corrected angular correlation of the  $2_2^+ - 2_1^+ - 0_1^+$  cascade. The minimum  $\chi^2/\nu$  of this fit was 1.43, and yielded  $\delta = -1.83(8)$ , corresponding to  $A_{22} = +0.31$  and  $A_{44} = +0.25$ .

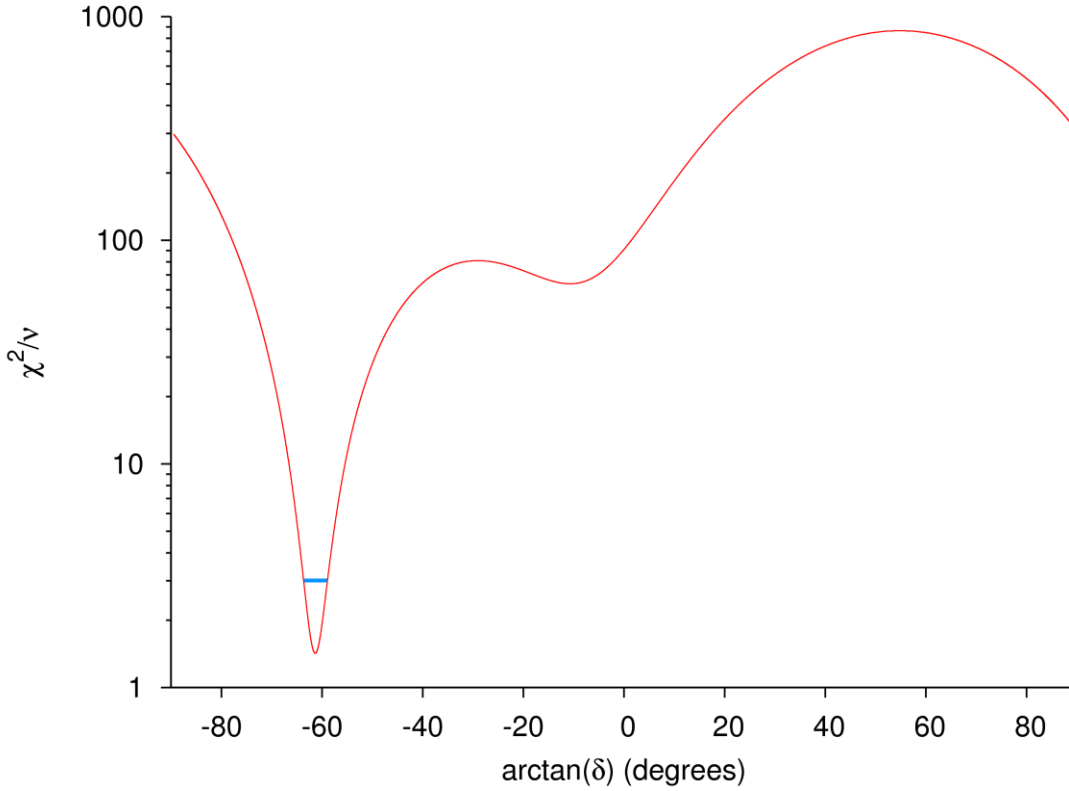


**Figure 71.** Plot of  $\chi^2/\nu$  as a function of  $\arctan(\delta)$  in degrees for the 819-1294 cascade. The blue bar indicates the uncertainty limits at  $\chi^2 + 1$ .

The resulting analysis of the angular correlation of the 819-1294 cascade (Figure 70 and Figure 71) yielded a value of  $\delta = -1.83(8)$ , corresponding to  $A_{22} = +0.31$  and  $A_{44} = +0.25$ . The method of Arns and Wiedenbeck was used here to double check the validity of the measurement (see Appendix I). To do this, the program LEGFT [144] was used to fit the data points in Figure 70, obtaining  $A_{22} = +0.304(12)$  and  $A_{44} = +0.226(14)$ , corresponding to  $\delta = -1.76(11)$ . The agreement of the two different methods of obtaining  $\delta$  values for this cascade indicates that for other angular correlations the values reported in Table 14 are correct. In addition, as the present measurement of  $\delta$  is consistent with that obtained by Yamaguchi *et al.* [57], it is also consistent with the negligible  $E0$  component  $\mu_K \leq 6.1 \times 10^{-4}$  reported in that work, as a re-computation of  $\mu_K$  via Equation (55) in the present work yields an upper limit of  $2.2 \times 10^{-4}$ .

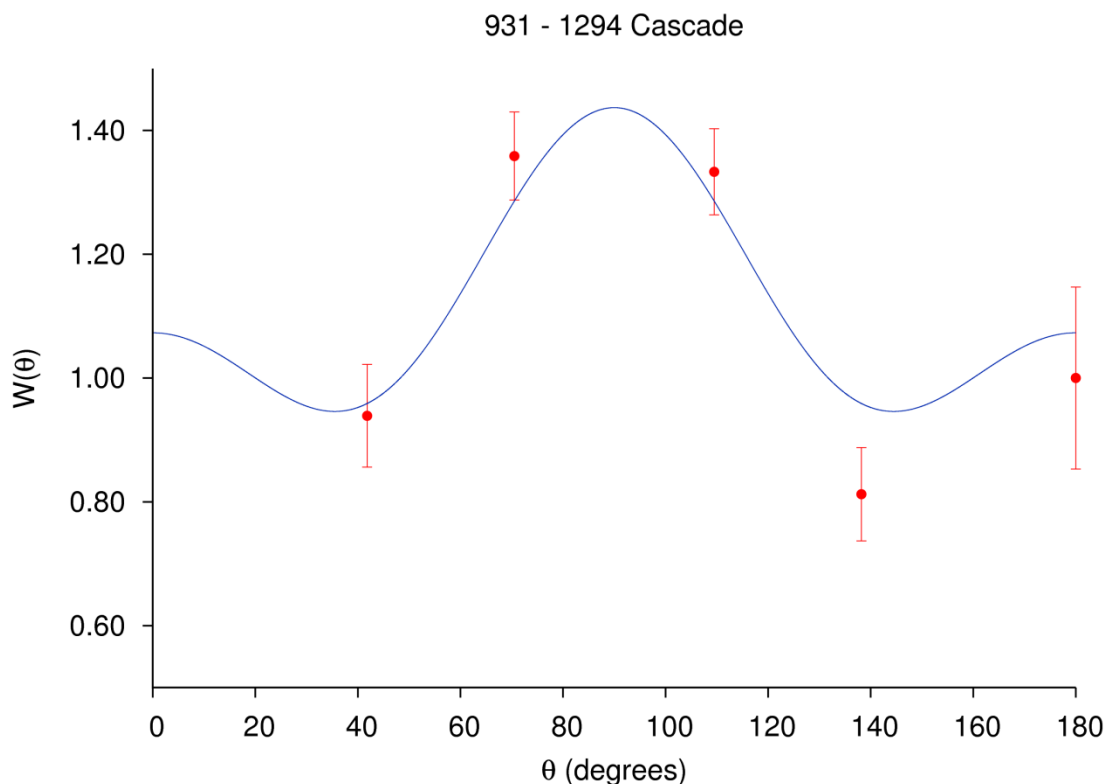


**Figure 72.** Plot of the efficiency-corrected angular correlation of the  $2_3^+ - 2_1^+ - 0_1^+$  cascade. The minimum  $\chi^2/\nu$  of this fit was 1.87, and yielded  $\delta = +1.75_{-0.47}^{+0.74}$ , corresponding to  $A_{22} = -0.31$  and  $A_{44} = +0.25$ .

The next re-measurement was for the 931-1294 cascade (Figure 72 and Figure 73), originating from the 2225 keV  $2_3^+$  level, passing through the 1294 keV  $2_1^+$  level and ending at the  $0_1^+$  ground state. The value of  $\delta$  for the 931-1294 cascade was measured previously by Kantele *et al.* [93], yielding  $A_2 = -0.31(2)$  and  $A_4 = +0.37(4)$  (equivalent, respectively, to  $A_{22}$  and  $A_{44}$  in this work), yielding  $\delta = -1.9_{-0.7}^{+0.5}$ , the sign indicated to be in the Krane & Steffen convention. However, the measurement reported here,  $\delta = +1.75_{-0.47}^{+0.74}$  (corresponding to  $A_{22} = -0.31$  and  $A_{44} = +0.25$ ), conflicts with the previously reported value of  $\delta$ . Upon substituting the reported values of  $A_2$  and  $A_4$  from Kantele *et al.* into the quadratic in  $\delta$  formed from combining Equations (53) and (54), the value which results is  $+1.9_{-0.5}^{+0.7}$  in the Krane & Steffen convention, consistent with the measurement reported here. This is further confirmed by the experiment of Urban *et al.* [149], reporting  $\delta = +3.44(40)$  having the smallest  $\chi^2/\nu$  from their measurements.

As with the 819 keV transition, it is possible to obtain an  $E0$  component for the 931 keV transition. From the values of  $\delta$  and  $\alpha_K$  reported in the present work, the resulting  $\mu_K \leq 1.8 \times 10^{-3}$ , a negligible value. This is consistent with the sizable uncertainty in the experimental  $\alpha_K$  value, such that the lower limit of 0.0012 is consistent with the previous literature as well as the pure  $E2$  limit.

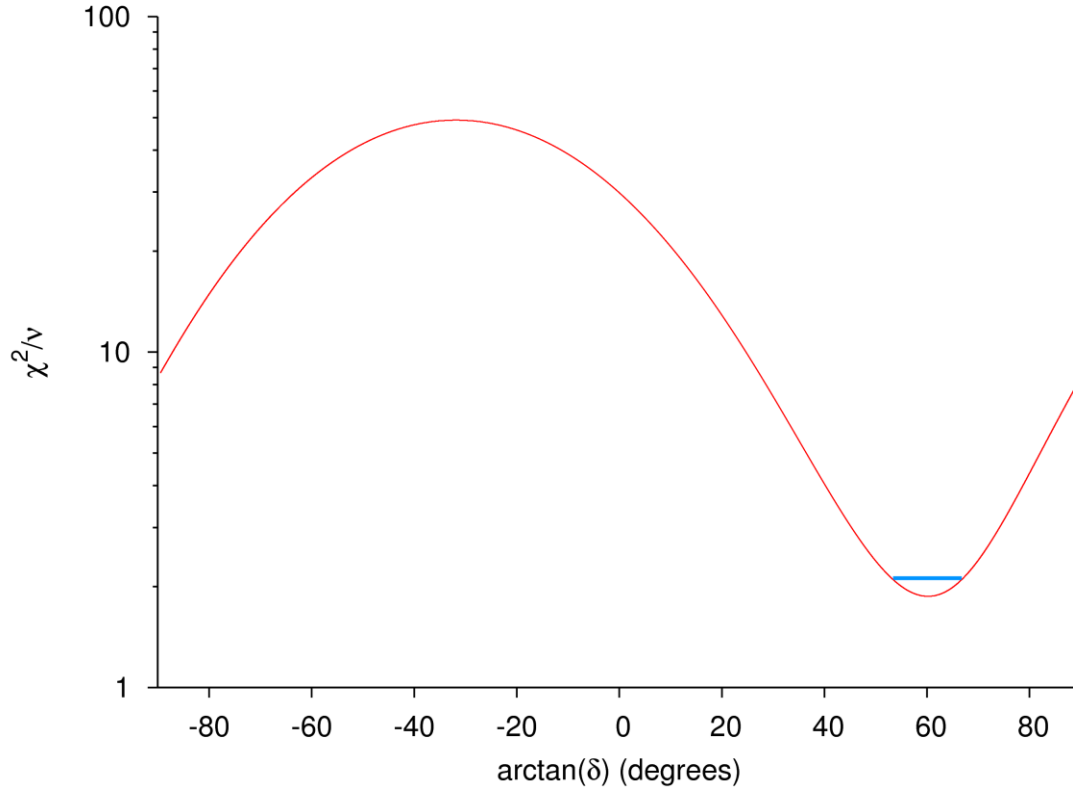


**Figure 73.** Plot of  $\chi^2/\nu$  as a function of  $\arctan(\delta)$  in degrees for the 931-1294 cascade. The blue bar indicates the uncertainty limits at  $\chi^2 + 1$ .

Another re-measurement checked the  $E1$  assignment of the 973 keV transition, originating from the 2266 keV  $3_1^-$  level, passing through the 1294 keV  $2_1^+$  level and ending at the  $0_1^+$  ground state. The  $E1$  assignment was given on the basis of conversion-electron spectroscopy [76,88,98]; here, an  $M2$  component may compete with the  $E1$  component. Since  $L' = 1$  and  $L = 2$  the mixing ratio  $\delta$  is expressed in terms of  $E1/M2$  mixing so that  $\delta = 0$  is pure  $E1$ .

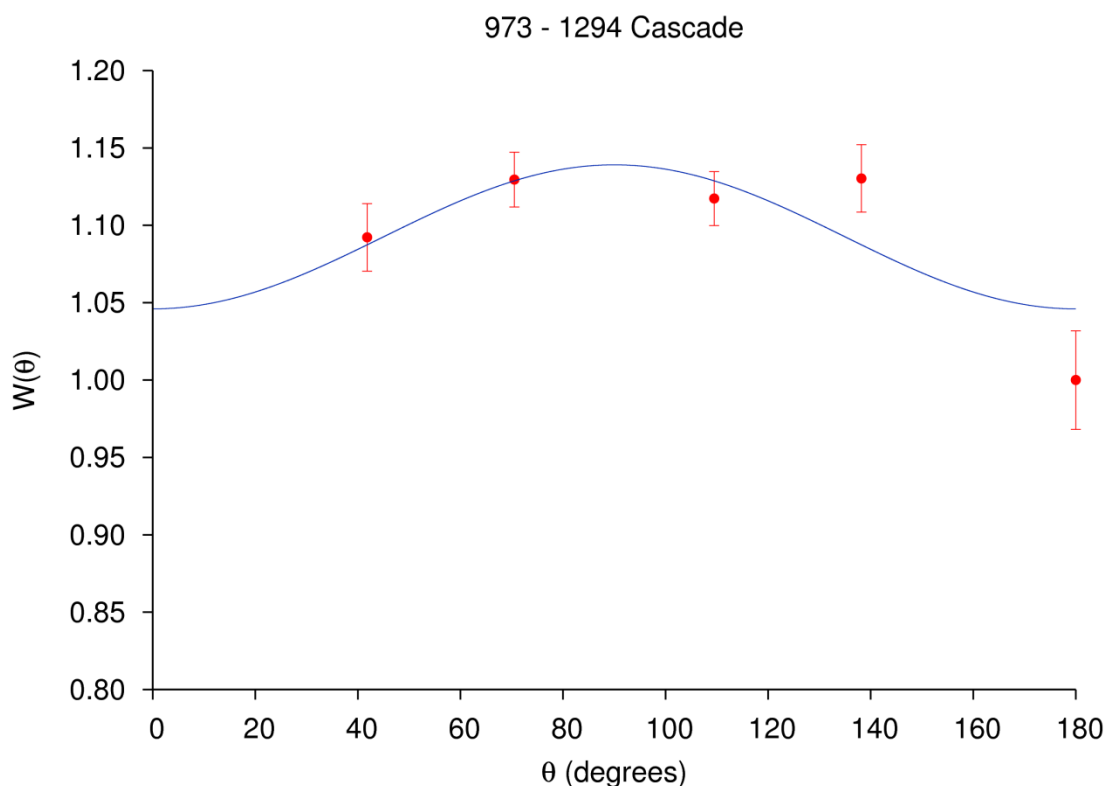


**Figure 74.** Plot of the efficiency-corrected angular correlation of the  $3_1^- - 2_1^+ - 0_1^+$  cascade. The minimum  $\chi^2/\nu$  of this fit was 1.60, and yielded  $\delta = +0.02(6)$ , corresponding to  $A_{22} = -0.058$  and  $A_{44} = -0.000023$ .

For the 973-1294 cascade, Figure 75 shows that there are two possible values of  $\delta$  consistent with the angular correlation in Figure 74. One of the values,  $\delta = +0.02(6)$  ( $\chi^2/\nu = 1.60$ ), is equivalent to  $\sim 99.9\%$   $E1$  character, and the other value  $\delta = +4.81(6)$  ( $\chi^2/\nu = 0.62$ ) is equivalent to  $\sim 95.8\%$   $M2$  character. Arguably the value with the lower  $\chi^2/\nu$ , corresponding to the  $M2$  assignment, should be chosen. However, as noted by Schmelzenbach and Loats, there can be cases where two  $\chi^2/\nu$  minima will be clearly identifiable, yet for physical reasons the minimum with the higher  $\chi^2/\nu$  value should be chosen [47,48]. This is the case here, based both on previous assignments of this transition and also the fact that electromagnetic theory predicts a  $10^5$  larger  $E1$  decay rate compared to the  $M2$  decay rate, so that a nearly-pure  $M2$  973 keV transition is unlikely.

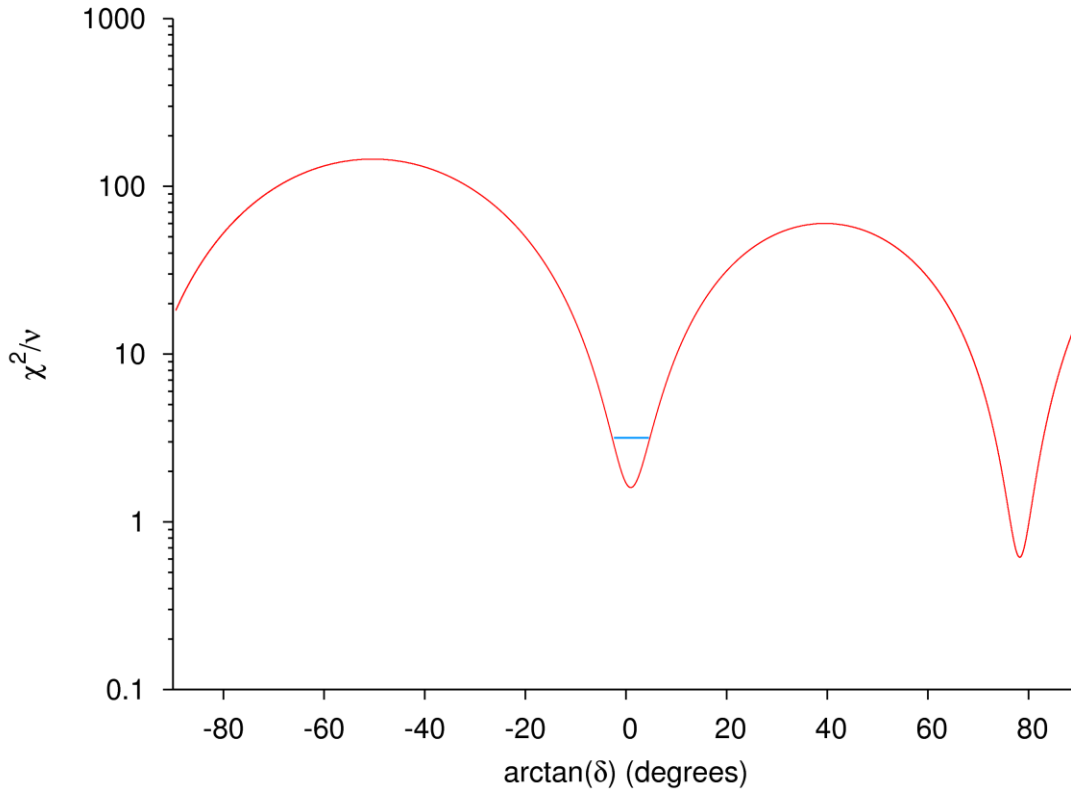


**Figure 75.** Plot of  $\chi^2/\nu$  as a function of  $\arctan(\delta)$  in degrees for the 973-1294 cascade. The blue bar indicates the uncertainty limits for the chosen value of  $\delta$ .

Turning to transitions among the  $4^+$  states, the first mixing ratio measured was for the  $4_2^+ \rightarrow 4_1^+$  138 keV transition in  $^{116}\text{Sn}$ , which is part of the 138-1097 cascade, originating at the 2529 keV  $4_2^+$  level, passing through the 2391 keV  $4_1^+$  level, and ending at the  $2_1^+$  1294 keV state. This transition has only been measured once previously by Bron *et al.*, yielding  $A_2 = 0.20(7)$  and  $A_4 = -0.10(11)$  [88]; no mixing ratio was obtained (the  $A_k$  coefficients yield an unphysical value for  $\delta$ ). In previous conversion-electron spectroscopy measurements, it was assigned a multipolarity of pure  $MI$ , primarily due to large experimental uncertainties in past measurements. The  $\sim 5\%$  relative uncertainty in the present work  $\alpha_K = 0.215(13)$  is low enough to give confidence that a possible  $E0$  component may be present in addition to the  $E2$  component.

The resulting angular correlation and measurement of  $\delta$  for the 138 keV transition (Figure 76 and Figure 77) yielded  $\delta = -0.13(8)$ , corresponding to  $A_{22} = +0.23$  and  $A_{44} =$

+0.0026. This is consistent with the measured K/L ratio in Table 8, which indicates a multipolarity of close to pure  $M1$ ; there is only  $1.7_{-1.4}^{+2.6}\%$   $E2$  character as computed from Equation (51a). The resulting  $\mu_K = 0.95_{-0.95}^{+6.52}$  from Equation (55). The corresponding  $X$ -value, from Equation (56), is  $0.049_{-0.049}^{+0.339}$ . Turning to the  $E0$  strengths which can be deduced from  $X$  via Equation (57), the lower limit of  $\mu_K$  is consistent with  $\rho^2(E0) \times 10^3 = 0$ . However, the central value and upper limit on  $\mu_K$  can give an idea as to the expected magnitude of the  $E0$  strength, assuming that the half-life of the 2529 keV  $4_2^+$  state is 100 ps.

**Table 15.** For each row, the mixing ratio consistent with the associated absolute  $B(E2)$  value,  $\mu_K$  and  $X$  is given, yielding the  $E0$  strength in the final column for those values.

$\delta$	$B(E2)$ [W.u.]	$\mu_K$	$X$	$\rho^2(E0) \times 10^3$
-0.13	6.37	0.95	0.049	8.97
-0.05	0.95	7.47	0.388	10.6

Table 15 gives the values of  $\delta$  consistent with the absolute  $B(E2)$  values,  $\mu_K$  and  $X$  for both the central value of  $\mu_K$  and also at the upper limit of  $\mu_K$ . The resulting deduced  $E0$  strengths are realistic possible nonzero lower limits, consistent with the half-life of the 2529 keV state being potentially smaller than 100 ps, and with realistic maximum values for  $E0$  strengths being on the order of  $\rho^2(E0) \times 10^3 \approx 10^2$  [28].

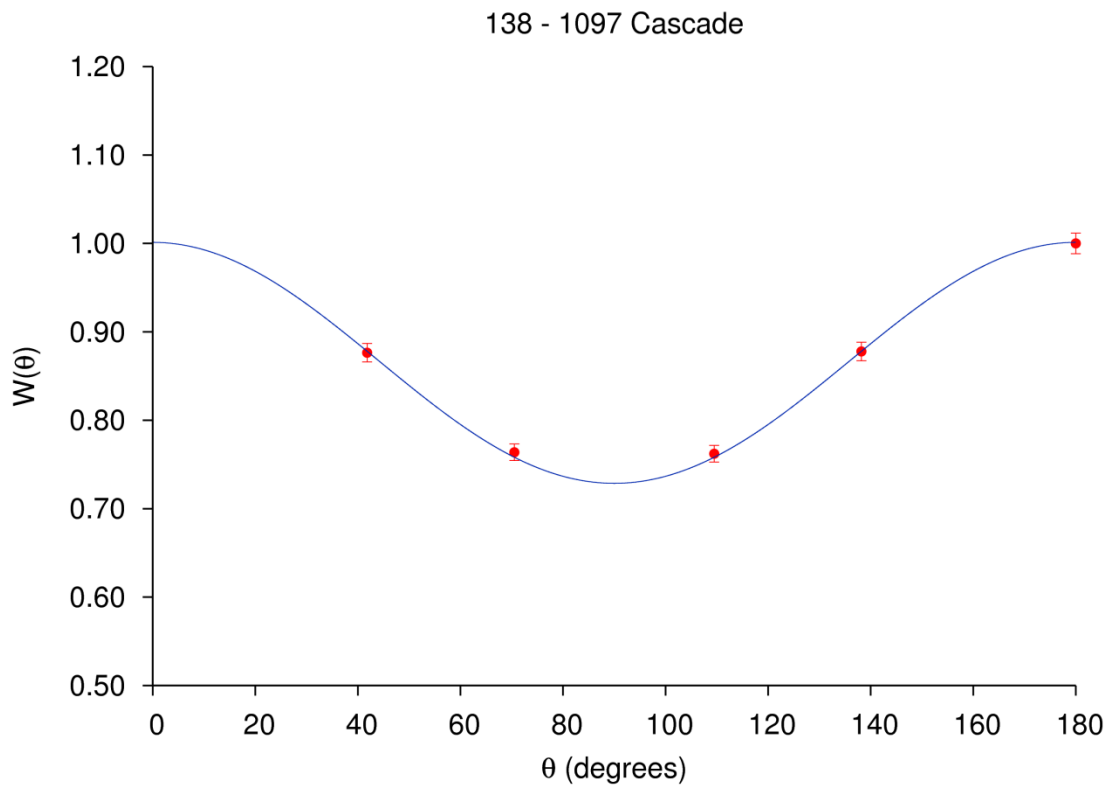


**Figure 76.** Plot of the efficiency-corrected angular correlation of the  $4_2^+ - 4_1^+ - 2_1^+$  cascade. The minimum  $\chi^2/\nu$  of this fit was 0.10, and yielded  $\delta = -0.13(8)$ , corresponding to  $A_{22} = +0.23$  and  $A_{44} = +0.0026$ .

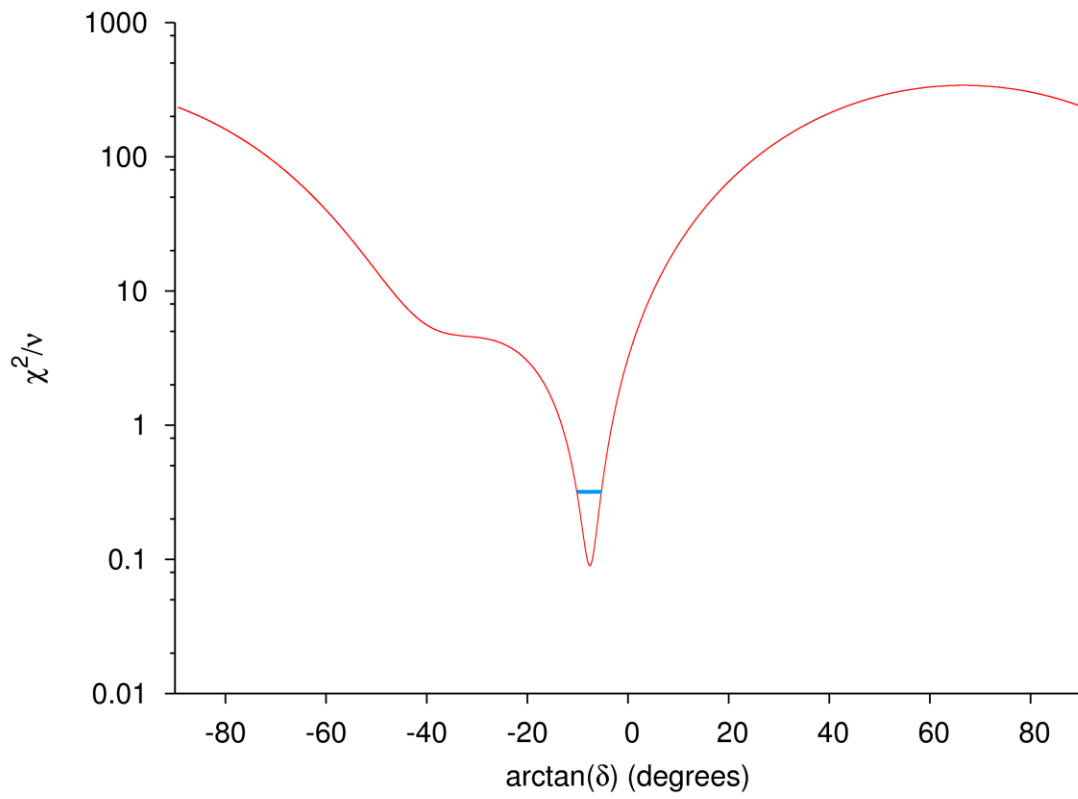


**Figure 77.** Plot of  $\chi^2/\nu$  as a function of  $\arctan(\delta)$  in degrees for the 138-1097 cascade. The blue bar indicates the uncertainty limits at  $\chi^2 + 1$ .

## Chapter 7. Discussion

The comprehensive review of the level energies in  $^{116}\text{Sn}$  below 4.3 MeV by Raman *et al.* [84] characterized them in terms of proton 2p-2h excitations, phonon states, and broken-pair states; in doing so the level energies could be reasonably well-reproduced, although there was no investigation of spectroscopic data such as  $B(E2)$  values or mixing ratios. The theoretical work on  $^{116}\text{Sn}$  is comparatively sparse; comprehensive attempts to describe the wavefunctions of the ground and excited states in  $^{116}\text{Sn}$  are essentially restricted to four works: Wenes *et al.* [104], Song *et al.* [108], Chen *et al.* [109], and Guazzoni *et al.* [90]. Only the first three of these attempted to predict  $B(E2)$  values (refer to Section 4.2) from  $4^+$  to  $2^+$  states. Furthermore, the works of Song *et al.* and Chen *et al.* were unable to shed light on discrepancies in predicted versus experimental  $B(E2)$  values first brought up in Wenes *et al.*, indicating that the models of  $^{116}\text{Sn}$  must be improved, in part through improved data for comparison to predictions.

In the present work, deduced relative  $E2$  and  $MI$  transition strengths will be used to suggest possible wavefunction components in the  $2_{2-4}^+$  and  $4_{1-5}^+$  states. The absolute  $B(E2)$  and  $B(M1)$  values given in Appendix C have fairly large uncertainties, especially for transitions out of the higher-lying  $4^+$  states, and so they are not as insightful in terms of qualitatively discussing the possible wavefunction admixtures present in those states. In addition, the open questions about the  $2^+$  and  $4^+$  states raised in Section 4.7 can be addressed with the new information presented in this thesis.



distributions that do not overlap well, explaining the lack of mixing of the 2112 keV and 2225 keV states.

A related aspect to probing the character of the 2225 keV  $2_3^+$  state in particular is that the  $B(E2)$  value of the 931 keV  $2_3^+ \rightarrow 2_1^+$  transition is 5(3) W.u., which suggests that this state is not part of the two-phonon triplet. This will be discussed further in the answer to Question 2 in the next section.

### 7.1.2. The 2650 keV $2_4^+$ Level

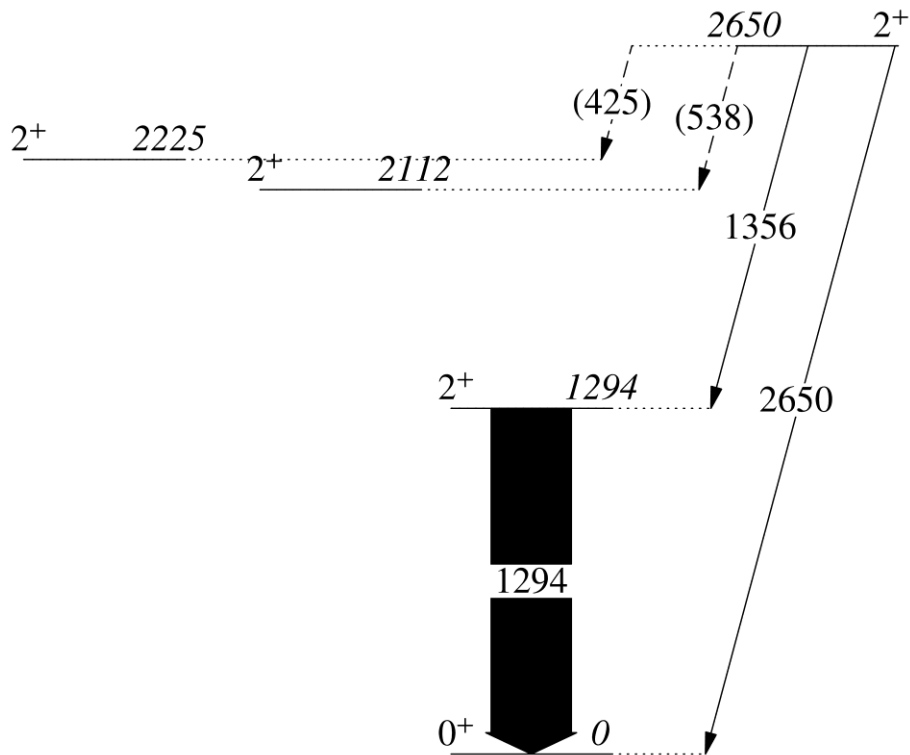


**Figure 79.** Selected transitions de-exciting the 2650 keV  $2_4^+$  state are shown, adapted from Figure 26. Transitions indicated by parentheses have not been observed (see text for more detail).

The  $2_4^+$  level at 2650 keV is reported to decay to the 1294 keV  $2_1^+$  and 2112 keV  $2_2^+$  levels with transitions of 1356 and 538 keV, respectively [55] (refer to Figure 79). However, the  $\gamma$ - $\gamma$  coincidence analysis by Pore *et al.* [102,103] has not confirmed the existence of the 538 keV transition, indicating that there may be very weak mixing

between the  $2_4^+$  and lower-lying  $2^+$  states. It is possible that this state contains two-phonon character not found in the  $2_2^+$  or  $2_3^+$  levels, which leads naturally to addressing the second open question.

**Question 2:** Consequently, is the phonon  $E2$  strength actually spread out across the  $2_2^+$ ,  $2_3^+$  and  $2_4^+$  states, or does another explanation exist which better rationalizes the discrepancy between the experimental  $B(E2)$  values and vibrational model predictions?

**Answer 2:** In the modified phonon model by Heyde *et al.* incorporating intruder-phonon mixing [116] (briefly discussed in Section 4.5) the  $E2$  strength normally concentrated in one  $2^+$  (2-phonon)  $\rightarrow 2^+$  (1-phonon) transition is divided among multiple  $2^+ \rightarrow 2^+$  (1-phonon) transitions. As a result, the  $B(E2)$  values of the multiple allowed transitions can be added together to satisfy the proportionality of the  $B(E2)$  strength according to the vibrational model as discussed in Section 1.2.3.

However, intruder-phonon mixing depends on mixing of at least two of the higher-lying  $2^+$  states, and as established in the previous section, a strong argument can be made that the differing underlying configurations of the  $2_2^+$  and  $2_3^+$  states prevents mixing between them. Further arguing against the applicability of intruder-phonon mixing is that the 538 keV  $2_4^+ \rightarrow 2_2^+$  transition was not confirmed by Pore *et al.* [103], and the 425 keV  $2_4^+ \rightarrow 2_3^+$  transition has been observed neither in the literature nor by Pore *et al.*. As such, one final possibility is that the  $2_4^+$  state alone contains all the two-phonon character, and the experimental  $B(E2)$  values for the 931 keV  $2_3^+ \rightarrow 2_1^+$  and 819 keV  $2_2^+ \rightarrow 2_1^+$  transitions would be explained by non-phonon wavefunction components in the initial states.

The 1356 keV  $2_4^+ \rightarrow 2_1^+$  transition is very weak and had poor statistics in the angle matrices created in the present work, so it was not possible to extract the mixing ratio which would give the percentage of  $E2$  character; a large  $E2$  component would be suggestive of a  $B(E2)$  value consistent with the phonon model. As the  $2_4^+$  state half-life is not well-known (Section 4.3), the uncertainty in its absolute  $B(E2)$  is substantial with an

upper limit of  $\sim 10$  W.u. (assuming a pure  $E2$  transition). Based on the systematics of  $^{116}\text{Sn}$  compared to  $^{118}\text{Sn}$ , this value is consistent with the equivalent  $2_4^+ \rightarrow 2_1^+$  transition in that nucleus with a  $B(E2)$  value of 22(10) W.u. [150], although it falls short of the predicted  $B(E2)$  value of 24.8 W.u. for  $^{116}\text{Sn}$ .

However even if the  $2_4^+$  state were to carry all the two-phonon character and the  $B(E2)$  value of the 1356 keV  $2_4^+ \rightarrow 2_1^+$  transition were to be  $\sim 22$ -25 W.u., arguing strongly against the phonon model's applicability is that the 734 keV  $0_3^+ \rightarrow 2_1^+$  transition has an absolute  $B(E2) = 0.49(7)$  W.u., which is significantly smaller than the vibrational model prediction of 24.8 W.u.. Therefore it is more likely that alternative explanations exist for the absolute  $B(E2)$  values measured for  $^{116}\text{Sn}$  among its low-lying  $2^+$  states, and that the wavefunction component for the  $2_4^+$  state is based on neutron broken-pair configurations of the form  $(3s_{1/2})^{-1}(2d_{5/2})$  or  $(2d_{5/2})^{-1}(3s_{1/2})$  [89], depending on which orbital is lower in energy.

It is clear that with respect to the  $2_2^+$ ,  $2_3^+$ , and  $2_4^+$  states in  $^{116}\text{Sn}$ , the experimental  $B(E2)$  values cannot be combined together according to the intruder-phonon mixing model to reproduce the predicted  $B(E2)$  value of the vibrational model, and the vibrational model's applicability itself is open to question, as with the cadmium isotopes. Additionally, the opposite signs of the mixing ratios of the 931 and 819 keV transitions reflect the underlying differences in the character of the  $2_2^+$  and  $2_3^+$  states.

## 7.2. The $4^+$ States

The low-lying  $4^+$  states in  $^{116}\text{Sn}$  can be discussed as a group, due to the high degree of mixing suggested by the fragmentation of the  $L = 4$  strength in the  $(p,p')$  work of Wienke *et al.* [83], indicating that the  $4^+$  states share similar neutron broken-pair components in their wavefunctions (refer to Section 4.4 for more detail regarding existing interpretations in the literature), which can be described as  $\nu(1g_{7/2})^{-1}(3s_{1/2})$ .

### 7.2.1. The 2391, 2529, 2801, 3046 and 3097 keV $4_{1-5}^+$ Levels

To further probe the mixing of the  $4_{1-5}^+$  states, the mixing ratios measured in the present work (Table 14) can be used along with gamma ray intensities (Appendix B) to examine their decay patterns (refer to Figure 80 for a partial level scheme). Ideally, absolute transition probabilities would be used to do this. However, the sizable uncertainties in the absolute  $B(M1)$  and absolute  $B(E2)$  values in Appendix C prevent using these values to make substantive arguments about the character of the  $4_{1-5}^+$  states.

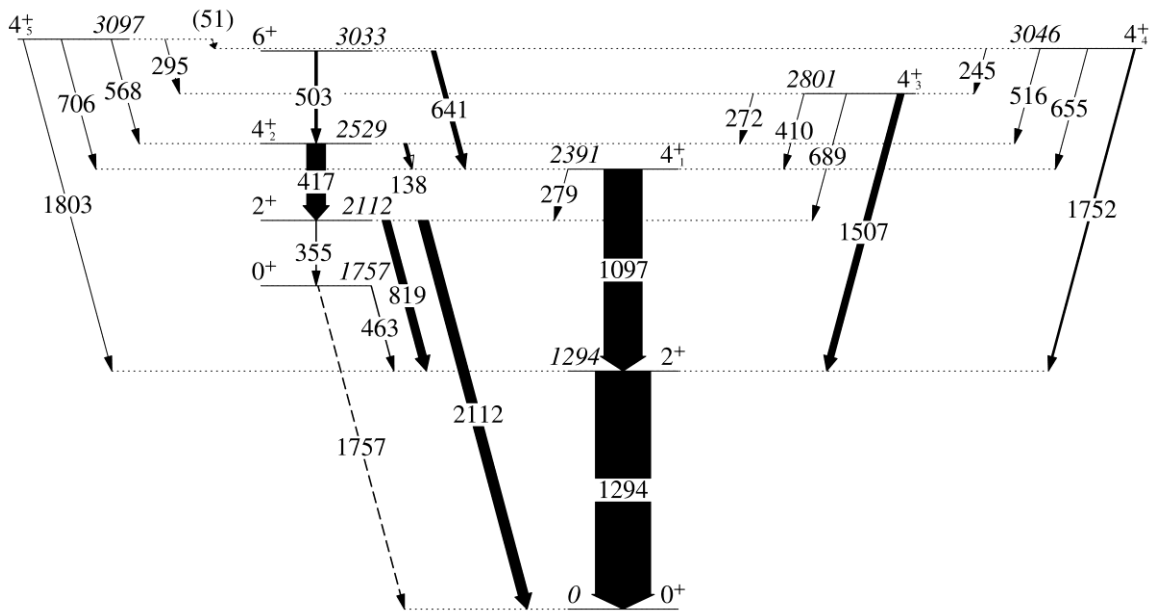


**Figure 80.** Partial level scheme showing the  $4_{1-5}^+$  states as well as the 3033 keV  $6^+$  state, and selected transitions to lower-lying states. Arrow widths are proportional to gamma-ray relative intensities ( $I_\gamma(1294) = 100$ ).

Therefore, relative  $MI$  strengths between the  $4^+$  states can be computed based on the gamma ray intensities, and they are particularly convenient because they can convey information about the similarities or differences of transitions de-exciting a given state. Equation (76) expresses relative  $MI$  strengths as a ratio with respect to a normalization (a chosen benchmark decay from a state),

$$\frac{B(M1)}{B(M1)_{\text{nomm}}} = \frac{(3.181 \times 10^{-14}) (\text{B.R.}) \frac{\ln 2}{t_{1/2} E_\gamma^3} \left( \frac{1}{1 + \delta^2} \right)}{(3.181 \times 10^{-14}) (\text{B.R.}) \frac{\ln 2}{(E_\gamma^3)_{\text{nomm}}} \left( \frac{1}{1 + \delta_{\text{nomm}}^2} \right)} = \frac{\left( \text{B.R.} / E_\gamma^3 \right) \left( \frac{1}{1 + \delta^2} \right)}{\left( \text{B.R.} / (E_\gamma^3)_{\text{nomm}} \right) \left( \frac{1}{1 + \delta_{\text{nomm}}^2} \right)} \quad (76)$$

Thus, the relative magnitude of the  $MI$  strengths of multiple mixed-multipolarity transitions out of the same state with respect to one another is a probe of how similar the wavefunctions of the connected states are. It should be cautioned that *quantitatively* comparing relative transition strengths in this way is only strictly applicable for analyzing transitions de-exciting the same state. Qualitatively, however, it may be possible to make arguments about the corresponding wavefunction overlaps when comparing decays from different states.

**Table 16.** Relative  $B(MI)$  values for transitions among the  $4^+$  states, based on gamma ray intensities computed by Pore *et al.* (see Appendix B), and mixing ratios from this work. The largest relative  $B(MI)$  exiting each level is normalized to 100. Transitions marked with an asterisk are assumed to be pure  $MI$ . The 51 keV transition was not observed in the present work but is included for completeness.

$E_{\text{level}}$ (keV)	$E_\gamma$ (keV)	$I_\gamma$	$I_{\text{initial}}^\pi$	$I_{\text{final}}^\pi$	Relative $B(MI)$ value
2529	138	4.63(11)	$4_2^+$	$4_1^+$	$100_{-2.6}^{+1.5}$
2801	410	0.0735(26)	$4_3^+$	$4_1^+$	$96.0_{-25.0}^{+3.0}$
	272	0.0404(13)		$4_2^+$	$100_{-35.2}^{+86.5}$
3046	655	0.141(4)	$4_4^+$	$4_1^+$	$34.4_{-4.1}^{+2.2}$
	517*	0.0189(18)		$4_2^+$	$10.0_{-1.0}^{+1.0}$
	245	0.0360(12)		$4_3^+$	$100_{-35.9}^{+56.6}$
3097	706	0.187(5)	$4_5^+$	$4_1^+$	$100_{-7.3}^{+1.7}$
	568	0.0522(21)		$4_2^+$	$31_{-10.3}^{+22.4}$
	295*	0.00750(66)		$4_3^+$	$56_{-4.9}^{+4.9}$
	(51)	—		$4_4^+$	—

All the relative  $MI$  strengths that could be computed, with uncertainties generally dominated by the experimental mixing ratios, are of a similar order of magnitude for transitions out of any given state in Table 16. These results confirm the high degree of mixing among the  $4_{1-4}^+$  states, in accordance with transfer-reaction and proton-scattering data [83,89]. Most notable is that transitions which decay from the 3097 keV  $4_5^+$  state, not accessed in  $(p,p')$ , show similar relative  $B(MI)$  behaviors as the lower-lying  $4^+$  states, with the 568 keV  $4_5^+ \rightarrow 4_2^+$  transition being the weakest with  $\sim 30\%$  of the  $MI$  strength of the 706 keV  $4_5^+ \rightarrow 4_1^+$  transition (the 51 keV  $4_5^+ \rightarrow 4_4^+$  transition could not be observed due to experimental limitations in both the  $\gamma\text{-}\gamma$  and  $\gamma\text{-}e^-$  data sets). This behavior indicates that it is highly-mixed with the lower-lying  $4_{1-4}^+$  states.

It is also possible to determine relative  $E2$  strengths (Table 17) of transitions from the  $4_{1-5}^+$  states into lower-lying  $2^+$  states in a similar way to Equation (76), cancelling out half-lives and leaving the gamma ray intensity along with the fifth power of the transition energy and the  $E2$  mixing ratio factor. The resulting relative  $MI$  and  $E2$  strengths will be used to address the open questions regarding the  $4^+$  states, brought up in Section 4.7.

**Table 17.** Relative  $B(E2)$  values for transitions to  $2^+$  states, based on gamma ray intensities computed by Pore *et al.* (see Appendix B). The largest relative  $B(E2)$  exiting each level is normalized to 100. Gamma rays in parentheses were not found in the level scheme but are included to illustrate the differences in decay patterns.

$E_{\text{level}}$ (keV)	$E_{\gamma}$ (keV)	$I_{\gamma}$	$I^{\pi}_{\text{initial}}$	$I^{\pi}_{\text{final}}$	Relative $B(E2)$ value
2391	1097	69.2(8)	$4_1^+$	$2_1^+$	42.2(5)
	279	0.158(5)		$2_2^+$	91(3)
	166	<0.013		$2_3^+$	<100
2529	1236	0.0683(36)	$4_2^+$	$2_1^+$	0.00089(5)
	417	33.7(10)		$2_2^+$	100(3)
	304	0.142(3)		$2_3^+$	2.05(4)
2801	1507	11.7(3)	$4_3^+$	$2_1^+$	100(3)
	689	0.208(7)		$2_2^+$	90(3)
	(576)	—		$2_3^+$	—
	(151)	—		$2_4^+$	—
3046	1752	2.79(7)	$4_4^+$	$2_1^+$	26.4(7)
	(934)	—		$2_2^+$	—
	(821)	—		$2_3^+$	—
	396	0.00620(33)		$2_4^+$	100(5)
3097	1803	<0.00545	$4_5^+$	$2_1^+$	<0.333
	(985)	—		$2_2^+$	—
	871	0.00609(44)		$2_3^+$	14(1)
	447	0.00153(15)		$2_4^+$	100(10)

**Question 1:** Given the very intense apparently pure  $MI$   $4_2^+ \rightarrow 4_1^+$  138 keV transition, how do the 2529 keV  $4_2^+$  and 2391 keV  $4_1^+$  states mix amid the clear evidence of intruder-yrast mixing between the 2p-2h and ground state bands?

**Answer 1:** There are several ways to probe the intruder-yrast mixing. The  $E2$  and  $MI$  relative strengths reported above, as well as other obtained spectroscopic data either

from the present work in this thesis, or previously reported in the literature, all combine to help give a better understanding of the mixing.

As discussed in Section 4.4, Raman *et al.* [84] particularly based their conclusions regarding the structure of the  $4^+$  states on the experimental work by Wienke *et al.* [83]. Consequently, the 2391 keV  $4_1^+$  state was assigned to be the  $4^+$  member of the two-phonon triplet (albeit sharing phonon character with the 2801 keV  $4_3^+$  state), with predominant neutron character of seniority  $\nu = 2$ . The 2529 keV  $4_2^+$  state, however, was assigned proton 2p-2h character, supported by experiments that populated the collective quasirotational band in  $^{116}\text{Sn}$  [88,99]. However, the  $(p,p')$  experiment performed by Wienke *et al.*, although not sensitive to rotational components, reported an  $L = 4$  strength fragmentation that included the 2529 keV  $4_2^+$  state. This implies that a wavefunction component of the 2529 keV  $4_2^+$  state includes a neutron broken-pair admixture similar in character to that of the 2391 keV  $4_1^+$  state.

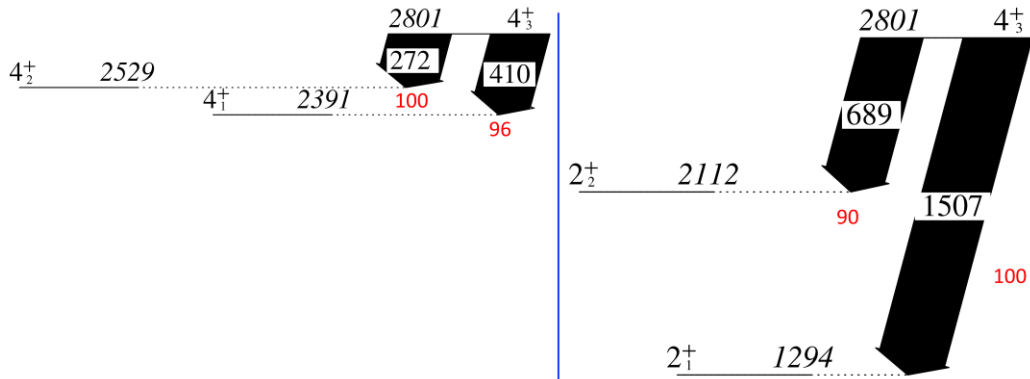


**Figure 81.** The decays of the 2801 keV state, with transitions to the lower-lying  $4_{1,2}^+$  states on the left and to the  $2_{1,2}^+$  states on the right, with corresponding central values of the relative  $MI$  and  $E2$  strengths in red text (arrow widths are proportional to these values).

There is further evidence from the work in this thesis that supports the above inference. The 2801 keV  $4_3^+$  state, in de-exciting to the 2112 keV  $2_2^+$  2p-2h state and the 1294 keV  $2_1^+$  neutron broken-pair dominant state (Figure 81, right), shows approximately equal  $E2$  strengths for these two transitions. In addition, there are also transitions to the lower-lying proton 2p-2h dominant 2529 keV  $4_2^+$  and neutron broken-pair dominant 2391

keV  $4_1^+$  states (Figure 81, left), which have approximately equal central values for their  $MI$  strengths. Further analysis shows two possible extreme cases for the  $MI$  case:

- The  $4_3^+ \rightarrow 4_1^+$  410 keV transition having about 40% of the  $MI$  strength of the  $4_3^+ \rightarrow 4_2^+$  272 keV transition, or
- Vice versa, the  $4_3^+ \rightarrow 4_2^+$  272 keV transition having about 66% of the  $MI$  strength of the  $4_3^+ \rightarrow 4_1^+$  410 keV transition.

Since these decays show similar relative transition probabilities to states which were assumed to have very different character in the analysis by Raman *et al.* [84], then in combination with the 2529 keV  $4_2^+$  state being included in  $(p,p')$   $L = 4$  strength-fragmentation [83], these results support the suggestion that the 2529 keV  $4_2^+$  state contains a neutron broken-pair admixture and the 2391 keV  $4_1^+$  state contains a 2p-2h admixture.

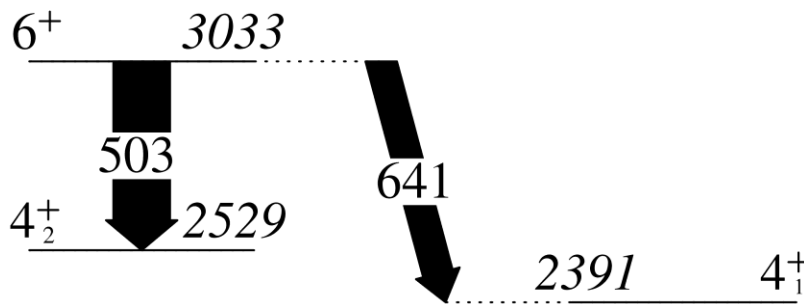


**Figure 82.** The decays of the 3033 keV state. The arrow widths are proportional to the relative  $E2$  transition probabilities ( $B(E2; 503 \text{ keV}) = 100$  [88]).

Another supporting piece of evidence involves the decays of the 3033 keV  $6_1^+$  state (Figure 82). This state has pure proton 2p-2h quasi-rotational [88,99] character based on the cross-section measurements by Guazzoni *et al.* [90]. There are two transitions at 503 keV and 641 keV, with relative  $E2$  strengths in a  $\sim 2:1$  ratio [88], proceeding to the 2529 keV  $4_2^+$  and 2391 keV  $4_1^+$  states, respectively. It is clear from the similar order of magnitude of the relative strengths that the  $4_2^+$  and  $4_1^+$  states share proton 2p-2h character.

The nature of the 2801 keV  $4_3^+$  state can also be elucidated based on the above data. Since the 3033 keV  $6_1^+$  state does *not* de-excite to the 2801 keV  $4_3^+$  state, shared 2p-2h character does not explain the similar  $MI$  and  $E2$  strengths out of the 2801 keV state. Therefore, it must be that the  $4_3^+$  state is a pure neutron broken-pair state, with similar components in the lower-lying  $4_2^+$  and  $4_1^+$  states.

Turning to the possibility of shape coexistence as an aspect of the intruder-yrast mixing, this thesis also established a possible  $E0$  component to the 138 keV transition from the deduced  $\mu_K = 0.95_{-0.95}^{+6.52}$ , for which potentially  $\rho^2(E0) \times 10^3 > 8.97$  at the central value of  $\mu_K$ . The quantitative analysis follows by analogy to the  $0^+$  two-state mixing model developed by Wood *et al.* [28], utilizing mixed wavefunctions as discussed in Section 1.3.1. To start out, the experimental  $4_2^+$  and  $4_1^+$  eigenstates can be expressed as linear combinations of intruder and yrast states, in which the mixing is parameterized by a variable  $a$ .

$$\begin{aligned} |4_1^+\rangle &= a|4_{\text{intruder}}^+\rangle + \sqrt{1-a^2}|4_{\text{yrast}}^+\rangle \\ |4_2^+\rangle &= -\sqrt{1-a^2}|4_{\text{intruder}}^+\rangle + a|4_{\text{yrast}}^+\rangle \end{aligned}$$

The formula developed by Wood *et al.* in the context of this model relates the  $E0$  strength to both the mixing and the difference in nuclear deformation (i.e. the change in shape). If the quadrupole deformations ( $\beta_2$  values) are known, then the mixing parameter  $a$  may be found from Equation (77), which is Equation (51) in Ref. [28],

$$\rho^2(E0) = \left(\frac{3}{4\pi} Z\right)^2 a^2(1-a^2) [\Delta(\beta^2)]^2, \quad (77)$$

where  $\Delta(\beta^2) = (\beta_2)^2(\text{intruder}) - (\beta_2)^2(\text{yrast})$ .

Assuming that the quadrupole deformations<sup>20</sup> obtained from the respective  $2^+ \rightarrow 0^+$  transitions in the intruder and yrast bands are negligibly changed for the  $4^+$  members of each band, then  $((\beta_2)^2)^{1/2} = 0.1118(16)$  for the 2391 keV  $4_1^+$  state [151], and  $((\beta_2)^2)^{1/2} = 0.209(8)$  for the 2529 keV  $4_2^+$  state, based on the  $B(E2)$  value for the 355 keV transition [103]. In applying Equation (77) with the assumption that  $\rho^2(E0) \times 10^3 = 8.97$ , it is found that  $|a| = 0.26$ , implying  $\sim 7\%$  2p-2h intruder character in the 2391 keV  $4_1^+$  state, or conversely  $\sim 7\%$  neutron broken-pair character in the 2529 keV  $4_2^+$  state.

While the above indicates relatively weak mixing of the  $4_2^+$  and  $4_1^+$  states compared to that reported by Pore *et al.* [103], it is not in contradiction since this analysis only quantifies the shape coexistence aspect of the mixing, and is furthermore based on a limit on  $\rho^2(E0)$  from  $\mu_K$ , so the mixing could be possibly stronger than indicated here. Additionally, if the quadrupole deformation of the  $4_1^+$  state were to rise due to a phenomenologically assumed softness in the yrast band of the  $^{116}\text{Sn}$  nucleus [130], it might be closer to  $((\beta_2)^2)^{1/2} \approx 0.14$ , and consequently the mixing parameter  $a$  would be larger.

In conclusion, the intruder-yrast mixing of the 2529 keV  $4_2^+$  and 2391 keV  $4_1^+$  states occurs through shared proton 2p-2h components, shared neutron broken-pair components, and shape coexistence.

**Question 2:** What is the nature of the 3046 keV  $4_4^+$  and 3097 keV  $4_5^+$  states?

**Answer 2:** In analyzing the structure of  $^{116}\text{Sn}$ , in referencing the work of Wienke *et al.*, Raman *et al.* suggested that the  $L = 4$  strength fragmentation in  $(p, p')$  meant that the two-phonon character of a vibrational-model  $4^+$  state was fragmented over the experimentally observed  $4_{1-5}^+$  states [84]. However, it has already been argued that the phonon model is not applicable to the low-lying  $2^+$  states in  $^{116}\text{Sn}$ , requiring revisiting the

---

<sup>20</sup> Since the deformation obtained from  $B(E2)$  data is actually from a square root, it is more correctly expressed as the square root of the expectation value squared.

configuration assignments of the  $4_{1-5}^+$  states, part of which was done in the answer to Question 1.

The similar order of magnitude of the central values of the  $MI$  strengths of the transitions listed in Table 16, in addition to suggesting that the  $4_4^+$  and  $4_5^+$  states are both highly mixed with lower-lying  $4^+$  states, also indirectly qualitatively suggests that these states share similar neutron broken-pair character, and are thus mixed with each other. Supporting this inference is the observation of similar spectroscopic strengths in transfer reactions performed by Schippers *et al.* [89], suggesting similar overlap in entering the neutron  $1g_{7/2}$  orbital from the ground states of  $^{115}\text{Sn}$  or  $^{117}\text{Sn}$ .

In examining the  $E2$  decay patterns in Table 17, it can be seen that both the  $4_{4,5}^+$  states have strongly-preferred decays to the 2650 keV  $2_4^+$  state. The  $2_4^+$  state itself does not decay out to the lower-lying  $4_{1-3}^+$  states. Consequently, the wavefunction admixtures present in the  $4_{4,5}^+$  states likely contain components that overlap with the  $2d_{5/2}$  and/or  $2d_{3/2}$  wavefunction component of the 2650 keV  $2_4^+$  state [89]. Thus, an admixture of  $\nu(1g_{7/2})^{-1}(2d_{5/2})$  could be present in addition to the common  $4^+$  state  $\nu(1g_{7/2})^{-1}(3s_{1/2})$  configuration<sup>21</sup>; alternatively,  $\nu(2d_{5/2})^2$  or  $\nu(2d_{3/2})^2$  components could be present in their wavefunctions.

Further, the different  $E2$  strengths of the  $4_4^+ \rightarrow 2_1^+$  1752 keV and  $4_5^+ \rightarrow 2_1^+$  1803 keV transitions with respect to the  $4_4^+ \rightarrow 2_4^+$  395 keV and  $4_5^+ \rightarrow 2_4^+$  447 keV transitions suggest that the 3046 keV  $4_4^+$  state is probably similar in deformation to the 1294 keV  $2_1^+$  state while the 3097 keV  $4_5^+$  state is not. This is somewhat analogous to how the different charge distributions are reflected in the matrix elements of the transitions that de-excite the 2112 keV  $2_2^+$  and 2225 keV  $2_3^+$  states, albeit with not as profound an effect as to forbid mixing between the  $4^+$  states.

---

<sup>21</sup> Depending on the exact shell-model ordering, the particle-hole configurations might be reversed, but the basic argument is unchanged.

In conclusion, the 3046 keV  $4_4^+$  and 3097 keV  $4_5^+$  states share similar neutron broken-pair character with different admixtures influenced, in particular, by their overlap with lower-lying  $2^+$  states. One remaining aspect which merits further analysis is the very small relative  $B(E2)$  of the 1803 keV  $4_5^+ \rightarrow 2_1^+$  transition, suggesting weakly collective character to this transition. The half-life of the  $4_5^+$  state should be measured in order to obtain absolute  $B(E2)$  data which will help elucidate the nature of this state in particular.

**Question 3:** Is there an alternative explanation to shared phonon character for the existence of multiple  $4^+$  states within an energy range of 800 keV, especially given that the  $0^+$  and  $2^+$  states indicate possible deficiencies in applying the phonon model?

**Answer 3:** This question is not readily answered from the body of current literature, nor from this work. However, the relative  $B(M1)$  and  $B(E2)$  transition probabilities discussed in the previous two questions have shed some light on the possible configurations of the  $4_{1-5}^+$  states. As a result, alternative explanations may come from the incorporation of the new data presented here into theoretical models of  $^{116}\text{Sn}$ .

The analysis by Raman *et al.* [84] showed that neutron broken-pair configurations were a valid description in obtaining reasonable agreement to level energies, and justified from the results reported by Wienke *et al.* [83]. The differences among these states are then attributable to different neutron broken-pair admixtures in combination with the common  $\nu(1g_{7/2})^{-1}(3s_{1/2})$  configuration, or in the case of the 2529 keV  $4_2^+$  and 2391 keV  $4_1^+$  states analyzed in this work, distribution of 2p-2h character as well as shape coexistence. In short, splitting of phonon character is not the only viable explanation, especially given the issues with the phonon selection rules as discussed previously.

Further issues with the applicability of phonon selection rules can be explored qualitatively using Krane's two-state phonon mixing model [29]. This model suggests that observing  $M1$  components of transitions between vibrational states implies that states of predominantly (n)-phonon and (n+1)-phonon character are mixed. Thus, the  $4_1^+$  and  $4_3^+$  states could mix two- and three-phonon character together, which is one way to

explain the suggestion of shared phonon character between the  $4_1^+$  and  $4_3^+$  states by Raman *et al.* [84], as well as the lack of a conclusive set of three-phonon states in  $^{116}\text{Sn}$ . However, if the phonon selection rules are approximately obeyed in this case, then the  $4_3^+ \rightarrow 4_2^+$  272 keV transition should be considerably weaker, a postulation clearly contradicted by the measured relative transition probabilities in Table 16. This discrepancy with respect to the phonon model reinforces arguments made in Section 7.1 about the deficiencies of the phonon model's applicability to  $^{116}\text{Sn}$ .

A further analysis of how the  $4^+$  states mix is to consider that the proton 2p-2h intruder band clearly affects them. The proton 2p-2h dominant component in the 2529 keV  $4_2^+$  state means it is comparatively unique among the low-lying  $4^+$  states, although it has been established in this thesis that it must contain neutron broken-pair admixtures. Given the common base neutron  $(1g_{7/2})^{-1}(3s_{1/2})$  configuration of the  $4_{1-5}^+$  states, and having already treated the 2529 keV  $4_2^+$  and 2391 keV  $4_1^+$  states separately in a two-state mixing model to understand their characteristics, turning now to the  $4_1^+$ ,  $4_3^+$ ,  $4_4^+$  and  $4_5^+$  states, the multistate mixing-model as discussed in Section 1.3.2 can be used to parameterize the interaction strength that brings down the  $4_1^+$  state somewhat compared to the other three.

Supposing that the 2p-2h admixture in the  $4_1^+$  state is what brings it closer to the  $4_2^+$  state, then since the  $4_3^+$ ,  $4_4^+$  and  $4_5^+$  states likely have negligible 2p-2h admixtures, they are raised in energy and the  $4_1^+$  state is lowered in energy. The  $4_{3-5}^+$  states are raised to an average of 2981 keV, and the  $4_1^+$  state lowered to 2391 keV. Given  $N = 4$  states in total, the interaction parameter  $V$  is equal to 148 keV, and this quantifies the effect of the proton 2p-2h intruder band on the neutron broken-pair states. Further, in the multi-state mixing model described by Casten [27], the wavefunction for the 2391 keV  $4_1^+$  state could be qualitatively written as a coherent linear combination of the major constituents of the higher-lying  $4_{2-5}^+$  states, which accounts for the presence of transitions that enter into the  $4_1^+$  state with generally similar magnitudes of their mixing ratios. An appropriate model could be used to incorporate this feature when constructing  $4_{1-5}^+$  state

wavefunctions, and in concert with this, a better and fuller understanding will come from absolute transition probabilities, discussed in the next section.

In conclusion, the  $4_{1-5}^+$  states are confirmed to be highly mixed, with qualitative wavefunction admixtures consisting of neutron broken-pair components, along with proton 2p-2h character distributed over the 2391 keV  $4_1^+$  and 2529 keV  $4_2^+$  states, and possible shape coexistence as well for those two states. It is also unlikely that fragmented phonon character is necessary to explain their nature.

### **7.3. Absolute Transition Probabilities**

With the level half-life information presented in Section 4.4, experimental absolute  $B(E2)$  and  $B(M1)$  values can be obtained using the experimentally measured mixing ratios listed in Table 14 and are reported in Appendix C. Based on those results, the  $M1$  components of the transitions listed are predominantly of single-particle nature, but the collective character of the  $E2$  components is harder to ascertain, given the wide ranges of the  $B(E2)$  values. This is because the half-life uncertainties are sizable, limiting the usefulness of the absolute transition probabilities. Further investigation is merited in order to obtain better lifetime limits, which will constrain the absolute transition probabilities and allow more meaningful analysis of the single-particle or collective character of the transitions between the  $4_{1-5}^+$  states, which in turn can be used to better elucidate their underlying wavefunction components.

## Chapter 8. Conclusion

A high-statistics  $\beta$ -decay experiment involving the decay of  $^{116\text{m}}\text{In}$  to  $^{116}\text{Sn}$  using the  $8\pi$  spectrometer at TRIUMF-ISAC has provided a robust data set which has given rise to several new measurements of K-shell internal conversion coefficients, mixing ratios and relative transition probabilities. While the mixing ratio measurements in several cases are statistics-limited, they do shed light on the configuration mixing of the  $2^+$  and  $4^+$  states, enabling a better understanding of the nature of the excited states of  $^{116}\text{Sn}$ . However, more precise absolute  $B(E2)$  and  $B(M1)$  values determined from lifetime data are required to better understand the underlying wavefunction admixtures.

The conversion-electron study in the present work has led to new measurements of the K-shell internal conversion coefficients for the 85, 304 and 463 keV transitions, and a conclusive confirmation of the presence of the 85 keV transition in  $^{116}\text{Sn}$ . When combined with angular-correlation measurements, the 138 keV  $\alpha_{\text{K}} = 0.215(13)$  and mixing ratio  $\delta = -0.13(8)$ , were used to obtain the  $E0$  component  $\mu_{\text{K}} = 0.95_{-0.95}^{+6.52}$  of this mixed  $E0/M1/E2$  transition, leading to  $\rho^2(E0) \times 10^3 = 8.97$  at the central value of  $\mu_{\text{K}}$ , indicating the possibility of shape coexistence as one of several factors in the mixing of the 2529 keV  $4_2^+$  and 2391 keV  $4_1^+$  states.

The angular-correlation measurements also yielded insights into the lack of configuration mixing of the  $2^+$  states, as the sign of the mixing ratio for the 931 keV transition has been corrected, and is now opposite to that for the 819 keV transition, signifying that the originating states do not overlap well with each other. Overall, the mixing ratio measurements,  $\rho^2(E0) \times 10^3$  values and deduced relative  $E2$  and  $M1$  transition strengths produced in this work give new information about the configuration mixing of the  $4_{1-5}^+$  states in  $^{116}\text{Sn}$ . More specifically, the wavefunction admixtures in the

$4_4^+$  and  $4_5^+$  states are clearly somewhat different from the lower-lying  $4_{1-3}^+$  states, in which the  $4_1^+$  and  $4_2^+$  states share neutron broken-pair and proton 2p-2h character.

The additional spectroscopic information reported in this work will aid in the refinement of models to try to account for the experimental and theoretical discrepancies highlighted by Allmond *et al.* (Section 4.5) for the  $B(E2; 0_{gs}^+ \rightarrow 2_1^+)$  values computed using the seniority scheme in addition to the current deficiencies in applying LSSM or QRPA models to the proton 2p-2h band. Further, there are other discrepancies reported by Wenes *et al.* [104] and Bonsignori *et al.* [105] which remain to be reconciled, especially if the phonon model is not appropriate for describing states in  $^{116}\text{Sn}$ .

More generally in the realm of theoretical analysis, the evolution of states and transitions de-exciting those states from one even- $A$  isotope of tin to the next will reveal how the underlying wavefunctions evolve with mass number. In this light, the new spectroscopic data found in this work suggests that systematically re-investigating existing data, as well as adding new data, is vital to constructing consistent models of tin isotopes that can predict  $B(E2)$  and  $B(M1)$  values as well as mixing ratios. Clearly, much work remains to be done to develop a unified model of  $^{116}\text{Sn}$  that can be extended to the neighboring even- $A$  isotopes of tin, and this work is one of the stepping-stones to achieve that goal.

As part of an ongoing campaign to better understand the evolution of states in the mid-shell isotopes of tin, a  $(n,n'\gamma)$  experiment will be performed at ILL Grenoble in France. The resulting gamma rays emitted will be detected with HPGe and  $\text{LaBr}_3(\text{Ce})$  detectors, utilizing the Doppler shift technique as well as the lifetime-measurement capabilities of  $\text{LaBr}_3(\text{Ce})$ <sup>22</sup> to measure the lifetimes of the excited  $4^+$  states in  $^{116}\text{Sn}$ , further adding to the body of data to refine theoretical models.

---

<sup>22</sup> The timing-response behavior of this scintillator crystal is very similar to that of  $\text{BaF}_2$ , discussed in detail in Refs. [25,125].

## References

- [1] E. Wigner, Phys. Rev. **51**, 2, 106 (1937).
- [2] K. S. Krane, *Introductory Nuclear Physics*, edited by D. Halliday (Wiley, New York, 1987).
- [3] Wikimedia Commons, Nuclear chart available from [https://commons.wikimedia.org/wiki/File:NuclideMap\\_stitched\\_small\\_preview.png](https://commons.wikimedia.org/wiki/File:NuclideMap_stitched_small_preview.png), , 2008.
- [4] Georgia State University and R. Nave. Nuclear Size and Density (Hyperphysics). <<http://hyperphysics.phy-astr.gsu.edu/hbase/nuclear/nucuni.html>> Accessed 05/04 2015.
- [5] Georgia State University and R. Nave. Nuclear Potential and the Shell Model (Hyperphysics). <<http://hyperphysics.phy-astr.gsu.edu/hbase/nuclear/shell.html>> Accessed 05/04 2015.
- [6] R. D. Woods and D. S. Saxon, Phys. Rev. **95**, 2, 577 (1954).
- [7] M. Goeppert Mayer, Phys. Rev. **75**, 1969 (1949).
- [8] O. Haxel, J. H. D. Jensen, and H. E. Suess, Phys. Rev. **75**, 11, 1766 (1949).
- [9] Brookhaven National Laboratory. Interactive Chart of Nuclides. <<http://www.nndc.bnl.gov/chart/>> Accessed 06/02 2015.
- [10] P. E. Cavanagh, C. F. Coleman, A. G. Hardacre, G. A. Gard, and J. F. Turner, Nucl. Phys. A **141**, 1, 97 (1970).
- [11] A. Mizukami, H. Miyake, and K. Hara, Revista Brasileira de Fisica **8**, 3 (1978).
- [12] P. Möller, A. J. Sierk, T. Ichikawa, and H. Sagawa, *Nuclear ground-state masses and deformations: FRDM(2012)*, LA-UR-15-26310, 2015).
- [13] B. R. Mottelson and S. G. Nilsson, Phys. Rev. **99**, 1615 (1955).

- [14] I. Talmi, Nucl. Phys. A **172**, 1, 1 (1971).
- [15] A. Poves (private communication).
- [16] E. K. Warburton, J. A. Becker, and B. A. Brown, Phys. Rev. C **41**, 1147 (1990).
- [17] RIKEN. Too many neutrons break the rules, by Dr. Heiko Scheit.  
<<http://www.riken.jp/en/research/rikenresearch/highlights/6041/>> Accessed 09/08 2016.
- [18] K. Heyde, C. De Coster, P. van Isacker, J. Jolie, and J. L. Wood, Physica Scripta **1995**, T56 (1994).
- [19] K. Heyde and J. L. Wood, Rev. Mod. Phys. **83**, 1467 (2011).
- [20] J. L. Wood (unpublished).
- [21] A. Bohr and B. Mottelson, *Nuclear Structure (Volume II)* (W. A. Benjamin, Inc., Don Mills, Ontario, Canada, 1975).
- [22] E. Browne and H. Junde, Nuclear Data Sheets **87**, 15 (1999).
- [23] D. D. Frenne and E. Jacobs, Nuclear Data Sheets **79**, 639 (1996).
- [24] A. Arima and F. Iachello, Phys. Rev. Lett. **35**, 1069 (1975).
- [25] D. S. Cross, *Building an Array of Barium Fluoride Radiation Detectors for Nuclear Lifetime Measurements* (Simon Fraser University, 2009).
- [26] P. E. Garrett, K. L. Green, and J. L. Wood, Phys. Rev. C **78**, 4, 044307 (2008).
- [27] R. F. Casten, *Nuclear Structure from a Simple Perspective, Second Edition* (Oxford University Press, New York, NY, USA, 2001).
- [28] J. L. Wood, E. F. Zganjar, C. De Coster, and K. Heyde, Nucl. Phys. A **651**, 4, 323 (1999).
- [29] K. S. Krane, Phys. Rev. C **10**, 3, 1197 (1974).
- [30] F. Bosch, T. Faestermann, J. Friese, *et al*, Phys. Rev. Lett. **77**, 5190 (1996).
- [31] G. Audi, A. H. Wapstra, and C. Thibault, Nuclear Physics A **729**, 1, 337 (2003).

- [32] P. E. Garrett, A. Andreyev, R. A. E. Austin, *et al*, Acta Phys. Pol. B **38**, 1169 (2007).
- [33] C. E. Svensson, R. Dunlop, P. Finlay, *et al*, AIP Conf. Proc., 1560, 610 (2013).
- [34] J. Lilley, *Nuclear Physics: Principles and Applications* (Wiley, New York, 2001).
- [35] I. M. Band, M. B. Trzhaskovskaya, C. W. Nestor Jr., P. O. Tikkanen, and S. Raman, Atomic Data and Nuclear Data Tables **81**, 1-2 (2002).
- [36] T. Kibédi, T. W. Burrows, M. B. Trzhaskovskaya, P. M. Davidson, and C. W. Nestor Jr., Nucl Instr Meth A **589**, 202 (2008).
- [37] A. N. Andreyev, M. Huyse, P. Van Duppen, *et al*, Nature **405**, 430 (2000).
- [38] M. Baranger and E. Vogt, *Advances in Nuclear Physics* (Kluwer Academic Publishers, 1977), 11.
- [39] R. B. Firestone and V. S. Shirley, *Table of Isotopes* (John Wiley & Sons, 1996).
- [40] D. R. Hamilton, Phys. Rev. **58**, 122 (1940).
- [41] L. C. Biedenharn and M. E. Rose, Rev. Mod. Phys. **25**, 729 (1953).
- [42] H. J. Rose and D. M. Brink, Rev. Mod. Phys. **39**, 306 (1967).
- [43] K. S. Krane and R. M. Steffen, Phys. Rev. C **2**, 724 (1970).
- [44] A. J. Becker and R. M. Steffen, Phys. Rev. **180**, 4, 1043 (1969).
- [45] F. K. McGowan and E. C. Campbell, Phys. Rev. **92**, 2, 523 (1953).
- [46] F. K. McGowan, Phys. Rev. **92**, 2, 524 (1953).
- [47] P. Schmelzenbach, *The Study of  $^{150}\text{Sm}$  Through the Beta Decay of  $^{150}\text{Pm}$ ,  $^{150m}\text{Eu}$  and  $^{150g}\text{Eu}$*  (Oregon State University, 2003).
- [48] J. Loats, *Angular Correlation Measurements from the  $\beta$  Decay of  $^{166m}\text{Ho}$  and  $^{166}\text{Tm}$  and the Properties of the Gamma Vibrational Band in  $^{166}\text{Er}$* . (Oregon State University, 2004).
- [49] A. Chester, *Monitoring rainwater and seaweed reveals the presence of  $^{131}\text{I}$  in southwest and central British Columbia, Canada following the Fukushima nuclear accident in Japan* (Simon Fraser University, 2013).

- [50] H. Frauenfelder and R. M. Steffen, *Alpha-, Beta-, and Gamma-Ray Spectroscopy*, edited by K. Siegbahn (North-Holland Publishing Company, Amsterdam, The Netherlands, 1965).
- [51] D. Miller, *Intermediate-energy Proton Knockout to Probe Single-particle Structure and Nuclear Spin Alignment in the 'Island of Inversion' Isotopes  $^{31,33}\text{Mg}$*  (Michigan State University, 2009).
- [52] F. W. J. Olver, D. W. Lozier, R. F. Boisvert, and C. W. Clark, *NIST Handbook of Mathematical Functions* [<http://dlmf.nist.gov/>, Release 1.0.9 of 2014-08-29].
- [53] Anthony Stone. Anthony Stone's Wigner coefficient calculator. <<http://www-stone.ch.cam.ac.uk/wigner.shtml>> Accessed 05/22 2015.
- [54] M. Ferentz and N. Rosenzweig, *TABLE OF F COEFFICIENTS, ANL-5324* (Argonne National Laboratories, 1955).
- [55] J. Blachot, Nuclear Data Sheets **111**, 3, 717 (2010).
- [56] M. J. Martin, *Phase Conventions for Mixing Ratios in Electromagnetic Transitions from Angular Correlations and Angular Distributions* (Oak Ridge National Laboratory, 1987).
- [57] Y. Yamaguchi, J. Runan(Gen), and T. Nagahara, J. Phys. Soc. Japan **38**, 4, 911 (1975).
- [58] T. Kibédi, G. D. Dracoulis, A. P. Byrne, and P. M. Davidson, Nucl. Phys. A **688**, 3-4, 669 (2001).
- [59] A. Bäcklin, N. Jonsson, R. Julin, J. Kantele, M. Luontama, A. Passoja, and T. Poikolainen, Nucl. Phys. A **351**, 3, 490 (1981).
- [60] G. F. Knoll, *Radiation Detection and Measurement* (Wiley, New York, 2000).
- [61] G. Grinyer, *High-Precision Measurements of  $^{26}\text{Na}$  Beta Decay* (University of Guelph, 2004).
- [62] J. Kalef-Ezra, Y. S. Horowitz, and J. M. Mack, Nucl Instr Meth **195**, 3, 587 (1982).
- [63] Nucleonica. Gamma Ray Spectrum.  
<[https://www.nucleonica.com/wiki/index.php?title=File%3ADetector\\_Response\\_Components\\_Spectrum.jpg](https://www.nucleonica.com/wiki/index.php?title=File%3ADetector_Response_Components_Spectrum.jpg)> Accessed 12/20 2017.

- [64] EG&G Ortec. HPGe and Si(Li) Radiation Detectors - Types. <<http://www.ortec-online.com/Products-Solutions/RadiationDetectors/Type.aspx>> Accessed 09/16 2016.
- [65] W. J. Gallagher and S. J. Cipolla, Nucl Instr Meth **122**, 405 (1974).
- [66] *X-ray Data Booklet*, edited by A. C. Thompson (Lawrence Berkeley National Laboratory, 2009).
- [67] P. Fettweis and J. Vervier, Phys. Lett. **3**, 1, 36 (1962).
- [68] H. H. Bolotin, Phys. Rev. **136**, 6B, 1557 (1964).
- [69] J. J. Reidy and M. L. Wiedenbeck, Nucl. Phys. **70**, 3, 518 (1970).
- [70] D. Rabenstein, Z. Physik **240**, 3, 244 (1970).
- [71] F. Pleiter, Nucl. Phys. A **184**, 2, 443 (1972).
- [72] P. Fettweis and S. Sadasivan, Z. Physik **259**, 3, 195 (1973).
- [73] K. Okano and Y. Kawase, Nucl Instr Meth **108** (1973).
- [74] G. Ardisson, Radiochem. Radioanal. Letters **16**, 5, 241 (1974).
- [75] G. Garcia-Bermudez, S. L. Gupta, N. C. Singhal, A. V. Ramayya, J. Lange, J. H. Hamilton, and N. R. Johnson, Phys. Rev. C **9**, 3, 1060 (1974).
- [76] Z. Gácsi and S. Raman, Phys. Rev. C **49**, 5, 2792 (1994).
- [77] K. S. Krane and J. Sylvester, Phys. Rev. C **73**, 054312 (2006).
- [78] O. Beer, A. El Behay, P. Lopato, Y. Terrien, G. Vallois, and K. K. Seth, Nucl. Phys. A **147**, 2, 326 (1970).
- [79] D. A. McClure and J. W. Lewis III, Phys. Rev. C **5**, 3, 922 (1972).
- [80] A. Bäcklin, W. Dietrich, R. Julin, J. Kantele, M. Luontama, and L. Westerberg, Physics Letters B **62**, 4, 402 (1976).
- [81] M. Luontama, J. Kantele, R. Julin, A. Passoja, T. Poikolainen, and M. Pylvanainen, Nucl Instr Meth **159**, 2, 339 (1979).

- [82] N. Jonsson, A. Bäcklin, J. Kantele, R. Julin, M. Luontama, and A. Passoja, Nucl. Phys. A **371**, 2, 333 (1981).
- [83] H. Wienke, H. P. Blok, and J. Blok, Nucl. Phys. A **405**, 2, 237 (1983).
- [84] S. Raman, T. A. Walkiewicz, S. Kahane, E. T. Journey, J. Sa, Z. Gácsi, J. L. Weil, K. Allaart, G. Bonsignori, and J. Shriner J. F., Phys. Rev. C **43**, 2, 521 (1991).
- [85] E. J. Schneid, A. Prakash, and B. L. Cohen, Phys. Rev. **156**, 4, 1316 (1967).
- [86] D. G. Fleming, M. Blann, H. W. Fulbright, and J. A. Robbins, Nucl. Phys. A **157**, 1, 1 (1970).
- [87] H. W. Fielding, R. E. Anderson, C. D. Zafiratos, D. A. Lind, F. E. Cecil, H. H. Wieman, and W. P. Alford, Nucl. Phys. A **281**, 3, 389 (1977).
- [88] J. Bron, W. H. A. Hesselink, A. van Poelgeest, J. J. A. Zalmstra, M. J. Uitzinger, H. Verheul, K. Heyde, M. Waroquier, H. Vincx, and P. van Isacker, Nucl. Phys. A **318**, 3, 335 (1979).
- [89] J. M. Schippers, J. M. Schreuder, S. Y. van der Werf, K. Allaart, N. Blasi, and M. Waroquier, Nucl. Phys. A **510**, 1, 70 (1990).
- [90] P. Guazzoni, L. Zetta, A. Covello, A. Gargano, B. F. Bayman, T. Faestermann, G. Graw, R. Hertenberger, H. Wirth, and M. Jaskola, Phys. Rev. C **83**, 044614 (2011).
- [91] P. H. Stelson, F. K. McGowan, R. L. Robinson, and W. T. Milner, Phys. Rev. C **2**, 5, 2015 (1970).
- [92] R. Graetzer, S. M. Cohick, and J. X. Saladin, Phys. Rev. C **12**, 5, 1462 (1975).
- [93] J. Kantele, R. Julin, M. Luontama, A. Passoja, T. Poikolainen, A. Bäcklin, and N. Jonsson, Z. Physik A **289**, 2, 157 (1979).
- [94] N. Jonsson, A. Bäcklin, R. Julin, and M. Migahed, *UIIP-1000 Report* (University of Uppsala Institute of Physics, 1979).
- [95] R. Julin, *E0 and E2 Decay of Low-lying  $0^+$  States in the Even-even Nuclei  $^{206}\text{Pb}$ ,  $^{208}\text{Po}$ ,  $^{112-120}\text{Sn}$  and  $^{112,114}\text{Cd}$*  (University of Jyväskylä, 1979).
- [96] A. Jungclaus, J. Walker, J. Leske, *et al*, Physics Letters B **695**, 1-4, 110 (2011).

- [97] J. M. Allmond, A. E. Stuchbery, A. Galindo-Uribarri, *et al*, Phys. Rev. C **92**, 041303 (2015).
- [98] A. van Poelgeest, J. Bron, W. H. A. Hesselink, K. Allaart, J. J. A. Zalmstra, M. J. Uitzinger, and H. Verheul, Nucl. Phys. A **346**, 1-2, 70 (1980).
- [99] A. Savelius, S. Juutinen, K. Helariutta, *et al*, Nucl. Phys. A **637**, 4, 491 (1998).
- [100] E. R. Flynn and P. D. Kunz, Physics Letters B **68**, 1, 40 (1977).
- [101] T. Kibédi and R. H. Spear, Atomic Data and Nuclear Data Tables **89** (2005).
- [102] J. L. Pore, *An examination of the mixing of low-lying excited  $0^+$  states in  $^{116}\text{Sn}$*  (Simon Fraser University, 2013).
- [103] J. L. Pore, D. S. Cross, C. Andreoiu, *et al*, Eur. Phys. J. A **53**, 27 (2017).
- [104] G. Wenes, P. van Isacker, M. Waroquier, K. Heyde, and J. van Maldeghem, Phys. Rev. C **23**, 2, 2291 (1981).
- [105] G. Bonsignori, M. Savoia, K. Allaart, A. van Egmond, and G. te Velde, Nucl. Phys. A **432**, 2, 389 (1985).
- [106] R. Arvieu, E. Baranger, and M. Veneroni, Phys. Lett. **4**, 2, 119 (1963).
- [107] H. H. Bolotin, Phys. Rev. **136**, 6B, 1566 (1964).
- [108] T. Song and L. M. Yang, Phys. Rev. C **40**, 4, 1782 (1989).
- [109] X. Chen, D. Lu, and L. M. Yang, Commun. Theor. Phys. (Beijing, China) **34**, 2, 267 (2000).
- [110] I. O. Morales, P. van Isacker, and I. Talmi, Physics Letters B **703**, 5, 606 (2011).
- [111] Z. P. Li, C. Y. Li, J. Xiang, J. M. Yao, and J. Meng, *Enhanced collectivity in neutron-deficient Sn isotopes in energy functional based collective Hamiltonian* (e-print arXiv:1209.6076v1 [nucl-th], 2012).
- [112] J. Weil (private communication).
- [113] P. E. Garrett and J. L. Wood, J. Phys. G: Nucl. Part. Phys. **37**, 064028 (2010).

- [114] P. E. Garrett, K. L. Green, R. A. E. Austin, *et al*, Acta Phys. Pol. B **42**, 3-4, 799 (2011).
- [115] P. E. Garrett, J. Bangay, A. Diaz Varela, *et al*, Phys. Rev. C **86**, 044304 (2012).
- [116] K. Heyde, J. L. Wood, C. De Coster, and J. Jolie, Phys. Rev. C **46**, 5, 2113 (1992).
- [117] N. Tsoneva and H. Lenske, Physics Letters B **695**, 174 (2011).
- [118] K. Jayamanna, Hyperfine Int. **225**, 1-3, 51 (2014).
- [119] TRIUMF Design Office, Artistic rendition of TRIUMF-ISAC, available from <http://trshare.triumf.ca/~hackman/Unsink/I2/i2.png>.
- [120] J. Äystö, Nuclear Physics A **805**, 1-4, 162c (2008).
- [121] P. G. Bricault, F. Ames, M. Dombisky, P. Kunz, and J. Lassen, Hyperfine Int. **225**, 1-3, 25 (2014).
- [122] P. E. Garrett, A. J. Radich, J. M. Allmond, *et al*, Journal of Physics: Conference Series **639**, 012006 (2015).
- [123] G. C. Ball, T. Achtzehn, D. Albers, *et al*, J. Phys. G: Nucl. Part. Phys. **31**, S1491 (2005).
- [124] A. B. Garnsworthy and C. E. Svensson, Hyperfine Int. **225**, 1-3, 127 (2014).
- [125] D. S. Cross, G. C. Ball, P. E. Garrett, *et al*, JINST **6**, P08008 (2011).
- [126] J. Michetti-Wilson, *Characterization of LaBr<sub>3</sub>(Ce) Detectors for Picosecond Lifetime Measurements* (University of Guelph, 2013).
- [127] E. F. Zganjar, T. Achtzehn, D. Albers, *et al*, Acta Phys. Pol. B **38**, 1179 (2007).
- [128] S. Ritt, computer code MIDAS, available from <http://midas.psi.ch/download>.
- [129] I. Bylinskii and M. K. Craddock, Hyperfine Int. **225**, 1-3, 9 (2014).
- [130] P. E. Garrett (private communication).
- [131] G. A. Demand (private communication).

- [132] R. J. Gehrke, R. G. Helmer, and R. C. Greenwood, Nucl Instr Meth **147**, 2, 405 (1977).
- [133] Z. Kis, B. Fazekas, K. Östör, Z. Révay, T. Belgya, G. L. Molnár, and L. Koltay, Nucl Instr Meth A **418**, 2-3, 374 (1998).
- [134] K. G. Leach, *High-Precision Measurement of the Superallowed Beta Decay Branching Ratio of  $^{38m}\text{K}$*  (University of Guelph, 2008).
- [135] R. Dunlop, *High-Precision Branching Ratio Measurement for the Superallowed  $\beta^+$  Emitter  $^{74}\text{Rb}$*  (University of Guelph, 2012).
- [136] J. B. Willett, Nucl Instr Meth **84**, 2, 157 (1970).
- [137] B. Jigmeddorj, P. E. Garrett, A. Diaz Varela, *et al*, Eur. Phys. J. A **52**, 36 (2016).
- [138] P. E. Garrett, B. Jigmeddorj, A. J. Radich, *et al*, EPJ Web of Conferences **123** (2016).
- [139] B. Jigmeddorj, *Nuclear Structure Study of Cd-110 through Internal Conversion Electrons* (University of Guelph, 2012).
- [140] D. C. Radford, computer code gf3, available from <http://radware.phy.ornl.gov/info.html>.
- [141] C. Amsler and *et al*, Physics Letters B **667**, 1 (2008).
- [142] CERN, computer code ROOT, available from <http://root.cern.ch/>.
- [143] P. Taras and B. Haas, Nucl Instr Meth **123**, 1, 73 (1975).
- [144] D. C. Radford, computer code legft, available from <http://radware.phy.ornl.gov/info.html>.
- [145] R. G. Arns and M. L. Wiedenbeck, Phys. Rev. **111**, 6, 1631 (1958).
- [146] M. B. Martin, R. G. Arns, and M. L. Wiedenbeck, Phys. Rev. **121**, 6, 1732 (1961).
- [147] G. C. Ball, J. S. Forster, F. Ingebretsen, and C. F. Monahan, Can. J. Phys. **48**, 22, 2735 (1970).
- [148] R. J. Barlow, *Statistics: A Guide to the Use of Statistical Methods in the Physical Sciences* (Wiley, Toronto, Ontario, Canada, 1993).

- [149] W. Urban, M. Jentschel, B. Maerkisch, *et al*, JINST **8**, P03014 (2013).
- [150] K. Kitao, Nuclear Data Sheets **75**, 99 (1995).
- [151] S. Raman, C. W. Nestor Jr., and P. Tikkanen, Atomic Data and Nuclear Data Tables **78** (2001).
- [152] R. Dunlop (private communication).
- [153] A. B. Garnsworthy and A. Mathews (private communication).
- [154] M. L. Wiedenbeck, *Technical Report to 1 January 1958: Investigation of Nuclear-Energy Levels* (University of Michigan, Ann Arbor, Michigan, 1958), p. 62.

# Appendix A. Level Scheme of $^{116}\text{Sn}$

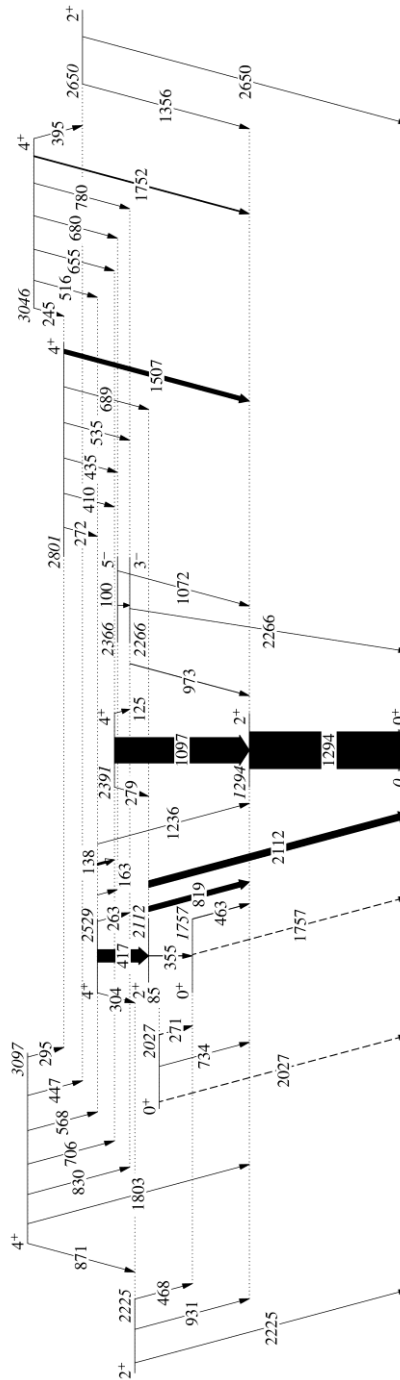


**Figure A1.** Level scheme of the nucleus  $^{116}\text{Sn}$  below 3.4 MeV adapted from the work of J. L. Pore [102,103] and combined with  $E0$  transition data from the literature.

## Appendix B. Gamma Ray Intensities and Branching Ratios

The table below gives level energies, state half-lives (from the Nuclear Data Sheets only for this table), gamma ray energies, gamma ray intensities and branching ratios (see Section 2.2.2 for how they are computed) scaled so that the strongest branching ratio out of each level is equal to 100, with an uncertainty reported if the underlying  $I_\gamma$  has an uncertainty. This table is drawn from the work of Pore *et al.* [103], and includes only the transitions and states shown in the level scheme in Appendix A.

$E_{\text{level}}$ (keV)	$t_{1/2}$ (ps) [55]	$E_\gamma$ (keV)	$I_\gamma$	Branching Ratio
1293.76(20)	0.374(10)	1293.641(84)	100(0)	100(0)
1756.80(14)	44(6)	463.244(23)	0.824(21)	100(4)
2026.91(20)	160(20)	733.65(90)	0.00369(13)	100(4)
2112.19(14)	1.89(10)	85.294(88)	0.00166(10)	0.0091(5)
		355.432(18)	0.939(23)	5.16(14)
		818.546(41)	14.2(3)	78.0(19)
		2112.346(90)	18.2(2)	100.0(15)
2225.37(16)	2.4(12)	468.41(15)	0.000868(87)	0.75(8)
		931.394(47)	0.116(6)	100(7)
		2225.28(11)	0.0584(7)	50.3(18)
2266.12(15)	0.34(4)	972.743(14)	0.631(16)	100(4)
		2266.21(11)	0.00133(14)	0.21(3)
2366.10(17)	$348(19) \times 10^3$	99.815(13)	0.0304(9)	87(4)
		1071.53(9)	0.0348(16)	100(6)
2390.80(14)	0.47(9)	124.634(24)	0.0140(5)	0.0203(7)
		165.43(21)	<0.013	<0.019
		278.850(14)	0.158(5)	0.228(8)

$E_{\text{level}}$ (keV)	$t_{1/2}$ (ps) [55]	$E_{\gamma}$ (keV)	$I_{\gamma}$	Branching Ratio
2390.80(14)	0.47(9)	1096.761(55)	69.2(8)	100(2)
2529.40(14)	<100	138.252(7)	4.63(11)	13.7(5)
		163.300(51)	0.0242(9)	0.072(4)
		263.271(14)	0.16(4)	0.47(12)
		304.017(15)	0.142(3)	0.421(14)
		417.001(21)	33.7(1)	100(4)
		1235.838(90)	0.0683(36)	0.203(12)
2650.42(33)		1356.10(13)	0.00471(37)	100(11)
		2650.34(21)	0.000609(6)	12.9(9)
2801.28(15)		272.203(15)	0.0404(13)	0.345(14)
		409.901(36)	0.0735(26)	0.63(3)
		434.573(37)	0.0288(11)	0.246(11)
		535.016(31)	0.0405(13)	0.346(14)
		688.737(35)	0.209(7)	1.786(75)
		1507.123(94)	11.7(3)	100(4)
3045.90(18)		244.685(24)	0.0360(12)	1.3(5)
		395.190(50)	0.0062(33)	0.22(12)
		516.06(16)	0.0189(18)	0.68(7)
		655.046(30)	0.141(4)	5.05(18)
		679.892(41)	0.0246(11)	0.88(5)
		779.656(39)	0.301(8)	10.8(4)
		1752.12(10)	2.79(7)	100(4)
3096.67(19)		100.49(7)	0.0229(17)	12(1)
		295.47(9)	0.00750(66)	4.0(35)
		447.08(10)	0.00153(15)	0.82(9)
		567.510(30)	0.0522(21)	27.9(14)
		705.743(36)	0.187(5)	100(4)
		829.83(47)	0.0443(14)	24(1)
		870.53(13)	0.00609(44)	3.3(3)
		1802.83(51)	<0.00545	<3.00

## Appendix C. $B(E2)$ and $B(M1)$ Values for Selected Transitions

Based on the gamma ray energies, gamma ray intensities and branching ratios given in Appendix B, the mixing ratios given in Table 14 and level half-lives of the  $4^+$  states in Table 2 (as well as the half-life for the 2650 keV  $2_4^+$  state), absolute  $B(E2)$  and/or  $B(M1)$  values are given for pure  $E2$ , pure  $M1$  or mixed  $E2/M1$  transitions de-exciting those states. The 2529 keV  $4_2^+$  level has only upper and lower limits on its half-life, so the corresponding  $B(E2)$  and  $B(M1)$  values are also only limits. Note that transitions marked with an asterisk (\*) are assumed to be pure  $M1$  and if marked with a dagger (†) are assumed to be pure  $E2$ . A dash indicates that no value was computed for a transition.

$E_{\text{level}}$ (keV)	$E_{\gamma}$ (keV)	$B(E2)$ [W.u.]	$B(M1)$ [W.u.]
2650.42(33)	1356.10(13)†	$5.8^{+4.3}_{-4.0}$	–
	2650.34(21)	$0.026^{+0.020}_{-0.018}$	–
2529.40(14)	138.252(7)	0.95 – 5800	0.0092 – 3.4
	304.017(15)	0.23 – 78	–
	417.001(21)	11 – 3839	–
	1235.838(90)	$9.9 \times 10^{-5} - 0.34$	–
2801.28(15)	272.203(15)	$70^{+78}_{-70}$	$0.008^{+0.007}_{-0.003}$
	409.901(36)	$1.1^{+8.0}_{-1.1}$	$0.007^{+0.004}_{-0.002}$
	688.737(35)	$7.4^{+3.9}_{-3.5}$	–
	1507.123(94)	$8.2^{+4.3}_{-3.9}$	–
3045.90(18)	244.685(24)	$120^{+80}_{-85}$	$0.012^{+0.020}_{-0.004}$
	395.190(50)	$4.2^{+5.1}_{-2.6}$	–
	516.06(16)*	–	$0.0012^{+0.0014}_{-0.0007}$
	655.046(30)	$0.49^{+0.86}_{-0.27}$	$0.004^{+0.007}_{-0.002}$
	1752.12(10)	$1.1^{+1.3}_{-0.7}$	–

## Appendix D. Derivation of B(M1) and B(E2) Formulas

The formulas for B(M1) values (Equation (42)) and B(E2) values (Equation (36)) in the text of the thesis in Section 2.2.2 were obtained from Baranger and Vogt [38], but can be derived from first principles using formulas given in Appendix I of the 1996 edition of the Table of Isotopes [39]. The derivations that follow assume pure transitions for simplicity, but inserting the mixing ratio factor is trivial, as seen from Equations (40) and (43).

Beginning with the definition of the branching ratio, repeated from Equation (38), which is the ratio of a chosen gamma ray intensity to the total gamma and conversion-electron intensity for a desired state,

$$\text{B.R.} = \frac{I_{\gamma,k}}{\sum_i I(\gamma + ce)_i} = \frac{I_{\gamma,k}}{\sum_i I_{\gamma,i}(1 + \alpha_i)},$$

it can be combined with the formula for a partial half-life given the total half-life and the branching ratio of the transition in question,

$$t_{1/2,\gamma} = \frac{t_{1/2}}{\text{B.R.}},$$

or equivalently a partial decay rate can be obtained,

$$\lambda_\gamma = \lambda(\text{B.R.}).$$

In performing a careful rearrangement of Equation (5) from Appendix I in the Table of Isotopes to yield for the B(M1),

$$B(M1) \downarrow = \lambda_\gamma \frac{(1)[(2(1)+1)!]^2 \hbar}{8\pi(1+1)\mu_N^2 b^{1-1}} \left( \frac{\hbar c}{E_\gamma} \right)^{2(1)+1}$$

$$B(M1) \downarrow = \lambda(M1)(\text{B.R.}) \frac{[3]^2 \hbar}{8\pi(2)\mu_N^2} \left( \frac{\hbar c}{E_\gamma} \right)^3 = \lambda(M1)(\text{B.R.}) \frac{9\hbar}{16\pi\mu_N^2} \left( \frac{\hbar c}{E_\gamma} \right)^3$$

$$B(M1) \downarrow = \lambda(M1)(\text{B.R.}) \frac{9\hbar^4 c^3}{16\pi\mu_N^2} \left( \frac{1}{E_\gamma^3} \right)$$

$$B(M1) \downarrow [\mu_N^2] = \frac{9\hbar^4 c^3}{16\pi} \lambda(M1)(\text{B.R.}) \left( \frac{1}{E_\gamma^3} \right)$$

The square brackets around the square of the nuclear magneton mean that the  $B(M1)$  is in those units, as derived.

Similarly for the  $B(E2)$ , Equation (5) can be carefully rearranged,

$$B(E2) \downarrow = \lambda_\gamma \frac{(2)[(2(2)+1)!]^2 \hbar}{8\pi(2+1)e^2 b^2} \left( \frac{\hbar c}{E_\gamma} \right)^{2(2)+1}$$

$$B(E2) \downarrow = \lambda(E2)(\text{B.R.}) \frac{(2)[15]^2 \hbar}{8\pi(3)e^2 b^2} \left( \frac{\hbar c}{E_\gamma} \right)^5 = \lambda(E2)(\text{B.R.}) \frac{450\hbar}{24\pi e^2 b^2} \left( \frac{\hbar c}{E_\gamma} \right)^5$$

$$B(E2) \downarrow = \lambda(E2)(\text{B.R.}) \frac{450\hbar}{24\pi e^2 b^2} \left( \frac{\hbar c}{E_\gamma} \right)^5$$

$$B(E2) \downarrow [e^2 b^2] = \frac{450\hbar^6 c^5}{24\pi} \lambda(E2)(\text{B.R.}) \left( \frac{1}{E_\gamma^5} \right)$$

As with the  $B(M1)$ , the square brackets around the  $e^2 b^2$  indicate that the  $B(E2)$  is in those units, as derived. Noting that the barn is  $100 \text{ fm}^2$ , the conversion to  $e^2 \text{-fm}^4$  is trivial, and given the decay rate  $\lambda = \ln 2 / t_{1/2}$  that conversion is also trivial.

To convert the  $B(M1)$  and  $B(E2)$  values to Weisskopf units, dividing the  $B(M1)$  by Equation (7) in Appendix I of the Table of Isotopes, or the  $B(E2)$  by Equation (6) in Appendix I, will perform the necessary conversion. Implicit in the division is a units cancellation, removing either  $\mu_N^2$  or  $e^2b^2$  to replace the charge-based unit with W.u. instead. Following is the  $B(M1)$  conversion:

$$B(M1) \downarrow = \frac{\frac{9\hbar^4 c^3}{16\pi[\mu_N^2]} \lambda(M1)(B.R.) \left( \frac{1}{E_\gamma^3} \right)}{\frac{10}{\pi b^{1-1}} \left( \frac{3}{3+1} \right)^2 R^{2(1)-2}}$$

$$B(M1) \downarrow = \frac{\frac{9\hbar^4 c^3}{16\pi[\mu_N^2]} \lambda(M1)(B.R.) \left( \frac{1}{E_\gamma^3} \right)}{\frac{10}{\pi} \left( \frac{9}{16} \right)}$$

$$B(M1) \downarrow [W.u.] = \frac{\hbar^4 c^3}{10} \lambda(M1)(B.R.) \left( \frac{1}{E_\gamma^3} \right)$$

Substitution of the factors  $\hbar$  and  $c$  in units based on the gamma-ray energy being quoted in MeV will yield the final formula as quoted in Baranger and Vogt. In a similar manner, the  $B(E2)$  can be converted to W.u. as follows:

$$B(E2) \downarrow = \frac{\frac{450\hbar^6 c^5}{24\pi[e^2b^2]} \lambda(E2)(B.R.) \left( \frac{1}{E_\gamma^5} \right)}{\frac{1}{4\pi b^2} \left( \frac{3}{3+2} \right)^2 R^{2(2)}}$$

$$B(E2) \downarrow = \frac{\frac{450\hbar^6 c^5}{24\pi[e^2b^2]} \lambda(E2)(B.R.) \left( \frac{1}{E_\gamma^5} \right)}{\frac{1}{4\pi b^2} \left( \frac{3}{3+2} \right)^2 R^{2(2)}}$$

Here, substituting  $R = R_o A^{1/3}$  yields

$$B(E2) \downarrow = \frac{\frac{450 \hbar^6 c^5}{24\pi [e^2 b^2]} \lambda(E2)(\text{B.R.}) \left( \frac{1}{E_\gamma^5} \right)}{\frac{1}{4\pi b^2} \left( \frac{9}{5} \right)^2 (R_o A^{1/3})^4}$$

$$B(E2) \downarrow = \frac{\frac{450 \hbar^6 c^5}{24\pi [e^2 b^2]} \lambda(E2)(\text{B.R.}) \left( \frac{1}{E_\gamma^5} \right)}{\frac{1}{4\pi b^2} \left( \frac{9}{5} \right)^2 (R_o A^{1/3})^4}$$

$$B(E2) \downarrow = \frac{450 \hbar^6 c^5}{24\pi [e^2 b^2]} \lambda(E2)(\text{B.R.}) \left( \frac{1}{E_\gamma^5} \right) \left[ \frac{25}{9} \left( \frac{4\pi b^2}{(R_o)^4 A^{4/3}} \right) \right]$$

$$B(E2) \downarrow [\text{W.u.}] = \frac{1250 \hbar^6 c^5}{6 [e^2]} \lambda(E2)(\text{B.R.}) \left( \frac{1}{E_\gamma^5} \right) \left[ \left( \frac{1}{(R_o)^4 A^{4/3}} \right) \right]$$

The physical constants  $R_o = 1.2 \times 10^{-13}$  cm and  $e^2 = 1.43996 \times 10^{-13}$  MeV-cm. These can be used to obtain the necessary final formula as given in Baranger and Vogt, given gamma-ray energies in MeV.

## Appendix E. Nilsson Model Energy Level Diagrams

On the next two pages are diagrams that show the Nilsson model orbitals with respect to the nuclear deformation parameter  $\epsilon_2$ , which is approximately equal to  $\beta_2$ , the more usual measurement of deformation. The first diagram (Figure E1) is for protons covering the region  $Z = 50 - 82$ . The second (Figure E2) is for neutrons, covering  $N = 50 - 82$ . Both are from the Table of Isotopes, 1996 [39], and are reproduced with permission.

The Nilsson model quantum numbers label nondegenerate shell-model states in brackets  $[Nn_zm_\ell]$  and with a projected angular momentum  $\Omega$ . The originating harmonic oscillator shell number  $N = 4$  for the occupancies  $50 - 82$ ; the number of nodes in the  $z$ -direction is  $n_z$ ; and  $m_\ell$  is the projection of the shell-model angular momentum  $\ell$  along the  $z$ -axis. The projected angular momentum  $\Omega$  can be related to the  $m_j$  of the originating shell-model state when the  $2j+1$  degeneracy is lost. The parity of the Nilsson model state is the same as the originating shell-model state.



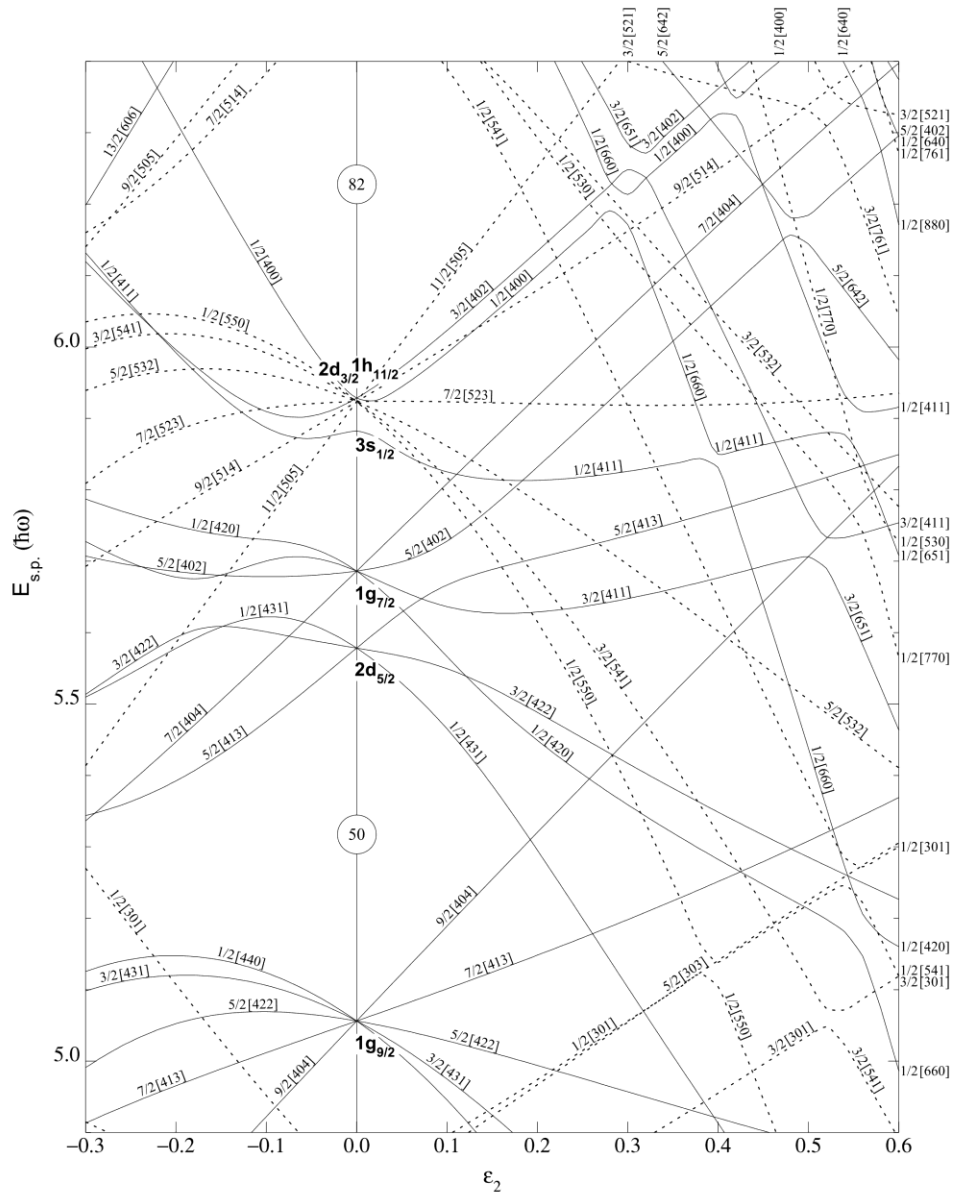


**Figure E2.** Nilsson-model energy level diagram for  $N = 50 - 82$  [39].

## Appendix F. The $m$ -scheme

The coupling of states (or quanta) with even angular momentum, such as phonons, but also coupled quasiparticles in the seniority scheme, can be worked out rather simply by enforcing the requirement that a generated set of quantum numbers from projections of the coupled angular momenta cannot be “re-used”.

In this way it can be seen that for a one-phonon state, where the phonon carries an intrinsic angular momentum of 2 (i.e.  $\lambda = 2$ ), then since it can couple to no other state,  $m_\lambda = +2, +1, 0, -1$  and  $-2$ . Therefore the corresponding nuclear spin can only be  $I = 2$  (the parity would be positive since the phonon wavefunction is symmetric), since  $I = 1$  and  $I = 0$  would “re-use” the projected angular momenta  $+1, 0$  and  $-1$ . A similar argument holds for a state with a seniority of 1 being only  $I^\pi = 2^+$  (the two underlying protons or neutrons would multiply their parities and produce a result of  $+$ ).

Now, given two coupled angular momenta  $\lambda_1 = 2$  and  $\lambda_2 = 2$ , their corresponding projections  $m_1$  and  $m_2$  can be added algebraically ( $M = m_1 + m_2$ ). The corresponding nuclear angular momentum for a unique set of combined  $m$ -states is therefore  $I = M_{\max}$ , and in the two-phonon case,  $M_{\max} = 4$ . Regarding the uniqueness of the nuclear spins for two-phonon states, as one example the combination of  $m_1 = +1, m_2 = +1, M = +2$  would “re-use” an overall projected angular momentum of  $+2$  assigned to the combination  $m_1 = +2, m_2 = 0, M = +2$  so the former combination is removed from the grouping leading to  $I = 4$  and is placed with the grouping leading to  $I = 2$ , preserving the uniqueness of both combinations. It should also be noted that, for example,  $m_1 = +2, m_2 = +1, M = 3$  can generate a state of  $I = 3$ . But this would “re-use” the same combination leading to  $I = 4$ , and this is why no two-phonon states of  $I = 3$  would occur in nuclei. Similar arguments hold for why no two-phonon states of  $I = 1$  occur in nuclei.

The following tables will generate, for phonons, the two-phonon triplet of  $0^+, 2^+$  and  $4^+$ , organized by their  $I = M_{\max}$ .

<b><math>I = 4</math></b>		
<b><math>m_1</math></b>	<b><math>m_2</math></b>	<b><math>M</math></b>
+2	+2	+4
+2	+1	+3
+2	0	+2
+2	-1	+1
+2	-2	0
0	-1	-1
0	-2	-2
-2	-1	-3
-2	-2	-4

<b><math>I = 2</math></b>		
<b><math>m_1</math></b>	<b><math>m_2</math></b>	<b><math>M</math></b>
+1	+1	+2
+1	0	+1
+1	-1	0
+1	-1	+1
-1	-2	0

<b><math>I = 0</math></b>		
<b><math>m_1</math></b>	<b><math>m_2</math></b>	<b><math>M</math></b>
0	0	0

## Appendix G. Wigner 3-j and 6-j Symbols

The Wigner 3-j symbol is related to a Clebsch-Gordan coefficient by the following relationship, given any general angular momentum quantum numbers  $j_{1-3}$  and  $m_{1-3}$ ,

$$\begin{pmatrix} j_1 & j_2 & j_3 \\ m_1 & m_2 & m_3 \end{pmatrix} = \frac{(-1)^{j_1-j_2-m_3}}{\sqrt{2j_3+1}} \langle j_1 m_1 j_2 m_2 | j_3 (-m_3) \rangle .$$

The Wigner 6-j symbol is composed of multiple 3-j symbols as follows, given angular momentum quantum numbers  $j_{1-6}$ :

$$\begin{Bmatrix} j_1 & j_2 & j_3 \\ j_4 & j_5 & j_6 \end{Bmatrix} = \sum_{m_1, \dots, m_6} (-1)^{\sum_{k=1}^6 (j_k - m_k)} \begin{pmatrix} j_1 & j_2 & j_3 \\ m_1 & m_2 & -m_3 \end{pmatrix} \begin{pmatrix} j_1 & j_5 & j_6 \\ -m_1 & m_5 & m_6 \end{pmatrix} \begin{pmatrix} j_4 & j_5 & j_3 \\ m_4 & -m_5 & m_3 \end{pmatrix} \begin{pmatrix} j_4 & j_2 & j_6 \\ -m_4 & -m_2 & -m_6 \end{pmatrix}$$

## Appendix H. GEANT4 Simulated Efficiency Comparison

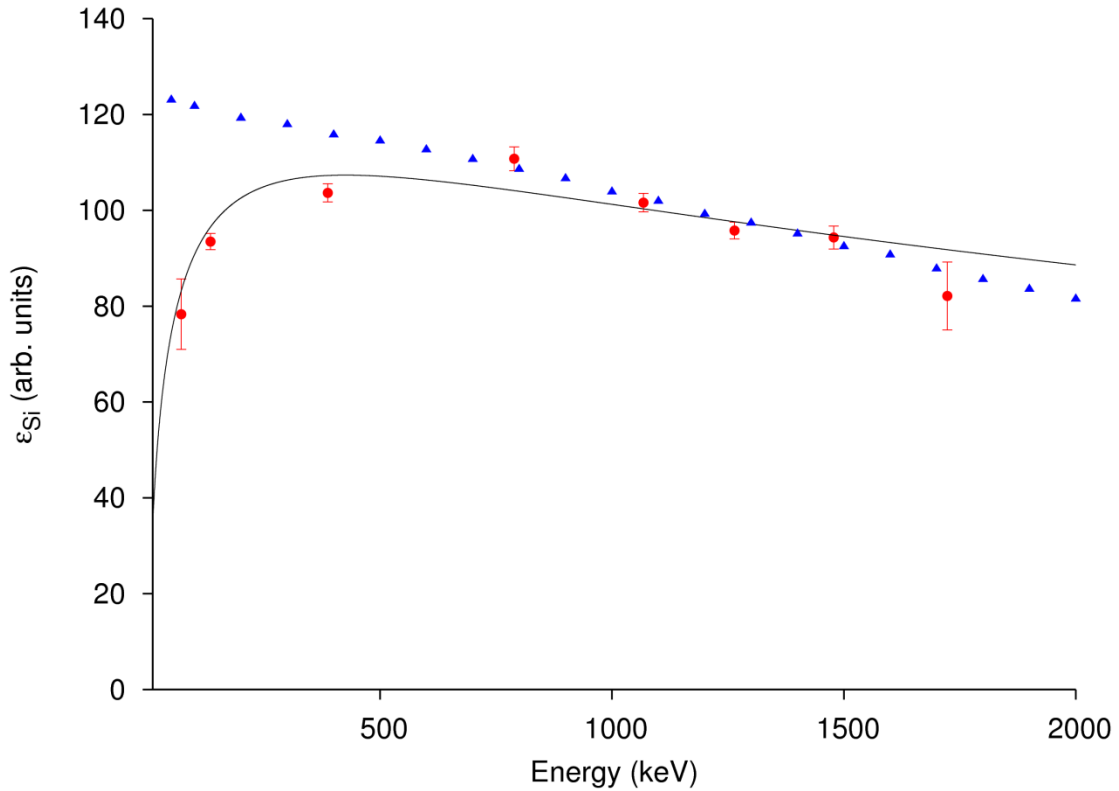


**Figure H1.** GEANT4 simulated data (blue triangles) from Refs. [135,152] overlaid on the efficiency curve in Figure 55.

A GEANT4 simulation was performed by Ryan Dunlop [135] in order to characterize the PACES array in an analysis of the decay of  $^{74}\text{Rb}$ . This simulation involved a single Si(Li) detector being struck by electrons, and the resulting simulated efficiency data was then used to deduce the absolute efficiency of PACES in that work.

The data from the GEANT4 simulation, provided by Dunlop [152], was normalized to the 789, 1068, 1264 and 1478 keV efficiency data points to compare it to the experimental efficiency curve (Figure H1). There is excellent agreement between the experimental data points and the simulated data at energies above  $\sim 800$  keV, while below 800 keV the experimental data (and curve) deviates from the simulation. At high energy, the effects of electrons interacting with the active layer of the Si(Li) detectors are

correctly simulated, while at low energy, the simulation is not accounting for such effects as incomplete depletion (i.e. a larger dead layer than simulated) or condensation on the front faces of the detectors (possibly due to water vapor in incomplete vacuum inside the Delrin chamber).

A fruitful avenue of study would be to build a more complex simulation of PACES in order to better characterize its efficiency over the range from 10 – 2000 keV, as it is now in use with the GRIFFIN spectrometer, and the increased  $\gamma$ - $e^-$  coincidence efficiency will need to be better understood, especially in order to quantify the behavior of PACES at low energy. Preliminary results obtained by Adam Garnsworthy and Anita Mathews [153] do show more realistic behavior of the PACES efficiency when using a more complex GEANT4 simulation, as seen in Figure H2.

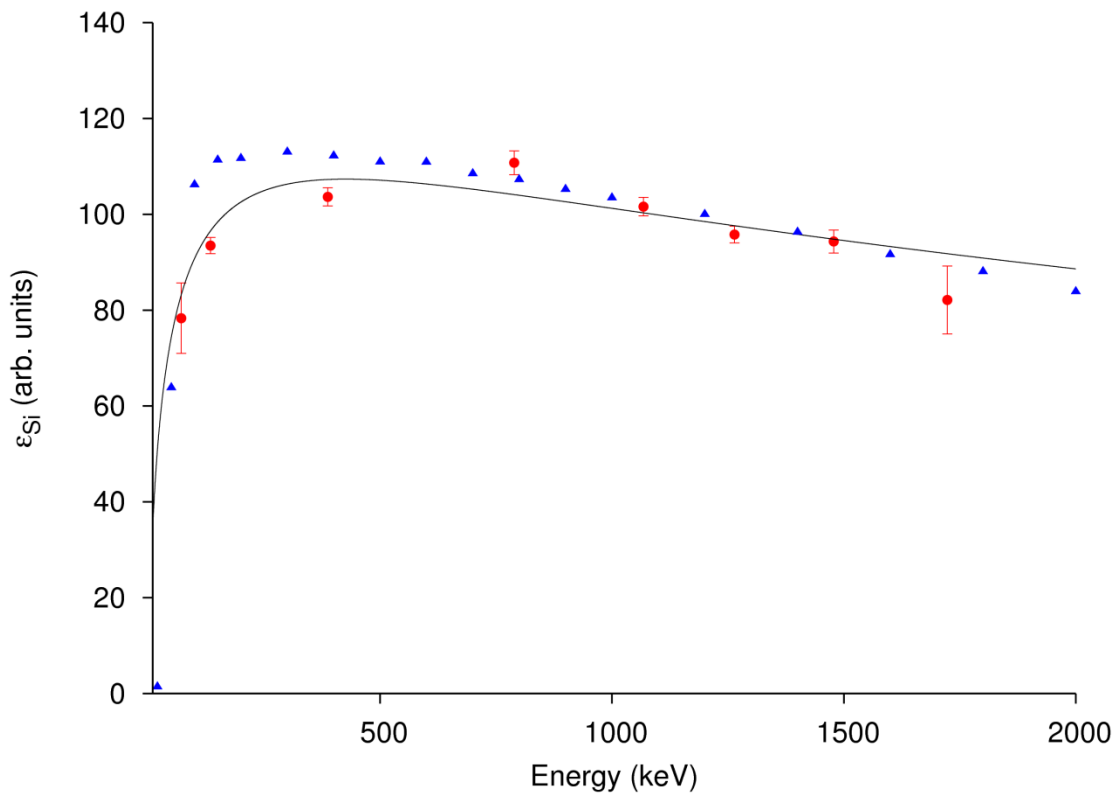


**Figure H2.** GEANT4 simulated data (blue triangles) from Ref. [153] overlaid on the efficiency curve in Figure 55.

## Appendix I. The Arns-Wiedenbeck Plot for the 819 keV $\delta$

The technical report of the University of Michigan “Investigation of Nuclear Energy Levels / ERI Project 2375”, issued on 1 January 1958 [154], has a detailed discussion of the method of Arns and Wiedenbeck [145], including the shapes of the graphs (one is an ellipse associated with the  $A_{22}$  coefficient of  $W(\theta)$ , and one is a straight line associated with the  $A_{44}$  coefficient) from which one can “read off” the quadrupole content of a mixed  $E2/M1$  transition for a  $2^+-2^+-0^+$  cascade.

Given the LEGFT results of  $A_{22} = +0.304(12)$  and  $A_{44} = +0.226(14)$ , the value of  $Q$  (the quadrupole content), which is related to  $\delta$  through the formula

$$\delta^2 = \frac{Q}{1-Q},$$

is 0.679 from  $A_{22}$  and 0.778 from  $A_{44}$ , neglecting uncertainty propagation (a full treatment would also involve taking an appropriate weighted average). Taking the square root will yield the value of  $\delta$ ; the sign depends on the convention as discussed in some detail in Section 2.3.3. In this method the convention used was that of Biedenharn & Rose, which, for the cascade type analyzed in the 819-1294 cascade, corresponds to changing the sign of  $\delta$  to properly express it in the Krane & Steffen convention.

The graph used to apply the method of Arns and Wiedenbeck to the 819 keV transition is shown on the next page. It can be seen that the two decimal places of accuracy generally obtainable for values of  $\delta$  can be obtained by careful graphical analysis.

2 (D,Q) 2

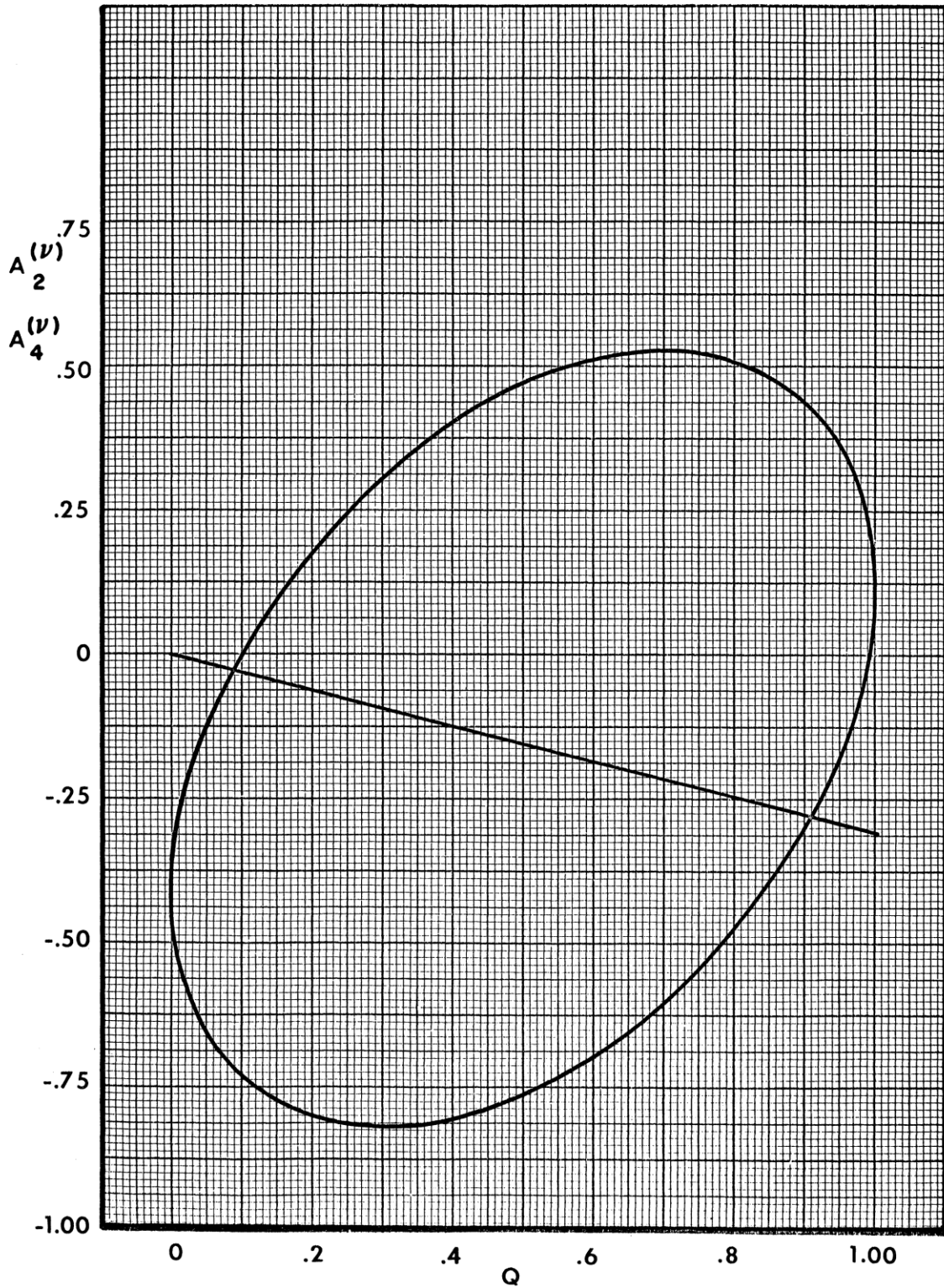


Figure II. Arns-Wiedenbeck plot for a  $2^+-2^+-0^+$  cascade [154].

## Appendix J. Angular Correlation and $\chi^2/\nu$ Plots

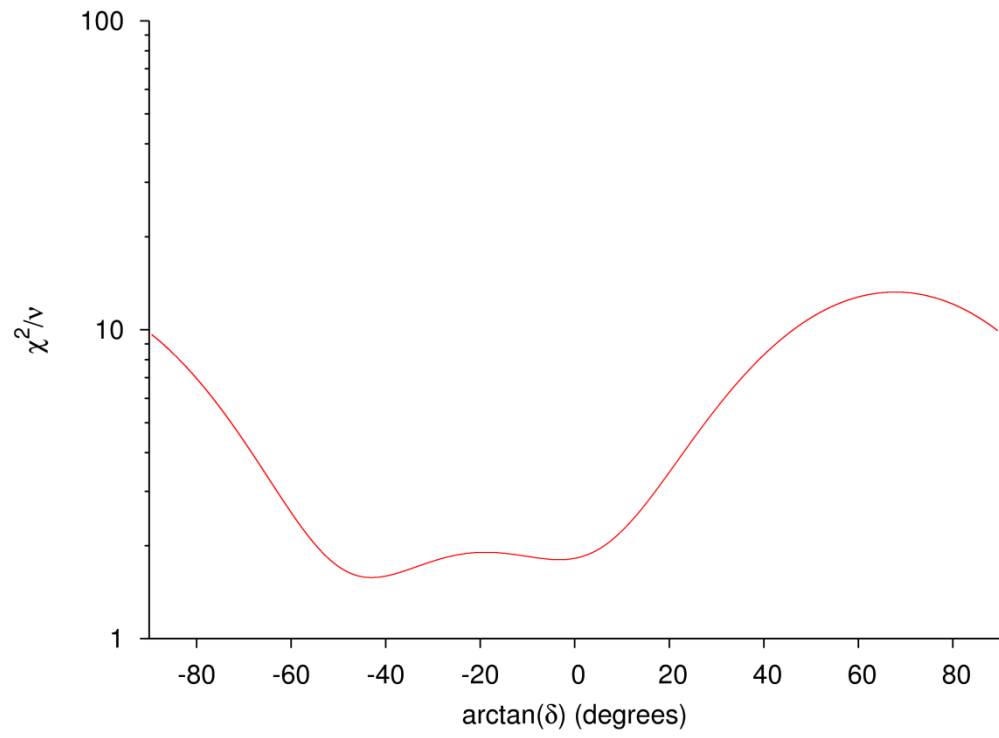
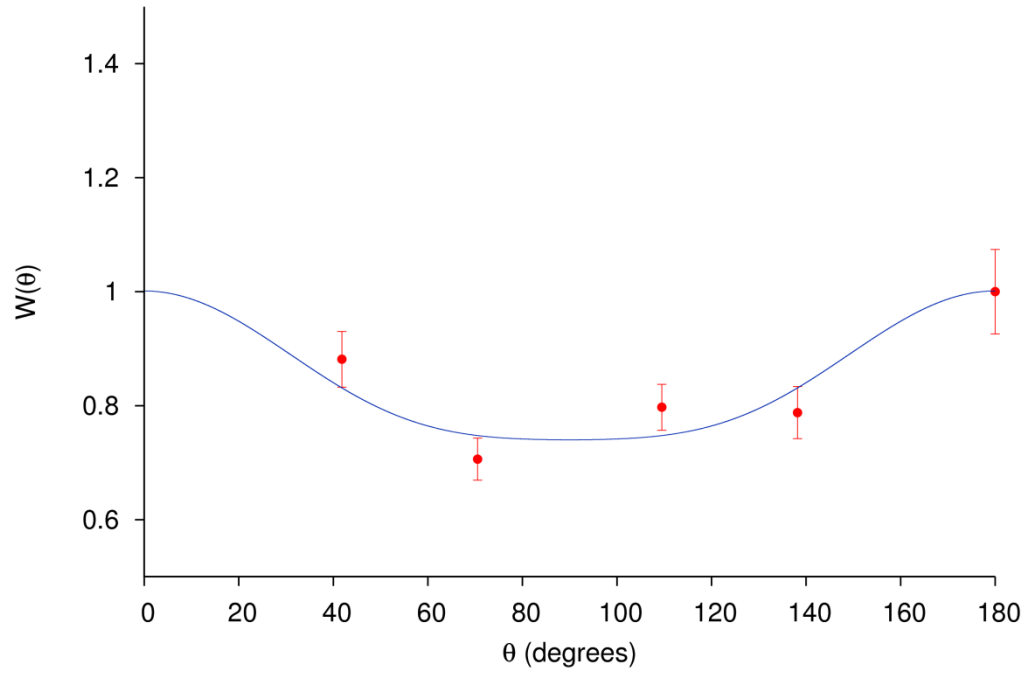
The following graphs (not individually numbered) on the following pages are plots for all the cascades listed in Table 14 which are not discussed in detail in Section 6.3.2. The uncertainty limits are omitted on the  $\chi^2/\nu$  plots.

Additionally, Table J1 gives the associated probabilities (P) for the  $\chi^2/\nu$  values obtained for the mixed-multipolarity transitions analyzed in this work.

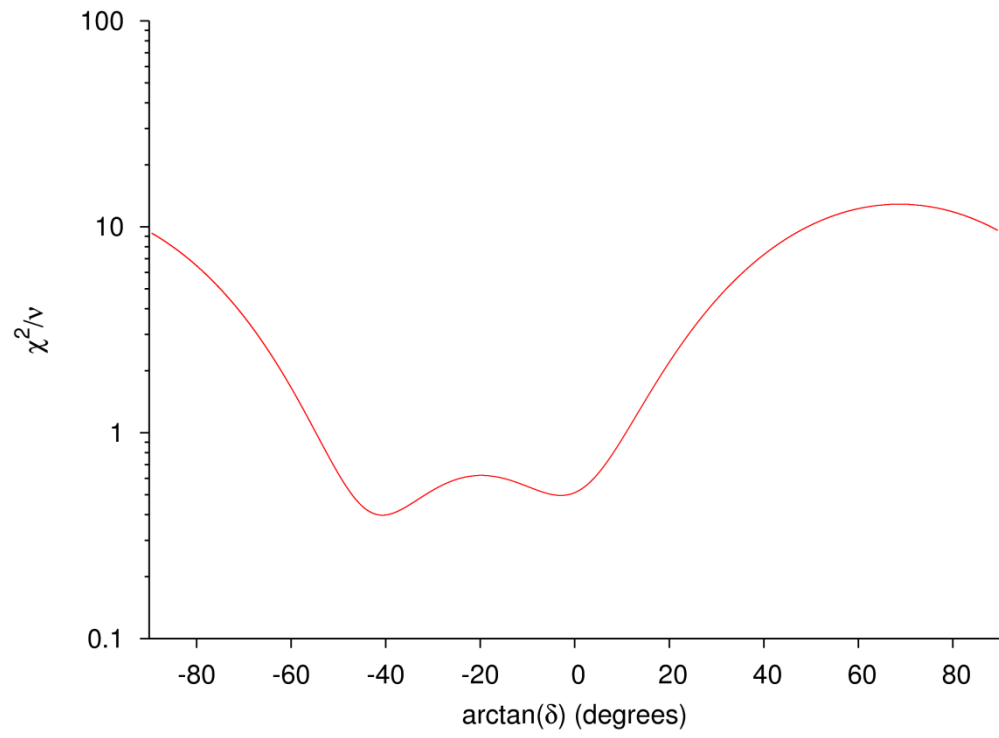
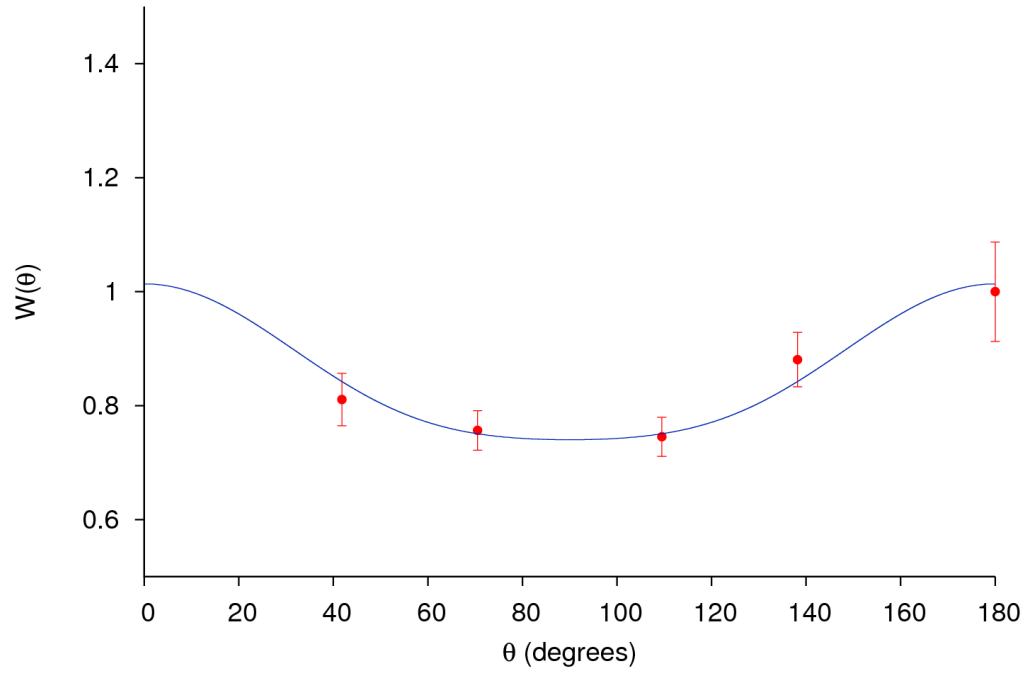
**Table J1.** The probabilities associated with the  $\chi^2$  distribution for each mixed-multipolarity angular correlation.

Cascade $\gamma$ rays ( $E_\gamma$ in keV)	$\chi^2/\nu$	P
272-417	1.58	0.76
568-417	0.40	0.25
138-1097	0.10	0.04
410-1097	0.52	0.33
655-1097	0.55	0.35
706-1097	0.71	0.45
819-1294	1.43	0.77
931-1294	1.87	0.87
973-1294	1.60	0.81
245-1507	0.34	0.20

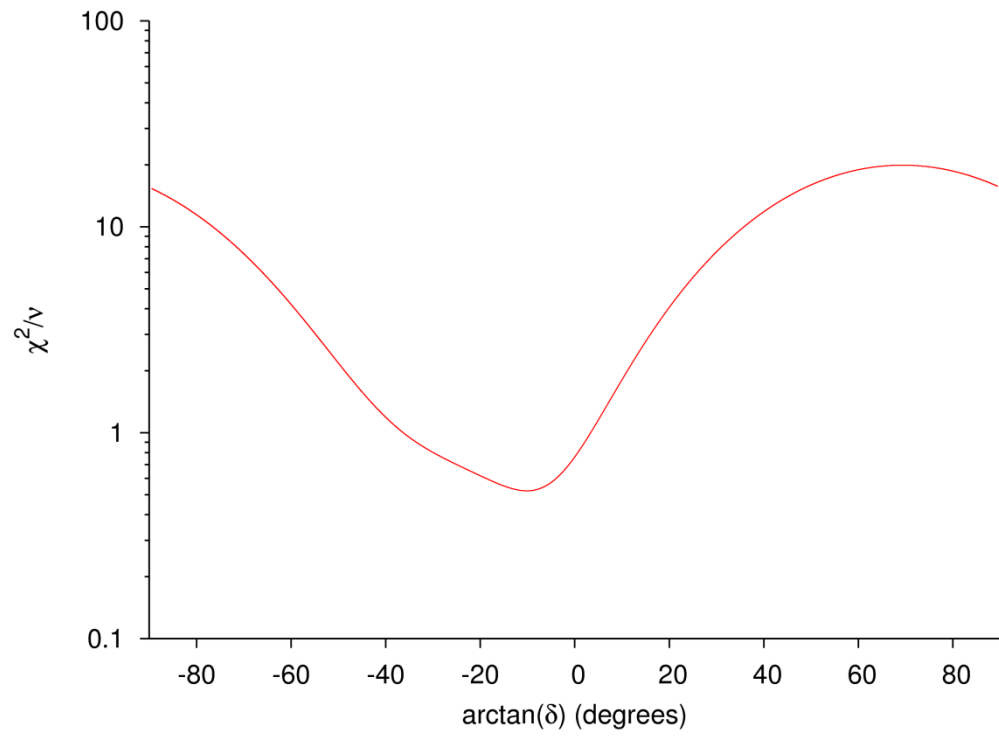
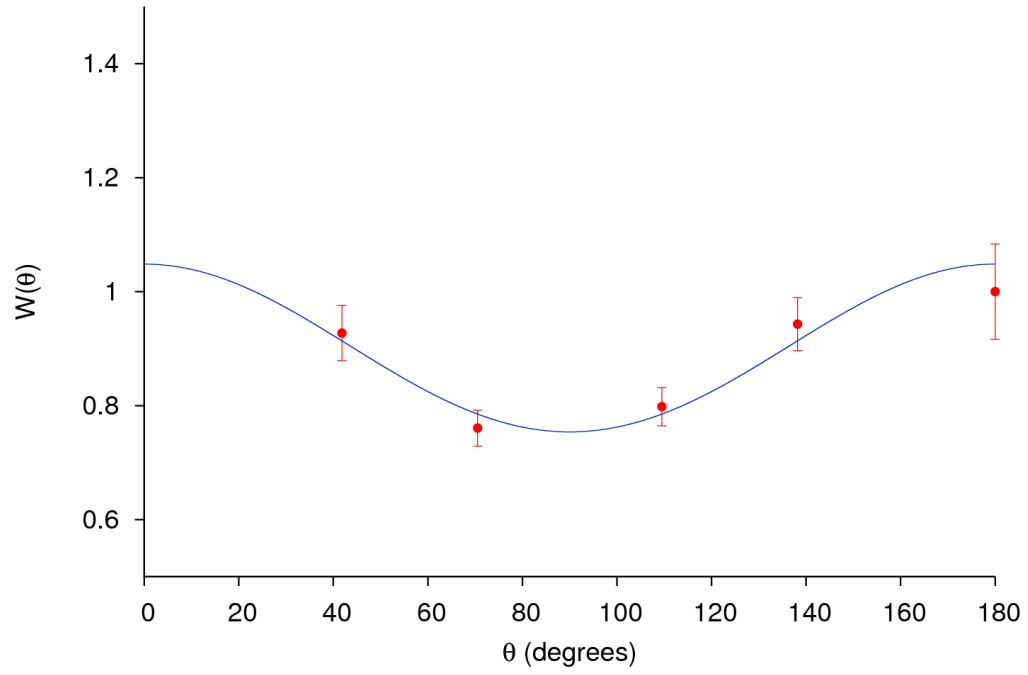
272 - 417 Cascade



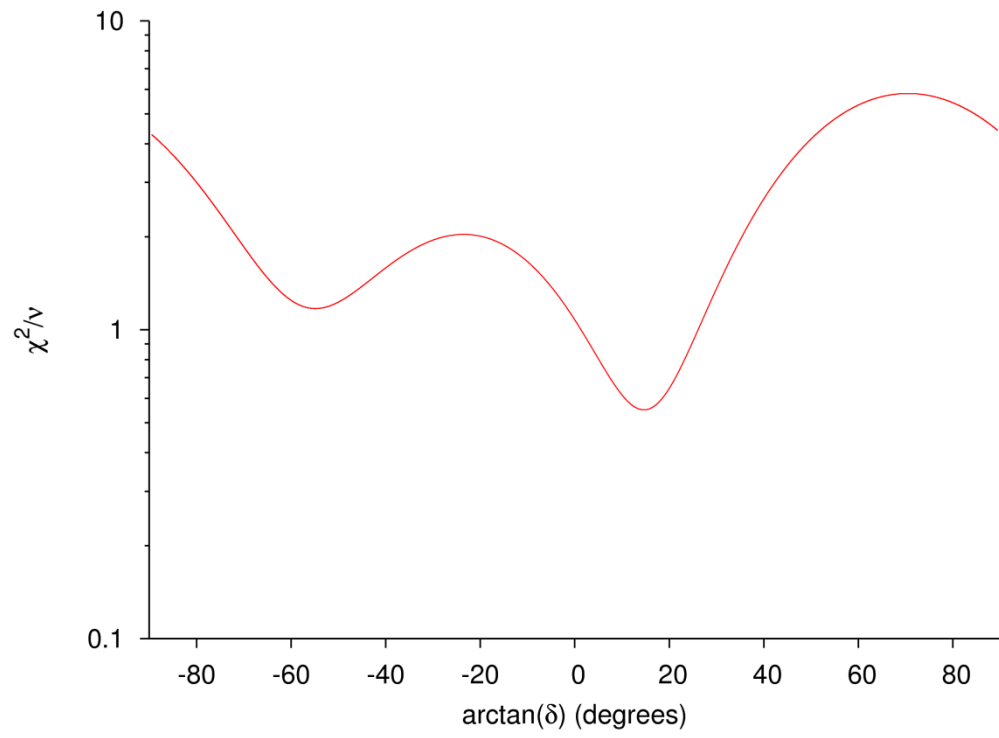
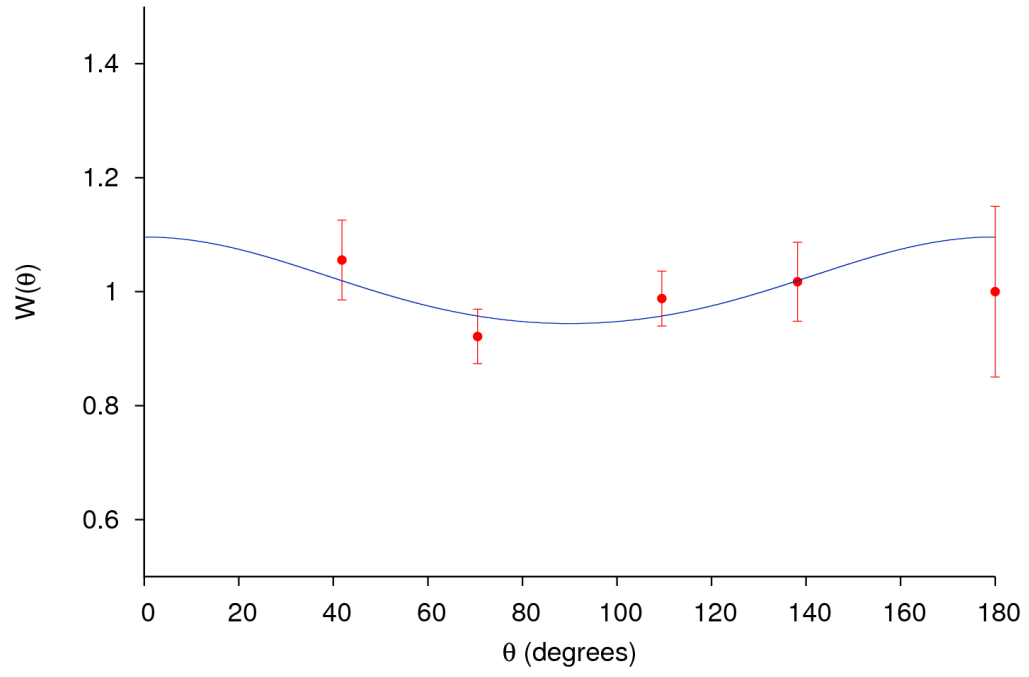
568 - 417 Cascade



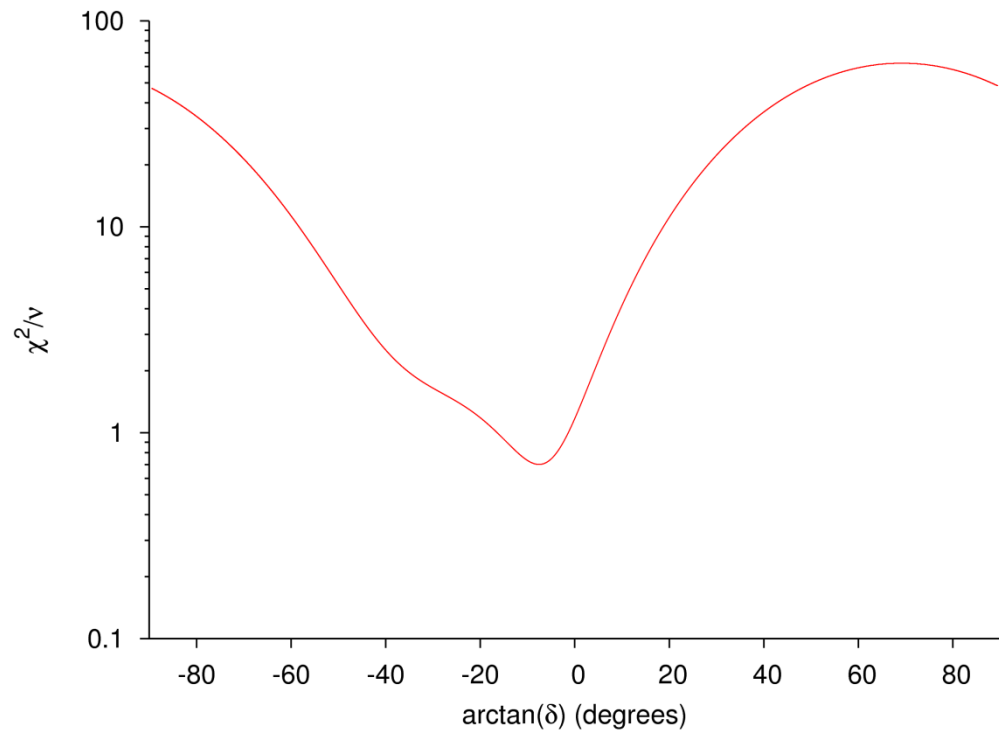
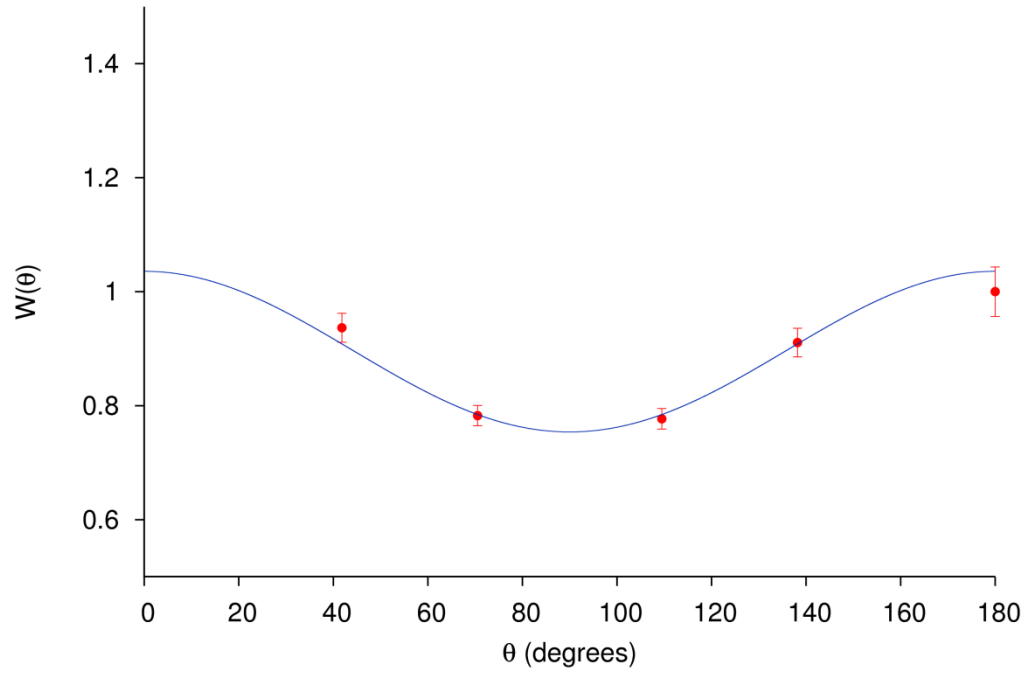
410 - 1097 Cascade



655 - 1097 Cascade



706 - 1097 Cascade



245 - 1507 Cascade

